School of Earth and Planetary Sciences

Department of Applied Geology

Petrochronology of detrital accessory phases & implications for the evolution of the Capricorn Orogen (Western Australia)

Sonia Armandola

This thesis is presented for the degree of
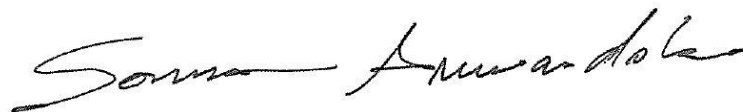**Doctor of Philosophy**
of
Curtin University

August 2018

DECLARATION

To the best of my knowledge and belief, I declare that this work of thesis contains no material published by any other person, except where due acknowledgments have been made. This thesis contains no material which has been accepted for the award of any other degree or diploma in any university.

Sonia Armandola

Date 28/08/2018

ABSTRACT

The Capricorn Orogen, in north Western Australia, is a Palaeoproterozoic to Neoproterozoic orogenic system that developed during the amalgamation of the Yilgarn and Pilbara cratons and the crustal blocks that lay between them. Following final amalgamation, the region underwent multiple intracratonic tectonic events and the formation of multiple Mesoproterozoic sedimentary basins (Yerrida Basin, Edmund Basin and Collier Basin). The Capricorn region is particularly well endowed in economically important ore deposits and these basins play an important role in the formation of basin-hosted deposits, and potential erosion and burial of older basement deposits. Hence, there is an economic driver to understand the evolution and provenance of the Capricorn's Mesoproterozoic basins. Furthermore, the provenance of these basins provides a valuable record of the synorogenic exhumation and erosion of Capricorn basement and places constraints on the tectonic evolution of the region. In this thesis, sedimentary facies analysis is combined with geochemical and geochronological analysis of detrital zircons to investigate the provenance and evolution of the Mesoproterozoic sedimentary basins of the Capricorn Orogen and provide constraints on the tectonic evolution of the region.

Facies analyses combined with U-Pb geochronology and geochemistry of detrital zircons from the Yerrida Basin revealed that the intracontinental rifting of the north margin of the Yilgarn Craton occurred at 2175 ± 39 Ma. The sediments were entirely derived from the Yilgarn Craton and the erosion of the crystalline rocks occurred from east toward west contemporaneously to the spread of the Yerrida Basin rifting. Separation of the Marymia Inlier likely occurred coevally to the final stages of the Yerrida Basin development. The Yerrida Basin rifting was characterized by active volcanism as it is suggested by the trace elements of the youngest detrital zircons examined, which are consistent with intermediate to mafic source rocks interpreted to coincide with local lava flows interbedded to the stratigraphy. Rifting of the Yilgarn Craton was synchronous to the continental collision of the Pilbara Craton and Glenburgh Terrane. However, the data suggest that the Yilgarn Craton was separated from the Pilbara Craton and Glenburgh Terrane, hence other mechanism promoting intracratonic rifting can be considered, such as mantle plume activity.

Stratigraphic analysis, U-Pb geochronology and geochemistry of detrital zircons from Edmund Basin highlight age gaps and palaeoenvironment changes in its lowermost part. Detrital zircons confer maximum depositional age of 1626±70 Ma to the Irregully Formation, which underlies the Abra deposit. The detrital zircon provenance investigation shows a shift of sources within the overlying Blue Billy Formation, which hosts the Abra deposit and indicate that the deposition of the Blue Billy formation occurred during an extensional tectonic reactivation of the Yilgarn Craton north margin. New age constraints for the Kiangi Creek Formation, which accumulated after 1484±30 Ma over the Abra deposit, point out an age gap of c. 100 Ma between the deposition of the basal and top successions of the Edmund Basin. Overall the provenance study of the detrital zircons from these formations shows that the sediments derived from different catchments, located eastward and indicates that the Abra deposit formed in a sub-basin located to the south of the Edmund Basin. This suggests that the stratigraphy of the Edmund Basin should be revised and that the basin should be subdivided within two distinct sub-basins.

U-Pb geochronology, geochemistry of detrital zircon grains and metamorphic titanate minerals revealed the presence of Collier Basin sediments to the south of the Capricorn Orogen. The Collier Basin sediments in the area examined are characterized by dolerite intrusions and peperitic margins, consistent with what has been observed in previous studies. The age of the mafic intrusions, indirectly dated with metamorphic titanite from the contact metamorphosed sediments, at 1093±21 Ma, is considered close to the depositional age of the hosting sediments. The facies analysis links the sediment with deposition in deep anoxic-water conditions of a large intracratonic sea, consistent with the Ilgarri Formation depositional environment. While the few detrital zircon minerals recovered indicate exotic sources of sediment. An intracratonic rift setting for the Capricorn Orogen is recognized during deposition of the Collier Basin topmost Ilgarari Formation. The Edmund Basin detrital zircons examined from an adjacent succession gave a maximum depositional age of 1539±10 Ma and were characterized by a 60% of detrital zircons with mafic parent rocks, interpreted to be eroded from intrusive mafic sills and dykes, correlative of the Waldburg Dolerite, which intrude the lower succession of the Edmund Basin.

U-Pb geochronology, geochemistry of detrital zircons from the Collier Basin gave new maximum depositional age constraints of 1117±34 Ma for the topmost Ilgarari Formation. The provenance analysis highlighted exotic sources of sediments within the Collier Basin, derived from the Musgrave Complex. The existence of a large intracratonic rift setting (Ngaanyatjarra Rift) between the Western Australian Craton and central Australia is inferred to be the carrier of the detritus, that was transported from southeast into the Capricorn Orogen.

The pooled trace element data of the detrital zircons from the three sedimentary basins examined, and their statistical analysis though regression models revealed that the detrital zircon trace elements coupled with their ages, can be effectively used as pathfinder to reconstruct the geodynamic history of long-lived orogens, such as the Capricorn Orogen. In particular, Y content in zircons records secular changes in the chemical composition of the continental crust by increasing its abundance after 2500 Ma, marking the establishment of a subduction regime on Earth. Then Y abundance increases in correspondence of the Glenburgh Orogeny, and a subduction-related setting, indicating potential subduction of older tonalite–trondhjemite–granodiorite rocks. Elemental ratios of zircon trace element data (Gd/Yb, HREE/LREE and Eu/Eu* ratios) show systematic variations that indicate a change in geodynamic setting from continental arc setting at c. 2000 Ma, coeval to the Glenburgh Orogeny, to a collisional setting contemporaneous to the c. 1800 Ma Capricorn Orogen, and a post-collisional setting established during the c. 1680 Ma Mangaroon Orogeny. The last orogenic event records both crustal recycling and a component of mantle influx associated with the relaxation of the continental crust under the Capricorn Orogen at c. 1620 Ma.

The data gathered in this research provide new stratigraphic constraints for the Yerrida, Edmund and Collier basins depositional history and tectonic evolution. Moreover, the data offer new insight into the tectonic activity of the Capricorn Orogen and adjacent crustal units, between 2200 and 1100 Ma. The sedimentary provenance technique, which was carried out with statistical tools including multidimensional scaling plot, Kolmogorov-Smirnov test, probability density plot, demonstrated to be effective in reconstructing the origin of the sediment and exhumation history of the source rocks. The detrital zircon trace elements, when examined through established geochemical plots, present limitations in

differentiating between diverse crustal rock types (e.g. large scatter and overlap of compositional fields). However, they were successfully used to distinguish between felsic and mafic protoliths for the detrital zircons.

ACKNOWLEDGEMENTS

CONTENTS

Chapter 5. Footprint of a large intracontinental rifting event: coupled detrital zircon geochronology and geochemistry from the Mesoproterozoic Collier Basin, Western Australia   109

Chapter 6. Unravelling secular change in geodynamic setting with detrital zircon: a study from the Capricorn Orogen, Western Australia 143

CHAPTER 1

INTRODUCTION

1. The provenance of sedimentary rocks, overview

The term "provenance" originates from the Latin ''provenire'' and means to originate (Weltje & von Eynatten, 2004; Mazumder, 2017). Sediment provenance investigations are the study of siliciclastic sediment origin and the evolutionary history of the ancient and modern sedimentary systems hosting them (Weltje & von Eynatten, 2004; Kemp et al., 2006; Garzanti et al., 2007). According to this concept, provenance investigations encompass all factors related to sediment production and include the composition and age of the parental rocks, as well as their paleotopography and paleogeography (Weltje & von Eynatten, 2004; Mazumder, 2017). Sedimentary provenance data play a critical role in assessing paleogeographic reconstructions, constraining lateral displacements in orogens, characterizing crust that is no longer exposed, mapping depositional systems, correlation the in subsurface, and predicting reservoir quality (Haughton et al., 1991; Weltje & von Eynatten, 2004; Garzanti et al., 2008; Mazumder, 2017).

Numerous studies have demonstrated a direct correlation between packages of sediments found within sinks and the tectonic activity of adjacent orogens (Cawood et al., 2003; Weltje & von Eynatten, 2004; Garzanti et al., 2007; Mazumder), 2017. In fact, the tectonic activity of crustal units represents a principal trigger for the generation of detritus, by eroding the exposed continental crust (Weltje & von Eynatten, 2004; Kemp et al., 2006; Garzanti et al., 2007; Capaldi et al., 2017; Mazumder, 2017). Sediments may carry distinct geochemical and mineralogical characteristics during their accumulation by preserving information on the source rocks' age and compositions. Thus sediments represent a primary archive to investigate source-to-sink links, transportation history, hydraulic sorting and the extent of recycling of material (Cawood et al., 2003; Weltje & von Eynatten, 2004; Allen & Allen, 2013; Nagarajan et al., 2014; Mazumder, 2017; Li et al., 2018). Since this relationship was established, the links between orogenic events and subsequent sedimentary basins has become the major target of provenance studies that extract information related to the source rocks from sediments and sedimentary rocks, through

the application of geological disciplines and a wide range of traditional and modern analytical techniques (Spaggiari et al., 2015; Haines et al., 2016; Barham et al., 2018).

Consolidated approaches to solve provenance investigations are based on the analysis of the bulk sediment textural and chemical composition, which are broadly employed to track the composition, origin and the tectonic setting of the parent rocks (e.g. Vezzoli et al., 2010; Nagarajan et al., 2014; Campodonico et al., 2016; Licht & Hemming, 2017). The composition of trace elements and rare earth elements (REEs) of sediments allow discriminating between the input of juvenile crustal material versus highly differentiated crustal material within the sediments, e.g. mafic and felsic source rocks (e.g. Lewin et al., 2017; Natali & Bianchini, 2017). While petrographic analysis of clast particles (e.g. sandstone) can assess the maturity and the transportation history of the sediments (e.g. Morton et al., 2002; Amorosi & Sammartino, 2017; Lewin et al., 2017). The two methods combined have the advantage of being applicable to all types of sediments, including clay minerals, and to be effective in originating lithofacies profiles that outline shifts in provenance, according to the chemical signature recorded in the sediments (Greggio et al., 2018). However, recycled sediments and long-distance transported and mixed sediments often lose distinctive chemical signals characteristic of a single origin. While chemical modification of the sediment composition can occur in environments characterized by strong weathering. For this reason, bulk chemical analysis and petrography of sediments are largely applied to modern sediments and less widespread for the study of ancient terrigenous systems (Basu et al., 2016; Schneider et al., 2016).

In the last decade improvement in analytical techniques e.g. ion probe - high-sensitivity instruments (SHRIMP; Slama et al., 2008) and laser ablation inductively coupled plasma mass spectrometry (LA-ICPMS; Kylander-Clark et al., 2013; Stearns et al., 2016), boosted the application of single accessory minerals to solve provenance studies (Janots et al., 2008; Taylor et al., 2012; Bracciali et al., 2013; Gehrels, 2014; Kirkland et al., 2017). Accessory mineral phases like zircon, titanite, garnet, apatite, monazite, rutile, muscovite and biotite have become increasingly important for provenance investigations. Such minerals retain source rock age and composition information that when measured offer insight to the genesis and evolutionary history of their parent rocks, which, in turn provide data to reconstruct provenance and infer aspects of regional tectonic histories (e.g. Frost et al., 2000; Spencer et al., 2016).

Geochronology of accessory minerals provides maximum depositional age to the sediment (e.g. Th-U-Pb, Sm-Nd, K-Ar, Rb-Sr and Lu-Hf) and give information fundamental to carry out intrabasinal stratigraphic correlations, by conferring time limits to the sedimentary rock units (Kemp et al., 2006; Stendal et al., 2006; Dickinson & Gehrels, 2009). Additionally, the age data can be interpreted as the protolith crystallization age and used to link the sediments with potential source rocks, while some phases (e.g. apatite, monazite and xenotime) record the exhumation age of their protolith and thus can be analysed to unravel the exhumation history of the crustal units being eroded to produce the detritus (Kemp et al., 2006; Stendal et al., 2006; Dickinson & Gehrels, 2009; Capaldi et al., 2017; Gemignani et al., 2017; Natali & Bianchini, 2017; Stutenbecker et al., 2017). Geochemistry of accessory minerals is another significant depository of information on the genetic conditions in which they crystallized and on their protolith's composition and evolution (e.g. Frost et al., 2000; Ksienzyk et al., 2012; Taylor et al., 2012; Barth et al., 2013; Grimes et al., 2015; Capaldi et al., 2017). For example, the trace element concentrations of zircon and titanite are dependent on the metamorphic or magmatic setting existing during their crystallization and can be used to discriminate between (e.g. Frost et al., 2000; Hoskin & Schaltegger, 2003).

2. Zircon and titanite accessory minerals in provenance studies, rationale

Zircon accessory phase

Zircon is a particularly stable accessory mineral. It forms in intermediate to felsic melts at ~750 °C (Watson et al., 2006) and due to its high crystallization temperature and chemical stability it can survive subsequent magmatic, metamorphic and erosional processes that destroy most other common minerals (Corfu et al., 2003; Dickinson & Gehrels, 2009; Gehrels, 2014). Zircon incorporates radiogenic U and Th in its structure, and thus can be used as a geochronometer, reaching high precision and accuracy in age measurements with three systems ($^{238}U{\rightarrow}^{206}Pb$, $^{235}U{\rightarrow}^{207}Pb$, and $^{232}Th{\rightarrow}^{208}Pb$; Andersen, 2005; Gehrels, 2014). Moreover, the structure of the zircon crystalcan be constituted by segments, each recording a specific growth phase, and a core that retains the zircon crystallization age (Corfu et al., 2003; Kemp et al., 2007). While crystallizing, zircon incorporates O and Lu-Hf isotopes, which can be employed to assess the parent melt genesis (e.g. primitive mantle versus contaminated melts) and

establish the geodynamic setting at the time of its crystallization (Kemp et al., 2006; Johnson et al., 2017). Furthermore, zircon incorporates large proportions of high field strength incompatible elements (HFSE) present in the melt. Trace elements are incorporated in zircon in equilibria with the protolith chemical system and co-genetic minerals, and thus, give information about the composition of the parental melt and the geodynamic setting in which the melt originated (Belousova et al., 2002; Griffin et al., 2004; Barth et al., 2013; Grimes et al., 2015; Lu et al., 2016). For instance, the enrichment of Y within zircon minerals is an indicator of the melt affinity with felsic magmas (Belousova et al., 2002). While for example, Eu/Eu* and (Eu/Eu*)/Y ratios can be used as a pathfinder for porphyry Cu-Mo-Au deposits and to constrain the protolith melt fertility (Lu et al., 2016).

Although zircon trace elements are largely employed in the characterization of magmatic zircon crystals and their protolith (Hoskin & Ireland, 2000; Rubatto, 2002; Hoskin & Schaltegger, 2003; Kirkland et al., 2015; Chapman et al., 2016), to date they have played a relatively minor role in provenance investigations, especially when compared to Lu-Hf and O isotopes (e.g. Wang et al., 2010; Iizuka et al., 2013; Chamberlain et al., 2014; Haines et al., 2016; Johnson et al., 2017). Moreover, uncertainty related to the trace element distribution between melt and minerals, which is highly influenced by both regional and local factors including temperature gradient, pressure and redox conditions of the melt, further complicate their interpretation (e.g. Chapman et al., 2016).

Besides the widespread discrimination diagrams approach, another effective way to examine detrital zircon trace elements to decipher the information contained in the trace element signature of zircon, is through the application of statistical methods. Statistical approaches are routinely applied to aid provenance studies by examining the distribution of the age data of zircon grains. For example, they can track the affinity between sediments and source rocks and compare the similarity of sedimentary units with multidimensional scaling plots (MDS) and Kolmogorov-Smirnov tests (K-S test; Vermeesch et al., 2016). Whereas trace elements can be investigated through principle component analysis (PCA; Vermeesch et al., 2016), or with the help of descriptive statistics (bootstrap methods; McKenzie et al., 2018). Statistical analysis applied to trace element data, might reveal a key approach to encompass their intrinsic

compositional variability (Chamberlain et al., 2014; Chapman et al., 2016; Spencer et al., 2016; McKenzie et al., 2018).

Titanite accessory phase

Tracking tectonic processes becomes increasingly difficult when subsequent tectono-thermal episodes occur in a region. Dating and correlating tectonomagmatic events requires the help of ''sensitive'' accessory phases that due to their physical properties are reactive to thermal variations (Frost et al., 2000; Gao et al., 2011; Gao et al., 2012; Plavsa et al., 2018). Minerals that record the age of these events, such as titanite are capable of recrystallizing from pre-existing titanite minerals or from the break-down of pre-existing minerals, both in igneous, metamorphic and sedimentary rocks (Frost et al., 2000; Gao et al., 2011; Gao et al., 2012). Titanite crystallizes between ~600 and ~700 °C and has a considerable capacity for element substitutions, which makes it an important carrier of trace elements, particularly the rare-earth elements (REE) and high field strength elements (HFSE; Plavsa et al., 2018). The ability for incorporating appreciable quantities of U into its lattice (10 to >100 ppm; Frost et al., 2000) makes titanite an important mineral for U–Pb dating (Bonamici et al., 2015). However, titanite is highly reactive, because most rocks contain numerous phases with Ti and Ca, thus titanite in contrast to zircon, recrystallizes resetting its age according to subsequent tectono-thermal events (Gao et al., 2011; Bonamici et al., 2015). Hence, titanite is helpful in constraining metamorphic and magmatic episodes, and in establishing a time frame for pulsed magmatic heating, fluid infiltration, deformation events and rock cooling history (Gao et al., 2011; Bonamici et al., 2015). Metamorphic titanite obtained from sedimentary successions can be used to aid the provenance study of those basins that originated in extensional tectonic settings and are characterized by mafic sills and dykes' intrusions in their stratigraphy. In this context, titanite can be used to indirectly date the timing of the extensional events and to provide the minimum depositional age to the sediments hosting the melt intrusions.

3. The long-lived Capricorn Orogen and its subsequent sedimentary basins, an overview

A challenging application of provenance studies is represented by looking at Precambrian terranes that record billions of years of tectonic history during which they were deformed and eroded multiple times. Moreover, Precambrian terranes are

typically, poorly preserved and commonly tectonically dissected in separate continents, due to supercontinent amalgamation and break up cycles (Evans & Mitchell, 2011). Consequently, finding links between Precambrian source rocks and subsequent sedimentary basins is difficult (e.g. Halilovic et al., 2004; Pirajno & Bryah, 2007). Nonetheless, Precambrian terranes, along with their covers, constitute the largest reservoir of ore minerals in the continental crust, and their study is critical for understanding both ancient lithospheric processes and ore-forming mechanisms (Pirajno, 2004). A remarkable case is found in north Western Australia, in the Capricorn Orogen, which is an exceptionally preserved Palaeoproterozoic belt of 1000 km width (Fig. 1). The area was subject to intense tectonic activity from 2.2 Ga till 1.9 Ga, when the Pilbara Craton, Glenburgh Terrane and Yilgarn Craton collided to form the West Australia Craton (Cawood & Tyler, 2004), and evolved over a billion years of subsequent intracratonic tectonic and magmatic episodes (Johnson et al., 2013; Dentith et al., 2014; Alghamdi et al., 2017).

The Capricorn Orogen history is poorly constrained and is still the object of ongoing research, from the cratonic margins to the sedimentary cover. In its central part and on the craton margins, the Capricorn Orogen is characterized by thick sedimentary basins of Palaeoproterozoic to Mesoproterozoic age. These reach up to 12 km in thickness and accumulated during several discrete tectonic events over a time span of one billion years (Martin & Thorne, 2004; Johnson et al., 2013; Alghamdi et al., 2017).

The area, which is highly prospective for mineral deposits, has inadequate geological data, especially in regards to its sedimentary cover, due to the volume of sediments that they host, the numerous environmental transitions recorded in their sedimentary units and the long tectonic history that deformed and displaced them (e.g. Halilovic et al., 2004; Cutten et al., 2016; Hocking et al., 2017; Krapež et al., 2017).

Herein we examine three sedimentary basins of the Capricorn Orogen region that range in age from Palaeo to Mesoproterozoic. The Palaeoproterozoic Yerrida Basin (Fig. 1) formed on the northern margin of the Yilgarn Craton within a rift environment at c. 2175 Ma, while the Pilbara Craton collided the Glenburgh Terrane. Its sediments have poor age constraints and the geodynamic setting linked with its origin is obscure (Hocking et al., 2017). The Edmund and Collier basins are middle to late Mesoproterozoic basins that formed after the last significant tectonic reactivation in

6

the Capricorn Orogen region (1640-1680 Ma Mangaroon Orogeny). The Edmund Basin hosts the giant stratabound base metals Abra Pb–Zn–Cu deposit, while the Collier Basin hosts Cu-Ag stratabound mineralization related to the intrusion of dykes and sills in its uppermost formations (Pirajno & Bagas, 2008). The sedimentary successions of the two basins accumulated during two distinct events, that in complex lasted almost half a billion year, with scarce data available for their age, spatial distribution and sources (Martin & Thorne, 2004).
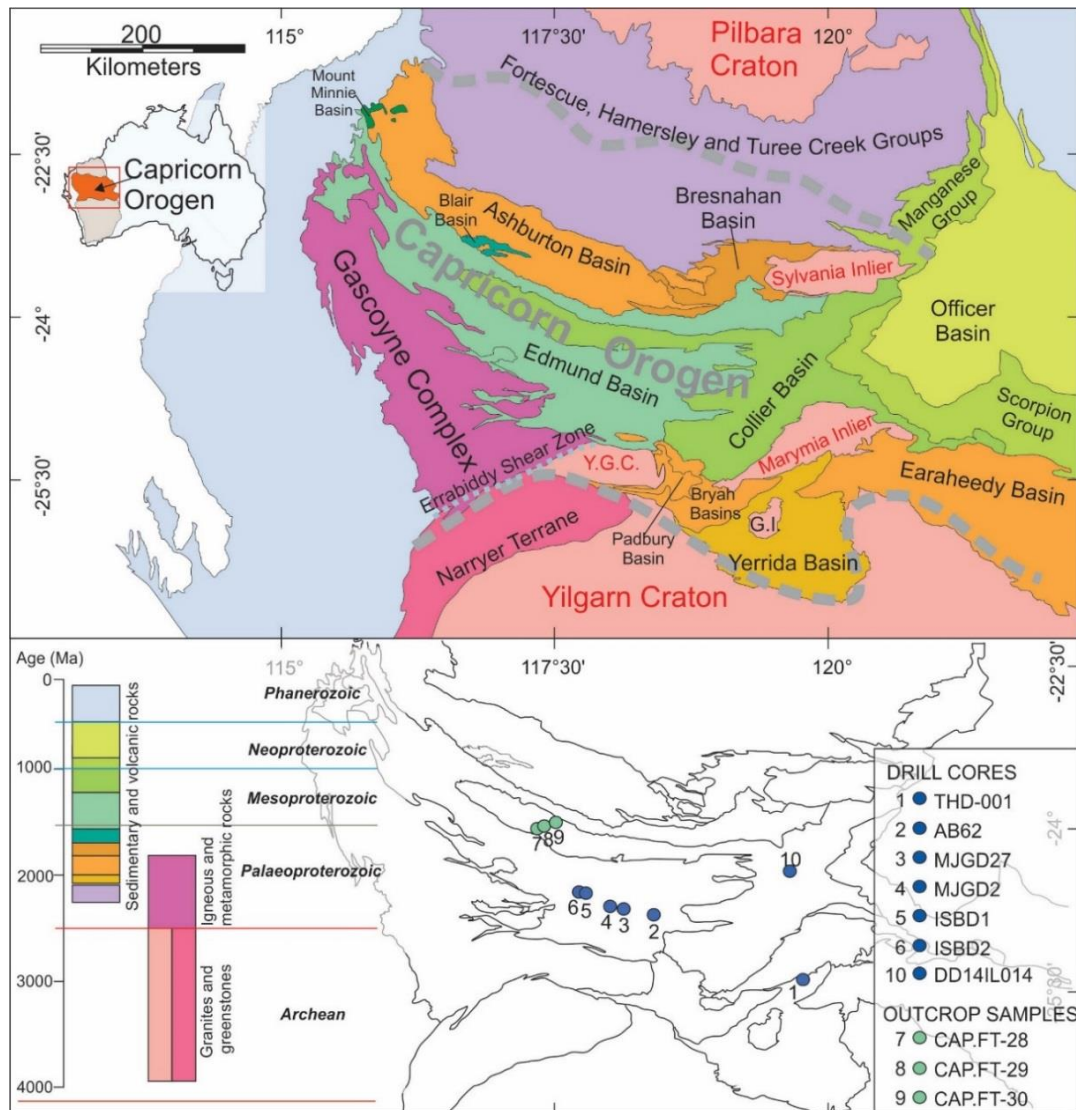
Fig. 1. Map of the main tectonic units of the Capricorn Orogen modified after Cawood & Tyler (2004) and Johnson et al. (2013). The grey dashed line defines the Capricorn Orogen extent. Samples and drill core locations with respect to the Capricorn Orogen are shown by green and blue circles. Five drill cores were analysed from the Edmund Basin and one drill core was analysed for the Collier Basin in the central-eastern

Capricorn Orogen area with the addition of three surface samples from the centre. The Yerrida Basin was investigated through a single drill core of 1 km.

4. Aims of this work

In this work, the provenance of the Palaeoproterozoic Yerrida Basin and Mesoproterozoic Edmund and Collier basins in the Capricorn Orogen is resolved with an original approach that integrates geochronology (U-Pb) and geostatistical tools (K-S test and MDS), with more novel same-grain trace-element geochemistry. Laser ablation split stream inductively coupled plasma mass spectrometry (LASS-ICP-MS) is used to measure both the U-Pb isotopes and the elemental abundances simultaneously and is set to enhance the application of trace element geochemistry in provenance studies. With this original approach this work aims to:

(I)   Resolve the sources and routing of sediments of the Palaeoproterozoic Yerrida Basin and the Mesoproterozoic Edmund and Collier basins;

(II)   Unravel the tectonic evolution of the basins and their sources;

(III) Develop tectonic models for the three basins examined;

(IV) Integrate the tectonic models in the tectonic history of the Capricorn Orogen;

(V)   Test the application of trace element geochemistry to the solution of provenance problems as pathfinder for source terranes and tectonic events and constrain shifts of geodynamic environments in long-lived orogenic systems.

(VI)   Ultimately inform the tectonic history of the Capricorn Orogen and deliver new knowledge to enhance the mineral exploration in Western Australia under the ''Uncover the Distal Footprints of Giant Ore Systems'' project funded by the Science and Industry Endowment Fund (SIEF) and the Mineral Research Institute of Western Australia (MRIWA).

5. Thesis Outline

The provenance study of the Yerrida, Edmund and Collier basins is presented in individual chapters, in order from the oldest (Yerrida Basin, Chapter 2) to the youngest (Edmund Basin, Chapter 3 and then Collier Basin, Chapter 4). A final chapter presents the potential of the detrital zircon trace elements to unravel the geodynamic history of ancient orogenic belt. The chapters are structured as journal articles that have been either submitted or that will be submitted. The Tables containing all the data relative

to the accessory minerals are contained in Appendix 1. The mineral separation technique and the analytical methodology used are reported in every chapter for each provenance investigation and are described in Appendix 2.

Chapter 2 provides new geochronological and provenance constraints for the Palaeoproterozoic Yerrida Basin, based on the detrital zircon record and presents a detailed study of the stratigraphy that characterized the lower group of the Yerrida Basin, the Windplain Group (drill core THD001). The Yerrida Basin formed at c. 2175 Ga, during protracted rifting of the northern margin of the Yilgarn Craton and records volcanism in the western part. The tectonic evolution of the Yilgarn Craton is discussed in light of the sediment transport directions obtained from the detrital zircon, and the current model proposed.

Chapter 3 presents a geochronological and provenance study for the basal sediments of the Mesoproterozoic Edmund Basin, carried out in the Abra polymetallic deposit host rock (drill core AB62). The study was conducted as part of a broader investigation on the genesis and age of the mineralization of Abra in the "Uncover the Distal Footprints of Giant Ore Systems" project. It aims to characterize the Abra deposit host rocks stratigraphy and provenance and constrain the broad tectonic setting coeval to the mineralization.

Chapter 4 reports data for both the Edmund and Collier basins. It contains age constraints of the Edmund and Collier basins middle to top formations and of their mafic sill intrusions (drill core MJGD2 and MJGD27), via coupled indirect and direct dating of metamorphic titanite and detrital zircon grains. Implications for an early rift of the Capricorn Orogen at c. 1.1 Ga is discussed.

Chapter 5 describes a provenance study and tectonic model for the late Mesoproterozoic Collier Basin. The provenance study is based on three surface samples and a single drill core DD14IL014. The study targets the centre and eastern part of the Collier Basin and explores the existence of a large intracratonic rift that is proposed to have existed between Western Australia and central Australia at c. 1.1 Ga.

Chapter 6 summarizes the age and elemental data acquired for the three basins in the previous chapters. The trace elements data are used in this section altogether to carry out a study on the secular changes and geodynamic history of the Capricorn Orogen

between the Palaeoproterozoic and the Mesoproterozoic. Limitations of the trace element methods are discussed.

Chapter 7 contains the conclusions of this work. It covers all the work done in this thesis with a review of all the outcomes.

References

Alghamdi, A. H., Aitken, A. R. A. & Dentith, M. C. (2018). The composition and structure of the deep crust of the Capricorn Orogen. *Australian Journal of Earth Sciences,* 65, 9-24.

Allen, P. A. & Allen, J. R. (2013*).* The sediment routing system. *Basin Analysis: Principles and Application to Petroleum Play Assessment,* (3rd ed, pp. 225-227). Oxford: Wiley-Blackwell.

Amorosi, A. & Sammartino, I. (2017). Shifts in sediment provenance across a hierarchy of bounding surfaces: A sequence-stratigraphic perspective from bulk-sediment geochemistry. *Sedimentary Geology,* 375, 145-156.

Andersen, T. (2005). Detrital zircons as tracers of sedimentary provenance: Limiting conditions from statistics and numerical simulation. *Chemical Geology,* 216, 249-270.

Barham, M., Reynolds, S., Kirkland, C. L., O'Leary, M. J., Evans, N. J., Allen, H. J., Haines, P. W., Hocking, R. M. & McDonald, B. J. (2018). Sediment routing and basin evolution in Proterozoic to Mesozoic east Gondwana: A case study from southern Australia. *Gondwana Research,* 58, 122-140.

Barth, A. P., Wooden, J. L., Jacobson, C. E. & Economos, R. C. (2013). Detrital zircon as a proxy for tracking the magmatic arc system: The California arc example. *Geology,* 41, 223-226.

Basu, A., Bickford, M. E. & Deasy, R. (2016). Inferring tectonic provenance of siliciclastic rocks from their chemical compositions: A dissent. *Sedimentary Geology,* 336, 26-35.

Belousova, E. A., Griffin, W. L., O'Reilly, S. Y. & Fisher, N. I. (2002). Igneous zircon: Trace element composition as an indicator of source rock type. *Contributions to Mineralogy and Petrology,* 143, 602-622.

Bonamici, C. E., Fanning, C. M., Kozdon, R., Fournelle, J. H. & Valley, J. W. (2015). Combined oxygen-isotope and U-Pb zoning studies of titanite: New criteria for age preservation. *Chemical Geology,* 398, 70-84.

Bracciali, L., Parrish, R. R., Horstwood, M. S. A., Condon, D. J. & Najman, Y. (2013). UPb LA-(MC)-ICP-MS dating of rutile: New reference materials and applications to sedimentary provenance. *Chemical Geology,* 347, 82-101.

Campodonico, V. A., García, M. G. & Pasquini, A. I. (2016). The geochemical signature of suspended sediments in the Parana River basin: Implications for provenance, weathering and sedimentary recycling. *Catena,* 143, 201-214.

Capaldi, T. N., Horton, B. K., McKenzie, N. R., Stockli, D. F. & Odlum, M. L. (2017). Sediment provenance in contractional orogens: The detrital zircon record from modern rivers in the Andean fold-thrust belt and foreland basin of western Argentina. *Earth and Planetary Science Letters,* 479, 83-97.

Cawood, P. A., Nemchin, A. A., Freeman, M. & Sircombe, K. (2003). Linking source and sedimentary basin: Detrital zircon record of sediment flux along a modern river system and implications for provenance studies. *Earth and Planetary Science Letters,* 210, 259-268.

Cawood, P. A. & Tyler, I. M. (2004). Assembling and reactivating the Proterozoic Capricorn Orogen: Lithotectonic elements, orogenies, and significance. *Precambrian Research,* 128, 201-218.

Chamberlain, K. J., Wilson, C. J. N., Wooden, J. L., Charlier, B. L. A. & Ireland, T. R. (2014). New Perspectives on the Bishop Tuff from Zircon Textures, Ages and Trace Elements. *Journal of Petrology,* 55, 395-426.

Chapman, J. B., Gehrels, G. E., Ducea, M. N., Giesler, N. & Pullen, A. (2016). A new method for estimating parent rock trace element concentrations from zircon. *Chemical Geology,* 439, 59-70.

Corfu, F., Hanchar, J. M., Hoskin, P. W. O. & Kinny, P. (2003). Atlas of Zircon Textures. *Reviews in Mineralogy and Geochemistry,* 53, 469-500.

Cutten, H., Johnson, S., Thorne, A., Wingate, M., Kirkland, C., Belousova, E., Blay, O. & Zwingmann, H. (2016). Deposition, Provenance, Inversion History and Mineralization of the Proterozoic Edmund and Collier Basins, Capricorn Orogen. Geological Survey Western Australia*,* Report 127.

Dentith, M., Johnson, S. P., Evans, S., Aitken, A., Joly, A., Thiel, S. & Tyler, I. M. (2014). A magnetotelluric traverse across the eastern part of the Capricorn Orogen. Geological Survey of Western Australia*,* Report 135.

Dickinson, W. R. & Gehrels, G. E. (2009). Use of U-Pb ages of detrital zircons to infer maximum depositional ages of strata: A test against a Colorado Plateau Mesozoic database. *Earth and Planetary Science Letters*, 288, 115-125.

Evans, D. A. D. & Mitchell, R. N. (2011). Assembly and breakup of the core of Paleoproterozoic-Mesoproterozoic supercontinent Nuna. *Geology,* 39, 443-446.

Frost, B. R., Chamberlain, K. R. & Schumacher, J. C. (2000). Sphene (titanite): phase relations and role as a geochronometer. *Chemical Geology,* 172, 131-148.

Gao, X. Y., Zheng, Y. F. & Chen, Y. X. (2011). U-Pb ages and trace elements in metamorphic zircon and titanite from UHP eclogite in the Dabie orogen: Constraints on P-T-t path. *Journal of Metamorphic Geology,* 29, 721-740.

Gao, X. Y., Zheng, Y. F., Chen, Y. X. & Guo, J. (2012). Geochemical and U-Pb age constraints on the occurrence of polygenetic titanites in UHP metagranite in the Dabie orogen. *Lithos,* 136-139, 93-108.

Garzanti, E., Vezzoli, G., Andò, S., Lavé, J., Attal, M., France-Lanord, C. & DeCelles, P. (2007). Quantifying sand provenance and erosion (Marsyandi River, Nepal Himalaya). *Earth and Planetary Science Letters,* 258, 500-515.

Garzanti, E., Andò, S. & Vezzoli, G. (2008). Settling equivalence of detrital minerals and grain-size dependence of sediment composition. *Earth and Planetary Science Letters,* 273, 138-151.

Gehrels, G. (2014). Detrital Zircon U-Pb Geochronology Applied to Tectonics. *Annual Review of Earth and Planetary Sciences,* 42, 127-149.

Gemignani, L., Sun, X., Braun, J., van Gerve, T. D. & Wijbrans, J. R. (2017). A new detrital mica 40Ar/39Ar dating approach for provenance and exhumation of the Eastern Alps. *Tectonics,* 36, 1521-1537.

Greggio, N., Giambastiani, B. M. S., Campo, B., Dinelli, E., Amorosi, A. & Tyrrell, S. (2018). Sediment composition, provenance, and Holocene paleoenvironmental evolution of the Southern Po River coastal plain (Italy). *Geological Journal,* 53, 914-928.

Griffin, W. L., Belousova, E. A., Shee, S. R., Pearson, N. J. & Reilly, S. Y. O. (2004). Archean crustal evolution in the northern Yilgarn Craton: U – Pb and Hf-isotope evidence from detrital zircons. *Precambrian Research*, 131, 231-282.

Grimes, C. B., Wooden, J. L., Cheadle, M. J. & John, B. E. (2015). "Fingerprinting" tectono-magmatic provenance using trace elements in igneous zircon. *Contributions to Mineralogy and Petrology,* 170, 46-46.

Haines, P. W., Kirkland, C. L., Wingate, M. T. D., Allen, H., Belousova, E. A. & Gréau Y., (2016). Tracking sediment dispersal during orogenesis: A zircon age and Hf isotope study from the western Amadeus Basin, Australia. *Gondwana Research,* 37, 324-347.

Halilovic, J., Cawood, P. A., Jones, J. A., Pirajno, F. & Nemchin, A. A. (2004). Provenance of the Earaheedy Basin: Implications for assembly of the Western Australian Craton. *Precambrian Research,* 128, 343-366.

Haughton, P. D. W., Todd, S. P. & Morton, A. C. (1991). Sedimentary provenance studies. *Developments in Sedimentary Provenance Studies* (vol. 57, pp. 1-11). London: Geological Society, Special Publications.

Hocking, R., Lindsay, M., Aitken, A., Copp, I., Jones, J., Martin, D., Pirajno, F., Metelka, V., Occhipinti, S., Hocking, R., Lindsay, M., Aitken, A., Copp, I., Jones, J., Sheppard, S., Pirajno, F. & Metelka, V. (2017). Paleoproterozoic basin development on the northern Yilgarn Craton, Western Australia. *Precambrian Research,* 300, 121-140.

Hoskin, P. W. O. & Ireland, T. R. (2000). Rare earth element chemistry of zircon and its use as a provenance indicator. *Geology,* 28, 627-630.

Hoskin, P. W. O. & Schaltegger, U. (2003). The composition of zircon and igneous and metamorphic petrogenesis. *Reviews in Mineralogy and Geochemistry,* 53, 27-62.

Iizuka, T., Campbell, I. H., Allen, C. M., Gill, J. B., Maruyama, S. & Makoka, F. (2013). Evolution of the African continental crust as recorded by U-Pb, Lu-Hf and O isotopes in detrital zircons from modern rivers. *Geochimica et Cosmochimica Acta,* 107, 96-120.

Janots, E., Engi, M., Berger, A., Allaz, J., Schwarz, J. O. & Spandler, C. (2008). Prograde metamorphic sequence of REE minerals in pelitic rocks of the Central Alps: implications for allanite–monazite–xenotime phase relations from 250 to 610 °C. *Journal of Metamorphic Geology*, 26, 509-526.

Johnson, S. P., Thorne, A. M., Tyler, I. M., Korsch, R. J., Kennett, B. L. N. N., Cutten, H. N., Goodwin, J., Blay, O., Blewett, R. S., Joly, A., Dentith, M. C., Aitken, A. R. A. A., Holzschuh, J., Salmon, M., Reading, A., Heinson, G., Boren, G., Ross, J., Costelloe, R. D. & Fomin, T. (2013). Crustal architecture of the Capricorn Orogen, Western Australia and associated metallogeny. *Australian Journal of Earth Sciences,* 60, 681-705.

Johnson, T. E., Brown, M., Gardiner, N. J., Kirkland, C. L. & Smithies, R. H. (2017). Earth's first stable continents did not form by subduction. *Nature,* 543, 239-242.

Kemp, A. I., Hawkesworth, C. J., Paterson, B. A. & Kinny, P. D. (2006). Episodic growth of the Gondwana supercontinent from hafnium and oxygen isotopes in zircon. *Nature,* 439, 580-583.

Kemp, A. I. S., Hawkesworth, C. J., Foster, G. L., Paterson, B. A., Woodhead, J. D., Hergt, J. M., Gray, C. M. & Whitehouse, M. J. (2007). Magmatic and Crustal Differentiation History of Granitic Rocks from Hf-O Isotopes in Zircon. *Science*, 315, 980-983.

Kirkland, C. L., Smithies, R. H., Taylor, R. J. M., Evans, N. & McDonald, B. (2015). Zircon Th/U ratios in magmatic environs. *Lithos,* 212-215, 397-414.

Kirkland, C. L., Hollis, J., Danišík, M., Petersen, J., Evans, N. J. & McDonald, B. J. (2017). Apatite and titanite from the Karrat Group, Greenland; implications for charting the thermal evolution of crust from the U-Pb geochronology of common Pb bearing phases. *Precambrian Research,* 300, 107-120.

Krapež, B., Müller, S. G., Fletcher, I. R. & Rasmussen, B. (2017). A tale of two basins? Stratigraphy and detrital zircon provenance of the Palaeoproterozoic Turee Creek and Horseshoe basins of Western Australia. *Precambrian Research,* 294, 67-90.

Ksienzyk, A. K., Jacobs, J., Boger, S. D., Košler, J., Sircombe, K. N. & Whitehouse, M. J. (2012). U–Pb ages of metamorphic monazite and detrital zircon from the Northampton Complex: evidence of two orogenic cycles in Western Australia. *Precambrian Research,* 198-199, 37-50.

Kylander-Clark, A. R. C., Hacker, B. R. & Cottle, J. M. (2013). Laser-ablation split-stream ICP petrochronology. *Chemical Geology,* 345, 99-112.

Lewin, A., Meinhold, G., Hinderer, M., Dawit, E. L. & Bussert, R. (2018). Provenance of sandstones in Ethiopia during Late Ordovician and Carboniferous–Permian Gondwana glaciations: Petrography and geochemistry of the Enticho Sandstone and the Edaga Arbi Glacials. *Sedimentary Geology,* 375, 188-202.

Li, Y., He, D., Li, D., Lu, R., Fan, C., Sun, Y. & Huang, H. (2018). Sedimentary provenance constraints on the Jurassic to Cretaceous palaeogeography of Sichuan Basin, SW China. *Gondwana Research,* 60, 15-33.

Licht, K. J. & Hemming, S. R. (2017). Analysis of Antarctic glaciogenic sediment provenance through geochemical and petrologic applications. *Quaternary Science Reviews,* 164, 1-24.

Lu, Y.-j., Loucks, R. R., Fiorentini, M., McCuaig, T. C., Evans, N. J., Yang, Z.-m., Hou, Z.-q., Kirkland, C. L., Parra-avila, L. A., Kobussen, A. & Al, L. U. E. T. (2016). Chapter 13 Zircon Compositions as a Pathfinder for Porphyry Cu ± Mo ± Au Deposits *. *Economic Geology Special Publication,* 19, 329-347.

Martin, D. M. B. & Thorne, A. M. (2004). Tectonic setting and basin evolution of the Bangemall Supergroup in the northwestern Capricorn Orogen. *Precambrian Research,* 128, 385-409.

Mazumder, R. (2017). Sediment Provenance: Influences on Compositional Change from Source to Sink. *Sediment Provenance: Influences on Compositional Change from Source to Sink,* (pp.1-4). Elsevier.

McKenzie, N. R., Smye, A. J., Hegde, V. S. & Stockli, D. F. (2018). Continental growth histories revealed by detrital zircon trace elements: A case study from India. *Geology,* 46, 275-278.

Morton, a., O'B. Knox, R. W. & Hallsworth, C. (2002). Correlation of reservoir sandstones using quantitative heavy mineral analysis. *Petroleum Geoscience,* 8, 251-262.

Nagarajan, R., Roy, P. D., Jonathan, M. P., Lozano, R., Kessler, F. L. & Prasanna, M. V. (2014). Geochemistry of Neogene sedimentary rocks from Borneo Basin, East Malaysia: Paleo-weathering, provenance and tectonic setting. *Chemie der Erde – Geochemistry,* 74, 139-146.

Natali, C. & Bianchini, G. (2017). Geochemical proxies of sediment provenance in alluvial plains with interfering fluvial systems: A study case from NE Italy. *Catena*, 157, 67-74.

Pirajno, F. (2004). Metallogeny in the Capricorn Orogen, Western Australia, the result of multiple ore-forming processes. *Precambrian Research,* 128, 411-439.

Pirajno, F. & Bryah, T. (2007). Geology and mineral systems of the Paleoproterozoic basins of the eastern Capricorn Orogen. *Geological Survey of Western Australia, extended abstracts: promoting the prospectivity of Western Australia,* 2007/2, 7-9.

Pirajno, F. & Bagas, L. (2008). A review of Australia's Proterozoic mineral systems and genetic models. *Precambrian Research,* 166, 54-80.

Plavsa, D., Reddy, S. M., Agangi, A., Clark, C., Kylander-Clark, A. & Tiddy, C. J. (2018). Microstructural, trace element and geochronological characterization of TiO_2 polymorphs and implications for mineral exploration. *Chemical Geology,* 476, 130-149.

Rubatto, D. (2002). Zircon trace element geochemistry: Partitioning with garnet and the link between U-Pb ages and metamorphism. *Chemical Geology,* 184, 123-138.

Schneider, S., Hornung, J., Hinderer, M. & Garzanti, E. (2016). Petrography and geochemistry of modern river sediments in an equatorial environment (Rwenzori Mountains and Albertine rift, Uganda) — Implications for weathering and provenance. *Sedimentary Geology,* 336, 106-119.

Slama, J., Kosler, J., Condon, D. J., Crowley, J. L., Gerdes, A., Hanchar, J. M., Horstwood, M. S. A., Morris, G. A., Nasdala, L., Norberg, N., Schaltegger, U., Schoene, B., Tubrett, M. N. & Whitehouse, M. J. (2008). Plešovice zircon - A new natural reference material for U-Pb and Hf isotopic microanalysis. *Chemical Geology,* 249, 1-35.

Spaggiari, C. V., Kirkland, C. L., Smithies, R. H., Wingate, M. T. D. & Belousova, E. A. (2015). Transformation of an Archean craton margin during Proterozoic basin formation and magmatism: The Albany-Fraser Orogen, Western Australia. *Precambrian Research,* 266, 440-466.

Spencer, C. J., Kirkland, C. L. & Taylor, R. J. M. (2016). Strategies towards statistically robust interpretations of in situ U-Pb zircon geochronology. *Geoscience Frontiers,* 7, 581-589.

Stearns, M. A., Cottle, J. M. & Hacker, B. R. (2016). Extracting thermal histories from the near-rim zoning in titanite using coupled U-Pb and trace-element depth profiles by single-shot laser-ablation split stream (SS-LASS) ICP-MS. *Chemical Geology,* 422, 13-24.

Stendal, H., Toteu, S. F., Frei, R., Penaye, J., Njel, U. O., Bassahak, J., Nni, J., Kankeu, B., Ngako, V. & Hell, J. V. (2006). Derivation of detrital rutile in the Yaoundé region from the Neoproterozoic Pan-African belt in southern Cameroon (Central Africa). *Journal of African Earth Sciences,* 44, 443-458.

Stutenbecker, L., Berger, A. & Schlunegger, F. (2017). The potential of detrital garnet as a provenance proxy in the Central Swiss Alps. *Sedimentary Geology,* 351, 11-20.

Taylor, R., Clark, C. & Reddy, S. M. (2012). The effect of grain orientation on secondary ion mass spectrometry (SIMS) analysis of rutile. *Chemical Geology,* 300-301, 81-87.

Vermeesch, P., Resentini, A. & Garzanti, E. (2016). An R package for statistical provenance analysis. *Sedimentary Geology,* 336, 14-25.

Vezzoli, G., Forno, M. G., Andò, S., Hron, K., Cadoppi, P., Rossello, E. & Tranchero, V. (2010). Tracing the drainage change in the Po basin from provenance of Quaternary sediments (Collina di Torino, Italy). *Quaternary International,* 222, 64-71.

Wang, Z., Wilde, S. A. & Wan, J. (2010). Tectonic setting and significance of 2.3-2.1 Ga magmatic events in the Trans-North China Orogen: New constraints from the Yanmenguan mafic-ultramafic intrusion in the Hengshan-Wutai-Fuping area. *Precambrian Research,* 178, 27-42.

Watson, E. B., Wark, D. A. & Thomas, J. B. (2006). Crystallization thermometers for zircon and rutile. *Contributions to Mineralogy and Petrology,* 151, 413-433.

Weltje, G. J. & von Eynatten, H. (2004). Quantitative provenance analysis of sediments: review and outlook. *Sedimentary Geology,* 171, 1-11.

CHAPTER 2

PROVENANCE AND AGE CONSTRAINTS ON THE PALAEOPROTEROZOIC INTRACONTINENTAL RIFTING OF THE NORTHERN YILGARN CRATON, WESTERN AUSTRALIA

Armandola S.[1], Barham M.[1,2], Clark C.[1], Reddy S. M.[1], Taylor R. J. M[3].

[1]School of Earth and Planetary Sciences, Curtin University, GPO Box U1987, Perth, WA 6845, Australia.

[2]Centre for Exploration and Targeting, School of Earth and Planetary Sciences, Curtin University, GPO Box U1987, Perth, WA 6845, Australia.

[3]Department of Earth Sciences, Downing Site, University of Cambridge, CB2 3EQ, Cambridge, United Kingdom.

Corresponding author: sonia.armandola01@gmail.com

Abstract

The Yilgarn Craton records protracted rifting of its northern margin between 2200 and 2100 Ma in the Yerrida Basin coincident with a global magmatic flare-up. Rifting and volcanism are recorded within a transgressive sequence changing from coastal to abyssal deposits, and hosting volcaniclastic deposits and mafic melt lava flows. Detrital zircon U-Pb geochronology and geochemistry indicate that 90% of the sediments derived from terranes within the Yilgarn Craton. According to the multidimensional scaling, sediment source regions changed from the Eastern Goldfields Superterrane (east) to the Southern Cross Domain (south), following the continental rifting. An important source of sediments during intracontinental rifting was the Marymia Inlier, a small crustal block that is interpreted to have rift from the Yilgarn Craton between 2200 and 2100 Ma, promoting magmatism in the Yerrida Basin. Trace element patterns of the youngest detrital zircon population with a mean age of c. 2175 Ma suggests that the parent source rocks had a mafic composition. These young detrital zircons are interpreted to derive from the local erosion of

contemporaneous basaltic lava flows and to essentially reflect the depositional age of the Yerrida Basin.

1. Introduction

Sedimentary basins record the processes that affect the underlying and adjacent lithosphere by accumulating thick sedimentary sequences contemporaneous to those processes facilitating accommodation space creation and sediment generation. Hence, the study of ancient basin sequences is critical to constrain lithospheric processes through time, including crustal thinning and continental break-up, and to reconstruct the continental crust evolution (Withjack et al., 2002; Pirajno et al., 2004). The Yerrida Basin developed between 2200 and 2100 Ma during intracratonic rifting of the northern Yilgarn Craton (Pirajno et al., 1998), coincident with renewed global magmatism and orogenic activity (Spencer et al., 2018). The Yerrida Basin depositional history is poorly constrained and lacks fundamental geochronological data and provenance study for its sedimentary succession. Moreover, the crustal thinning of the Yilgarn Craton at this time has yet to be linked with the main continent-continent collisional framework developed for the ultimate amalgamation of the West Australian Craton (Yilgarn and Pilbara cratons and Glenburgh terrane).

Precambrian basins typically lack sufficient exposure and biostratigraphic data that could be used to provide robust age limits for the sedimentary sequences (Fedo, 2003). The study of detrital zircons is a proven technique that establishes links between the sediments and their sources through provenance analysis and offers insights to the tectonic history of the adjacent continental crust (Fedo, 2003; Cawood et al., 2012). Zircon grains are resistant to chemical and physical modification processes and survive exhumation, weathering and erosion to ultimately be commonly found within clastic sediments. The zircon crystal lattice incorporates U-Th isotopes that can be measured to calculate the crystallization age of the primary mineral to provide the maximum depositional age of the host sediment and the age of potential source rocks. Zircon trace elements record the chemical signature of their parent rock and can be analysed to distinguish between tectono-thermal environments of origin (Belousova et al., 2002; Grimes et al., 2015).

In this work U-Pb geochronology and trace element geochemistry of detrital zircon grains integrated with lithofacies analysis of pre- to syn- and post-rift environments,

are used to reconstruct the depositional history of the Yerrida Basin and the tectonic evolution of the northern margin of the Yilgarn Craton between 2200 and 2100 Ma. With recent developments of *in-situ* laser ablation split stream inductively coupled plasma mass spectrometry (LASS-ICP-MS), provenance studies can integrate U-Pb and trace element data obtained from a single analysis of the same mineral volume (Kylander-Clark et al., 2013). The U-Pb ages are compared with age data from potential sources located in the Yilgarn Craton and the Glenburgh Terrane to constrain sediment routing. Combined U-Pb isotopes and trace elements allow accurate correlations between age and chemical data, which can establish higher fidelity on zircon grain provenance, by identifying the composition of their parent protolith, and the tectono-magmatic setting in which the protolith formed (Grimes et al., 2015).

2. Geological background

The Yilgarn Craton is one of the largest remnants of Archean crust preserved on Earth and records a history of continental crust from c. 3600 to c. 2600 Ma (Czarnota et al., 2010). Distinct terranes across the Yilgarn Craton are recognised. In the far northwest of the craton, the Narryer Terrane consists of ~3730–2600 Ma high-grade gneiss, supracrustal and granitic rocks accreted to the craton (Fig. 1; Czarnota et al., 2010). The Murchison Domain and the Southern Cross Domain in the centre consist of ~3010–2630 Ma greenstones and granitic rocks and are divided by a major shear zone (Fig. 1). To the east, younger ages ranging from ~2940 to ~2620 Ma are recorded in the Eastern Goldfields Superterrane (Czarnota et al., 2010; Mole et al., 2015). Granites were emplaced in the Yilgarn Craton during several discrete episodes, at c. 2680–2670, 2660–2650 and 2640–2620 Ma (Champion & Cassidy, 2007; Czarnota et al. 2010). Before being amalgamated in the West Australian Craton, the northern margin of the Yilgarn Craton underwent a period of extension/rifting between 2200–2100 Ma Ga (Hoking et al., 2017). This event is coeval with the collision of the Glenburgh Terrane and Pilbara Craton during the 2215–2145 Ma Ophthalmia Orogeny (Johnson et al., 2013).

The Yerrida Basin is located on the northern margin of the Yilgarn Craton (Fig. 1), and is now included in the Capricorn Orogen province, an area associated with the protracted assembly of the Yilgarn and Pilbara cratons and subsequent intracratonic reworking over ~1 Ga in north-western Australia. The base of the Yerrida Basin is in

nonconformable contact with Yilgarn Craton granites and in faulted contact with the Marymia and Goodin Inliers (Fig. 1; Hocking et al., 2017). In the northwest, the Yerrida Basin sedimentary sequence is overlain by the Bryah Group dated at c. 2000 Ga, which is considered coeval to the topmost sediments of the Yerrida Basin, and the younger c. 1800 Ga Padbury Basin (Fig. 1; Hocking et al., 2017). To the east, the Yerrida Basin is overlain by the sediments of the Earaheedy Basin, accumulated at about 1800 Ga (Fig. 1; Hocking et al., 2017).
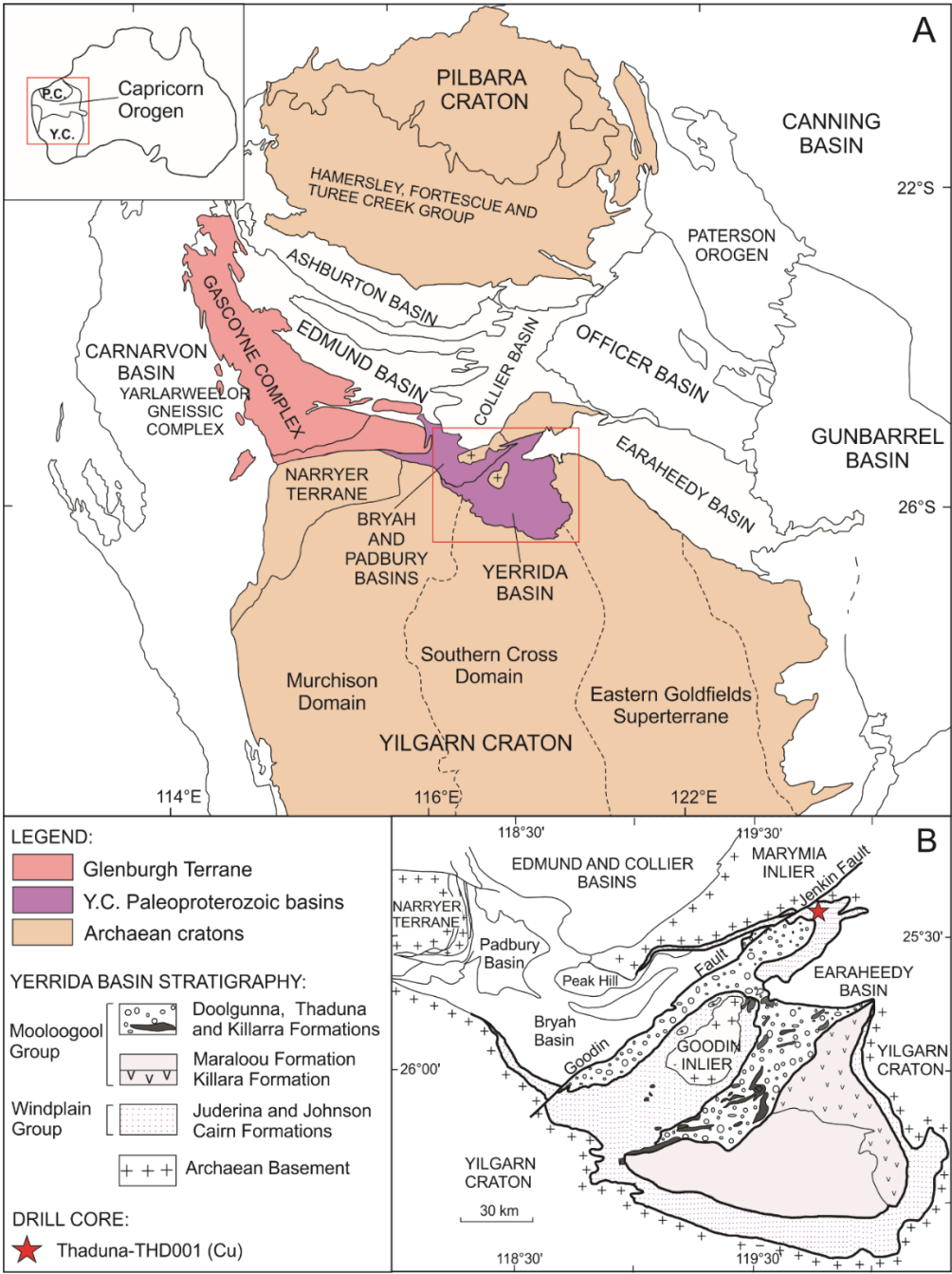
Fig. 1. A - Regional geological map of the Capricorn Orogen and adjacent cratonic regions and fringing basins. Tectonic subdivision of the Yilgarn Craton from Mole et al. (2015). Y.C. - Yilgarn Craton; P.C. - Pilbara Craton. A red box indicates the area covered in B. B - Simplified geological map of the Yerrida Basin (map modified after Pirajno & Occhipinti, 2000), with the location of drill core THD-001 (774304E, 7187543N, Zone 50).

2.1 Yerrida Basin stratigraphy

The Yerrida Basin comprises two distinct sequences separated by a *hiatus*: the lower Windplain Group, which includes the Juderina and Johnson Cairn Formations, and the Mooloogool Group, which includes the Thaduna, Doolgunna, Killara and Maraloou Formations (Fig. 2; Pirajno et al., 1998; 2004; Pirajno & Adamides, 2000). The oldest unit of the Windplain Group, the Juderina Formation, is up to 1000 m thick and comprises mainly cross-bedded and parallel-laminated quartz sandstone, siltstone and conglomerate layers (Woodhead & Hergt, 1997). The Juderina Formation consists of a basal unit called the Finlayson Member that lies non-conformably on Archaean basement with a gentle northward dip (Pirajno et al., 1998; Pirajno & Occhipinti, 2000). Above the Finlayson Member, a sequence (up to 160 m thick) of interbedded evaporites and coastal stromatolites defines the Bubble Well Member (Pirajno et al., 1998; Pirajno & Occhipinti, 2000). The remainder of the Juderina Formation records a transition from a coastal/shallow marine environment to subtidal environment (Pirajno et al., 1998; Pirajno & Occhipinti, 2000). The maximum depositional age of the Juderina Formation is constrained to 2169±19 Ma (Fig. 2; Nelson, 2002). The Juderina Formation has a transitional contact with the Johnson Cairn Formation, which is up to 1250 m thick and made up of pyritic, parallel and finely-laminated black mudstone, iron-rich shale, with subordinate graded silty layers and thin dolomite bands (Fig. 2 b., Hawke et al., 2015).

The Mooloogool Group overlies the Windplain group with an angular unconformity. It contains high-energy conglomerates and turbidite facies of the Thaduna and Doolgunna Formations, and the contemporaneous Killara Formation volcanoclastics and mafic volcanics (Fig. 2; Pirajno et al., 1998; Pirajno & Occhipinti, 2000). The Killara Formation volcanic rocks are disconformably overlain by sulphidic shale and siltstone of the Maraloou Formation formed during a period of subsidence and

interpreted to represent anoxic lacustrine facies (Fig. 2; Pirajno et al., 1998; Pirajno & Occhipinti, 2000).
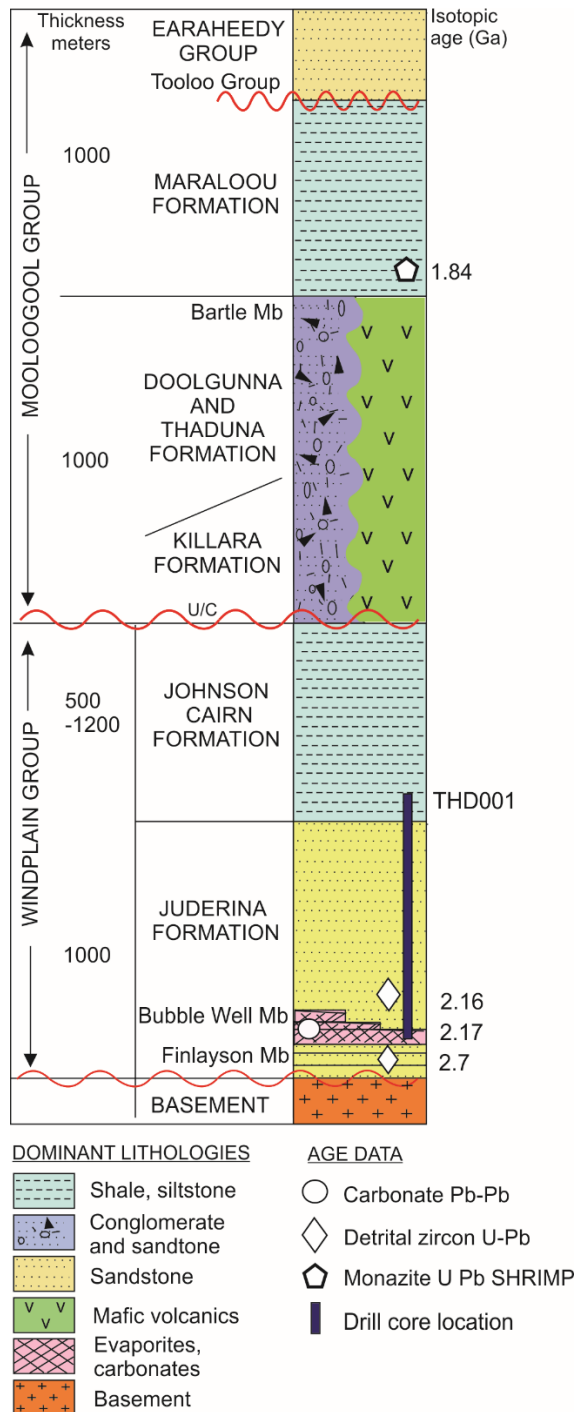
Fig. 2. Schematic stratigraphic column and chronostratigraphic chart of the Yerrida Basin, with approximate thicknesses. Modified after Pirajno et al. (2004) and Occhipinti et al. (2017). Depositional age for the stromatolitic carbonate rock of the Bubble Well Member from Woodhead & Hergt, (1997); Detrital zircon U-Pb maximum depositional ages from Nelson (2002); Monazite U-Pb from Pirajno et al. (2004). Stratigraphic coverage of THD-001 indicated using a vertical blue line.

3. Analytical method

Ten samples from the sediments of drill core THD-001 (Fig. 3) of approximatively two kilos each were disaggregated using the SelFrag high-voltage pulse power fragmenter at the John de Laeter Centre, Curtin University. The fragmented rocks were sieved with 500 µm and 360 µm disposable mesh to separate two fractions (<360 and 360-500 µm), that were then manually panned to concentrate heavy minerals. From the concentrated aliquot detrital zircon grains were hand-picked and mounted in epoxy resin discs. The epoxy resin disc surface was polished with 2000 grit wet sandpaper, 5 µm and 3 µm wet plastic cloth and 3 µm and 1 µm soft cloth with diamond paste, to reach half-grain thickness and reveal grain interiors. Cathodoluminescence (CL) imaging of zircon grains was performed on a Tescan Mira3 VP-FESEM using a panchromatic CL detector with a wavelength range of 185–850 nm, at 10 kV accelerating voltage and a working distance of 16.5 mm, to provide constraints on grain history and target locations for laser ablation analyses. Detrital zircon grain cores were targeted for primary source crystallization ages.

Uranium-lead and trace element analyses were performed simultaneously with a laser ablation split stream inductively coupled plasma mass spectrometer (LASS-ICP-MS). The LASS is fitted with a Resonetics S-155-LR 193 nm excimer laser ablation system coupled to an Agilent 7700x quadrupole ICPMS and a Nu Instruments Plasma HR multi-collector ICPMS. Isotopic data pertaining to the U–Pb system were collected in time-resolved mode for a total of 90 s for each analysis. Operating conditions followed those set out by Kylander-Clark (2013). During the first session of measurement for samples TD1–5, ion counters were used to measure Pb isotopes and a Faraday cup used for ^{238}U. For samples TD6–10, Faraday cups were used to measure both U and Pb isotopes and the ion counters were switched off. Between the two sessions, the spot size was adapted from 23 µm to 33 µm, due to the larger size of zircon grains in samples TD6–10. Every 20 analyses, the accuracy of the data were checked by analysing zircon mineral standards including GJ1 (608.5±0.4 Ma; Jackson et al., 2004), used as a primary standard for the U-Pb ages and trace elements calculations, Plešovice (337.13±0.37 Ma; Slama et al., 2008), Z91500 (1061±4.3 Ma; Wiedenbeck et al., 1995) and OG1 (3465.4±0.6 Ma; Bodorkos et al., 2009) as secondary standards.

Data were reduced with *Iolite v2.5* within the Igor Pro programme (Paton et al., 2010). The 1σ uncertainties calculated with the Iolite software were integrated with percentage errors calculated on the standard material analysed (Appendix 1, standard material). Detrital zircon grains with $^{206}Pb/^{207}Pb$ and $^{206}Pb/^{238}U$ ages >90% concordance on the Tera-Wasserburg concordia diagrams (Fig. 5) were selected for the data interpretation and discussion. Tera-Wasserburg concordia diagrams and probability density plots (PDP) were done with *Isoplot v4.15* (Ludwig, 2003), for individual samples. Stacked probability density plots were created with *jAgeDisplay* (Thomsen et al., 2016), to display broader source rocks and formations age records. Detrital zircon trace elements were normalized to Chondrite values following those given by Anders & Grevesse, (1989) and are given in Appendix 1.

The U-Pb detrital zircon data were plotted using a multidimensional scaling plot (MDS) calculated by the software *Provenance* (Vermeesch et al., 2016). The non-metric MDS plot is based on the probability of goodness of fit between two sets of samples calculated by the Kolmogorov-Smirnov (K-S) test. The K-S test produces a *p*-value that expresses the probability of shared derivation between two samples (>95%). The *p*-value is used in the MDS to produce plots that display the degree of sample similarity or dissimilarity using distances between the samples (Vermeesch et al., 2016).

4. Results

4.1 Stratigraphy and sedimentology of THD-001 drill core

The vertical borehole THD-001 is 1017.8 m-deep and lies in the northeast corner of the Yerrida Basin, proximal to the major Goodin–Jenkin Fault system (Fig. 1). The lithostratigraphy exposed in THD-001 includes from the base, the uppermost part of the Bubble Well Member (1017.8–768.5 m), the Juderina Formation (768.5–334 m) and the lower part of the Johnson Cairn Formation (334–0 m; Fig. 3; Table 1).

4.2 Detrital zircon U-Pb ages and trace elements

U-Pb isotopic and trace element data for the detrital zircon grains are provided in Appendix 1. Detrital zircon grains vary from 30 to 500 µm in size, depending on the host sediment grain size, and are typically rounded to subrounded, elongate, and rare sub-spherical (Fig. 4). Cathodoluminescence (CL) demonstrated that most zircon

grains exhibit oscillatory zoning and core-rim structure (Fig. 4). The Th/U ratio of near-concordant zircon grains is >0.1 for all but four grains, which suggests a magmatic origin for the majority of the analysed material (Hoskin & Schaltegger, 2003).
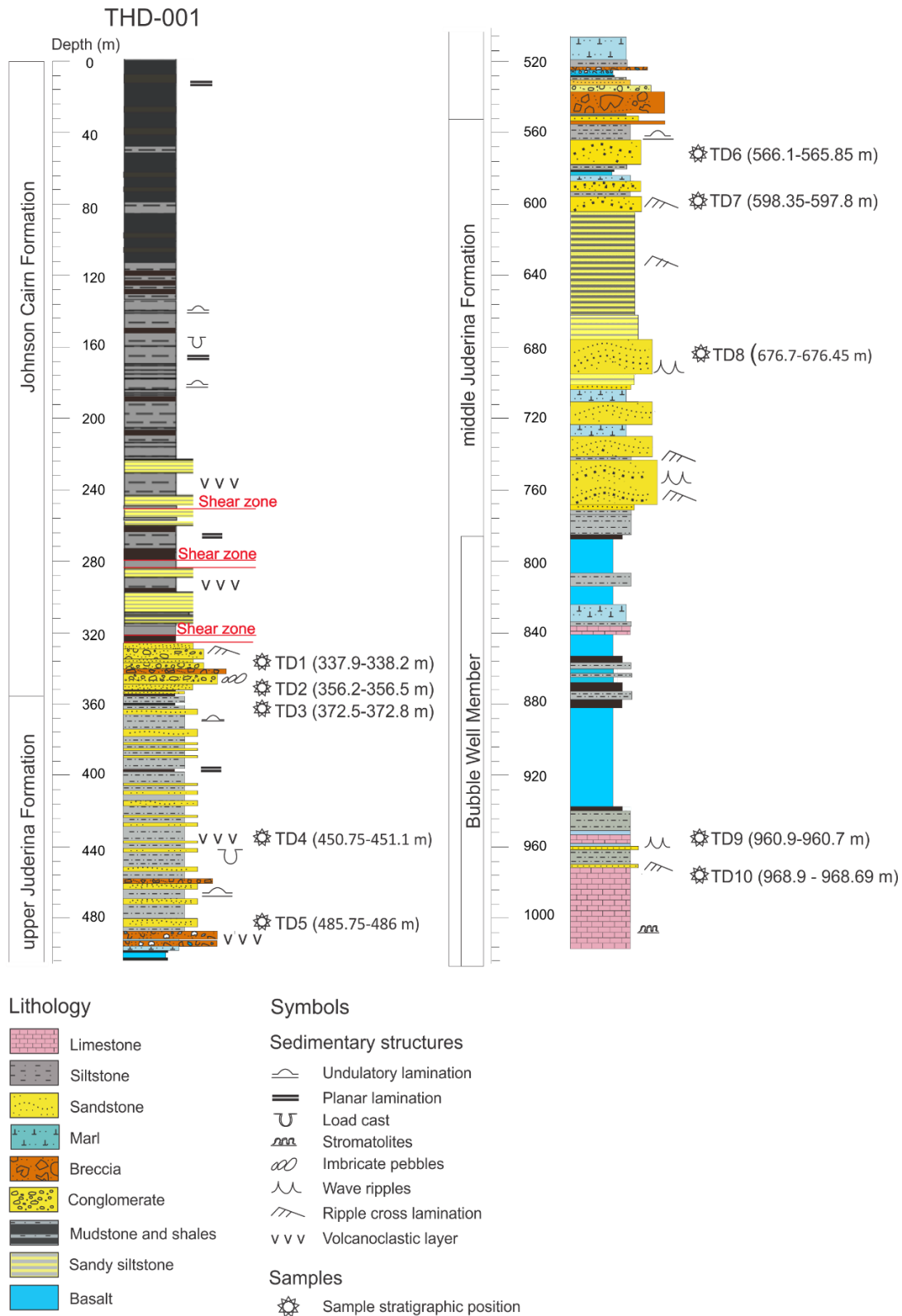
Fig. 3. Stratigraphic log of THD-001 the drill core. The stratigraphic positions of the samples analysed are reported with their depth (m).

26

Table 1. Sedimentology and lithostratigraphy of the drill core THD-001.

Formation		Facies association	Lithology	Sedimentary structures
Johnson Cairn Formation	Continental rise			
		a. Distal turbidite sequence	Siltstone and mudstone occasional fine sandstone layers; basal breccia and conglomerate lag.	Alternating siltstone and mudstone at centimetre scale with convolute, planar parallel, thin current ripple laminations, flames and lenses, occasional basal coarser sand layers.
	Abyssal plain			
		a. Abyssal deposits	Fine mudstone and siltstone alternating in cm scale layers.	Planar lamination and occasional planar silt layers or lenses, coarse pyroclastic deposit with rare pumice clasts present.
		b. Abyssal deposits	Shales and cherts.	Laminated shales and brown-red cherts horizons interbedded toward the top.
Juderina Formation	Continental slope - deep marine; Upper Juderina Formation			
		a. Proximal turbidite sequence	Medium-coarse grained sandstone, siltstone and mudstone, repetitively interbedded in cycles up to 20 m thick, subordinate marl beds; breccia and conglomerates beds (up to 6 m beds thickness); tuffs and pyroclastic deposits interbedded and mixed within the sediments.	Unidirectional current ripple lamination, load structures, fluid escape structures and flames, sand lenses in the mudstones; erosive basal contacts and fining-upward cycles; basal coarse breccia and polymictic conglomerates with imbricated clasts, tuffaceous layers and pumice load casts.
	Continental shelf – marine; Middle Juderina Formation			
		a. Tidal flats - intertidal beach deposits	Thick, coarse, medium-grained sandstone beds (up to 7 m thick beds).	Cross ripple-lamination and wave-lamination, coarse base and fining upward, black sand (associated with b.).
		b. Subtidal - lagoons	Interbedded siltstone and medium-fine-grained sandstone evenly alternating (sandstone beds up to 40 cm), subordinate interbeds of mudstone and marl layers (up to 20 cm thick).	Occasional thin current ripple lamination (asymmetric ripples).
		c. Subtidal - front bars and channels	Thick coarse-medium grain sized sandstone beds, (up to 10 m thick) and subordinate mudstone and siltstone beds.	Mudstone and siltstone associated at the base with wavy bedding, sandstone with erosive basal surface, and thick cross and tabular bedding and massive beds upward.
		d. Subtidal - open marine	Sandstone, siltstone, mudstone alternating in up to 6 m thick cycles.	Ripple lamination in mudstone and sandstone, tabular lamination, convolute lamination and erosive basal contacts of sandstone; fining upward cycles.
	Coastal -intercontinental sea – Bubble Well Member			
		a. Sabkha	Pink limestone with alternating evaporitic mineral horizons and stromatolites (up to 7 m thick).	Convolute algal mats alternating with evaporitic layers, fan structures and liminites occasionally visible.
		b. intertidal, shallow sea	Subordinate fine-grained pink-green sandstone and siltstone (up to 2-3 m thick beds).	Sharp basal contact on the limestone, planar/undulatory lamination, dominant thin centimetre current ripple cross-lamination and wave-lamination.
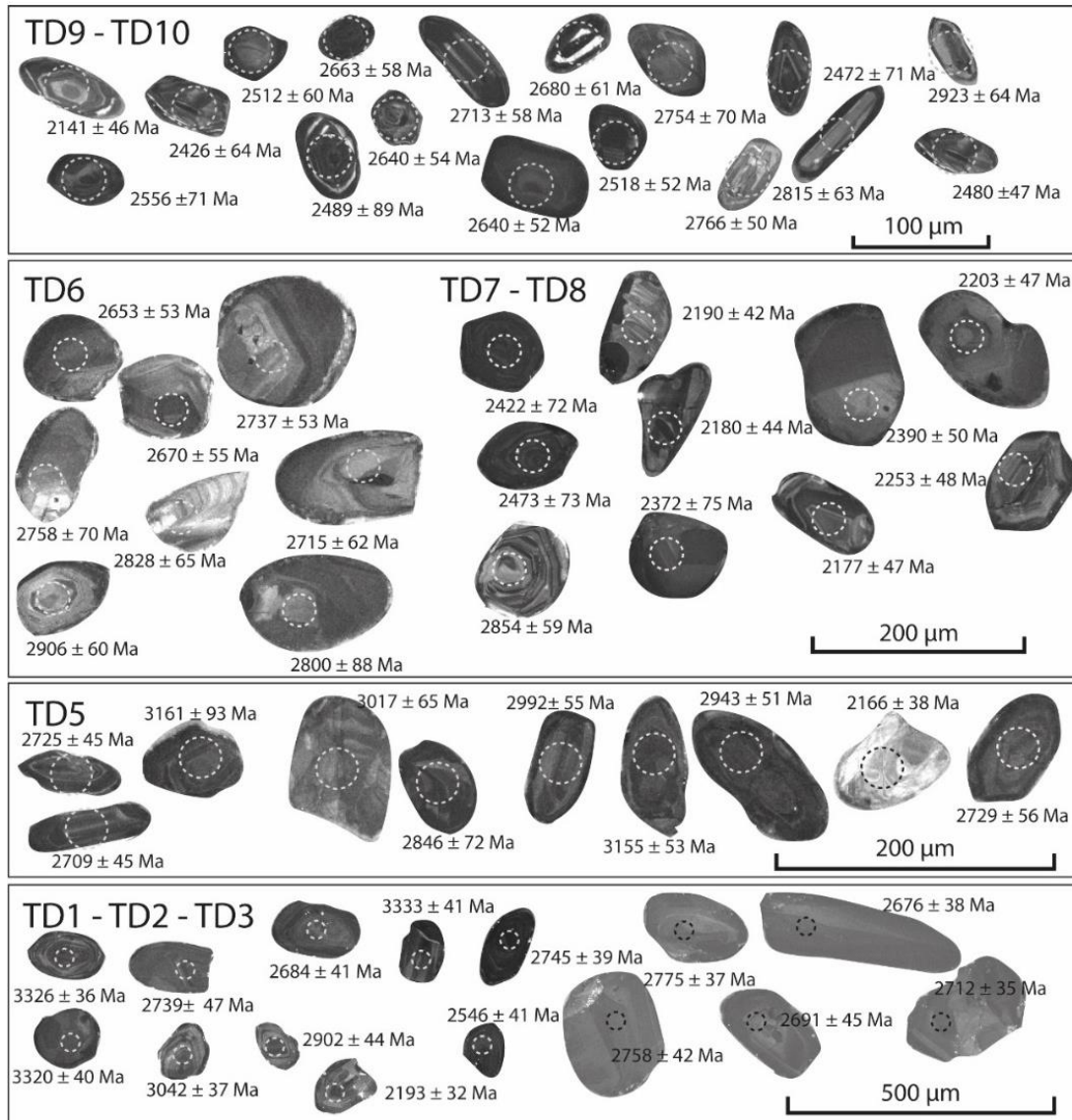
Fig. 4 Cathodoluminescence (CL) images of representative concordant detrital zircons analysed for each sample are shown with locations of the analytical spots.

4.2.1 Bubble Well Member

From sample TD10 74 detrital zircon grains were analysed 41 of which resulted to be concordant and yielding a dominant age population ranging from 2650 to 2500 Ma (Fig. 6), with a weighted average age of 2585 ± 15 Ma (MSWD=0.02, n=29; Fig. 5). 159 detrital zircons grain were analysed to represent sample TD9 and 131 were concordant with a unimodal age population between 2700 and 2600 Ma, and a weighted average age of 2633 ± 7 Ma (MSWD=1, n=77; Fig. 5). Sample TD9 gave smaller groups of grains between 2600 and 2400 Ma. Trace elements of the zircon grains younger than 2600 Ma from both samples have Y>850 ppm, which is consistent

with a granitoid parent (Fig 7). Detrital zircons older than 2700 Ma display variable trace-element compositions that plot within the granite, syenite pegmatite and larvikite protolith fields, and overall indicate granitoid for the protolith rocks of the zircons (Fig 7).

4.2.2 Juderina Formation coastal deposits

From samples TD8 and TD7 were analysed respectively 158 and 160 grains, obtaining 106 and 129 concordant analyses respectively, that show similar age distributions. Both the two samples yield weakly bimodal age distributions with dominant subpopulations ranging between 2800 and 2600 Ma (modal age peaks at ~2.7 Ga; Fig. 6 -7), and a subordinate subpopulation with modal age peaks at ~2.2 Ga (Fig. 5). The subordinate subpopulation is more significant in TD7 compared to TD8. Sample TD7 yielded the youngest detrital zircon found at 2102 ± 64 Ma, and the youngest detrital zircon cluster/group/subpopulation of 2175 ± 39 Ma (MSWD=1, n=9). Sample TD6 yielded 66 concordant detrital zircons over a total of 81 grains analysed, with ages ranging between 2.3 Ga and 3.25 Ga. The dominant detrital zircon population ages are distributed between 2900 and 2600 Ma, with a modal age peak centred at ~2772 Ma (Fig. 5).

The trace element composition of the detrital zircon grains in samples TD6-8 indicates compositional similarity of source rocks for zircons aged 2800–2600 Ma (Fig. 7). These zircon grains generally have Y values of 1200–100 ppm and plot in the granitoid, and nepheline syenite and syenite pegmatite compositional rock fields. Zircon grains younger than 2600 Ma have relatively high Y values ranging from 9000 to 150 ppm, with the youngest group of 2400–2100 Ma having the highest Y contents, ranging from 9000 to 4000 ppm (Fig 7). The younger <2600 Ma grains plot within syenite, nepheline syenite, and syenite pegmatite, larvikites and dolerite compositional rock fields (Fig 7).

4.2.3 Juderina Formation turbidite deposits

Samples TD5 and TD4 from sandstones of the turbidite deposits found in the upper part of the Juderina Formation yielded 84 and 21 concordant zircon analyses over 188 and 145 detrital zircon grains respectively. TD5 has a polymodal age distribution and dominant age group between 2800 and 2650 Ma, which peaks at 2723 ± 12 Ma

(MSWD=2, n=39), while smaller age subgroups have modes of ~2184 Ma and ~2951 Ma (Fig. 5). Sample TD4 has a polymodal age distribution and two almost equal principal age modes of ~2709 and ~2920 Ma and a smaller subpopulation with an age mode of ~3374 Ma. The trace-elemental composition of the detrital zircon grains of sample TD4 is variable, with no clear age-related clustering within the compositional rock fields (Fig 6, A9 and A10). This is especially true for the largest detrital zircon subpopulation of 2800–2650 Ma that spread across the syenite, nepheline syenite, syenite pegmatite, larvikites and dolerite compositional rock fields. Only eight concordant detrital zircon grain analyses were obtained from sample TD3, all of which are dated between 2800 and 2600 Ma (Fig. 5).

4.2.4 Johnson Cairn Formation

Samples TD2 and TD1 yielded 44 and 51 concordant ages over a complex of 181 and 160 detrital zircon grains respectively (Fig. 5), with dominant zircon subpopulations with ages between 2600 and 2800 Ma and weighted average age of 2715 ± 14 Ma (MSWD=3.3, n=32) and 2720 ± 12 Ma (MSWD=4, n=43 Fig. 5 - 6). In both TD1 and TD2 a secondary detrital zircon age group is visible at ~3.35 Ga (Fig. 5). Zircon grains that contribute to the 2600–2800 Ma subpopulation have Y concentrations (1100–400 ppm), and Eu/Eu* consistent with derivation from granitoids, dolerite and syenite pegmatite and larvikite rocks (Fig 7). Notably, the older age group of c. 3335 Ma found in TD2 and TD1 has a distinct composition with many grains having less pronounced Eu/Eu* ratios, ranging from 0.1 to 0.02, and high $(Yb/Sm)_N$ values between 120 and 40. These detrital zircon grains match the compositional fields of granitoids and dolerite (Fig 7).
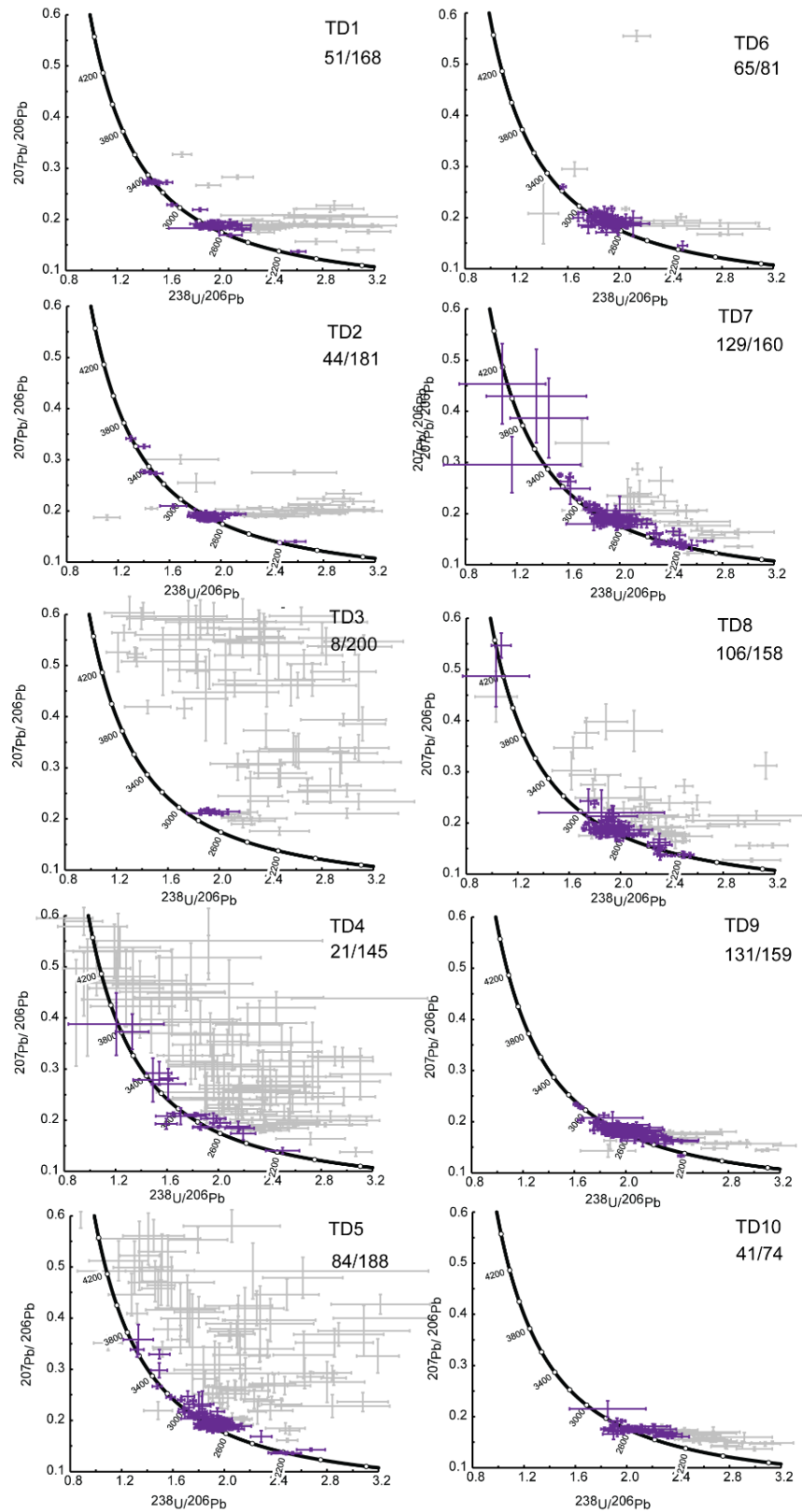
Fig. 5. Tera-Wasserburg Concordia diagrams (*Isoplot4.15*, Ludwig, 2003). Grains with concordancy >90% are plotted in purple, while discordant grains are grey. The number of concordant grains versus the total number of grains analysed is given.
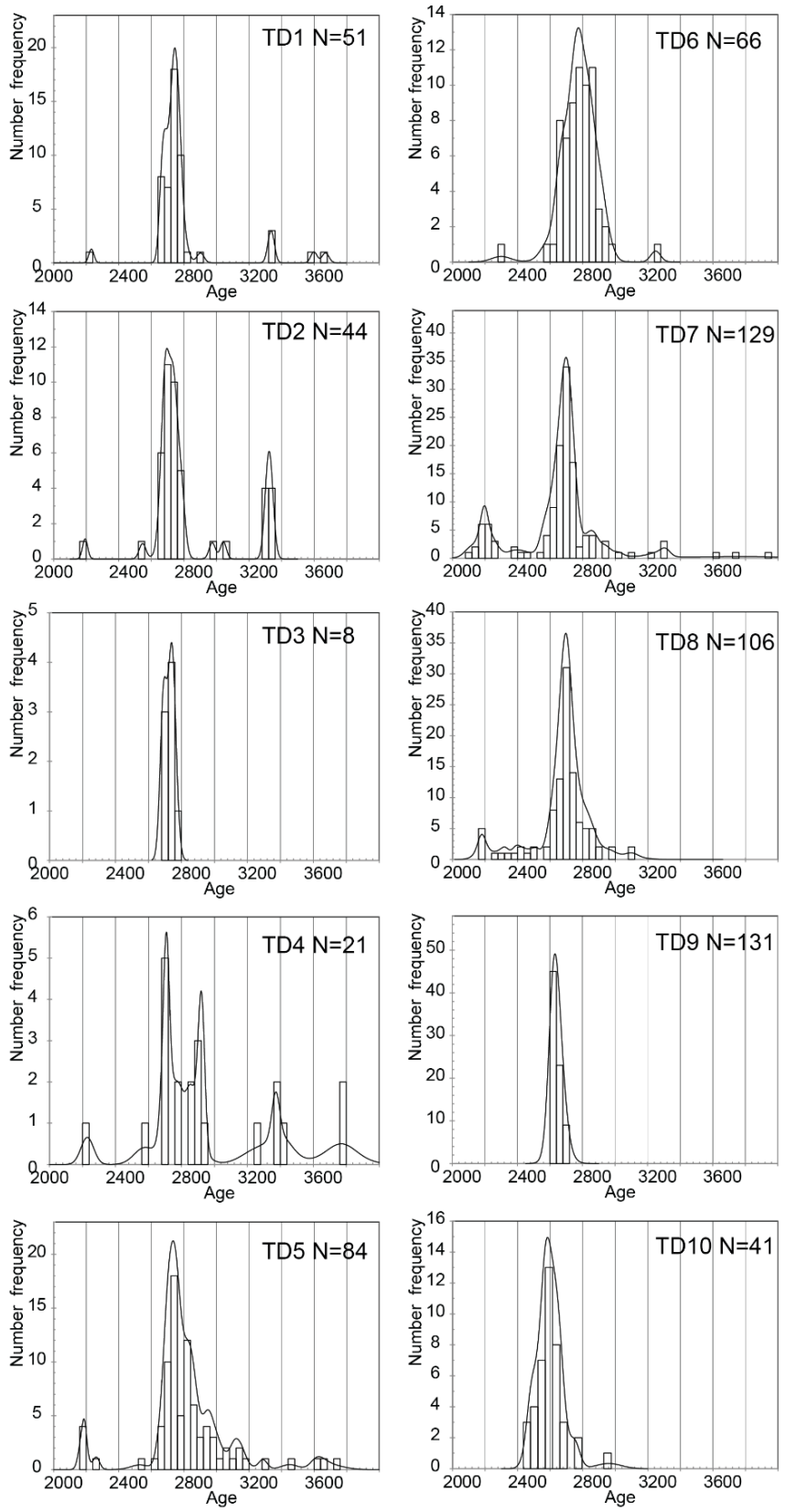
Fig. 6. Probability density plots for concordant detrital zircon grain analyses. Histogram bins plotted at 40 Ma intervals (*Isoplot4.15*, Ludwig, 2003).
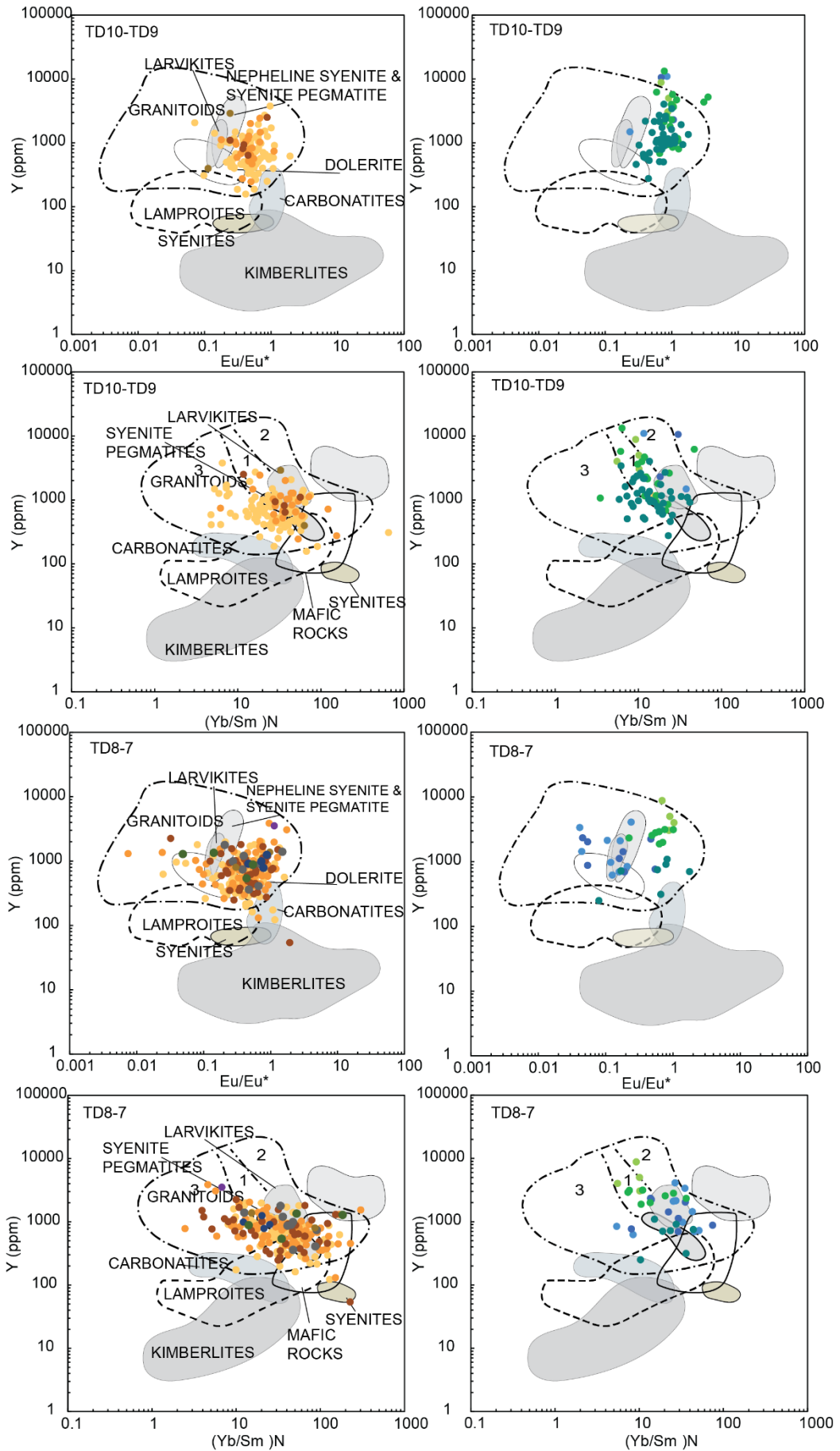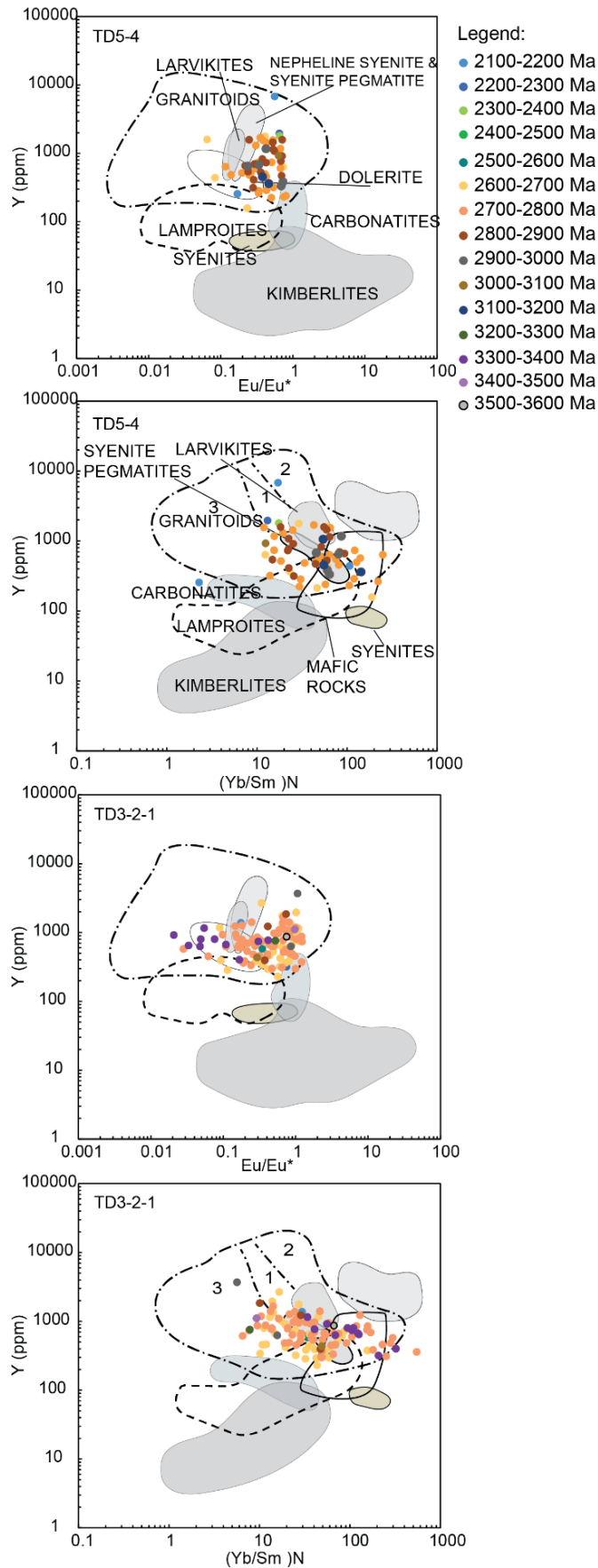
Fig. 7. Zircon geochemical discrimination diagrams of Eu/Eu* versus Y (ppm) and $(Yb/Sm)_N$ versus Y (ppm), with compositional parental rock fields marked (Belousova et al., 2002). The zircons used are those within 90% of concordancy for their ages. Chondrite values from Anders & Grevesse, 1989. Zircon grains are plotted separately according to age. Samples TD5-4-3-2-1 yielded few grains younger than 2500 Ma and are represented by a single diagram without age break.

5. Discussion

5.1 Provenance of the Windplain Group sedimentary rocks

The detrital zircon age spectra of the Windplain Group from drill core THD001 change from unimodal to polymodal age distributions, with peak ages shifting progressively older up section. Characteristic age spectra for potential crystalline source terranes from the major proximal tectonic domains of the Yilgarn Craton were compiled to assess ultimate sediment provenance. Potential sources of sediments include the Eastern Goldfields Superterrane (EGS), the Murchison and Southern Cross Domains (MD and SCD respectively), the Narryer Terrane, as well as the Archean Goodin and Marymia inliers and the Glenburgh Terrane (Moogie Metamorphics and Halfway Gneiss) (Fig. 8).

Samples from the Bubble Well Member (TD9-10) yield dominant population dated at c. 2600 Ma and a smaller group of detrital zircon grains dated c. 2750 Ma that in complex correlates with the age of granites from the Goodin Inlier and the EGS (Fig. 8 - 9). The dominant age peak (~2.7 Ga) of the coastal deposits of the Juderina Formation (TD8-7-6) and the subpopulation at c. 2850 Ma coincide with the dominant age mode of the SCD of the Yilgarn Craton (Fig. 8 - 9). The coastal facies in the lower section of the Juderina Formation also host the largest contribution of younger detrital zircons between 2400 and 2100 Ma. The c. 2200–2100 Ma group likely derived locally, from the erosion of intercalated mafic volcanics. This hypothesis is supported by the presence of volcanic sediment (Fig. 3) and, more importantly, the elemental compositions of the younger zircons. Grains dated 2200–2100 Ma yield high Nb/Yb ratio, ranging from 0.1 to 0.01, with peak values at about 0.8, and low U/Yb ratio of 0.35–0.9, consistent with a continental flood basal or oceanic island setting for their origin and broadly mafic source rocks (Fig. 10; Pearce, 2008; Grimes et al., 2015). These grains may have originated from the erosion of mafic dykes emplaced in the north and northwest the Yilgarn Craton between 2.4 and 2.2 Ga, (Wilde et al., 1996; Libby et al., 1999).

The turbiditic deposits of the Juderina Formation (TD5-4) are characterized by several distinct detrital zircon age peaks at 2187 Ma, 2719 Ma, 2820 Ma, 2919 Ma and a particularly substantial number of old zircons between 3000 and 2800 Ma. Given their polymodal age spectra, these sediments are likely the result of source mixing, with a

35

probable contribution of older Archean detrital zircons, between 2900–2700 Ma from either the Marymia Inlier and/or the Southern Cross Domain (Fig. 9 - 10).

The distinctive peaks of the Johnson Cairn Formation (TD3-2-1) sequence at ~2.75 (dominant) and ~3.3 (subordinate) Ga might indicate an almost unique source for the sediments. These modes approximately coincide with the Marymia Inlier age spectrum, with an addition of exotic zircons aged between 2800–2700 Ma that according to the MDS (Fig. 9), might derive from the recycling of underlying sediments or additional sedimentary input from the Southern Cross Domain and/or the Murchison Domain granites within that age range.

The relative lack of Eo- to Paleoarchean zircons recovered from the Juderina Formation sediments precludes significant derivation from the Narryer Terrane (Myers, 1988; 1993; Myers et al., 1996; Maas & McCulloch, 1991; Nelson, 2001). Furthermore, the Halfway Gneiss and Moogie Metamorphics of the Glenburgh Terrane, to the west, exhibit distinct age modes not observed herein. Consequently, sedimentary input from the Glenburgh Terrane microcontinent was not occurring during deposition within the Yerrida Basin, demonstrating physical separation from the Yilgarn Craton at ~2.1 Ga (Fig. 8 - 9).

5.2 Maximum depositional age of the Windplain Group sedimentary sequence

The reported concordant detrital zircon ages place constraints on the maximum depositional age for the host sediments of the Juderina Formation at 2175 ± 39 Ma (MSWD=1, n=9), based on a weighted mean age of the youngest detrital zircon group from sample TD7. Since these grains have an affinity with a mafic protolith from their chemical analysis and have been interpreted to derive from local intercalated volcanic, the age of these minerals is interpreted to approximate the true depositional age of the Juderina Formation.
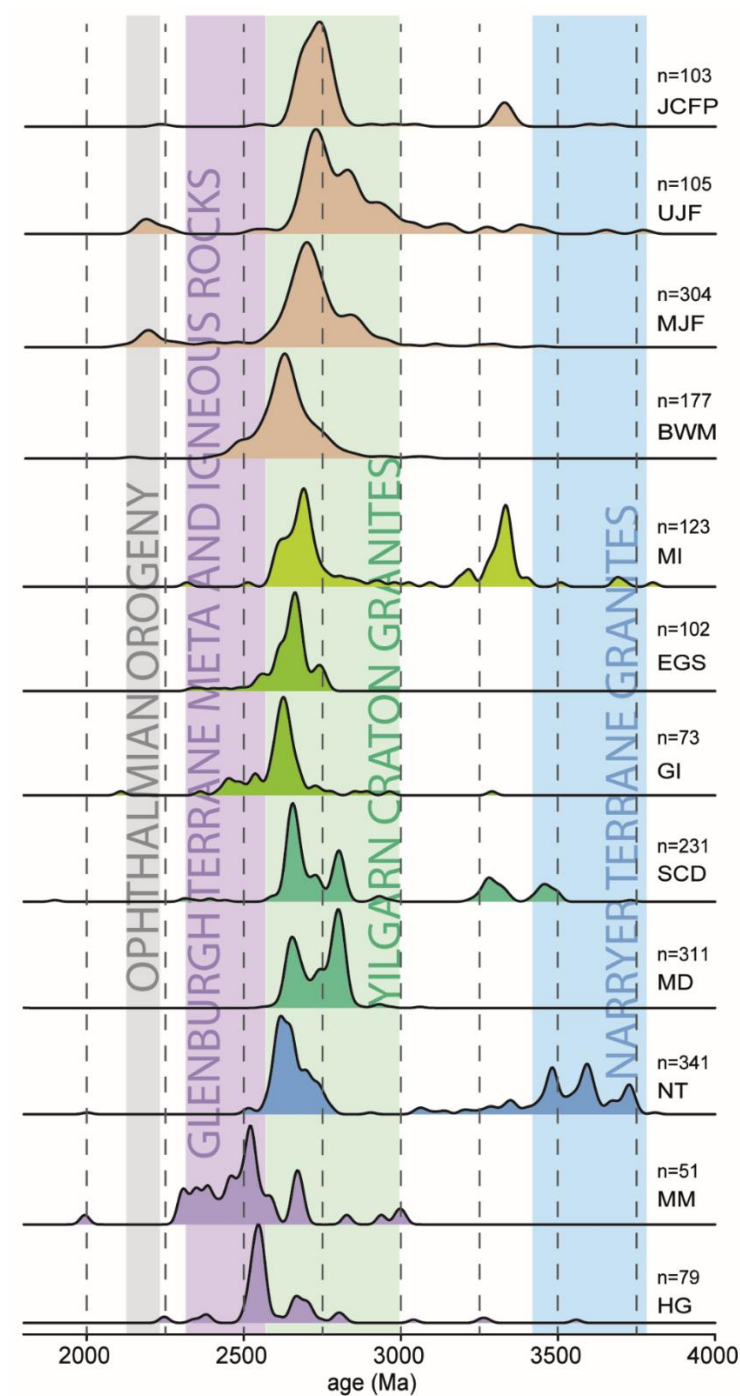
Fig. 8. Stacked probability density plots of zircon population age spectra for Yerrida Basin units and potential crystalline source regions (*jAgeDisplay* software, Thomsen et al., 2016). Zircon grain analyses <10% discordant plotted. JCF – Johnson Cairn Formation (samples TD1 and TD2); UJF – upper Juderina Formation (samples TD3-4-5); MJF –middle Juderina Formation (samples TD6-7-8); BWM - Bubble Well Member (samples TD9-10). Sources are compiled from the Western Australia Geological Survey geochronology catalog. GeoView.WA: MI - Marymia Inlier

(Nelson 1997; Vielreicher & McNaughton, 2002); EGS - Eastern Goldfields Superterrane (Nelson, 1997; 1998; 1999); GI - Goodin Inlier (Nelson 1997); SCD - Southern Cross Domain (Love et al., 2006; Wingate et al., 2008; 2007; Lu et al., 2016); MD - Murchison Domain (Nelson 2005; Wingate et al., 2008, 2011, 2012); NT - Narryer Terrane (Nutman et al., 1991; Nelson 1996, 1998, 2000; Lu et al., 2015); MM - Moogie Metamorphics (Kirkland et al., 2009); HG - Halfway Gneiss (Nelson, 2000b; 2000c).
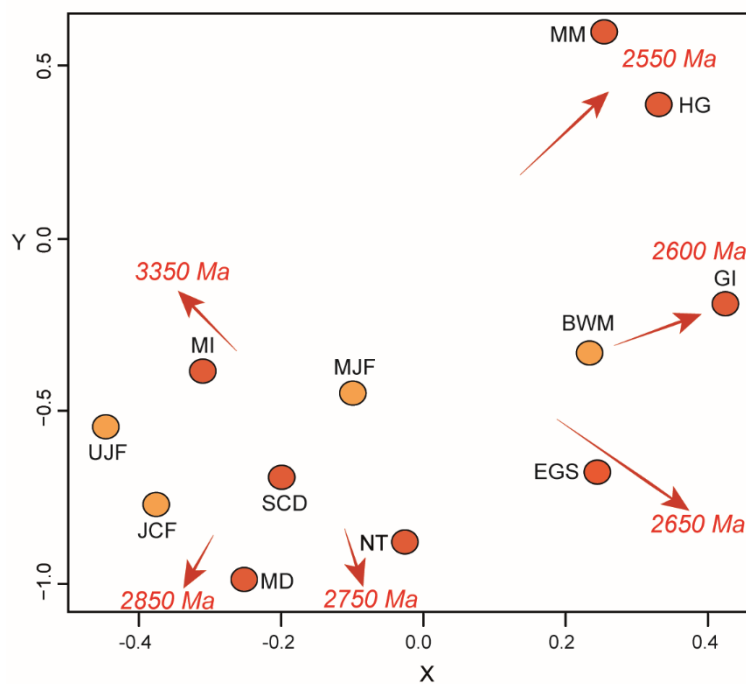
Fig. 9 Multidimensional scaling (MDS) plot for Yerrida Basin sedimentary units (orange circles) and potential source terranes (red circles). Generated using the *Provenance* package in ''*R*'' (Vermeesch, 2016). The resulting stress factor for the fit test is 0.171. JCF –Johnson Cairn Formation; UJF - upper Juderina Formation; MJF –middle Juderina Formation; BWM - Bubble Well Member; MI - Marymia Inlier; EGS - Eastern Goldfields Superterrane, GI - Goodin Inlier; SCD - Southern Cross Domain; MD - Murchison Domain; NT - Narryer Terrane; MM - Moogie Metamorphics; HG - Halfway Gneiss.
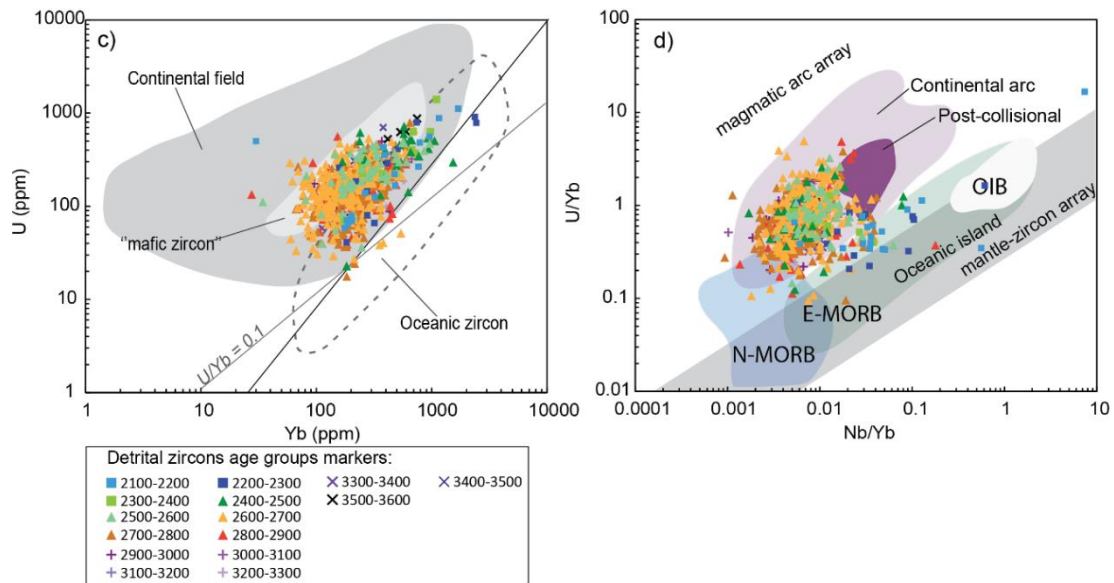
Fig. 10. Compositional and tectono-magmatic province discrimination diagrams for concordant detrital zircon grains (Grimes et al., 2015).

5.3 Tectonic evolution of the northern margin of the Yilgarn Craton

At c. 2175 Ma, the northern margin of the Yilgarn Craton underwent extension, characterized by mafic melt intrusion, lava flows and volcanism within the Yerrida Basin. Facies analysis indicates that the Yerrida Basin preserves a typical rifting succession, and records basin deepening from basal alluvial and carbonate platform deposits to deep-water abyssal deposits. A rift setting is also confirmed by the comparison of the detrital zircons' age distribution, with the typical rift PDP provided by Cawood et al., (2012). In this case, a peak coinciding with the youngest detrital zircon subpopulation coincide with the depositional age and the largest inputs of sediments are provided by much older crustal rocks, with less than 5% of grains having ages within 150 Ma of the depositional age (Cawood et al., 2012). Detrital zircon geochronology and multidimensional scaling plot suggest that the development of the proto-rift initiated in the Eastern Goldfields Superterrane, in the vicinity of the Goodin Inlier (Fig. 11-a). The finding of a relatively simple and unimodal age distribution of detrital zircon matching the EGS age interval, in the Bubble Well Member, reflects typical conditions of this early rift phase and is supportive of contributions from local sources (Withjack et al., 2002). Subsequently, syn-rift faulting and extension favoured the expansion of the rift towards the NW, involving sediment transportation from the SCD in the Juderina Formation. The Juderina Formation sediments record transition from subtidal to a continental shelf-edge environment, and intense volcanic activity,

adjacent to the Marymia Inlier (Fig. 11-b). Consistent transportation of sediments from the Southern Cross Domain (populations dated at 2900 and 3300 Ma) occurred along with sedimentary reworking. In a post-rift phase, deposition in abyssal environments took place within the Johnson Cairn Formation (Fig. 3; Table 2). Detrital zircon ages indicate the Marymia Inlier, SCD and possibly the MD as principal source regions, suggesting further rift expansion toward the north-west.

There is a general lack of knowledge of the tectonic setting of the Yilgarn Craton between 2200 and 2100 Ma, which has impeded the understanding of the tectonic evolution of its northern margin. The development of the Yerrida Basin is generally linked with subduction of the Yilgarn Craton under the Glenburgh Terrane and Pilbara Craton, coeval to the Ophthalmian Orogeny, (2215–2145 Ma; Hawke et al., 2015; Hocking et al., 2017). Such subduction is considered the likely trigger for intracontinental rifting of the Yilgarn Craton (Hawke et al., 2015; Hocking et al., 2017). However, this model is not supported by the finding of subduction-related magmatism in the Glenburgh Terrane or in the Pilbara Craton dated at c. 2200 My (Sheppard et al., 2004). On the contrary, many studies indicate that the Yilgarn Craton was isolated between 2200 and 2000 Ma (e.g., Johnson et al., 2010; Johnson et al., 2011; Alghamdi et al., 2017).

Another model relates to intracratonic rifting led by mantle upwelling or mantle plume activity (Pirajno, 2004). The detrital zircon ages found indicate discrete episodes of exhumation and erosion of the Marymia Inlier into the Yerrida Basin. Additionally, the basin records intense volcanic activity proximal to the Marymia Inlier in the form of lava flows and volcanoclastic detritus. All these data might suggest movement of the Marymia block towards the northeast, which could represent evidence of relatively localised rifting driven by a mantle plume (e.g. Mayborn & Lesher, 2004; Strand & Köykkä, 2012).

The 2400–2200 Ma interval is characterized by a global lull in the magmatism and decline in tectonic plate movement (O'Neill et al., 2007; Spencer et al., 2018; Condie et al., 2009). This would align with a lack of evidence for arc-related magmatism in the Glenburgh Terrane and Pilbara Craton during this time. Significantly, a global c. 2.1 Ga flare-up in melting and rejuvenated igneous activity (Spencer et al., 2018), coincides with the intracratonic rifting of the northern margin of the Yilgarn Craton in

the Yerrida Basin. This general concept is supportive of an intracratonic rifting model driven by the beginning of broad igneous activity and is consistent with an origin linked to mantle plume activity.
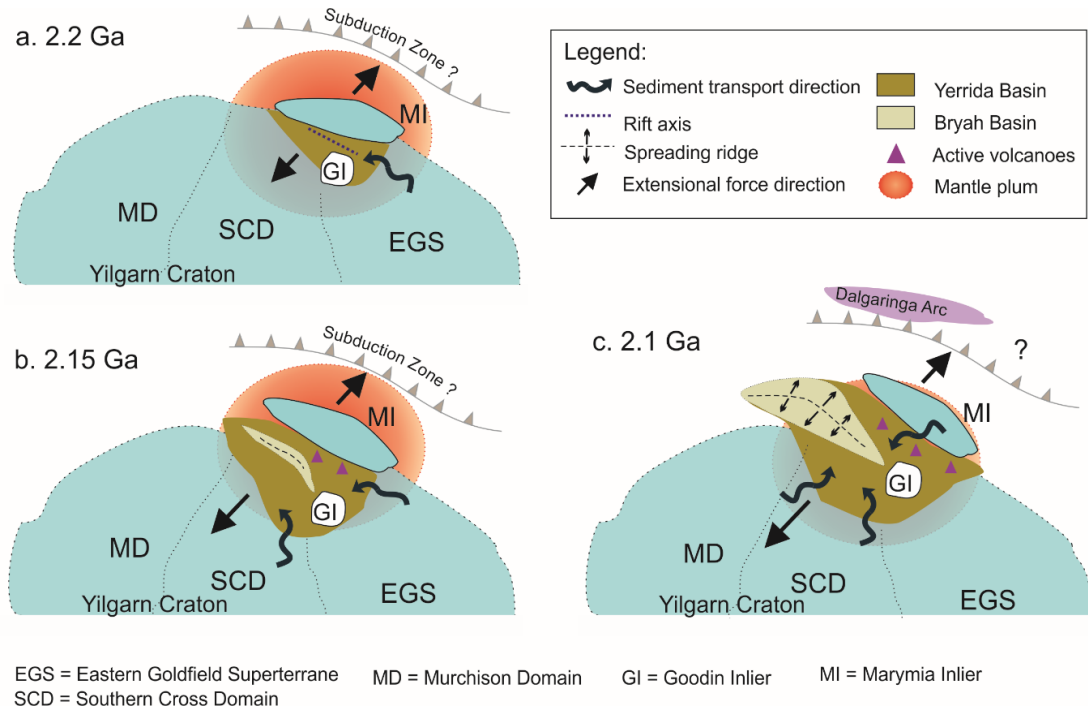
Fig. 11 Tectonic evolution of the northern Yilgarn Craton margin, with stages of the rift opening displayed (a, b, c).

6. Conclusions

Detrital zircon U-Pb geochronology and trace elements geochemistry (detrital zircons versus Grimes et al., 2015) constrain the depositional age of the Yerrida Basin at 2175 ± 39 Ma (MSWD=1, n=9) on the north margin of the Yilgarn Craton. Due to (i) the elemental composition of the youngest zircon grains analysed, which is consistent with mafic rock protoliths, (ii) the presence of mafic lava flows in drill core THD-001, and (iii) mafic detritus in the sediments, this age is interpreted to be the depositional age of the sediments.

The geochemistry of the detrital zircons compared with the plots of Belousova et al., (2002) indicated a general granitoid affinity for the zircon minerals and did not highlight significant patterns in the composition.

The stratigraphy of the Windplain Group in THD-001 records rifting of the northern Yilgarn Craton and deposition of pre-rift to syn- and post-rift sequences. These

correspond to the: coastal and sabkha deposits of the Bubble Well Member, tidal and subtidal siliciclastic deposits and shelf deposits of the Juderina Formation, and continental slope to abyssal plane deposits of the Johnson Cairn Formation. The deposition was accompanied by intracontinental magmatism and volcanic eruptions in the north-eastern part of the basin.

The provenance study of the detrital zircon grains analysed highlight that the detritus was locally derived from the Yilgarn Craton: Eastern Goldfield Superterrane, Southern Cross Domain and Marymia and Goodin Inliers. According to the provenance, the sediment was transported initially from the east and then from both the southwest and north, following rift development.

The impetus for the rifting remains unclear. The Yilgarn Craton at c. 2.2 Ga was isolated from the Glenburgh Terrane and Pilbara Craton. Thus, active rifting associated with a back-arc setting, driven by subduction to the north is not entirely supported, except for the occurrence of the Ophthalmian Orogeny, coeval with the rifting. The activity of mantle upwelling or plume activity can be equally taken into account as a mechanism for the formation of a passive rift in the Yerrida Basin. Mantle upwelling could be suggested by the rifting and volcanism associated with the Marymia Inlier that is interpreted to have separated at c. 2175 Ma from the Yilgarn Craton.

References

Alghamdi, A. H., Aitken, A. R. A. & Dentith, M. C. (2018). The composition and structure of the deep crust of the Capricorn Orogen. *Australian Journal of Earth Sciences,* 65, 9-24.

Anders, E. & Grevesse, N. (1989). Abundances of the elements: Meteoritic and solar. *Geochimica et Cosmochimica Acta,* 53, 197-214.

Belousova, E. A., Griffin, W. L., O'Reilly, S. Y. & Fisher, N. I. (2002). Igneous zircon: Trace element composition as an indicator of source rock type. *Contributions to Mineralogy and Petrology,* 143, 602-622.

Bodorkos, S., Stern, R. A., Kamo, S., Corfu, F. & Hickman, A. H. (2009). OG1: A Natural Reference Material for Quantifying SIMS Instrumental Mass Fractionation of Pb Isotopes During Zircon Dating. *American Geophysical Union, Fall Meeting 2009, abstract #V33B-2044.*

Cawood, P. A., Hawkesworth, C. J. & Dhuime, B. (2012). Detrital zircon record and tectonic setting. *Geology,* 40, 875-878.

Champion, D. C. & Cassidy, K. F. (2007). An overview of the Yilgarn Craton and its crustal evolution. *Proceedings of Geoconferences (WA) Inc., Kalgoorlie '07 Conference*, 8-12.

Condie, K. C., O'Neill, C. & Aster, R. C. (2009). Evidence and implications for a widespread magmatic shutdown for 250 My on Earth. *Earth and Planetary Science Letters,* 282, 294-298.

Czarnota, K., Champion, D. C., Goscombe, B., Blewett, R. S., Cassidy, K. F., Henson, P. A. & Groenewald, P. B. (2010). Geodynamics of the eastern Yilgarn Craton. *Precambrian Research,* 183, 175-202.

Fedo, C. M. (2003). Detrital Zircon Analysis of the Sedimentary Record. *Reviews in Mineralogy and Geochemistry,* 53, 277-303.

Grimes, C. B., Wooden, J. L., Cheadle, M. J. & John, B. E. (2015). "Fingerprinting" tectono-magmatic provenance using trace elements in igneous zircon. *Contributions to Mineralogy and Petrology,* 170, 46-46.

Hawke, M. L., Meffre, S., Stein, H., Hilliard, P., Large, R. & Gemmell, J. B. (2015). Geochronology of the DeGrussa volcanic-hosted massive sulphide deposit and associated mineralisation of the Yerrida, Bryah and Padbury Basins, Western Australia. *Precambrian Research,* 267, 250-284.

Hocking, R., Lindsay, M., Aitken, A., Copp, I., Jones, J., Martin, D., Pirajno, F., Metelka, V., Occhipinti, S., Hocking, R., Lindsay, M., Aitken, A., Copp, I., Jones, J., Sheppard, S., Pirajno, F. & Metelka, V. (2017). Paleoproterozoic basin development on the northern Yilgarn Craton, Western Australia. *Precambrian Research,* 300, 121-140.

Hoskin, P. W. O. & Schaltegger, U. (2003). The composition of zircon and igneous and metamorphic petrogenesis. *Reviews in Mineralogy and Geochemistry,* 53, 27-62.

Iizuka, T., Campbell, I. H., Allen, C. M., Gill, J. B., Maruyama, S. & Makoka, F. (2013). Evolution of the African continental crust as recorded by U-Pb, Lu-Hf and O isotopes in detrital zircons from modern rivers. *Geochimica et Cosmochimica Acta,* 107, 96-120.

Jackson, S. E., Pearson, N. J., Griffin, W. L. & Belousova, E. A. (2004). The application of laser ablation-inductively coupled plasma-mass spectrometry to in situ U-Pb zircon geochronology. *Chemical Geology,* 211, 47-69.

Inalee Jahn, (2018). Crustal evolution of the Capricorn Orogen, Western Australia. *PhD Thesis*, Curtin University (WA).

Johnson, S. P., Sheppard, S., Rasmussen, B., Wingate, M. T. D., Kirkland, C. L., Muhling, J. R., Fletcher, I. R. & Belousova, E. A. (2010). The Glenburgh Orogeny as a record of

Palaeoproterozoic continent-continent collision. Geological Survey of Western Australia, Record 2010/5.

Johnson, S. P., Sheppard, S., Rasmussen, B., Wingate, M. T. D., Kirkland, C. L., Muhling, J. R., Fletcher, I. R. & Belousova, E. A. (2011). Two collisions, two sutures: Punctuated pre-1950Ma assembly of the West Australian Craton during the Ophthalmian and Glenburgh Orogenies. *Precambrian Research,* 189, 239-262.

Johnson, S. P., Thorne, A. M., Tyler, I. M., Korsch, R. J., Kennett, B. L. N. N., Cutten, H. N., Goodwin, J., Blay, O., Blewett, R. S., Joly, A., Dentith, M. C., Aitken, A. R. A. A., Holzschuh, J., Salmon, M., Reading, A., Heinson, G., Boren, G., Ross, J., Costelloe, R. D. & Fomin, T. (2013). Crustal architecture of the Capricorn Orogen, Western Australia and associated metallogeny. *Australian Journal of Earth Sciences,* 60, 681-705.

Kirkland C. L., Wingate M. T. D., Bodorkos S., Sheppard S., Johnston S. P., (2009), 183275: psammitic schist, Mount Dalgety Geological Survey of Western Australia, Geochronology Record 836.

Kylander-Clark, A. R. C., Hacker, B. R. & Cottle, J. M. (2013). Laser-ablation split-stream ICP petrochronology. *Chemical Geology,* 345, 99-112.

Libby, W. G., De Laeter, J. R. & Armstrong, R. A. (1999). Proterozoic biotite Rb-Sr dates in the northwestern part of the Yilgarn Craton, Western Australia. *Australian Journal of Earth Sciences,* 46, 851-860.

Love G. J., Nelson D. R., Bodorkos S., Wingate M. T. D., (2006). 169096: coarse-grained monzogranite, Mica Well Geological Survey of Western Australia, Geochronology Record 621.

Lu Y., Wingate M. T. D., Kirkland C. L., Zibra I., (2016). 209610: clinopyroxene syenogranite, Paddy Bore. Geological Survey of Western Australia, Geochronology Record 1347.

Lu Y., Wingate M. T. D., Kirkland C. L., Goscombe B., Wyche S., (2015). 198654: quartzite, Mount Narryer. Geological Survey of Western Australia, Geochronology Record 1287.

Ludwig, K. R. (2003). Isoplot 3.00: A geochronological toolkit for Microsoft Excel. *Berkeley Geochronology Center Special Publication*, 39, 91-445.

Maas, R. & McCulloch, M. T. (1991). The provenance of Archean clastic metasediments in the Narryer Gneiss Complex, Western Australia: Trace element geochemistry, Nd isotopes, and U-Pb ages for detrital zircons. *Geochimica et Cosmochimica Acta,* 55, 1915-1932.

Mayborn, K. R. & Lesher, C. E. (2004). Paleoproterozoic mafic dike swarms of northeast Laurentia: Products of plumes or ambient mantle? *Earth and Planetary Science Letters,* 225, 305-317.

Mole, D. R., Fiorentini, M. L., Cassidy, K. F., Kirkland, C. L., Thebaud, N., McCuaig, T. C., Doublier, M. P., Duuring, P., Romano, S. S., Maas, R., Belousova, E. A., Barnes, S. J. & Miller, J. (2015). Crustal evolution, intra-cratonic architecture and the metallogeny of an Archaean craton (Vol. 393, pp. 23-80). London: *Geological Society, Special Publications.*

Myers, J. S. (1988). Early Archaean Narryer Gneiss Complex, Yilgarn Craton, Western Australia. *Precambrian Research,* 38, 297-307.

Myers, J. S.. (1993). Precambrian history of the West Australian Craton and adjacent orogens. *Annual Review of Earth and Planetary Sciences,* 21, 453-485.

Myers, J. S., Shaw, R. D. & Tyler, I. M. (1996). Tectonic evolution of Proterozoic Australia. *Tectonics,* 15, 1431-1446.

Nelson D. R., (1996). 105012.1: coarse-grained granite, south of Sharpe Bore. Geochrnology Record 511, Geological Survey of Western Australia.

Nelson D. R., (1997). 118961.1: coarse-grained fragmental chert, Beatty Park Bore. Geochronology Record 453, Geological Survey of Western Australia.

Nelson D. R., (1997) 118996.1: medium-grained, anhedral granular horneblende syenite, Teague Ring Structure. Geochronology Record 438, Geological Survey of Western Australia.

Nelson D. R., (1998). 142810.1, 142811.1, 142816.1, 142817.1: Characterization and metallogenic significance of Archaean granitoids of the Yilgarn Craton, Western Australia: Minerals and Research Institute of Western Australia (MERIWA), Report 222.

Lu, Y., Wingate, M. T. D., Blay, O. and Thorne A. M. (2017). 216142.1: granite gneiss, Lawson Well. Geochrnological Record 1430, Geological Survey Western Australia.

Nelson D. R. (1998). 142813.1: granite gneiss, Pamelia. Geochnological Record 381, Geological Survey Western Australia.

Nelson D. R., (1998). 142901.1: foliated porphyric monzogranite, No. 2 Bore. Geochronological Record 361, Geological Survey of Western Australia.

Nelson D. R., (1998). Sample 142816: biotite monzogranite, (Marymia Inlier), 2A Tank; Geochronology Record 383, Geological Survey of Western Australia.

Nelson D. R., (1999). 148397.1: horneblende monzogranite, No. 10 Bore. Geochronological Record 257, Geological Survey of Western Australia.

Nelson D. R., (2000a). 142986.1: metasandstone, Eranondoo Hill. Geochronology Record 289, Geological Survey of Western Australia.

Nelson D. R., (2000b). 164309: foliated porphyritic biotite granodiorite, Middle Well. Geochronology Record 217, Geological Survey of Western Australia.

Nelson D. R., (2000c). 142988: biotite tonalite, Dunnawah Bore. Geochronology Record 291, Geological Survey of Western Australia.

Nelson, D. R. (2001). An assessment of the determination of depositional ages for Precambrian clastic sedimentary rocks by U-Pb dating of detrital zircons. *Sedimentary Geology,* 141-142, 37-60.

Nelson, D. R., (2005). 178063.1: quartz micromonzonite, Barlangi Rock. Geochronology record 590, Geological Survey of Western Australia.

Nutman, A. P., Kinny, P. D., Compston, W. & Williams, I. S. (1991). SHRIMP U-Pb zircon geochronology of the Narryer Gneiss Complex, Western Australia. *Precambrian Research,* 52, 275-300.

O'Neill, C., Lenardic, A., Moresi, L., Torsvik, T. H. & Lee, C. T. A. (2007). Episodic Precambrian subduction. *Earth and Planetary Science Letters,* 262, 552-562.

Paton, C., Woodhead, J. D., Hellstrom, J. C., Hergt, J. M., Greig, A. & Maas, R. (2010). Improved laser ablation U-Pb zircon geochronology through robust downhole fractionation correction. *Geochemistry, Geophysics, Geosystems,* 11, 3.

Pearce, J. A. (2008). Geochemical fingerprinting of oceanic basalts with applications to ophiolite classification and the search for Archean oceanic crust. *Lithos,* 100, 14-48.

Pirajno, F., Occhipinti, S. A. & Swager, C. P. (1998). Geology and tectonic evolution of the Palaeoproterozoic Bryah, Padbury and Yerrida basins (formerly Glengarry Basin), Western Australia: implications for the history of the south-central Capricorn Orogen. *Precambrian Research*, 90, 119-140.

Pirajno, F. & Adamides, N. G. (2000). Geology and Mineralization of the Palaeoproterozoic Yerrida Basin, Western Australia. Geological Survey of Western Australia, Report 60.

Pirajno, F. & Occhipinti, S. A. (2000). Three Palaeoproterozoic basins—Yerrida, Bryah and Padbury—Capricorn Orogen, Western Australia. *Australian Journal of Earth Sciences,* 474, 675-688.

Pirajno, F. (2004). Oceanic plateau accretion onto the northwestern margin of the Yilgarn Craton, Western Australia: Implications for a mantle plume event at ca. 2.0 Ga. *Journal of Geodynamics,* 37, 205-231.

Pirajno, F., Jones, J. A., Hocking, R. M. & Halilovic, J. (2004). Geology and tectonic evolution of Palaeoproterozoic basins of the eastern Capricorn Orogen, Western Australia. *Precambrian Research,* 128, 315-342.

Sheppard, S., Occhipinti, S. A. & Tyler, I. M. (2004). A 2005-1970 Ma Andean-type batholith in the southern Gascoyne Complex, Western Australia. *Precambrian Research,* 128, 257-277.

Slama, J., Kosler, J., Condon, D. J., Crowley, J. L., Gerdes, A., Hanchar, J. M., Horstwood, M. S. A., Morris, G. A., Nasdala, L., Norberg, N., Schaltegger, U., Schoene, B., Tubrett, M. N. & Whitehouse, M. J. (2008). Plešovice zircon - A new natural reference material for U-Pb and Hf isotopic microanalysis. *Chemical Geology,* 249, 1-35.

Spencer, C. J., Murphy, J. B., Kirkland, C. L., Liu, Y. & Mitchell, R. N. (2018). A Palaeoproterozoic tectono-magmatic lull as a potential trigger for the supercontinent cycle. *Nature Geoscience,* 11, 97-101.

Strand, K. & Köykkä, J. (2012). Early Paleoproterozoic rift volcanism in the eastern Fennoscandian Shield related to the breakup of the Kenorland supercontinent. *Precambrian Research,* 214-215, 95-105.

Thomsen, T. B., Heijboer, T. & Guarnieri, P. (2016). jAgeDisplay : Software for evaluation of data distributions in U-Th-Pb geochronology. *Geologic survey of Denmark and Greenland bulletin*, 35, 103-106.

Van Kranendonk, M. J., Ivanic, T. J., Wingate, M. T. D., Kirkland, C. L. & Wyche, S. (2013). Long-lived, autochthonous development of the Archean Murchison Domain, and implications for Yilgarn Craton tectonics. *Precambrian Research,* 229, 49-92.

Vermeesch, P., Resentini, A. & Garzanti, E. (2016). An R package for statistical provenance analysis. *Sedimentary Geology,* 336, 14-25.

Vielreicher, N. M. & McNaughton, N. J. (2002). SHRIMP U-Pb geochronology of magmatism and thermal events in the Archaean Marymia Inlier, central Western Australia. *International Journal of Earth Sciences, 91/3, 406-432.*

Wiedenbeck, M., AllÉ, P., Corfu, F., Griffin, W. L., Meier, M., Oberli, F., Quadt, A. V., Roddick, J. C. & Spiegel, W. (1995). Three Natural Zircon Standards for U-Th-Pb, Lu-Hf, Trace Element and Ree Analyses. *Geostandards Newsletter,* 19, 1-23.

Wilde, S. a., Middleton, M. F. & Evans, B. J. (1996). Terrane accretion in the southwestern Yilgarn Craton: evidence from a deep seismic crustal profile. *Precambrian Research,* 78, 179-196.

Wingate M. T. D., Bodorkos S., (2007), 184107: metamorphosed quartz sandstone, Christmas Bore. Geochronology Record 67, Geological Survey of Western Australia.

Wingate M. T. D., Bodorkos S., (2007), 177933: hornblende granodiorite, Camel Bore. Geochronology Record 675, Geological Survey of Western Australia.

Wingate M. T. D. , Bodorkos S., Kirkland C. L., (2008), 183921,184113: felsic volcaniclastic rock, Lordy Bore. Geochronology Record 733, Geological Survey of Western Australia.

Wingate M. T. D., Kirkland C. L., and Van Kranendonk M. J., (2011), 183953: felsic metavolcaniclastic rock, Five Mile Well Mine; Geochronology Record 969, Geological Survey of Western Australia.

Wingate M. T. D., Kirkland C. L., Compston D., Wyche S., (2011), 185998: felsic metavolcaniclastic rock, Dan Well; Geochronology Record 979, Geological Survey of Western Australia.

Wingate M. T. D., Kirkland C. L., and Chen, S. F., (2012), 187655: biotite monzogranite, Yundobubba Bore; Geochronology Record 1009, Geological Survey of Western Australia.

Withjack, M. O., Schlische, R. W. & Olsen, P. E. (2002). Rift-Basin Structure and Its Influence on Sedimentary Systems. *Sedimentation in Continental Rifts*, (vol. 73, pp. 57-81). Society for Sedimentary Geology Special Pubblications.

Woodhead, J. D. & Hergt, J. M. (1997). Application of the `double spike' technique to Pb-isotope geochronology. *Chemical Geology,* 138, 311-321.

CHAPTER 3

GEOCHRONOLOGICAL AND PROVENANCE CONSTRAINTS ON THE SEDIMENTARY ROCKS HOSTING THE ABRA POLYMETALLIC DEPOSIT, CAPRICORN OROGEN, WESTERN AUSTRALIA

Armandola S.[1*], Barham M.[1,2], Reddy S. M.[1], Clark C.[1], Taylor R. J. M.[4], Spinks S. C.[3]

[1]School of Earth and Planetary Sciences, Curtin University, GPO Box U1987, Perth, WA 6845, Western Australia.

[2]Centre for Exploration and Targeting, Curtin Node, Curtin University, GPO Box U1987, Perth, WA 6845, Western Australia.

[3]Commonwealth Scientific and Industrial Research Organisation (CSIRO), PO box 1130 Bentley, WA 6102, Australia.

[4]Department of Earth Sciences, Downing Site, University of Cambridge, CB2 3EQ, Cambridge, United Kingdom.

Corresponding author: sonia.armandola01@gmail.com

 Abstract

Characterization of host rocks is an essential step towards understanding the genesis and history of sedimentary rock-hosted mineral deposits. Abra is a sedimentary rock-hosted polymetallic deposit, located within the Mesoproterozoic Edmund Basin, in the central Capricorn Orogen, (Western Australia). Stratigraphic analysis and detrital zircon geochronology and geochemistry of the Abra host rock revealed that the stratigraphy comprises four distinct units that correlate with three formations of the Edmund Basin (Irregully Formation, Gooragoora Formation, Blue Billy Formation, Kiangi Creek Formation). Detrital zircon U-Pb geochronology constrains the maximum depositional age for the Irregully to 1626 Ma, and for the Kiangi Creek Formation to 1484 Ma. The detrital zircon ages compared with available data on the

mineralization, highlight an age gap of c. 100 Ma between the deposition of the basal succession, which hosts the primary base metals deposit, and the topmost sedimentary succession, which records a second mineralization event. The lowest formations accumulated just after the 1680–1640 Ma Mangaroon Orogeny. Moreover, the Gooragoora and Blue Billy formations exhibit a sharp shift of sediment sources from west (Gascoyne Complex) to south (Yilgarn Craton granites), coincident with extensional tectonic reactivation of the northern Yilgarn Craton margin. The tectonic reactivation promoted basin deepening and local hydrothermal fluid circulation, which is interpreted to have boosted mineralization in the Abra polymetallic deposit.

1. Introduction

Sediment-hosted mineral deposits are key sources of base metals, such as Pb–Fe–Zn–Au–Ag–Cu–Ni–Mo–Ba (Spinks et al., 2016; Large et al., 2005). Such deposits are generally related to the depositional history of the sedimentary rocks hosting them because their genesis occurs either synchronous with sedimentation (Large et al., 2000; 2005), or during diagenesis (Cooke et al., 2000). Moreover, base metals accumulation take place under specific chemical conditions and within certain lithologies (e.g. Large et al., 2000; 2005; Spinks et al., 2016). Consequently, characterization of the host rock facies, depositional age and provenance, is essential to decipher the history of sediment-hosted base metal deposits and correlate them with the broad tectonic frame of the regions hosting them.

In the Capricorn Orogen (Western Australia) the giant polymetallic sediment-hosted Abra deposit contains economically significant concentrations of Fe, Pb, Zn, Ba, Cu, Au, Ag, Bi, and W, of enigmatic origin (Fig. 1-3). The Abra deposit has been the subject of a number of studies (e.g. Martin et al., 1995; Pirajno & Bagas, 2008; Pirajno et al., 2015; Zi et al., 2015), which characterized the mineralization, subdividing it in three main zones (e.g. Martin et al., 1995; Pirajno & Bagas, 2008; Pirajno et al., 2015), constrained the age of the primary base metal precipitation at ~1594 Ma (Zi et al., 2015), and recognised a subsequent stage of mineralization dated at ~1255 Ma (Pirajno et al., 2015). However, no previous studies have focused on characterizing the Abra sedimentary host rocks, which is poorly correlated with the Mesoproterozoic Edmund Basin and have scarce age and provenance data (Martin et al., 2008; Cutten et al., 2016).

Detrital zircons are widely present within sediments and preserve information on their source rock age (U-Pb) and composition (trace elements; e.g. Iizuka et al., 2013). Due to this, they are traditionally analysed to provide age limits (maximum depositional age) to the sedimentary successions hosting them. Additionally, the detrital zircon age data can be compared with the crystallization age of magmatic sources and the age spectra of older sedimentary sinks, to unravel the provenance of the sediments and reconstruct the tectonic evolution of the basin and sources (e.g. Iizuka et al., 2013; Barham et al., 2018).

To reconstruct the Edmund Basin stratigraphy and depositional history at Abra, U-Pb geochronology and geochemistry of detrital zircons are examined. Detrital zircon age data constrain the maximum depositional age of the Abra host rocks and are integrated with previous age data obtained from hydrothermal accessory phases, to unravel the chronology of the sediment-mineral system. The detrital zircon U-Pb ages coupled with the trace elements are compared to compiled age data from potential source rocks and regional sediment reservoirs in the Edmund Basin to constrain the provenance of the Abra host sediments. The results from the provenance study are used to determine the evolutionary history of the Edmund Basin and reconstruct the tectonic setting of the Capricorn Orogen region in the Mesoproterozoic.

2. Geological background

2.1 The Capricorn Orogen

The Capricorn Orogen records the amalgamation of the West Australian Craton through two distinct orogenic events. The 2215–2145 Ma Ophthalmian Orogeny (Johnson et al., 2011) records the collision of the Pilbara Craton and Glenburgh Terrane, while during the subsequent 2005–1950 Ma Glenburgh Orogeny the Pilbara–Glenburgh block accreted to the northern Yilgarn Craton (Johnson et al., 2010). The collision was accompanied by intense magmatism and emplacement of the 2100–2005 Ma Dalgaringa Supersuite and the 1965–1945 Ma Bertibubba Supersuite in the Gascoyne Complex (Johnson et al., 2013). After the continental accretion, the Capricorn Orogen experienced tectonic reactivation and magmatism during the 1820–1770 Ma Capricorn Orogeny and associated 1850–1750 Ma Moorarie Supersuite (Cawood & Tyler, 2004), and the 1680–1620 Ma Mangaroon Orogeny and Durlacher Supersuite emplacement (Sheppard et al., 2005). Later tectonic reactivations also

occurred during the 1320–1170 Ma Mutherbukin Tectonic Event, which is associated with the last magmatic unit emplaced known as Thirty Three Supersuite (Korhonen et al., 2015). Palaeoproterozoic and Mesoproterozoic depositional sequences associated with the Capricorn Orogen overlie and intervene crystalline basement on the two craton margins (e.g. Ashburton and Blair basins on the southern Pilbara Craton margin, Yerrida, Bryah and Padbury basins on the northern Yilgarn Craton margin). The youngest sequences found associated with the belt are the Mesoproterozoic Edmund Basin and overlying Collier Basin (Fig. 1; Cawood & Tyler, 2004).

Fig. 1. Structural units of the Capricorn Orogen. Location of the Abra deposit. PC – Pilbara Craton; YC – Yilgarn Craton.

2.2 The Edmund Basin

The Mesoproterozoic Edmund Basin is a 4-10 km thick siliciclastic and volcanoclastic succession, preserved in the centre of the Capricorn Orogen. Deposition within the Edmund Basin took place after the 1680–1640 Ma Mangaroon Orogeny (Fig. 2; Sheppard et al., 2005) and before the 1320–1170 Ma Mutherbukin Tectonic Event (Fig. 2; Korhonen et al., 2015). Mafic magmatism at 1515–1500 Ma (Fig. 2; Waldburg Dolerite; Wingate et al., 2012a) and c. 1465 Ma (Fig. 2; Wingate et al., 2002) suggest an intracratonic extensional setting during the deposition (Cutten et al., 2016). The morphology of the Edmund basin was characterized by a large shelf structure in the north, coinciding with the southern margin of the Pilbara Craton (Pingandy Shelf), and a rift sub-basin towards the centre and south (Martin & Thorne, 2004 Martin et

al., 2008). Consequently, deposition within the Edmund Basin took place across a variety of distinct environments from carbonate shelf to deep marine, some of which are time equivalent.
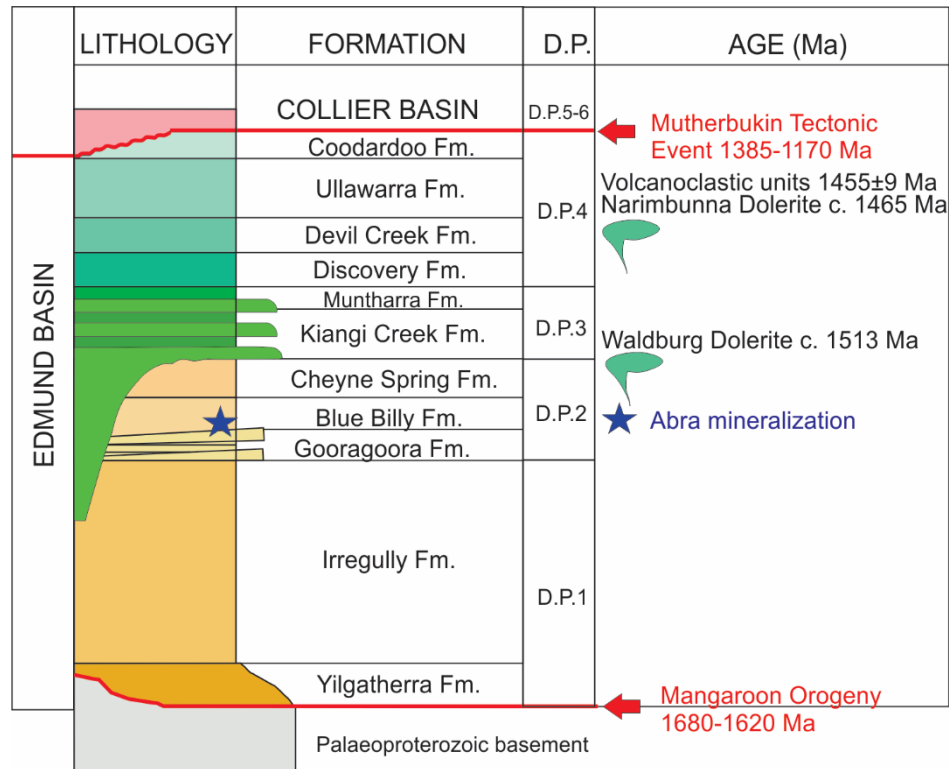
Fig. 2. Stratigraphic succession of the Edmund Basin, modified from Cutten et al. (2016), with significant age constraints (Martin & Thorne, 2004; Sheppard et al., 2005; Wingate, 2004; 2012a; Martin et al., 2008). D.P. - depositional package.

2.3 Mineralization at Abra

The Abra polymetallic (Fe, Pb, Zn, Ba, Cu, Au, Ag, Bi, and W) deposit is hosted at the eastern end of the Jillawarra Sub-Basin (Vogt, 1995), within the junction of two major faults, the northeast-trending Bujundunna Fault and the easterly-trending Quartzite Well Fault (Fig. 3; Vogt, 1995; Zi et al., 2015). The southern margin of the Abra deposit is delineated by the Coodardoo South Fault (Fig. 3). The main mineralization is hosted in the uppermost portion of the Irregully Formation, possibly in lithologies equivalent to the Gooragoora Formation and in the lower section of the overlying Kiangi Creek Formation, and is c. 400 m thick, buried at a depth of c. 230–250 m (Rasmussen et al., 2010; Zi et al., 2015; Pirajno et al., 2016; Lampinen et al., 2017).

The stratabound mineralization consists of several distinct portions: (i) a basal funnel-shaped Black Zone with brecciated rocks (Fig. 4; Stringer Zone), (ii) an overlying White Zone, and (iii) an upper Red Zone, hosting dolomitised units, which is truncated by a conglomeratic horizon. The Black Zone is considered the carrier pipe for the overlying stratabound mineralization (Fig. 4; Zi et al., 2015). The main mineralizing episode at Abra is considered syndiagenetic to the Red zone (Fig. 4; lower Kiangi Creek Formation), which has been dated at c. 1594 ± 10 Ma (Zi et al., 2015). The hydrothermal activity linked with the emplacement of the stratabound minerals was interpreted to have lasted c. 20–30 Ma, based on a cluster of xenotime minerals dated at. 1610 ± 16 Ma from the underlying Black Zone (Zi et al., 2015). A second generation of minerals is hosted in the upper units of the Kiangi Creek Formation. This second mineralizing event has been linked to hydrothermal activity after the deposition of the formation and has an uncertain age close to ~1255 Ma (Fig. 2; Pirajno et al., 2016).
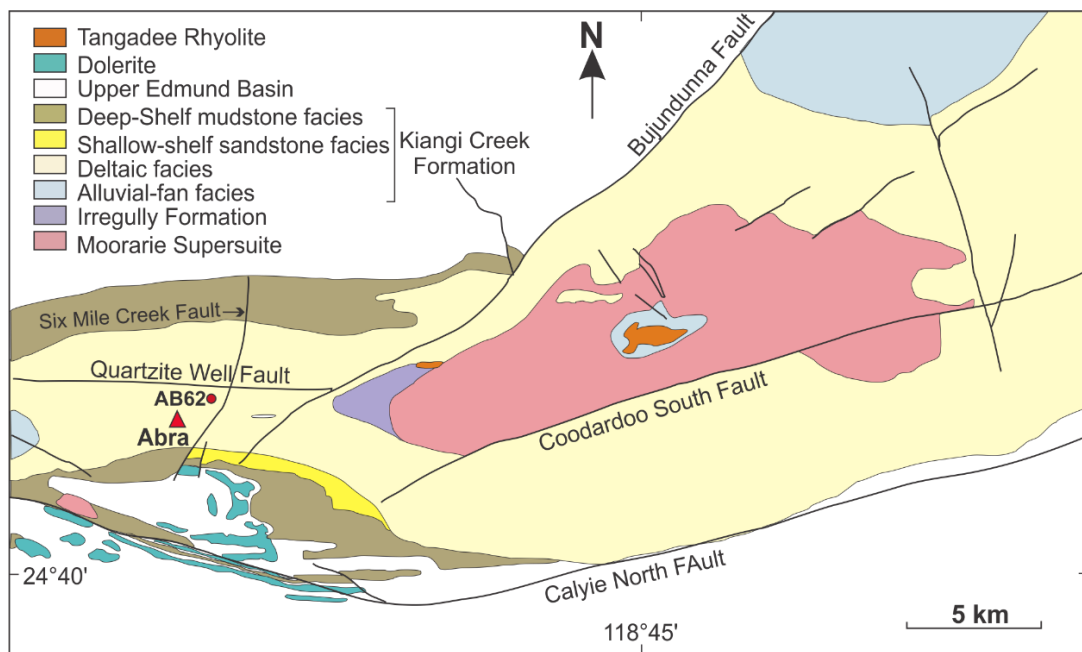
Fig. 3. Interpreted geology of the Abra area, modified from Zi et al. (2015).
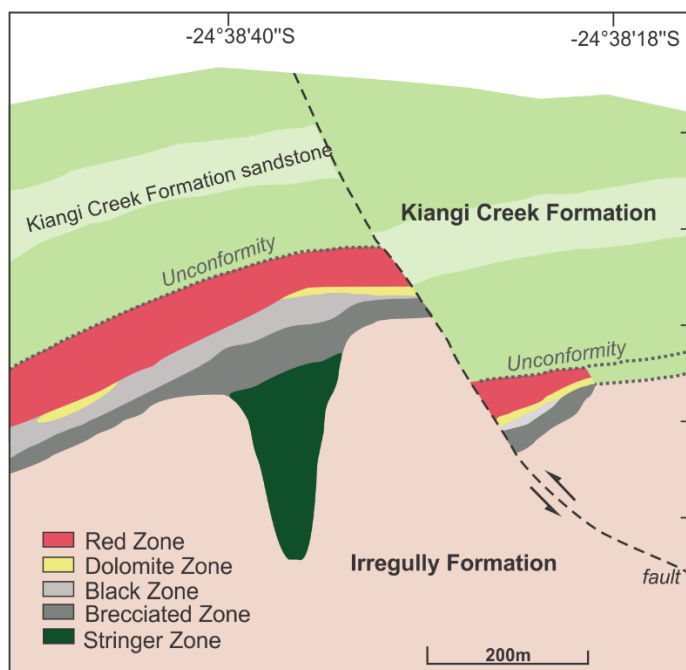
Fig. 4. Schematic cross-section of the Abra mineral deposit and its host rocks. Modified after Collins and McDonald (1994), Zi et al. (2015), and Pirajno et al. (2016).

3. Analytical method

Detrital zircons were separated, mounted and analysed in the John de Laeter Centre at Curtin University. Rock samples were disaggregated using SelFrag electro-pulse fragmentation, with electrical pulses of 3 Hz and 130 kV. The disaggregated material was hand panned to obtain a heavy mineral aliquot. A Frantz magnetic separator was used to isolate non-magnetic minerals with increments of magnetic field intensities from 0.5 to 1.7 A. Detrital zircon grains were handpicked from the non-magnetic fraction and mounted in 25 mm epoxy resin discs. Zircon grains were then hand polished with 2000 grit wet sandpaper, 6 µm, 3 µm diamond embedded lapping film and 1 µm diamond paste, through almost half of the mineral thickness, to expose internal grain surfaces.

Imaging of zircon grains was undertaken on a Tescan MIRA3 Field Emission SEM with Oxford Instruments Aztec, housed in the Microscopy & Microanalysis Facility (John de Laeter Centre) at Curtin University. Cathodoluminescence (CL) imaging was undertaken using a Tescan panchromatic CL detector at 10 kV accelerating voltage and a working distance of 16 mm. According to the zircon internal zoning, generally characterized by core-rim structures, the innermost homogeneous portion of the grains were selected for ablation to obtain igneous crystallization ages.

Detrital zircon U-Pb isotopes and trace elements compositions were measured synchronously on an ICP-MS Laser, fitted with a Resonetics S-155-LR 193 nm Excimer laser, coupled to a Nu Instruments Plasma HR multicollector inductively coupled plasma and an Agilent 7700x quadrupole ICP-MS. The laser beam size used for analysis was 33 µm with a fluence of 2 J/cm^2 and repetition rate of 4 Hz. The carrier gas was composed of a mixture of He 3.2 ml/min, Ar gas at 1 ml/min and N gas at 1.2 ml/min flow rates. Natural zircon standards Plešovice (337.13 ± 0.37 Ma; Slama et al., 2008) and GJ1 (608.5 ± 0.4 Ma; Jackson et al., 2004) were measured as primary standards for U-Pb and trace elements calculations respectively. OGC (3465.4 ± 0.6 Ma; Bodorkos et al., 2009) and 91500 (1061 ± 4.3 Ma; Wiedenbeck et al., 1995) were measured throughout all the analytical sessions to check the accuracy of the measurements. 91500 standard material provided an age of 1062.2 ± 2.9 Ma (MSWD=0.12, n=21), while OGC was recorded with an age of 3467 ± 19 Ma (MSWD=2, n=12). The U-Pb isotopes and trace elements abundances were calculated with the *Iolitev2.5* software on IgorPro, where background signal and down-hole fractionation corrections were applied (Paton et al., 2010).

Detrital zircon with ≥90% concordance between their ^{238}U/^{206}Pb and ^{207}Pb/^{206}Pb ages are used for the discussion. All ages of the zircons are indicated as ^{207}Pb/^{206}Pb ages (Appendix 1). The analysed detrital zircon populations are displayed through probability density plots (PDP; *jAgeDiaply;* Thomsen et al., 2016). The provenance study and the comparison between the analysed detrital zircons ages with pooled age data from potential source rocks is made with stacked kernel density plots (KDP; *Provenance*; Vermeesch et al., 2016). Probability of fit is evaluated with the Kolmogorov-Smirnov test, giving a probability value *p*>0.05 (Appendix 1; Table 2-3; Guynn & Gehrels, 2010).

4. Results

4.1 AB62 drill core stratigraphy and samples

Ten samples were analysed from the diamond drill core AB62, drilled in 2012 by Abra Mining Ltd. (662147E, 7274152N, Zone 50, Six-Mile Creek Fault Project; Fig. 6, Table 1). Drill core AB62 is distal to, and doesn't intersect Abra mineralization, but does penetrate equivalent stratigraphy to the main stratabound mineralization.

Drill core AB62 is divisible into four distinct sequences (Fig. 5). The lowermost section (601–348 m depth) corresponds to the Irregully Formation (Zi et al., 2015) and comprises two sub sequences: (i) from 610 to 410 m ripple and planar laminated sandstone is interbedded with thinner laminated mudstone and subordinate siltstone in fining-upward cycles that are interpreted to represent fluvial and alluvial deposits, similar to other mineralized drill cores (Zi et al., 2015); (ii) from 410 to 348 m, thick fining upward laminated siltstone and mudstone are rhythmically interbedded with thinner sandstone levels compatible with a lacustrine environment (Fig. 5). The latter subsequence is characterized by several post-lithification brecciated layers (Fig. 5), similar and perhaps correlative of the Brecciated Zone and Black Zone of equivalent mineralized drill cores analysed in the past (Fig. 5-10; Zi et al., 2015; Pirajno et al., 2016).

At the top of the Irregully Formation in AB62 a distinct c. 16 m thick white coarse-grained quartz sandstone is observed (c. 348–332 m) with disseminated pyrite cubes up to 1 to 2 cm in size. The unit is separated by disconformable contacts from the bounding formations and given its distinct lithology, could represent an equivalent of the Gooragoora Formation shallow deltaic deposits (Cutten et al., 2016).

Within the AB62 drill core, two distinct facies are generally correlated with the Kiangi Creek Formation: Facies 1 (330–265 m) and Facies 2 (265–9 m; Fig. 5; Zi et al., 2015; Pirajno et al., 2015). Facies 1 consists of mudstone alternating with medium to coarse-grained sandstone, with minor siltstone in coarsening upward depositional cycles, but locally showing fining upward gradation in sandstone beds. These sediments correspond to submarine fan deposits (continental slope), since they display: sharp bases, cm-scale unidirectional ripple lamination and convolute lamination, slumps, clay aggregates and angular clay chips, flames and load structures, and are interbedded with thick laminated mudstones units (Fig. 5-10, Facies 1). In equivalent mineralised drill cores, Facies 1 (alluvial-fan deposits) hosts the Red Zone and is inferred to be coeval with it (Fig. 5-10; Pirajno et al., 2015, Zi et al., 2015). Facies 2 corresponds to the uppermost part of the Kiangi Creek Formation and in AB62 is separated from the lower unit at c. 265 m by an angular unconformity, which is overlain by a thick basal conglomeratic horizon (Fig. 5). Facies 2 is composed of coarse siliciclastic, conglomeratic beds with rounded and subrounded clasts, thick and

coarse cross-bedded sandstone beds, poorly sorted, minor breccias, all showing an overall coarsening upward trend. These coarser lithologies of the Kiangi Creek Formation are consistent with coarse deltaic deposits (Zi et al., 2015), from a braided delta complex, characterized by short transportation capacity (Fig. 5).

Table 1. Details for the studied samples from AB62.

Sample ID	Depth from (m)	Depth to (m)	Lithology	Stratigraphic Unit
AB1	27	29.3	Medium to coarse-grained sandstone and conglomeratic levels containing small rounded pebbles and sand matrix.	Kiangi Creek Fm. Facies 2
AB2	62.2	64.95	Medium-grained sandstone with thin siltstone and mudstone levels at the base.	Kiangi Creek Fm. Facies 2
AB3	72	72.2	Alternating conglomerate and coarse sandstone.	Kiangi Creek Fm. Facies 2
AB4	103.7	103.85	Medium coarse sandstone, with conglomerates horizons poorly sorted, with elongated clasts aligned at the base of the bed.	Kiangi Creek Fm. Facies 2
AB5	153.2	153.4	Coarsening-upward grey sandstone with planar parallel lamination and coarse clast levels (imbricate clasts).	Kiangi Creek Fm. Facies 2
AB7	272.8	277.15	Brown to grey sandstone with thin mudstone levels and rounded small quartz clasts. Clay chips and load structures.	Blue Billy Fm.? (currently Kiangi Creek Fm. Facies 1)
AB8	326.9	327.1	Medium to coarse-grained sandstone, poorly sorted with small brown clasts.	Blue Billy Fm.? (currently Kiangi Creek Fm. Facies 1)
AB9	340	340.25	White rounded and well sorted coarse quartz sandstone with pyrite cubes disseminated.	Gooragoora Fm.? (currently Irregully Fm.)
AB12	494.8	495	Grey rounded medium to coarse sandstone.	Irregully Fm.
AB13	593.6	599.15	Fining-upward, ripple laminated medium coarse sandstone with siltstone layers interbedded.	Irregully Fm.
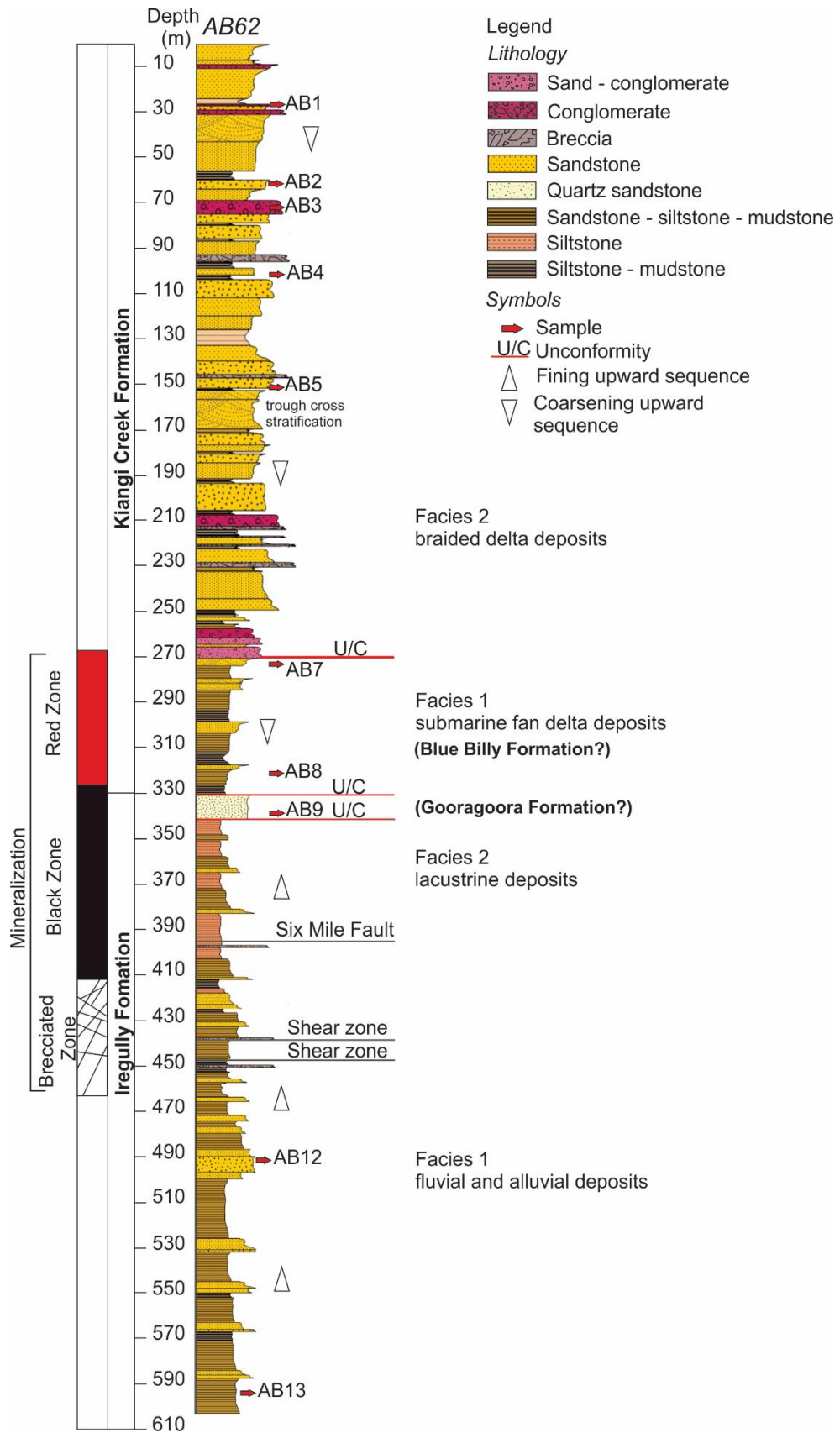
Fig. 5. Summarized stratigraphy of AB62 drill core. Sample stratigraphic depth is marked. Correlation with the mineralized drill core is inferred from Zi et al. (2015).

4.2 Detrital zircon geochronology and geochemistry

The geochronological and geochemical data for the detrital zircon grains analysed are listed in Appendix 1. The detrital zircon grains have spherical to elongate shapes and are rounded to subrounded, with grains up to 250 µm in length (Fig. 6). Zircon grains vary in colour from pink, milky, yellow to red. Their distribution in the samples is determined by the overall grain size of the hosting sediment, e.g. coarse sandstone and conglomeratic layers carried the largest detrital zircon grains. Cathodoluminescence (CL) imaging highlighted the presence of inner core and over-growth rims in the majority of the grains. Some zircon grains, based on the CL images, appeared to be rounded and elongated fragments of larger grains (Fig. 6).
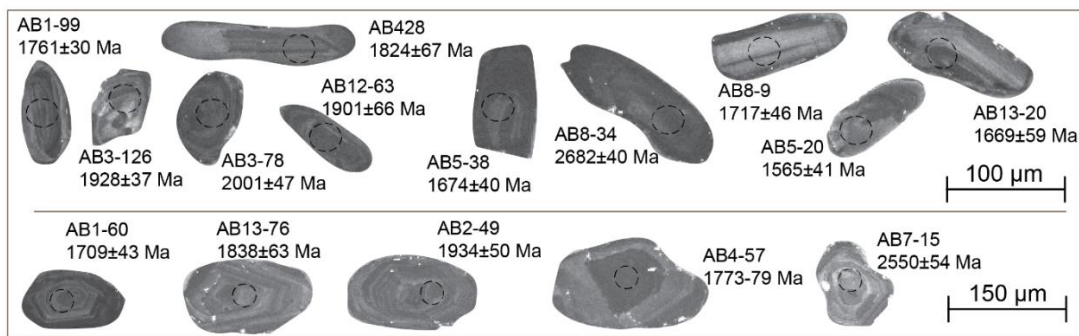
Fig. 6. Representative cathodoluminescence (CL) images of detrital zircon grains yielding ≥90% concordant ages. Dashed circles indicate the position of laser spot analyses.

4.2.1 Detrital zircon geochronology

Irregully Formation

Sample AB13 from the basal Irregully Formation yielded 74 concordant ages that define a broad, polymodal age spectra that ranges from 2400 to 1600 Ma, with the largest population between 1900 and 1800 Ma and a defined subordinate peak at ~2100 Ma (Fig. 7-8). Sample AB12 provided 95 concordant ages, with a polymodal age distribution, but a defined dominant detrital zircon peak at ~1700 Ma (Fig. 7-8). The age spectra of sample AB12 is positively skewed, with small age clusters between 2500 and 1800 Ma (Fig. 7-8). The youngest detrital zircon population found in the Irregully Formation is from sample AB12 with weighted average age of 1676 ± 19 Ma (MSWD=0.28; n=15; the youngest individual grain was dated at 1626 ± 70 Ma).

Gooragoora Formation

Sample AB9 yielded only seven concordant ages, the majority of which range between 1800 and 1700 Ma (Appendix 1).

Kiangi Creek Formation Facies 1

Sample AB8 (from the lowermost facies of the Kiangi Creek Formation) yielded 45 concordant detrital zircon ages and the largest age distribution observed. Ages range from the Archean, as old as 3000 Ma, to 1600 Ma. The dominant age group ranges from 1800 to 1700 Ma with a peak at c. 1740 Ma. Several smaller age clusters are present between 2300 and 1900 Ma (Fig. 7-8). Sample AB7 returned 47 concordant ages and the greatest proportion of late Archean detrital zircons in the stratigraphic section exposed in AB62 drill core. The youngest detrital zircon group is dated at 2120 Ma while the dominant age cluster is bimodal with a prominent ~2680 Ma peak and subordinate peak at 2540 Ma (Fig. 7-8).

Kiangi Creek Formation Facies 2

Sample AB5 (from the uppermost facies of the Kiangi Creek Formation) produced 75 concordant ages with a large polymodal age distribution and dominant age mode of c. 1740 Ma, similar to that in sample AB8 (Fig. 7-8). The youngest zircon found in this sample is 1484 ± 30 Ma, and together with two zircons produce a mean age of 1574 ± 28 Ma representing the youngest ages found in the stratigraphic section of AB62 (Fig. 7-8). Sample AB4 yielded 45 concordant ages spanning between 2100 and 1650 Ma, with a dominant age mode of c. 1800 Ma and a subordinate group at c. 1940 Ma (Fig. 7-8). Sample AB3 yielded 26 concordant ages with a dominant detrital zircon population dated at 1910 Ma and a small group of Archean detrital zircons between 2700 and 2500 Ma (Fig. 7-8). Sample AB2 produced 57 concordant detrital zircon ages with a weak bimodal age spectrum with peaks at c. 1980 Ma, and a subordinate peak at 1820 Ma. Sparse Archean detrital zircon grains are preserved within all samples (Fig. 7-8). Sample AB1 yielded an almost bimodal distribution with a dominant young population of zircon grains at c. 1770 Ma, and a subordinate subpopulation between 2000 and 1900 Ma (Fig. 7-8).
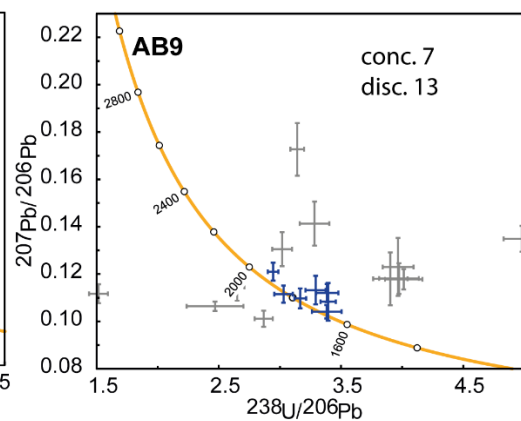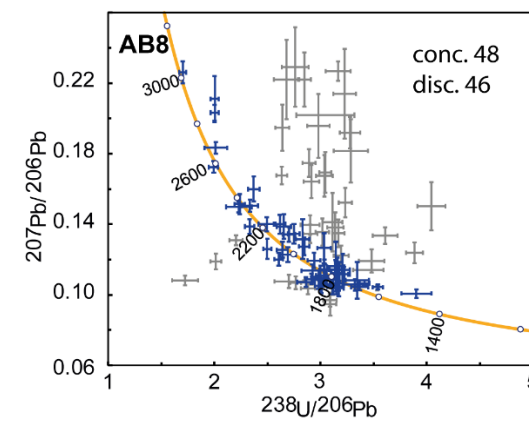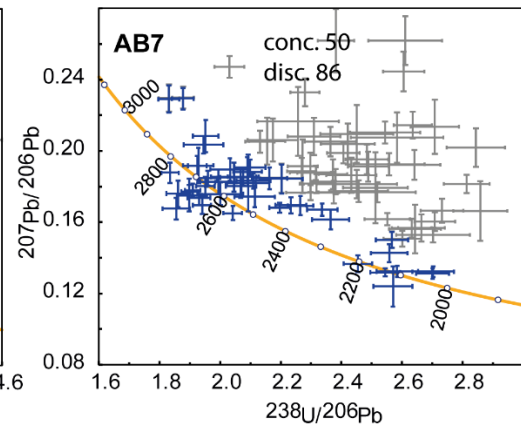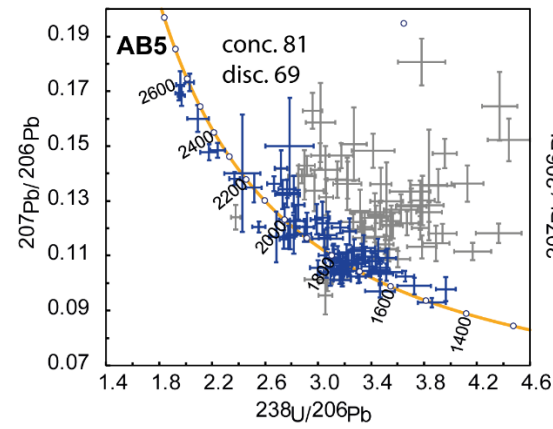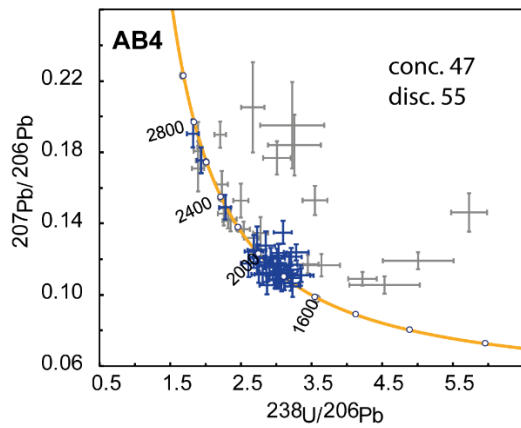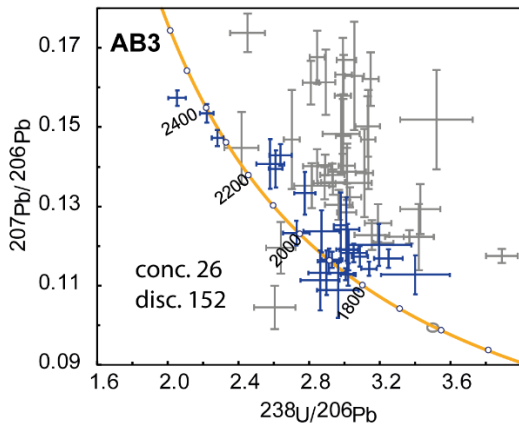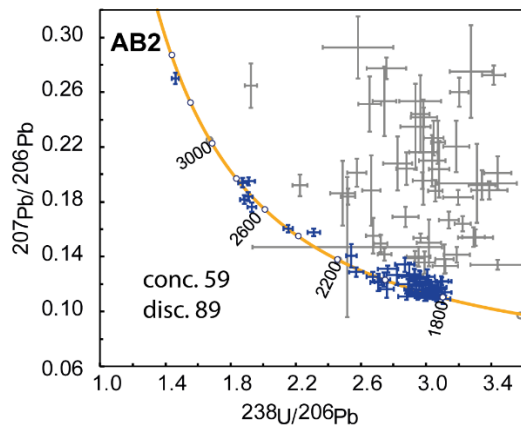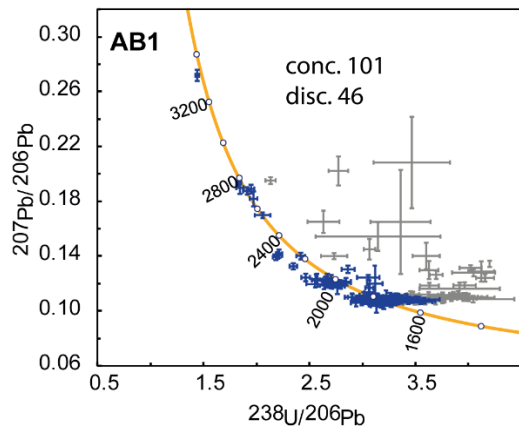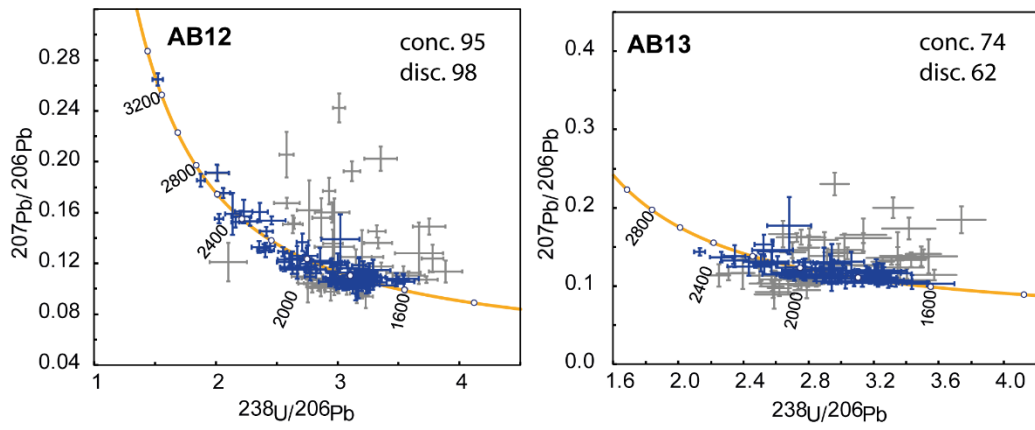
Fig. 7. Tera-Wasserburg Concordia diagrams for the concordant detrital zircon Spinks et al., and discordant detrital zircon (grey) analyses (*Isoplotv4.15;* Ludwig et al., 2003).
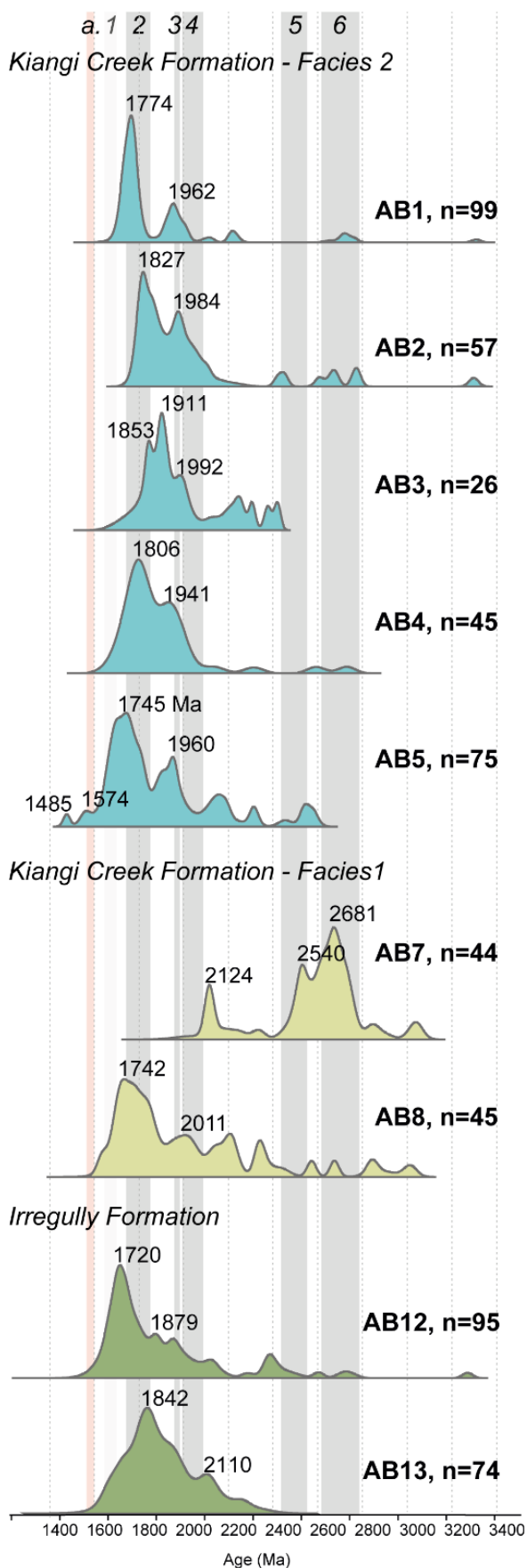
Fig. 8. Probability density plot (PDP) of the concordant detrital zircon grain ages (2σ errors; *jAgeDisplay*; Thomsen et al., 2016). Key subpopulations have modal ages reported; n is the total number of concordant zircons in each PDP plot; a. is the age of the mineralization event in Abra (Zi et al., 2015); 1- Durlacher Supersuite; 2- Moorarie Supersuite; 3- Bertibubba Supersuite; 4- Dalgaringa Supersuite; 5- Halfway Gneiss; 6- Yilgarn Craton granites (Johnson et al., 2013).

4.2.2 Detrital zircon trace elements

Most of the detrital zircon grains analysed have high Th/U ratios (> 0.1) and exhibit fractionated rare earth elements (REE) patterns when normalized to Chondritic values (Anders & Grevesse, 1989), with negative Eu anomalies and positive Ce anomalies (Eu calculated as SQRT(Sm*Gd), Ce calculated as SQRT(La*Pr)) typical of a magmatic origin (Appendix 1; Hoskin & Schaltegger, 2003). The detrital zircon grains analysed typically have high U/Yb values (0.09–33), intermediate Hf concentrations (4670–20000 ppm), and high Y content (90–8000 ppm; Fig. 9). Few detrital zircons grains have high LREE and less pronounced Eu negative anomaly, which can be linked to the fractionation history of the feldspar in the sourcing melt (Hoskin and Ireland, 2000; Hoskin and Schaltegger, 2003). For example, a positive Eu anomaly is most often associated with zircon alteration, melts effected by strong sphene fractionation, or, in rare cases, by when melt saturate in zircon prior the feldspar (Hoskin & Schaltegger, 2003; Hoskin, 2005). Oxygen fugacity also controls the distribution of Eu and Ce in zircon in extremely oxidic condition and/or without feldspar fractionation and is an indicator of metamorphic conditions for the zircon genesis (Trail et al., 2012).

In decreasing order, the detrital zircons analysed have trace element defined affinity with the continental arc field, oceanic island setting (felsic magma type, rhyolite and trachyte), and the post-collisional granitoids setting (Fig. 9; Grimes et al., 2015). The Irregully Formation and Kiangi Creek Formation Facies 1 contain a distinct subpopulation of zircon grains with age ranging 1800–1700 Ma that show low Hf (~6000 ppm Fig. 9c, e) in comparison to the same age population of the Kiangi Creek Formation Facies 2 (Hf ~8500 ppm; Fig. 9a). Similarly, 1900–1800 Ma zircon grains in the Irregully Formation and Kiangi Creek Formation Facies 1 have higher U/Yb ratios (Fig. 9c, e), than zircons in the same age group from the Kiangi Creek Formation Facies 2 (Fig. 9a). Conversely, zircons with age ranging 2100–1900 Ma plot in the same area of the compositional fields for the three units analysed, and do not display significant compositional differences (Fig. 9b, d, f). Zircons aged from 2700 to 2400 Ma show high compositional variability (Fig. 9b, d, f).
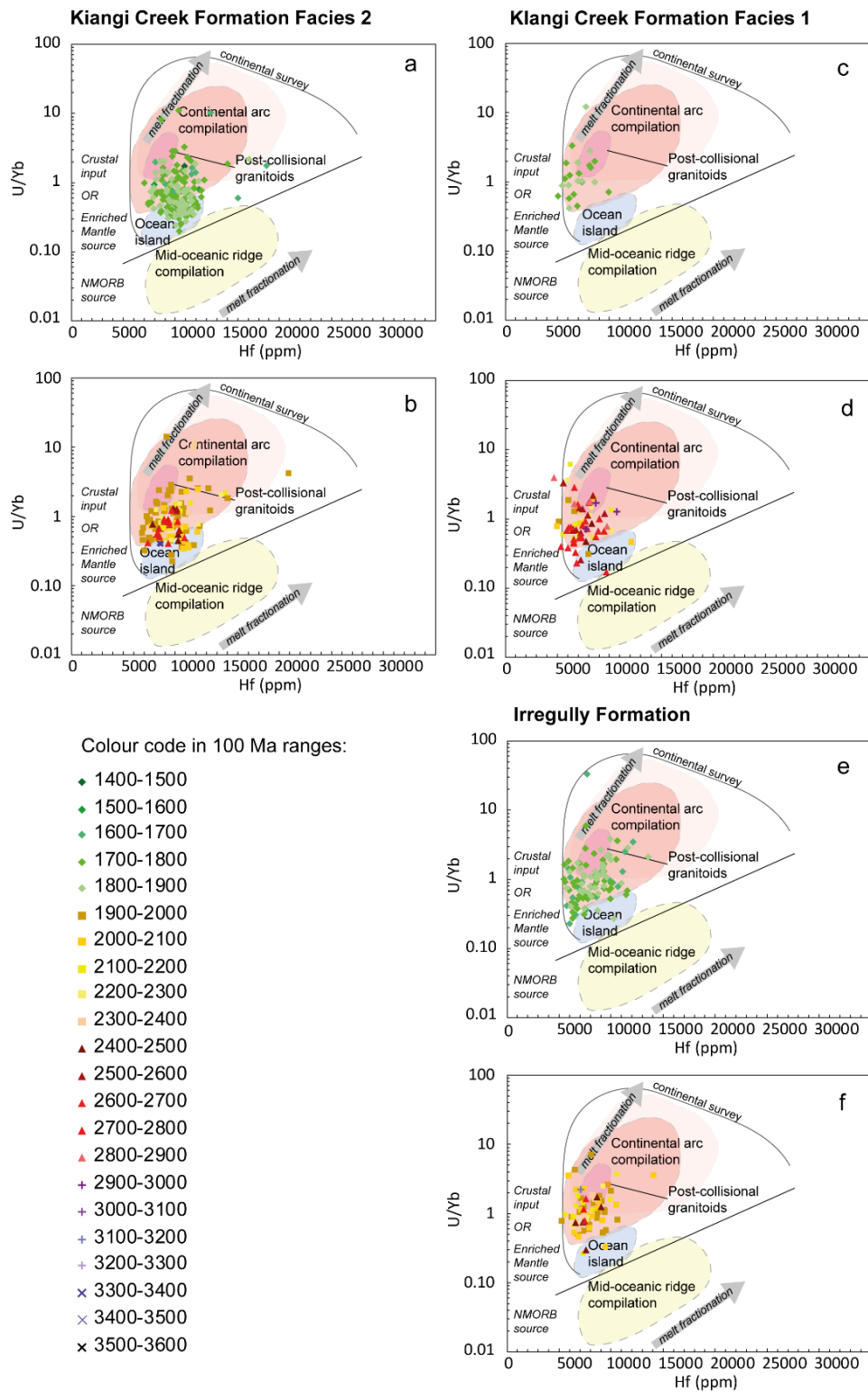
Fig. 9. Discrimination diagrams for the tectono-magmatic setting in which the detrital zircons' parent magma crystallized, MOR (mid-oceanic ridge), magmatic arc, continental collisional zones, and plume-influenced ocean island (Grimes et al.,

2015). Plots a, c, e display detrital zircons younger than 1900 Ma and plots b, d, f display detrital zircons > 1900 Ma.

5. Discussion

5.1 Provenance of the Edmund Basin in the Abra region (Jallawarra Sub-Basin)

The Edmund Basin stratigraphy in AB62 drill core presents polymodal and/or broad detrital zircon age spectra, spanning several distinct age modes (1750–1700 Ma, 1870–1750 Ma, 1970–1940 Ma, c. 2100 and 2350 Ma) that are relatively distinct from the peak ages and predominantly bimodal spectra recognised in previous studies (Martin et al., 2008).

The same young zircon population of c. 1720 Ma is found in the basal samples of the Irregully Formation and the overlying Facies 1 and 2 of the Kiangi Creek Formation. This zircon group broadly correlates with the age of the Moorarie Supersuite, although its slightly younger age is atypical elsewhere in the Capricorn Orogen. Moreover, zircons within this age cluster display consistent relatively low Hf concentrations (~6000 ppm; Fig. 9), suggesting a distinct, unknown, crystalline unit, for their origin.

Another more frequent age group in the analysed samples is constituted by zircons aged from 1880 to 1750 Ma, present in all the samples, but with distinct chemical signatures in each sample (low U/Yb ratios ~0.2 in the Kiangi Creek-Facies 2, and high U/Yb ratios ~0.8 in the Irregully Formation and Kiangi Creek Formation-Facies 1). This age group coincides more accurately with the crystallization age of the Moorarie Supersuite in the Gascoyne Complex (Johnson et al., 2013). Additionally, detrital zircons within this age range are broadly distributed across the Capricorn Orogen region in older Palaeoproterozoic basins (e.g. Capricorn Group and Mount Minnie Basin; Cutten et al., 2016). Finally, the majority of the samples yield subpopulations at 2000–1900 Ma and 2100–2000 Ma, matching the crystallization ages of the 1965–1945 Ma Bertibubba Supersuite and 2100–2050 Ma Dalgaringa Supersuite (Johnson et al., 2011). Small Archean zircon clusters are also present in many samples (e.g. c. 2700 Ma and c. 2650 Ma) and are correlated with widespread granitic magmatism in the Yilgarn Craton (Champion and Cassidy, 2007).

The variability of age modes, which changed slightly for zircons dated from 1750 to 1880 Ma and for zircons dated between 2100 and 2000 Ma, as well as inconsistencies

in the detrital zircons frequencies and age mode associations in each sample support predominant direct sourcing from distinct crystalline units of the Gascoyne Complex, rather than recycling of sediments from pre-existing basins (Fig. 10). Recycling of sediments is likely limited to the basal units of each succession where broad polymodal age mode associations indicate strong sediment mixing at the beginning of the deposition of each unit (Table 3, Appendix 1). The K-S tests indicate sediment contributions from the Capricorn Group in all the examined samples (Table 2, Appendix 1). However, from a visual comparison of the samples' age peaks with the age peaks of the Capricorn Group, and in light of the compositional diversity of detrital zircons aged 1880–1700 Ma, in samples from the Irregully Formation and Kiangi Creek Formation, sourcing from Capricorn Group sedimentary rocks is more likely to have occurred only for the topmost part of the sequence (e.g. Facies 2 AB2, AB1; Fig. 10; Table 2, Appendix 1).

Facies 1 of the Kiangi Creek Formation yields distinct age modes in comparison with the age modes of the adjacent sedimentary units. Archean zircons dated c. 2540 Ma c. 2650 and accompanied by subordinate age clusters at c. 2550 Ma, 2800 Ma and c. 3000 Ma and 3100 Ma, suggest sediments predominantly derived from the Yilgarn Craton granites (Champion and Cassidy, 2007). The dominant c. 2650 Ma mode also coincides with the dominant age mode of the Wyloo Group (Ashburton Basin; Cutten et al., 2016; Fig. 10) and might indicate derivation from recycling of Ashburton Basin sediments. However, the older subordinate age clusters are within the time interval of older magmatic episodes recorded in the Yilgarn Craton (Champion and Cassidy, 2007), and support direct derivation from it. Dominant Archean age modes haven't been recorded for the Edmund Basin elsewhere and could represent a distinctive characteristic of Facies 1 and/or the area examined, which is enclosed in the Jallawarra sub-basin in the southern part of the Edmund Basin.

Significantly, detrital zircon age spectra of Facies 1 of the Kiangi Creek Formation show similarity in age modes with those of the Blue Billy Formation (Martin et al., 2008; K-S test Table 2, Appendix 1), because both contain Archean to early Palaeoproterozoic detrital zircon clusters (e.g. c. 2750 and c. 2450 Ma), associated with the middle Palaeoproterozoic age peaks. However, the abundance of Archean zircons in the western part of the Edmund Basin (Martin et al., 2008) is significantly

reduced in comparison to the samples of Facies 1. The K-S test, as well as the sharp change in facies observed (fluvial to submarine fan deposits) and the finding of an angular unconformity limiting Facies 1 and 2, suggest that Facies 1 is likely spatially and temporally correlative with the Blue Billy Formation (Depositional Package 2).
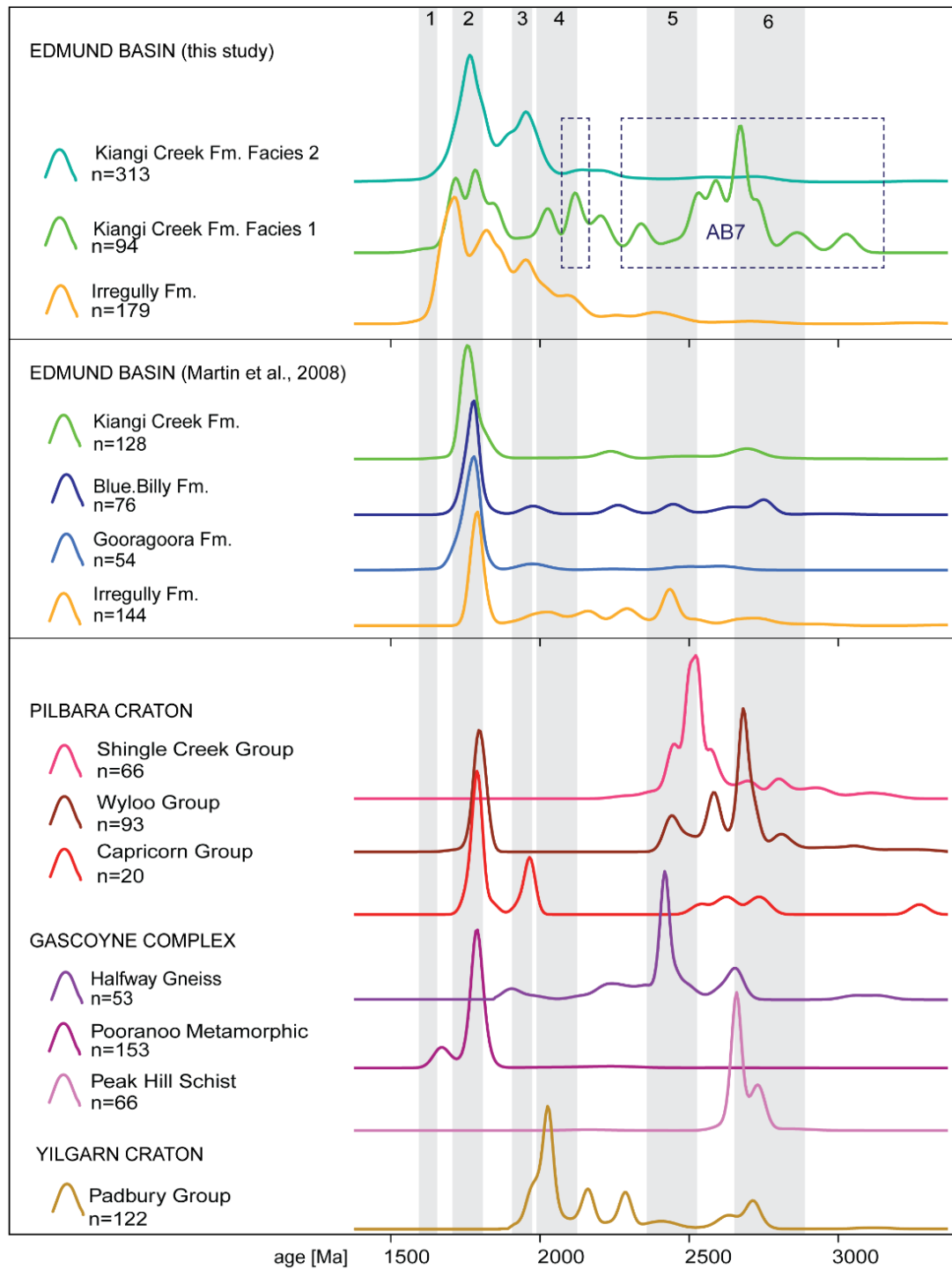
Fig. 10. Kernel density plot (KDP; Vermeesch et al., 2016) comparing detrital zircon age spectra of the three sequences analysed in the AB62 drill core (2σ errors). The

dashed box represents sample AB7 and its distinct detrital zircons ages. Pooled data from relevant formations within the Edmund Basin (Martin et al., 2008), Padbury Basin (Wingate et al., 2012b; Wingate et al., 2014d), Shingle Creek Group (Wingate et al., 2017a), Ashburton Basin (Wyloo Group; Nelson, 2004a,b,c) and Blair Basin (Capricorn Group; Wingate et al., 2017a), Halfway Gneiss (Nelson D. R., 2002a,b; Wingate et al., 2017b), Peak Hill Schist (Wingate et al., 2014b,c), Pooranoo Metamorphic (Bordokos et al., 2006; Wingate et al., 2014a). Magmatic events are marked with vertical grey bars and numbers. 1-Durlacher Supersuite; 2-Moorarie Supersuite; 3-Bertibubba Supersuite; 4-Dalgaringa Supersuite; 5-Halfway Gneiss; 6-Yilgarn Craton granites.

5.2 Temporal constraints on the Edmund Basin and Abra mineralization

The crystallization ages obtained from detrital zircon grains analysed place firm constraints on the maximum depositional age of the Edmund Basin sedimentary rocks that host them in the AB62 drill core, as well as correlative stratigraphy. The maximum depositional age for the Irregully Formation is c. 1626 ± 70 Ma, given by an individual concordant analysis, in sample AB12. The youngest concordant detrital zircon group from the same sample has an error weighted average age of 1667 ± 49 (MSWD=0.05, n=10). These ages match previous data of depositional ages for the Irregully Formation (Fig. 11; Martin et al., 2008).

The detrital zircons from submarine fan deposits (Facies 1) of the Kiangi Creek Formation provide a maximum depositional age of 1641 ± 41 Ma, given by a single zircon grain from sample AB8 (Fig. 11). A minimum depositional age of c. 1594 Ma was provided for the correlative of this unit by hydrothermal xenotime found to be coeval with ore mineralization (Zi et al., 2015). Based on the combined U-Pb detrital zircon ages and hydrothermal xenotime age data, the lower part of the Edmund Basin (Depositional Package 1 and 2) accumulated progressively after c. 1641 Ma and before c. 1594 Ma (Zi et al., 2015), without significant stratigraphic breaks (Fig. 11).

The maximum depositional age for the upper deltaic facies (Facies 2) of the Kiangi Creek Formation is given by the youngest single concordant analysis at 1484 ± 30 Ma from the sample AB5 (Fig. 11). This age is compatible with the maximum depositional age with a 90% of confidence (Dickinson and Gehrels, 2009). Sample AB5 also yielded other two young detrital zircon grains of c. 1574 ± 28 Ma

(MSWD=0.1; n=2), not recorded in the Kiangi Creek Formation in past. The age of c. 1484 Ma suggests that deposition in a deltaic system (Depositional Package 3), initiated c. 100 Ma later than the deposition of the underlying sequence.

Such a significant temporal gap suggests that it is unlikely that Facies 1 and Facies 2 correlate with the Kiangi Creek Formation alone, but rather they represent two distinct lithostratigraphic units within the Edmund Basin. More likely only the topmost Facies 2 (deltaic deposits) correlates with the Kiangi Creek Formation, based on its lithological similarity with the lithofacies recorded for the Kiangi Creek Formation elsewhere (Martin & Thorne, 2004). Conversely Facies 1 based on its characteristics (deep-water facies, ages and presence of an angular unconformity) represents a correlative of the Gooragoora and/or Blue Billy formations (Depositional Package 2) that overlie the Irregully Formation and are still poorly constrained in the southern part of the Edmund Basin.
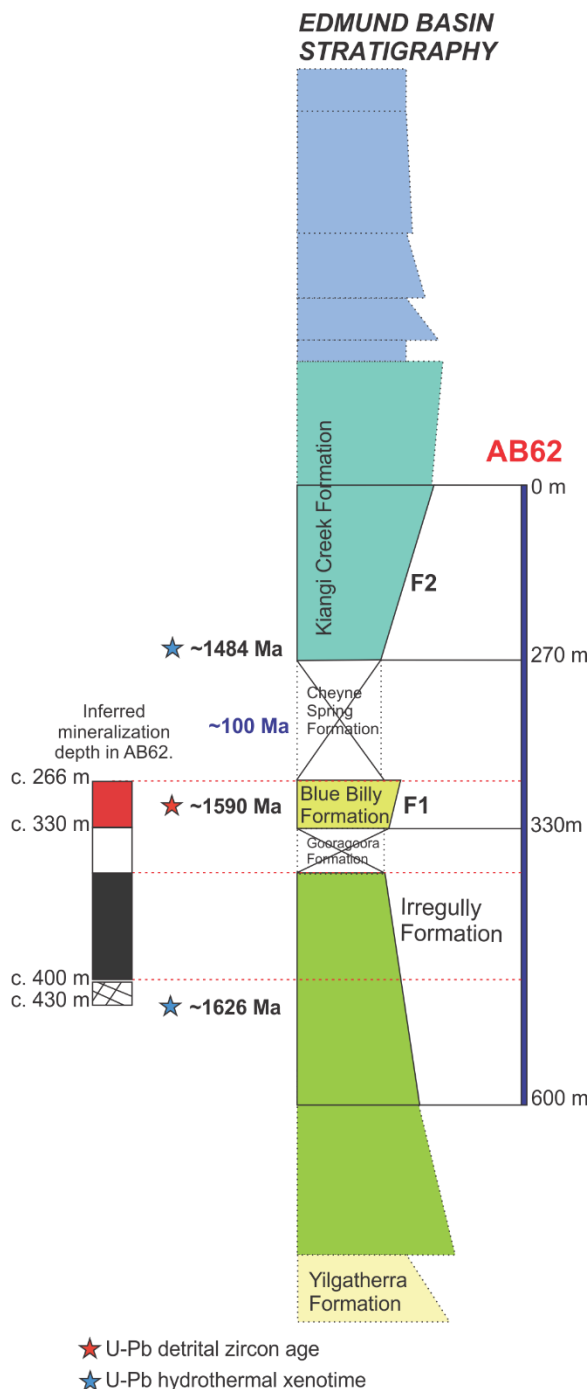
Fig. 11. Lithostratigraphy of the Edmund Basin in the proximity of the Abra deposit.

71

5.3 Depositional history of the Edmund Basin and intracontinental extension of the Capricorn Orogen

Based on dissimilar U-Pb age population characteristics, the Edmund Basin had different catchments in its southern and western portions. Southern areas were likely compartmentalised by rifting (Jallawarra Sub-Basin), hosting distinct but spatially and temporally equivalent lithofacies to those analysed by Martin et al. (2008). Inferring from the U-Pb age data compiled and lithostratigraphic relationships observed in AB62, suggests that the sedimentary sequence hosting Abra requires revision. A tripartite subdivision is proposed here: (i) the Irregully Formation (Depositional Package 1), (ii) the Gooragoora and Blue Billy formations (Depositional Package 2), and (iii) the Kiangi Creek Formation (Facies 2). The Irregully, Gooragoora and Blue Billy formations have disconformable contacts, while the Kiangi Creek Formation (Depositional Package 3) overlain the Depositional Packages 1 and 2 with an angular unconformity (Fig. 12).

In particular, the submarine fan-deposits inferred to be part of the Blue Billy Formation by the K-S test might represent unusual coarser basal units of the Blue Billy Formation, which is otherwise predominantly composed of deep-water mudstone (Martin & Thorne, 2004; Martin et al., 2008). Alternatively, the facies might represent an atypically deep-water facies of the Gooragoora Formation, elsewhere described as deltaic facies, containing remarkably coarse sandstone beds (Martin & Thorne, 2004; Martin et al., 2008).

The sedimentary sequence of AB62 record basin deepening from the Irregully to the Blue Billy formations, with change from fluvial to lacustrine and then submarine environments between c. 1626 and c. 1594 Ma. The overlying Kiangi Creek Formation records basin shallowing after c. 100 Ma, represented by braided delta deposits. According to the age limits established, deposition of the lower formations of the Edmund Basin (Irregully, Gooragoora and Blue Billy formations) took place soon after the 1680–1620 Ma Mangaroon Orogeny (Sheppard et al., 2005; Johnson et al., 2013) and sediment was primarily sourced from the Gascoyne Complex, which was tectonically active during the Mangaroon Orogeny. However, the provenance study also highlights a major switch in sedimentary sources occurred during deposition of the Depositional Package 2 (Gooragoora and Blue Billy formations), within the

Jallawarra Sub-basin (samples AB7, AB8). During this interval sources are inferred to have changed from the east (Gascoyne Complex) to the south (Yilgarn Craton). The change in provenance recorded by the Blue Billy Formation suggests renewed tectonic activity in the northern Yilgarn Craton, between 1626 and 1594 Ma (Fig. 12a). Furthermore, the event can be linked to intracratonic extensional fault reactivation of the southern part of the Capricorn Orogen according to the change in the depositional environment toward deeper water. This may have promoted hydrothermal fluid circulation and initiated the Abra mineralizing event, through the precipitation of base metal sulfides within the submarine fan deposits of the Gooragoora Formation and basal units of the Blue Billy Formation (Fig. 12a). The new time frame established indicates a window of c. 20–30 Ma for both the deposition of the mineral host-rocks (Irregully-Gooragoora-Blue Billy formations) and the mineral precipitation.

Deposition of the Kiangi Creek Formation (Facies 2) occurred after c. 1484 Ma with an interval of c. 100 Ma separating it from the deposition of the underlying Irregully, Gooragoora and Blue Billy formations (Fig. 12b). The age gap, presence of a basal unconformity and the polymodal age spectra found in the basal samples of the Kiangi Creek indicate that dramatic erosion of the lower Irregully, Gooragoora and Blue Billy formations took place sometimes after c. 1594 Ma (Fig. 12b). This implies that the main mineralization of Abra was probably thicker immediately after the mineralization event but was eroded significantly later in its history. The accumulation of the Kiangi Creek Formation was likely associated with a phase of poorly constrained extension, broadly contemporaneous with emplacement of the Narimbunna Dolerite (c. 1465 Ma, Wingate et al., 2002). This idea is supported by the ages of hydrothermal monazite and xenotime in sedimentary rocks at Abra underlying the Kiangi Creek Formation (c. 1460 Ma; Zi et al., 2015).
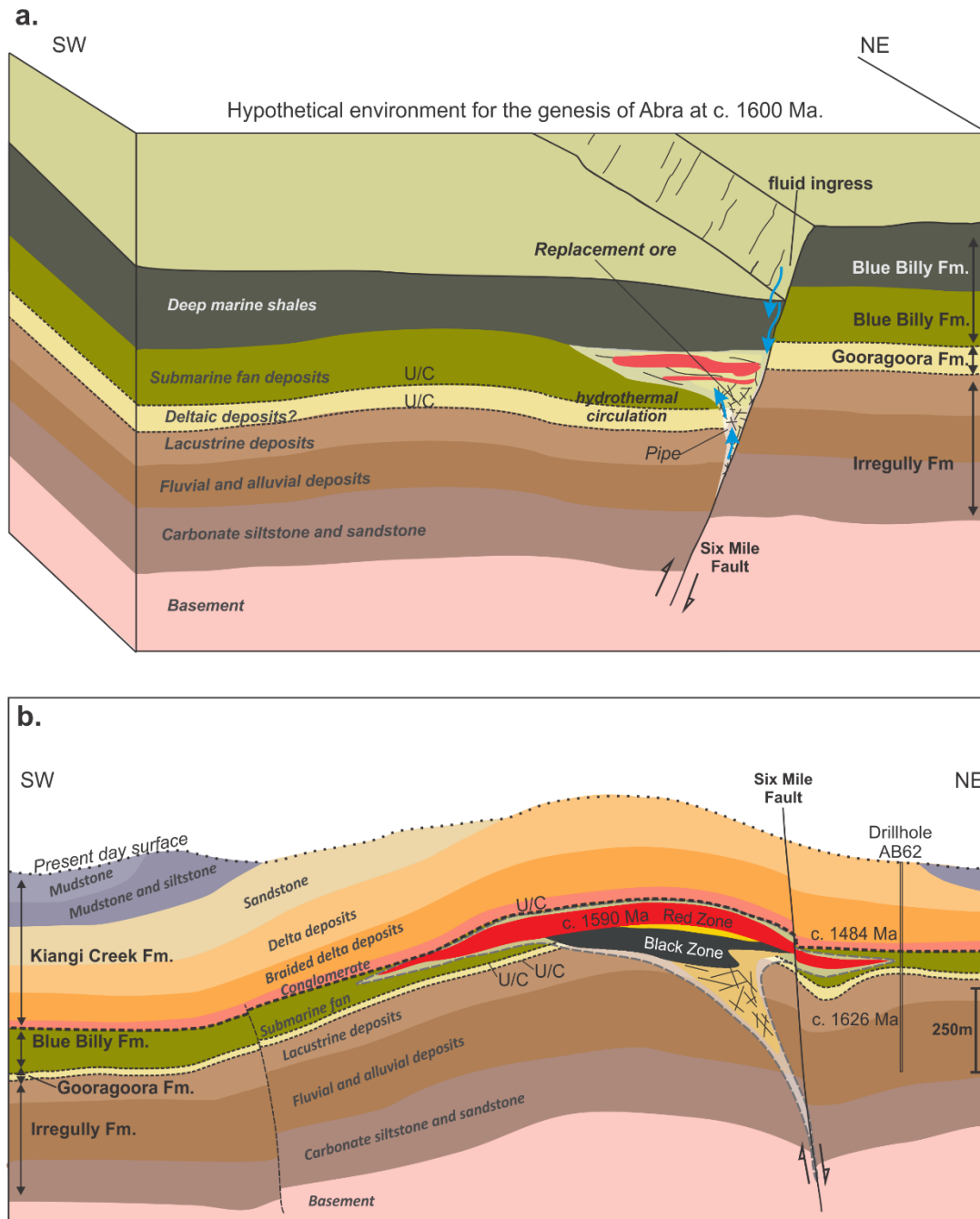
Fig. 12. a. Schematic cross-sections of the lower Edmund Basin during the Abra mineralizing event at c. 1600 Ma. b. Cross section of the Abra deposit at present day, with the reconstructed stratigraphy of the Edmund Basin sequence and age limits.

6. Conclusions

The stratigraphy of the drill core AB62 is divided into three main units: the Irregully Formation (fluvial and lacustrine facies, Depositional Package 1), the Gooragoora and Blue Billy formations (delta and submarine fan-delta deposits, Depositional Package 2) and Kiangi Creek Formation (Facies 2, braided delta deposits, Depositional Package 3).

The detrital zircons analysed establishes new age constraints for the deposition of the Edmund Basin in the central southern Capricorn Orogen and for the sedimentary host rock of the Abra polymetallic deposit. Deposition of the Irregully Formation took place after c. 1626 Ma. Facies 2 of the Kiangi Creek Formation accumulated c. 100 Ma later with respect to the lowermost sequence, yielding a maximum depositional age of c. 1484 Ma.

The provenance investigation demonstrates diverse sources for the Edmund Basin sediments in the Jallawarra Sub-Basin. Sources included the crystalline units of the Gascoyne Complex (Durlacher, Moorarie, Bertibubba, Dalgaringa supersuites), the northern Yilgarn Craton granitic units, and minor sedimentary recycling. Significantly, the provenance of the Blue Billy Formation, which hosts the Abra mineralization, is linked with a sharp switch in sources from the east to the south (northern Yilgarn Craton) that is interpreted to be due to a later tectonic reactivation. The tectonic reactivation to the south likely correlates to a phase of intracratonic extension of the Edmund Basin and is considered a probable large-scale factor promoting the hydrothermal circulation for the genesis of Abra.

The age of the Kiangi Creek Formation in Abra indicates a correlation with later extensional tectonic activity, possibly linked with the emplacement of the Narimbunna Dolerite (c. 1465 Ma, Wingate, 2004) or later tectonic episode. Facies 2 records expansion of the catchments towards the north with ages matching the Capricorn Group age record, and the overall expected age record for the Edmund Basin. This broad similarity of the topmost age spectra might mark a major change in the basin morphology (more uniform) and the end of compartmentalisation within the Jallawarra sub-basin.

References

Anders, E. & Grevesse, N. (1989). Abundances of the elements: Meteoritic and solar. *Geochimica et Cosmochimica Acta,* 53, 197-214.

Barham, M., Reynolds, S., Kirkland, C. L., O'Leary, M. J., Evans, N. J., Allen, H. J., Haines, P. W., Hocking, R. M. & McDonald, B. J. (2018). Sediment routing and basin evolution in Proterozoic to Mesozoic east Gondwana: A case study from southern Australia. *Gondwana Research,* 58, 122-140.

Bodorkos, S., Stern, R. A., Kamo, S., Corfu, F. & Hickman, A. H. (2009). OG1: A Natural Reference Material for Quantifying SIMS Instrumental Mass Fractionation of Pb Isotopes During Zircon Dating. *American Geophysical Union, Fall Meeting, abstract #V33B-2044.*

Cawood, P. A. & Tyler, I. M. (2004). Assembling and reactivating the Proterozoic Capricorn Orogen: Lithotectonic elements, orogenies, and significance. *Precambrian Research,* 128, 201-218.

Collins, P., and McDonald, I. (1994). A Proterozoic sediment-hosted polymetallic epithermal deposit at Abra in the Jillawarra sub-basin of the central Bangemall basin, Western Australia. *Geological Society of Australia*, Abstracts Series 37, 68–69.

Dickinson W. R., Gehrels G. E. (2009). Use of U–Pb ages of detrital zircons to infer maximum depositional ages of strata: A test against a Colorado Plateau Mesozoic database. *Earth and Planetary Science Letters,* 288, 115-125.

Grimes, C. B., Wooden, J. L., Cheadle, M. J. & John, B. E. (2015). "Fingerprinting" tectono-magmatic provenance using trace elements in igneous zircon. *Contributions to Mineralogy and Petrology,* 170, 46-46.

Guynn, J., & Gehrels, G.E. (2010). Comparison of detrital zircon age distributions in the K-S test. Tucson, University of Arizona, Arizona LaserChron Center, 16 p.

Hoskin P. W. O., (2005). Trace-element composition of hydrothermal zircon and the alteration of Hadean zircon from the Jack Hills, Australia. *Geochimica et Cosmochimica Acta*, 69, 637–648.

Hoskin, P. W. O. & Schaltegger, U. (2003). The composition of zircon and igneous and metamorphic petrogenesis. *Reviews in Mineralogy and Geochemistry,* 53, 27-62.

Jackson, S. E., Pearson, N. J., Griffin, W. L. & Belousova, E. A. (2004). The application of laser ablation-inductively coupled plasma-mass spectrometry to in situ U-Pb zircon geochronology. *Chemical Geology,* 211, 47-69.

Johnson, S. P., Sheppard, S., Rasmussen, B., Wingate, M. T. D., Kirkland, C. L., Muhling, J. R., Fletcher, I. R. & Belousova, E. A. (2010). The Glenburgh Orogeny as a record of Palaeoproterozoic continent-continent collision. Geological Survey of Western Australia, Record 2010/5.

Johnson, S. P., Sheppard, S., Rasmussen, B., Wingate, M. T. D., Kirkland, C. L., Muhling, J. R., Fletcher, I. R. & Belousova, E. A. (2011). Two collisions, two sutures: Punctuated pre-1950Ma assembly of the West Australian Craton during the Ophthalmian and Glenburgh Orogenies. *Precambrian Research,* 189, 239-262.

Johnson, S. P., Thorne, A. M., Tyler, I. M., Korsch, R. J., Kennett, B. L. N. N., Cutten, H. N., Goodwin, J., Blay, O., Blewett, R. S., Joly, A., Dentith, M. C., Aitken, A. R. A. A., Holzschuh, J., Salmon, M., Reading, A., Heinson, G., Boren, G., Ross, J., Costelloe, R. D. & Fomin, T. (2013). Crustal architecture of the Capricorn Orogen, Western Australia and associated metallogeny. *Australian Journal of Earth Sciences,* 60, 681-705.

Korhonen, F. J., Johnson, S. P., Fletcher, I. R., Rasmussen, B., Sheppard, S., Muhling, J. R., Dunkley, D. J., Wingate, M. T. D., Roberts, M. P. & Kirkland, C. L. (2015). Pressure – Temperature – Time Evolution of the Mutherbukin Tectonic Event, Capricorn Orogen Pressure – Temperature – Time Evolution of the Mutherbukin Tectonic Event, Capricorn Orogen. Geological Survey of Western Australia, Report 146.

Iizuka, T., Campbell, I. H., Allen, C. M., Gill, J. B., Maruyama, S. & Makoka, F. (2013). Evolution of the African continental crust as recorded by U-Pb, Lu-Hf and O isotopes in detrital zircons from modern rivers. *Geochimica et Cosmochimica Acta,* 107, 96-120.

Lampinen, H. M., Laukamp, C., Occhipinti, S. A., Metelka, V. & Spinks, S. C. (2017). Delineating Alteration Footprints from Field and ASTER SWIR Spectra, Geochemistry, and Gamma-Ray Spectrometry above Regolith-Covered Base Metal Deposits - An Example from Abra, Western Australia. *Economic Geology,* 112, 1977-2003.

Large, R.R., Bull, S.W., McGoldrick, P.J., Walters, S. (2005). Stratiform and strata-bound Zn–Pb–Ag deposits in Proterozoic sedimentary basins, Northern Australia. *Economic Geology,* 100, 931-963.

Large, R.R., McGoldrick, P.J. (2000). Lithogeochemical halos and geochemical vectors to stratiform sediment-hosted Zn–Pb–Ag deposits, part 1. Lady Loretta deposit, Queensland. *Journal of Geochemical Exploration,* 63, 37-56.

Ludwig, K. R. (2003). Isoplot 3.00: A geochronological toolkit for Microsoft Excel. *Berkeley Geochronology Center Special Publication*, 39, 91-445.

Martin, D. M., Thorne, A. M.(2001). *Another Jillawarra-style sub-basin in the Bangemall Supergroup - implications for mineral prospectivityn* (pp 31-35). Geological Survey of Western Australia Annual Review 1999-2000.

Martin, D. M. B. & Thorne, A. M. (2004). Tectonic setting and basin evolution of the Bangemall Supergroup in the northwestern Capricorn Orogen. *Precambrian Research,* 128, 385-409.

Nelson D. R. (2002a), 169048: leucocratic gneiss, Mount Remarkable Bore; in Compilation of geochronology data, 2001. Geological Survey of Western Australia, Record 2002/2, 24-27.

Nelson D. R. (2002b), 169050: leucocratic gneiss, Mount Remarkable Bore; in Compilation of geochronology data, 2001. Geological Survey of Western Australia, Record 2002/2, 28-30.

Nelson D. R. (2004a), 169081: pebbly sandstone, Meteorite Bore; Geochronology dataset 116; in Compilation of geochronology data. Geological Survey of Western Australia update June 2006.

Nelson D. R. (2004b), 148922: crystal-vitric tuff, Koonong Pool; Geochronology dataset 249; in Compilation of geochronology data. Geological Survey of Western Australia update June 2006.

Nelson D. R. (2004c), 169082: sandstone, Meteorite Bore; Geochronology dataset 42; in Compilation of geochronology data. Geological Survey of Western Australia update June 2006.

Paton, C., Woodhead, J. D., Hellstrom, J. C., Hergt, J. M., Greig, A. & Maas, R. (2010). Improved laser ablation U-Pb zircon geochronology through robust downhole fractionation correction. *Geochemistry, Geophysics, Geosystems,* 11, 3.

Pirajno, F. & Bagas, L. (2008). A review of Australia's Proterozoic mineral systems and genetic models. *Precambrian Research,* 166, 54-80.

Pirajno, F., Mernagh, T. P., Huston, D., Creaser, R. A. & Seltmann, R. (2016). The Mesoproterozoic Abra polymetallic sedimentary rock-hosted mineral deposit, Edmund Basin, Western Australia. *Ore Geology Reviews,* 76, 442-462.

Rasmussen, B., Fletcher, I. R., Muhling, J. R., Gregory, C., Thorne, A. M., Cutten, H. N., Pirajno, F. & Hell, A. (2010). In Situ U-Pb Monazite and Xenotime Geochronology of the Abra Polymetallic Deposit and Associated Sedimentary and Volcanic Rocks, Bangemall Supergroup, Western Australia. Geological Survey of Western Australia, Record 2010/12.

Sheppard, S., Occhipinti, S. A. S. A. & Nelson, D. R. (2005). Intracontinental reworking in the Capricorn Orogen, Western Australia: The 1680-1620 Ma Mangaroon Orogeny. *Australian Journal of Earth Sciences,* 52, 443-460.

Slama, J., Kosler, J., Condon, D. J., Crowley, J. L., Gerdes, A., Hanchar, J. M., Horstwood, M. S. A., Morris, G. A., Nasdala, L., Norberg, N., Schaltegger, U., Schoene, B., Tubrett, M. N. & Whitehouse, M. J. (2008). Plešovice zircon - A new natural reference material for U-Pb and Hf isotopic microanalysis. *Chemical Geology,* 249, 1-35.

Spinks, S. C., Schmid, S., Pagés, A. & Bluett, J. (2016). Evidence for SEDEX-style mineralization in the 1.7 Ga Tawallah Group, McArthur Basin, Australia. *Ore Geology Reviews,* 76, 122-139.

Thomsen, T. B., Heijboer, T. & Guarnieri, P. (2016). jAgeDisplay : Software for evaluation of data distributions in U-Th-Pb geochronology. *Geologic survey of Denmark and Greenland bulletin*, 35, 103-106.

Trail D., Watson E. B., Tailby N. D. (2012). Ce and Eu anomalies in zircon as proxies for the oxidation state of magmas. Geochimica et Cosmochimica Acta, 97, 70-87.

Vermeesch, P., Resentini, A. & Garzanti, E. (2016). An R package for statistical provenance analysis. Sedimentary Geology, 336, 14-25.

Wiedenbeck, M., AllÉ, P., Corfu, F., Griffin, W. L., Meier, M., Oberli, F., Quadt, A. V., Roddick, J. C. & Spiegel, W. (1995). Three Natural Zircon Standards for U-Th-Pb, Lu-Hf, Trace Element and Ree Analyses. Geostandards Newsletter, 19, 1-23.

Wingate, M. T. D., Pisarevsky, S. A., Evans, D. A. D. (2002). Rodinia connections between Australia and Laurentia: No SWEAT, no AUSWUS? Terra Nova, 14, 121-128.

Wingate, M. T. D., Kirkland, C.L., Cutten, H.N., Thorne, A.M. (2012a), 143445: dolerite sill, Waldburg Homestead. Geochronology Record 1077, Geological Survey of Western Australia.

Wingate, M. T. D., Kirkland, C. L., Thorne, A. M. (2012b), 156814: metasandstone, Mount Egerton No. 1 Well. Geochronology Record 1031, Geological Survey of Western Australia.

Wingate M. T. D., Lu Y., Kirkland C. L. and Johnson S. P. (2014a), 195849: quartzite, Star of Mangaroon mine. Geochronology Record 115, Geological Survey of Western Australia.

Wingate M. T. D., Lu Y., Kirkland C. L. and Johnson S. P. (2014b), 195866: metaconglomerate, Peak Hill mine. Geochronology Record 1153, Geological Survey of Western Australia.

Wingate M. T. D., Lu Y., Kirkland C. L. and Johnson S. P. (2014c), 195870: metamonzogranite, Stalley Well. Geochronology Record 1154, Geological Survey of Western Australia.

Wingate, M. T. D., Kirkland, C. L., Thorne, A. M. & Cutten H. N. (2014d), 156810: metasandstone, Mount Egerton No. 1 Well. Geochronology Record 1186, Geological Survey of Western Australia.

Wingate M. T. D., Lu Y., Sircombe K., Kirkland C. L. and Johnson S. P., (2017a), 203710: quartzite, Miningee Well. Geochronology Record 1355, Geological Survey of Western Australia.

Wingate M. T. D., Lu Y., Kirkland C. L. and Johnson S. P. (2017b), 188973: granodiorite gneiss, Mount James homestead. Geochronology Record 1361, Geological Survey of Western Australia.

Vielreicher, N. M., & McNaughton, N. J. (2002). SHRIMP U-Pb geochronology of magmatism and thermal events in the Archean Marymia Inlier, central Western Australia. *International Journal of Earth Sciences*, 91, 406–432.

Vogt, J.H., 1995. Geology of the Jillawarra area, Bangemall Basin, Western Australia. Geological Survey of Western Australia, Report 40, 1-107.

Zi, J. W., Rasmussen, B., Muhling, J. R., Fletcher, I. R., Thorne, A. M., Johnson, S. P., Cutten, H. N., Dunkley, D. J. & Korhonen, F. J. (2015). In situ U-Pb geochronology of xenotime and monazite from the Abra polymetallic deposit in the Capricorn Orogen, Australia: Dating hydrothermal mineralization and fluid flow in a long-lived crustal structure. *Precambrian Research,* 260, 91-112.

CHAPTER 4

INDIRECT DATING OF MAFIC SILLS BY U-Pb GEOCHRONOLOGY OF SEDIMENT-HOSTED TITANITE: IMPLICATIONS FOR THE MESOPROTEROZOIC INTRACONTINENTAL RIFTING OF THE CAPRICORN OROGEN.

S. Armandola*[1], M. Barham[1,2], S. M. Reddy[1], C. Clark[1], R. J. M. Taylor[3], A. Kylander-Clark[4], S. Spinks[5]

[1]*School of Earth and Planetary Sciences, Curtin University, GPO Box U1987, Perth, WA 6845, Western Australia.*

[2]*Centre for Exploration and Targeting, Curtin Node, Curtin University, GPO Box U1987, Perth, WA 6845, Western Australia.*

[3]*Department of Earth Sciences, Downing Site, University of Cambridge, CB2 3EQ, Cambridge, United Kingdom.*

[4]*Department of Earth Science, University of California, Santa Barbara, CA 93106, United States.*

[5]*Commonwealth Scientific and Industrial Research Organisation (CSIRO), PO box 1130 Bentley, WA 6102, Australia.*

Corresponding author: sonia.armandola01@gmail.com

Keywords: Warakurna Large Igneous Province, contact metamorphism, metamorphic titanite, detrital zircon, provenance.

Abstract

Extensional events can be recognised from the occurrence of sill and dyke swarms intruding rift sequences. Such swarms can be dated to establish the timing of their intrusion and to reconstruct the geological histories of the rifts they intrude. In situ U-Pb geochronology and trace element geochemistry of metamorphic titanite indirectly constrain the age of intrusion of a mafic sill from the central Capricorn Orogen to 1093 ± 21 Ma (MSWD = 2.1, n=41). This Proterozoic age coincides with an interval of extensional tectonic activity in central Western Australia, related to the Warakurna Large Igneous Province. Peperite textures were observed at the sill margins and are indicative of intrusion of melt into unconsolidated sediments. This relationship suggests that the crystallization age of the intrusion-related metamorphic titanite approximates the true depositional age of the sedimentary units. Detrital zircons

separated from the sedimentary rocks hosting the mafic sills were used to constrain the maximum depositional age of the sediments and correlate the sedimentary rocks with basin formation. Detrital zircon grains yield ages ranging from 1.3 to 1.1 Ga that are linked with sources exotic to the Capricorn Orogen and potentially match the Musgrave Complex and the Albany-Fraser Orogen, both of which are located more than 1000 km distant. The U-Pb titanite and detrital zircon data reveal that sedimentation and mafic magmatism within the Mesoproterozoic Collier Basin was a result of intracontinental rifting of the Capricorn Orogen, which in turn is linked to a larger scale rifting event that affected a larger proportion of Proterozoic Australia, during the Giles Event (1090 – 1040 Ma) linked with a mantle superplume under Central Australia.

1. Introduction

Lithospheric-scale extensional events are intrinsic to plate tectonic processes and their occurrence is often associated with the emplacement of mafic sills and dykes in the continental crust (e.g. Goldberg, 2010). In Precambrian terranes, preserved sill and dyke swarms often represent the last vestiges of extensional events in the local geological record, due to the intense reworking of rifted and passive margins and subsequent episodes of continental amalgamation (e.g. Wingate et al., 2004; Goldberg, 2010; Wang et al., 2004; Li et al., 2008; Stark et al., 2017). Moreover, the intrusion of sills and dykes happens almost instantaneously (geologically) and thus they are considered excellent temporal markers (e.g. Rasmussen & Fletcher, 2002; Wingate et al., 2002; Goldberg, 2010).

Precise ages from mafic sills and dykes can be obtained using several geochronological approaches. For example, the isotopic composition of constituent igneous minerals can be dated, e.g. U-Pb dating of baddeleyite, and Ar^{40}/Ar^{39} geochronology on plagioclase and pyroxene (e.g. Camacho et al., 1991; Rasmussen et al., 2008; McCormick et al., 2018; Ware & Jourdan, 2018). Also, whole rock dating by Sm-Nd or U-Pb can yield intrusion ages (e.g. Wang et al., 2004; Li et al., 2008). Another approach is to date the metamorphic accessory minerals that form as a result of contact metamorphism in host rocks, immediately adjacent to the dyke. In this case, accessory minerals like metamorphic monazite and xenotime can be dated to infer the timing of the mafic

intrusion event (e.g. Rasmussen & Fletcher, 2002; Khan et al., 2017; Sepahi et al., 2017).

Titanite is an accessory mineral that crystallizes in both magmatic and metamorphic environments (e.g. Frost et al., 2000; Stearns et al., 2016; Hu et al., 2017; Marsh & Smye, 2017). Its crystal lattice incorporates U during crystallization, and thus provides a radiometric geochronometer. However, during its growth titanite also incorporates elevated quantities of common Pb, meaning statistically reliable crystallization ages must be calculated with a linear regression, from the common Pb uncorrected age data (Stacey & Kramers, 1975; Spencer et al., 2013; Kirkland et al., 2017; 2018). Trace element abundances of titanite constrain the tectono-magmatic setting and discriminate between igneous (high concentrations of HFSE and marked negative Eu anomalies; Gao et al., 2012; Bonamici et al., 2015; Marsh et al., 2017; Hu et al., 2017) and metamorphic genesis (low HFSE concentrations, enriched M-HREE and depleted U concentrations Gao et al., 2011; Bonamici et al., 2015; Garber et al., 2017; Hu et al., 2017).

The Proterozoic Capricorn Orogen of Western Australia separates the Archaean Yilgarn and Pilbara cratons. The orogen has a complex tectonic history involving crustal-scale shortening, extension and strike-slip deformation spanning 2.5 to 0.5 Ga (Johnson et al., 2013; Piechoka et al., 2018). Within this geological framework, at least three discrete episodes of mafic sill and dyke emplacement into Mesoproterozoic sedimentary basins are reported between c. 1517 Ma and c. 1067 Ma (Blay et al., 2018). These dykes carry important information relating to the late stages of multiple extensional events within the overall tectonic history of the Capricorn Orogen region, but their age constraints are insufficient and correlations across different basins are difficult.

To test the potential of titanite as a geochronometer and provide constraints for the timing and patterns of the Capricorn Orogen mafic intrusions, the textures, geochemistry and age of titanite grains from metasediments hosting mafic units are investigated. In order to provide age constraints and provenance information for the sediments hosting the mafic dykes, U-Pb geochronology and geochemistry of detrital zircon are also investigated. Metamorphic titanite and detrital zircon data are finally

integrated to develop a tectonic model for host sediment deposition and magmatic emplacement. These regional geological events are discussed in relation to the broader–scale evolution of the Australian plate during the Mesoproterozoic.

2. Regional geological background

The Capricorn Orogen, in north Western Australia, developed during protracted assembly of the West Australian Craton. Initial collision and deformation occurred in the Palaeoproterozoic continental collision between the Pilbara Craton and the Glenburgh Terrane during the 2215–2145 Ma Ophthalmian Orogeny and was followed by a collision between the Yilgarn Craton and the newly accreted Pilbara-Glenburgh block during the 2005–1950 Ma Glenburgh Orogeny (Johnson et al., 2010; 2011). The Capricorn Orogen also records a prolonged history of intracratonic tectonic reactivation during the 1820–1770 Ma Capricorn Orogeny, the 1685–1620 Ma Mangaroon Orogeny (Sheppard et al., 2005; 2010), the 1321–1170 Ma Mutherbukin Tectonic Event (Korhonen et al., 2017) and the 1030–955 Ma Edmundian Orogeny (Sheppard et al., 2007).

The Mesoproterozoic history of the Capricorn Orogen is characterized by two major basin-forming episodes (Edmund and Collier basins) and intrusion of mafic intrusive swarms associated with several discrete tectonic reactivation events. The dyke and sill complexes intruding the Edmund and Collier basins generally extend along the basins axes and are folded in elongated syncline and anticline structures, with west-east trends along with the host sediments (Fig. 1). The dyke and sills reach thicknesses > 100 m and are mainly medium-grained, with locally exposed chilled margins and coarse-grained phases (Wingate et al., 2002; 2004). The 1514–1505 Ma Waldburg Dolerite intruded basal formations of the Edmund Basin (Fig. 2; Yilgatherra, Irregully and Kiangi Creek formations; Blay et al., 2018). Subsequently, the c. 1465–1450 Ma Narimbunna Dolerite intruded the upper stratigraphic units of the Edmund Basin (Kiangi Creek, Discovery and Ullawarra formations Fig. 1-2; Blay et al., 2018). The c. 1083–1075 Ma Kulkatharra Dolerite intruded both the Edmund Basin and the basal formation of the overlying Collier Basin (Backdoor Formation; Fig. 1-2; Wingate, 2002; Wingate et al., 2004; Martin, 2003). This later intrusion is characterized by the occurrence of peperites, formed during intrusion into unconsolidated, wet sediments.

Consequently, the age of c. 1070 Ma is considered close to the true depositional age of the oldest sediments in the Collier Basin (Fig. 1-2; Martin, 2003). The intrusion of the Kulkatharra Dolerite in the Capricorn Orogen was related to the Warakurna Large Igneous Province in Central Australia that intruded during a protracted extension event in the Musgrave Province (Wingate, 2004).
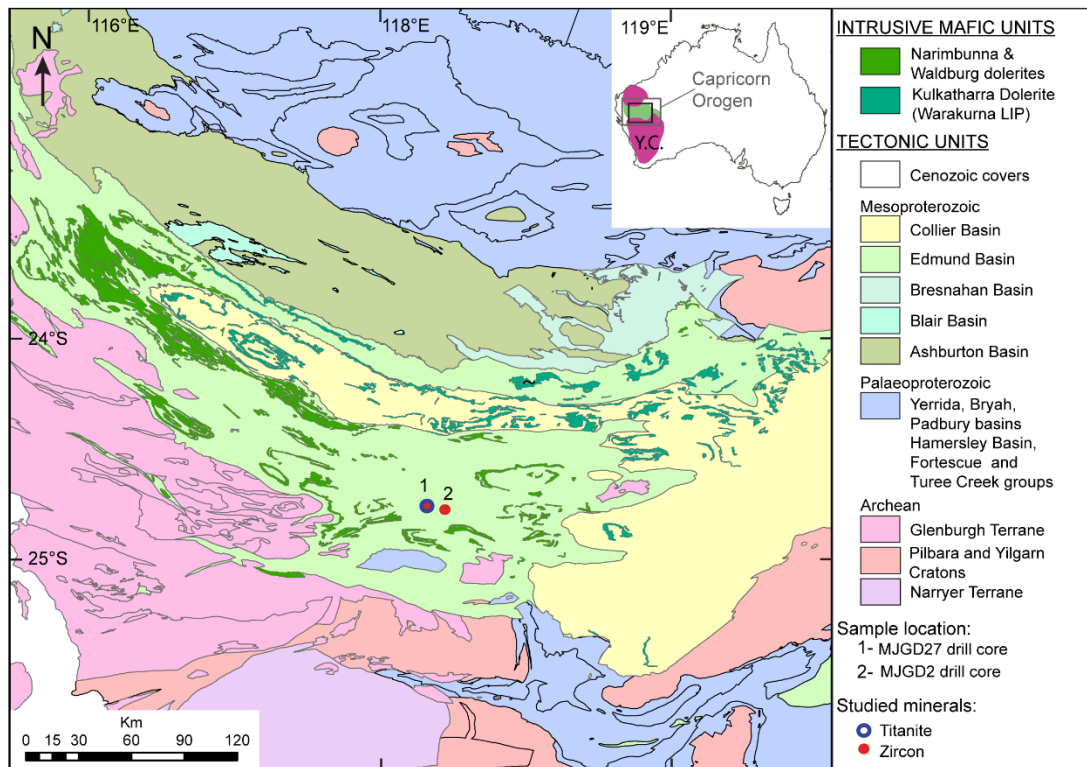
Fig. 1. Map of the central Capricorn Orogen showing the main tectonic units and sill and dyke outcrops. Intrusive outcrops interpreted by the Geological Survey of Western Australia (Wingate et al., 2004). The location of the samples analysed are indicated with red and blue circles.
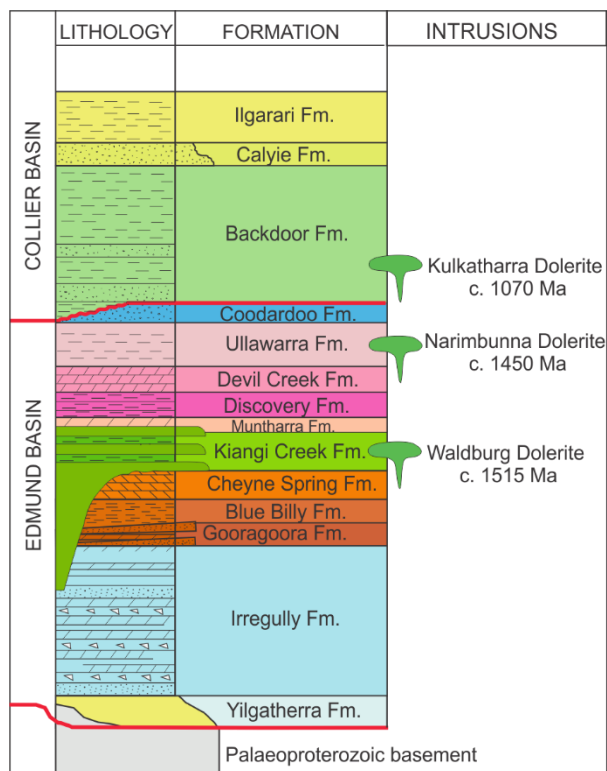
Fig. 2. Stratigraphic summary of the Edmund and Collier basins and illustration of the position of the major mafic intrusive units.

3. Drill core and sample material

The drill cores MJGD2 and MJGD27 were drilled in 1994 by Western Mining Corporation Limited to penetrate part of the Billycan Bore Zn-Cu prospect. Drill core MJGD2 (-24.692819S, 117.919714E; Fig. 1) is interpreted to intersect the Kiangi Creek Formation of the Edmund Basin (formerly inferred Jillawarra Formation, report A42068, Western Mining Corporation Limited). Drill core MJGD27 (24.692819° S, 117.919714° E; Fig. 1) intersects what is inferred to be the Devil Creek Formation of the Edmund Basin (Martin et al., 2016) and formerly interpreted Kiangi Creek Formation, (report A42068, Western Mining Corporation Limited). MJGD2 and MJGD27 are 6.1 km distant and are located in the hanging wall and footwall, respectively, of the regional-scale Tribulation Fault that displaces the Edmund Basin stratigraphy by a minimum of 500 m. Eight samples (MJGD2- 8-9-10-11-12-18-17-19) from sandstone and mudstone lithologies were collected from the stratigraphic section of MJGD2. Four samples (MJGD27-3-4-5-6) from metasandstone were selected from the rocks exposed in MJGD27. From all of these, detrital zircons were extracted. Accessory titanite was extracted from MJGD27 (Fig. 3).

The lithology in the lower part of drill core MJGD27 is dominated by silicified dark mudstone and ripple laminated green-grey siltstone in an overall fining upward

86

sequence between 164.5 and 150.2 m. Above 150.2 m depth, erosive, fining upward, medium-grained sandstone beds dominate, showing current ripple-lamination (Fig. 3). The upper part of the sandstone succession is contact metamorphosed into hornfels, intersected by quartz–garnet veins. The sediments are intruded at 142.4 by a mafic sill of 54 m thickness (Fig. 3). Drill core MJGD27 shows the presence of stratabound and vein-related mineralization, these mainly occur in the sediments adjacent to the mafic intrusion and consist of pyrite.

MJGD2 is a 207 m deep core, characterised by alternating mudstone and fine sandstone - siltstone layers arranged in fining-upward cycles. The siltstone beds are typically 3 to 5 cm thick, and subordinate to the significantly thicker, up to 5 m, mudstone intervals (Fig. 3). Dolerite sills are found at 185.2 m, 190.4 m, 197.1 m and 203.2 m (Fig. 3). Sediments surrounding the intrusive body found between 185.4 m and 146.9 m are graphitic and show a pervasive cleavage. Sulphide minerals in drill core MJGD2 are widespread within the sediment, and in some cases in veins adjacent to the sill margins (e.g. 135.6, 137 and 186. 5 m) and consists of stratabound pyrite, and pyrite-pyrrhotite-trace-chalcopyrite and rare sphalerite-quartz-dolomite veins.

3.1 Peperite

At the upper contact between host sediments and the sill of drill core MJGD2, at c. 203.2 m, peperite structures are observed. Peperite in MJGD2 formed in situ, by mingling between the intruding magma and unconsolidated wet sediment (Fig. 4). The peperite have aspect of fluidal fragments within a matrix of siltstone and fine sandstone and yield thin dark chilled margins (Fig. 4a-b). Some smaller elongated melt apophyses within the siltstone-sandstone matrix can be also observed (Fig. 4b). Probable peperite margins are also suggested by blocky parts of melt observed at the contact margin between the thickest sill and the sediments, at 188.9 m (e.g. Houle', 2008). However, due to missing parts of the drill core relative to this depth, the contact region is insufficiently defined (Fig. 4c).
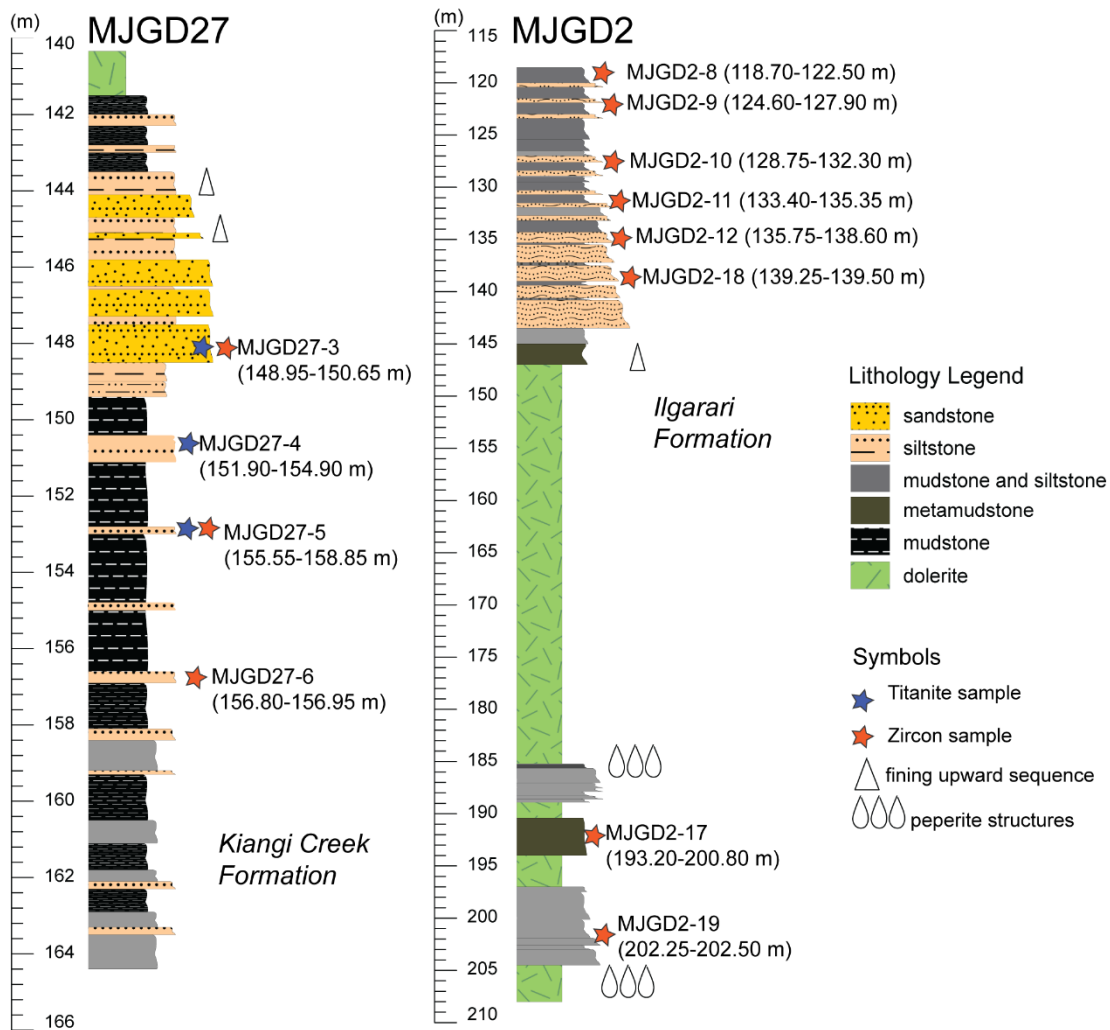
Fig. 3. Drill core lithostratigraphical logs with locations of the analysed samples. Correlative formations indicated based on the results of this study.
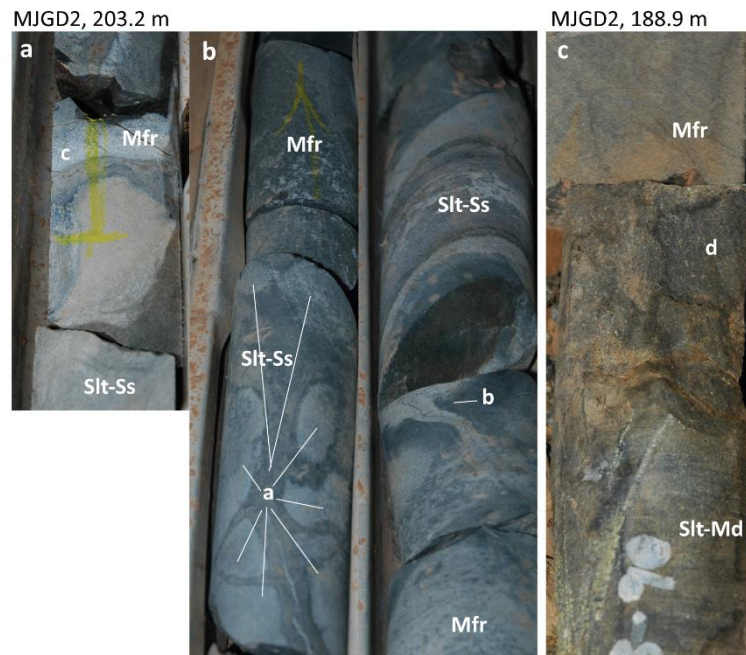
Fig. 4. Peperite at intrusion margins in drill core MJGD2; a-202.6 m contact between the mafic melt intrusion (Mfr), with thin chilled margin (c), and the siltstone-sandstone host rock (Slt-Ss); b- peperite margin at 203.2 m with several dispersed igneous bodies in the sedimentary host rock (a) and elongated melt apophysis (b) migrating through unconsolidated sediment, and small peperite to the sides; c- lower limit of the sill, at 188.9 m, with blocky peperite of melt (d) with chilled margins, within the siltstone-mudstone host rock.

4. Analytical techniques

Laboratory processing and mineral imaging were carried out at the John de Laeter Centre, Curtin University. Rock samples were disaggregated using a SelFrag electro-pulse disaggregation system. Disaggregated sediments were sieved to separate the fraction finer than 210 µm, and heavy minerals were separated from this fraction via heavy liquid (NaPT) with a specific gravity of 2.85 g/cm^3. The heavy mineral fraction was further refined using a Frantz Magnetic Separator. The zircon and titanite minerals were then handpicked and mounted in 25 mm diameter epoxy resin discs that were manually polished to expose interiors of the mounted grains for imaging and analysis. Imaging of titanite and zircon grains was undertaken on a Tescan Mira3 field emission scanning electron microscope (FESEM). Both minerals were imaged with back-scattered electron (BSE), atomic-number contrast techniques to characterise mineral inclusions, with zircon also imaged by cathodoluminescence (CL) to provide

constraints on growth zoning and recrystallization (Corfu et al., 2003; Dickinson & Gehrels, 2009). The FESEM was operated at an accelerating voltage of 10 kV with a beam current of 10 nA and a working distance of 16.5 mm. The images were used to select targets for geochemical and geochronological analysis. Mapping of thin sections of the metasedimentary samples from which titanite minerals were extracted was performed on a Tescan Integrated Mineral Analyser (TIMA GM) equipped with an analytical field emission scanning electron microscope (FESEM).

U-Pb isotopes and trace element concentrations were measured on a laser ablation split stream inductively coupled plasma mass spectrometer (LASS ICP-MS), at the University of California, Santa Barbara, USA. The laser is fitted with a Photon Machine 193 nm excimer laser, a Nu Plasma HR, high resolution multi collector inductively coupled mass spectrometer (MC-ICPMS), that was used to measure the U-Pb isotopes, and an Agilent 7700x quadrupole ICPMS, used to measure the trace elements abundance (Kylander-Clark et al., 2013; Stearns et al., 2016). For detailed operating conditions refer to Kylander-Clark et al. (2013). Titanite grains were ablated with a 30 µm diameter beam to increase radiogenic U counts (Kylander-Clark, 2013; Stearns et al., 2016). The reference material BLR_1 was measured as a primary standard during the titanite analysis (1047.1 ± 0.4 Ma; Aleinikoff et al., 2007); quality control was performed by analysing an in-house secondary reference material (Y1710C5; 390 Ma), which yielded an age within 2% of the accepted value. Zircon grains were ablated with a 20 µm diameter beam due to the small size of the zircon minerals. The reference material 91500 was used as the primary standard (1061 ± 4.3 Ma; Wiedenbeck et al., 1995), with reference material GJ1 (601 ± 0.7 Ma; Jackson et al., 2004), OGC (3465.4 ± 0.6 Ma; Bodorkos et al., 2009), and Plešovice (337 ± 0.37 Ma, Slama et al., 2008), analysed every 25 unknowns. Time-resolved intensity data from the LASS ICP-MS were exported as counts per second, and the raw data, laser-induced inter-element fractionation and time-dependent Pb/U fractionation of the $^{206}Pb/^{238}U$ ratio were corrected using Iolite v2.5 on the Igor Pro software (Paton et al., 2010). Individual uncertainties were then propagated to a minimum of 2% (2σ) to reflect long term reproducibility of secondary reference material (Kylander-Clark, 2013; Stearns et al., 2016).

An intersection for the crystallization age of the titanite grains was calculated on a Tera–Wasserburg concordia diagram for the low intercept ($^{206}Pb/^{238}U$ axes). The anchor point to calculate the intercept age was based on the terrestrial Pb value calculated by Stacey-Kramers of $^{207}Pb/^{206}Pb = 0.83$ (Stacey & Kramers, 1975). The $^{207}Pb/^{206}Pb$ zircon ages with less than 10% discordance are used for data interpretation. Concordia diagrams and weighted mean age calculations were made using Isoplot/Ex_ver4.15 (Ludwig, 2003). Detrital zircon age populations are visualised using probability density plots constructed with Isoplot/Ex_ver4.15 (Ludwig, 2003). The elemental composition of the zircons has been studied with the support of chemical discrimination diagrams from Grimes et al. (2015).

5. Results

5.1 Metamorphic titanite

5.1.1 Contact metamorphosed aureole within MJGD27 and titanite minerals

The contact metamorphosed sediment in the aureole underneath the sill intersected by MGJD27 was examined through representative thin sections from samples MJGD27-4 and MJGD27-5 in order to decipher the metamorphic history of the sediments. TIMA mapping and optical microscopy showed that fine quartz (up to 20 μm) constitutes the dominant mineral phase in thin section (Fig. 5). In addition, metamorphic garnet grains up to 300 μm in size are distributed both in garnet-rich layers (larger euhedral grains), and within the quartz matrix (smaller grains; Fig. 5). Optical microscopy identified abundant fine-grained epidote and calcite, with the latter replacing the epidote in crown textures (Fig. 5). The metasediments also contain abundant sulphide minerals such as pyrite, pyrrhotite and chalcopyrite that are distributed in sulphide rich layers (Fig. 5). The mineral mapping and the optical microscope analysis revealed that many euhedral titanite grains are present within the quartz-epidote-calcite finer matrix and oriented with the longer axis parallel to the sedimentary bedding (Fig. 5). The TIMA mapping, integrated with optical microscopy also showed that the majority of the titanite grains, averaging 50–80 μm in size, are remnants of larger titanite crystals. These larger titanite relicts now appear almost entirely substituted by fine-grained epidote and calcite but preserve typical diamond and bladed shapes up to 400 μm in size (Fig. 5). The smaller intact titanite crystals are dark brown under both crossed and plane polarized light and have bladed or diamond morphologies that approximate the

shape found in the titanite separates (Fig. 5). The titanite grains obtained from the separation are euhedral and angular, internally homogeneous and range in size from 30 to 140 µm, with an average of about 75 µm for the longer axis, they also exhibit some mineral inclusions, principally comprising thin, elongate apatite (Fig. 5).

TIMA maps, photomicrographs and BSE of the titanite minerals

MJGD27-5
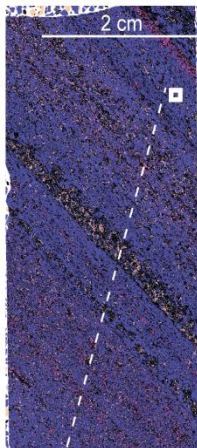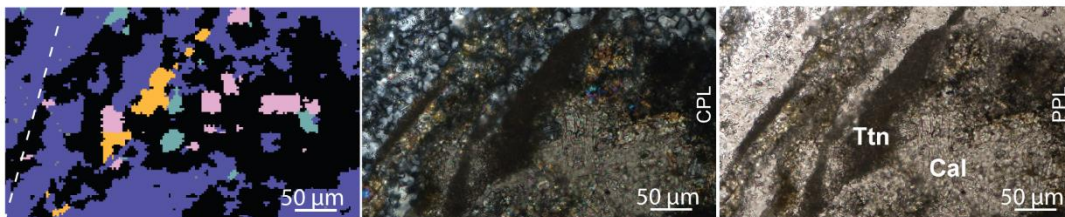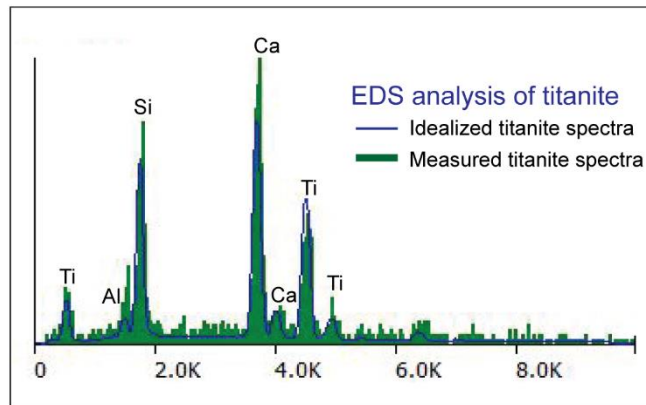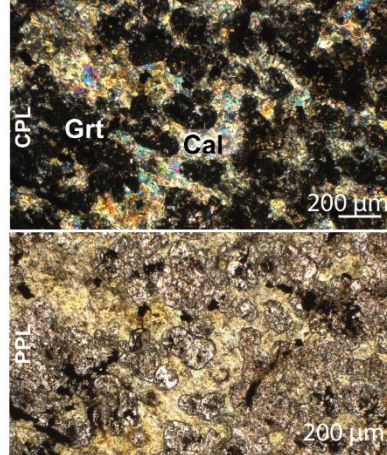
MJGD27-4

MJGD27-4

MJGD27-5
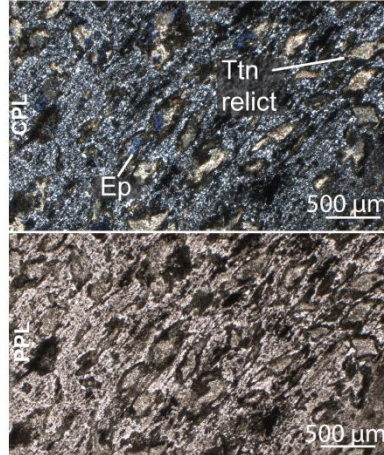
BSE titanite
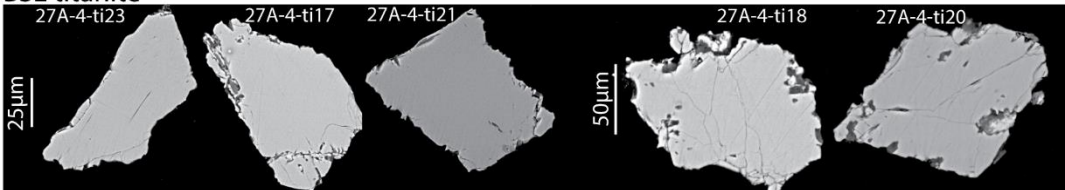
Fig. 5. Microscopic characterisation of titanite phases. TIMA maps of representative thin sections, and example EDS spectra of selected c. 100 µm titanite grain. Optical microscope photomicrographs of the mineral assemblage. Representative backscattered electron images (BSE) for the analysed liberated titanite grains.

5.1.2 Titanite U-Pb age and trace element geochemistry

U–Pb isotopes and trace elements were analysed in titanite from samples MJGD27-3, MJGD27-4 and MJGD27-5. Age and trace element compositions are given in Appendix 1. Sample MJGD27-4 was used to calculate an intercept age. In Tera-Wasserburg space, the U-Pb data of titanite grains from sample MJGD27-4, form a linear array between initial and radiogenic Pb components. Forty-one analyses from sample MJGD27-4 gave a lower intercept $^{238}U/^{206}Pb$ age of 1093 ± 21 Ma (MSWD = 2.1, n = 41; Fig. 6). This sample was chosen due to the consistent trace element geochemistry obtained from analyses of its grains which exhibit similar positive Ce anomalies and consistent abundances of MREE–HREE characterized by flat patterns and clear positive Eu anomalies (Eu/Eu*= 0.63–2.41 with Eu*=SQRT(Gd*Sm); Fig. 7). Samples MJGD27-3 and MJGD27-5 gave fewer titanite grains, and further regression calculated on the age of these minerals and on the full dataset resulted in ages within the range of that obtained from MJGD27-4. Additional plots are provided in Appendix 1.
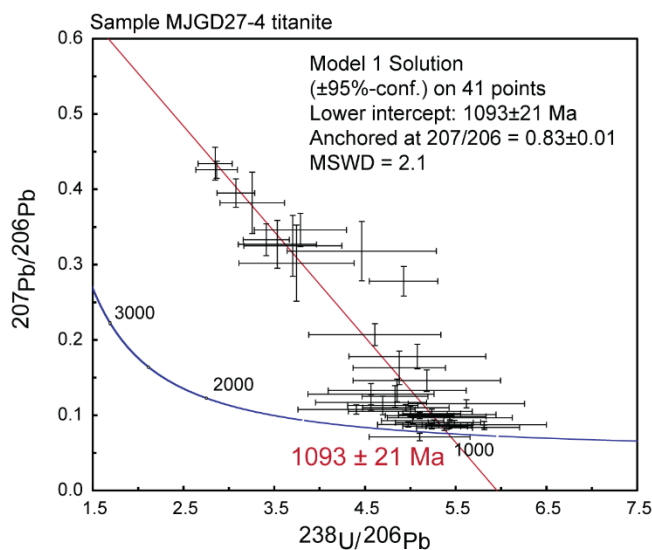
Fig. 6. Tera-Wasserburg concordia diagram with the low intercept $^{238}U/^{206}Pb$ age model calculated for the titanite minerals of sample MJGD27-4.

5.2 Detrital zircons

Detrital zircon grains were analysed from drill core MJGD27 and MJGD2 and their U-Pb age and trace element data are provided in Appendix 1. Zircon from drill core MJGD27 varies in shape from rounded to subrounded and range between 20 and 85 µm in size. Cathodoluminescence images commonly reveal core and rim features (Fig. 8). Zircon grains from drill core MJGD2 are more variable from subrounded to angular grain fragments, ranging between 35 and 120 µm and show both core-rim structures and homogeneous and/or structureless textures (Fig. 8).
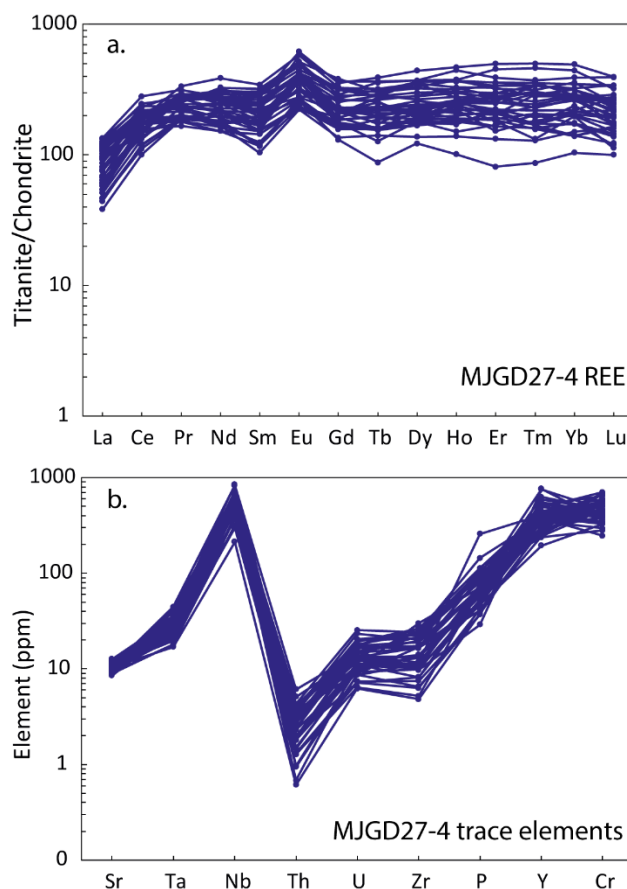
Fig. 7. Sample MJGD27-4 titanite trace element concentrations. a- Chondrite normalised REE concentrations; b- and trace elements content (chondrite values from Anders and Grevesse, 1989).

5.2.1 Zircon U-Pb age and trace element geochemistry

The Th/U ratios for all the analysed zircon (MJGD2 and MJGD27) range from 0.046 to 4.13, with the majority being > 0.1. Zircon grains display fractionated chondrite normalized REE patterns, with depleted HREE and relatively enriched (two to four orders of magnitude) LREE with respect chondrite values, $(Yb/Sm)_N = 3.25–1980$. Analysed zircons exhibit positive Ce anomalies and negative Eu anomalies (1.1–0.1) in accordance with a magmatic origin (Fig. 10; Hoskin, 2005, Pettke et al., 2005;).

94

Cores and innermost growth rings, in cases where cores were fractured or showed evidence of damage, were targeted for the analysis.
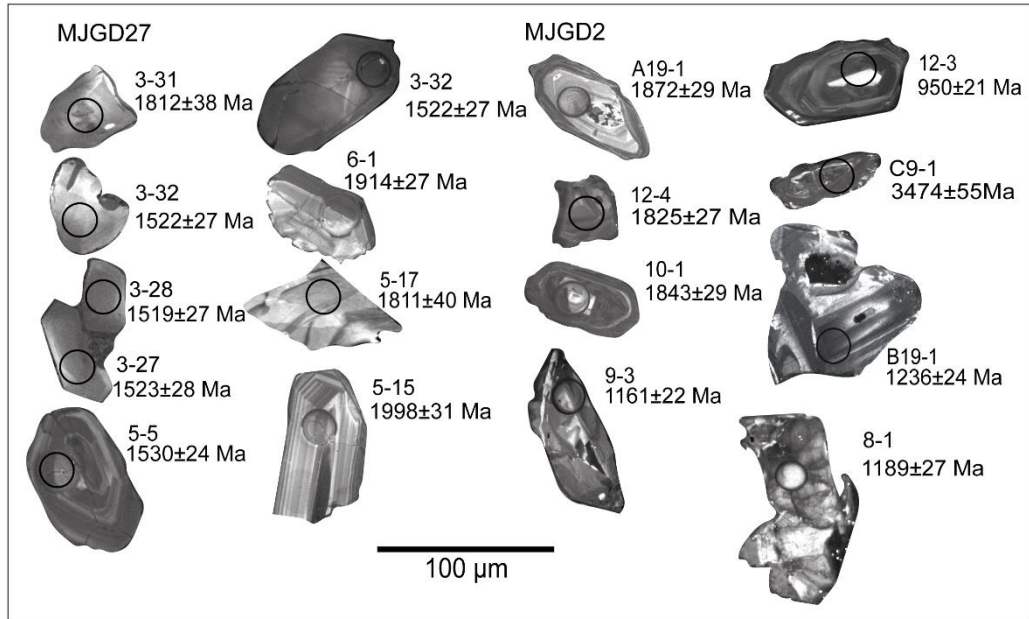
Fig. 8. Representative detrital zircon cathodoluminescence (CL) images, with spot locations and resulting ^{207}Pb/^{206}Pb ages indicated.

Forty concordant detrital zircons from samples MJGD27-3-5-6 gave crystallization ages spanning between 3072 ± 44 Ma and 1497 ± 31 Ma. A dominant age group is defined between 1600 and 1500 Ma from the analysis of the detrital zircon cores, with a weighted average age of 1539 ± 10 Ma (MSWD=2.8, n=22; Fig. 8). Grains aged 1600–1500 Ma exhibit similar compositions and plot at the boundary with the Oceanic Crust field, with a MORB affinity (U/Yb=0.2–0.6 and Hf= 800–900 ppm; Fig. 11; Grimes et al., 2015). A second subordinate age cluster from the analysis of the detrital zircon cores has a defined peak at 1800 Ma with a distinct shoulder to 1900 Ma (Fig. 9). Compositional data suggest that the zircon grains older than 1600 Ma originated in a continental setting and yield diverse trace element abundances (Fig. 11).

Eleven concordant ages were obtained from the analysis of the detrital zircon cores separated from MJGD2 (samples MJGD2-8-9-10-11-12-17-18-19). Their ages range from 950 ± 21 Ma to 3513 ± 50 Ma (Fig. 8). Two young grains have overlapping ages of 1161 ± 22 Ma and 1189 ± 27 Ma, while a second group has a weighted mean age of 1247 ± 14 Ma (MSWD=0.68; n=3) (Fig. 9). Detrital zircon grains younger than 1400 Ma express Chondrite normalized trace element characteristics of grains with a

magmatic origin (Fig. 10; Hoskin, 2005, Pettke et al., 2005) and have variable compositions (U/Yb = 0.6–5.0 and Hf=900–15000 ppm; Fig. 11), with the two zircon grains younger than 1200 Ma yielding similar U/Yb ≈ 0.88 (Fig. 9; Grimes et al., 2015). One zircon grain from sample MJGD2-12 has a concordant age of 950 ± 22 Ma, a Th/U ratio = 0.060 and a bright CL response for its core (Fig. 8), which may indicate recrystallization, following some metamorphic event. Metamorphic grains are not included in the age discussion (Rubatto, 2002; Hoskin & Schaltegger, 2003).
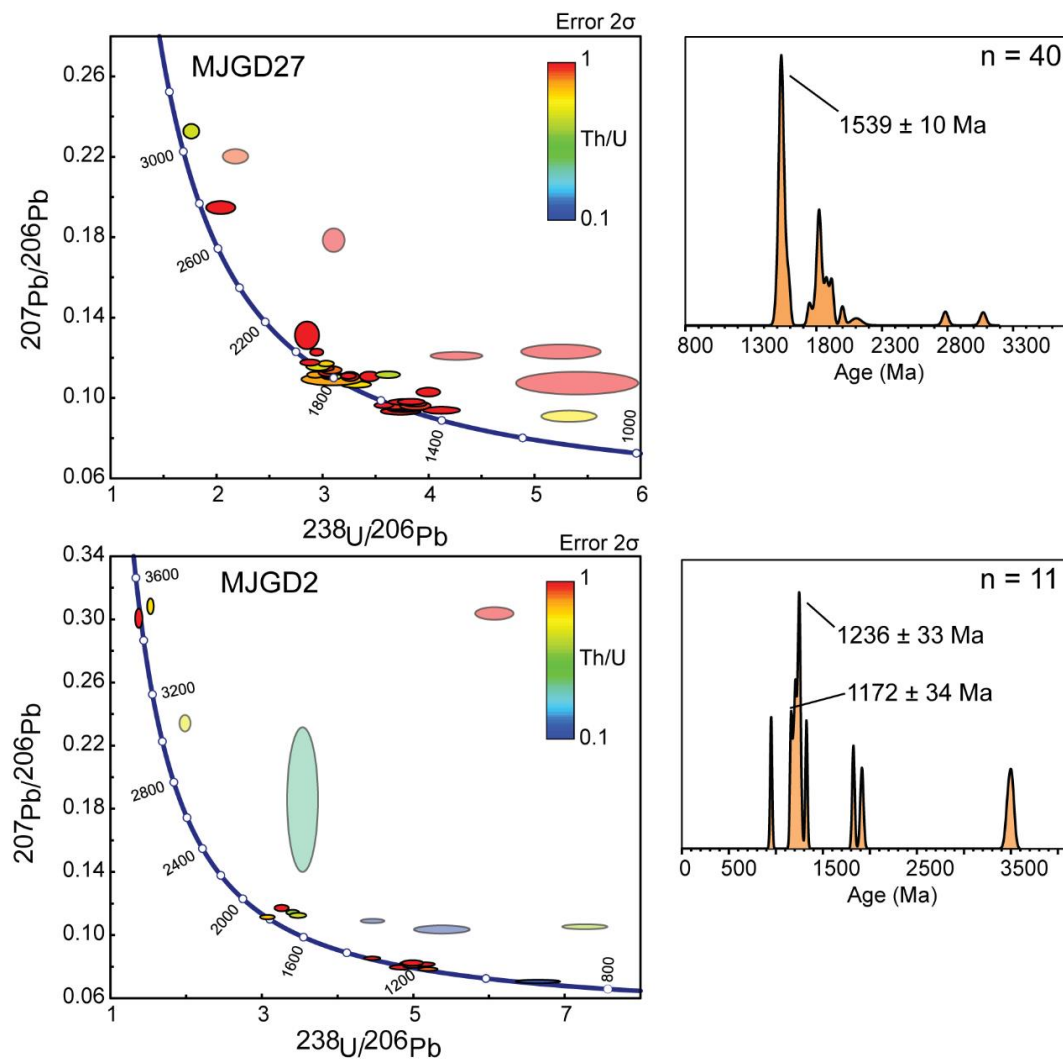
Fig. 9. Tera-Wasserburg concordia diagrams for concordant (> 90%) detrital zircon grains and discordant detrital zircons grains (transparent). Ellipse are coloured based on their Th/U ratio on a logarithmic scale. Probability density plots of detrital zircon age populations, with concordant grains and dominant population ages calculated using error weighted average ^{207}Pb/^{206}Pb ages.
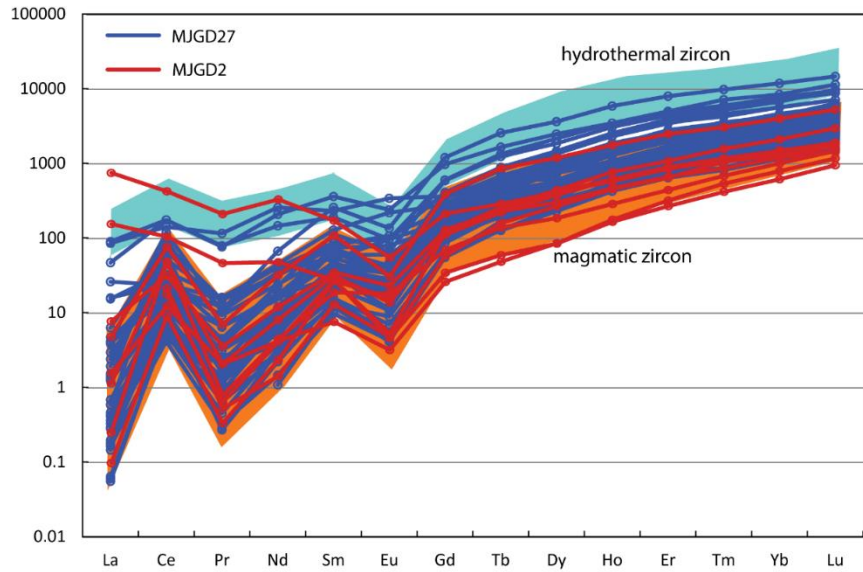
Fig. 10. Chondrite normalized trace element patterns of the concordant detrital zircons of MJGD27 and MJGD2 (Anders & Grevesse, 1989) versus trace elements patterns of hydrothermal and magmatic zircons from Hoskin (2005).

6. Discussion

6.1 Origin of titanite

The titanite grains analysed in this study were found only in the contact metamorphosed aureole within the metamorphosed sandstone of drill core MJGD27, underneath a thick dolerite sill (Fig. 3). Electron microscopy showed that the liberated titanite crystals are euhedral (angular and with diamond-blade shapes), and texturally homogeneous. These characteristics, and the singular age retrieved from the sample, suggest that the titanite formed within the sediments, rather than being of detrital origin (Fig. 5; Frost et al., 2000; Spandler et al., 2003; Gao et al., 2011; Hu et al., 2017).

Compositional analysis of the titanite grains demonstrate the low abundance of trace elements, with low U (<30 ppm), low Th/U ratios (<1), overall depleted REE concentrations with fractionation between LREE (depleted) and M-HREE (enriched). Such REE concentrations and distributions are overall consistent with metamorphic conditions for the titanite crystallization (Fig. 7; Frost et al., 2000; Gao et al., 2011; 2012). Moreover, the titanite REE patterns were characterized by flattened M to HREE patterns that are generally correlated with the presence of crystallizing accessory phases competing for M to HREE, such as garnet (Frost et al., 2000; Spandler et al.,

2003; Konrad-Schmolke et al., 2008; Gao et al., 2011). Abundant garnet is recorded in association with titanite in the metasediments (Fig. 5), which further support a metamorphic origin for titanite. Therefore, mobilization of U, Th, Pb and REE toward a major host of trace elements like garnet (HREE) likely took place, leaving the titanite minerals depleted of M to HREE (Spandler et al., 2003; Konrad-Schmolke et al., 2008; Gao et al., 2011).

Abundant titanite relics were also observed in metasediment thin sections (Fig. 5). The relicts preserve euhedral titanite shapes, but the titanite has almost been entirely substituted by epidote and calcite. The finding indicates that titanite was relatively unstable after its crystallization during contact metamorphism, and later on during cooling of the metasediments was replaced by more stable phases like epidote and calcite minerals, (Poli and Schmidt 1995; Frost et al. 2001; Spandler et al., 2003).

6.2 Timing of the mafic intrusion emplacement

The metamorphic titanite grains were exclusively found in the contact metamorphosed sediment underneath the intrusive sill of MJGD27, with sample MJGD27-5 being at the maximum distance of 12.5 m below the margin of the sill. Moreover, titanite grains displayed euhedral shape and yielded consistent elemental composition and regression ages. Hence the metamorphic titanite with a crystallization age of c. 1093 ± 21 Ma indirectly constrains the time of the mafic intrusion within MJGD27.

Drill core MJGD2 is separated from MJGD27 by a fault, displacing the stratigraphy by ~500 m. MJGD2 samples yielded detrital zircon grains as young as 1172 Ma, albeit in scarce numbers, that indicate that the sills must be younger than the c. 1172 Ma maximum depositional age. Additionally, in the MJGD2 drill core, peperite textures found between the sills and the sediments, suggest that intrusion occurred while the sediments were still unconsolidated, relatively soon after deposition and likely during shallow burial. Previous studies found similar conditions in the Collier Basin sediments, where the c. 1070 Ma Kulkatharra Dolerite intruded the basal sequence of the Collier Basin with peperitic margins (Wingate, 2002; Martin, 2003). Based on this similarity, and overlap of ages of the mafic units, it is likely that in drill core MJGD2 the mafic sills represent a correlative of the Kulkatharra Dolerite aged c. 1093 Ma.

6.3 Age and affiliation of the sedimentary sequences

The maximum depositional age for the sediments in drill core MJGD27, based on its detrital zircon record, is 1539 ± 10 Ma (MSWD=2.8, n=22), whereas the minimum depositional age is given by the age of the intruding sills of c. 1093 Ma. This detrital zircon population is identified by its relatively discrete elemental composition (Hf and Yb), as a distinct population, with a mafic protolith, close in age to the Waldburg Dolerite. The depositional age obtained for MJGD27 agrees with age ranges estimated for the Kiangi Creek Formation by previous authors (Martin et al., 2008; Cutten et al., 2016; Blay et al., 2018). Thus, due to its age limits the MJGD27 section most likely represents a portion of Edmund Basin stratigraphy.

Detrital zircon ages from MJGD2 are younger than the upper age limits of the Edmund Basin (c. 1465 Ma Narimbunna Dolerite; Wingate, 2002, 2012b, 2013a; Martin et al., 2008; Cutten et al., 2016), and thus, are inconsistent with either the Kiangi Creek Formation or the Edmund Basin (where the drill core is mapped). The maximum depositional age for the sediments of MJGD2 is given by the error weighted mean age of the two youngest concordant zircon grains found of 1172 ± 34 Ma (MSWD=0.65). The two grains are characterized by a similar elemental composition of Hf and Yb and protolith associated with felsic melt emplaced in a continental setting. The age of the intruding mafic sills yielding peperite margins is inferred to be of c. 1093 Ma and indicate the minimum depositional age for the sediments of MJGD2. Based on these data the sediments of MJGD2 are coeval with the sedimentary sequence of the Collier Basin.
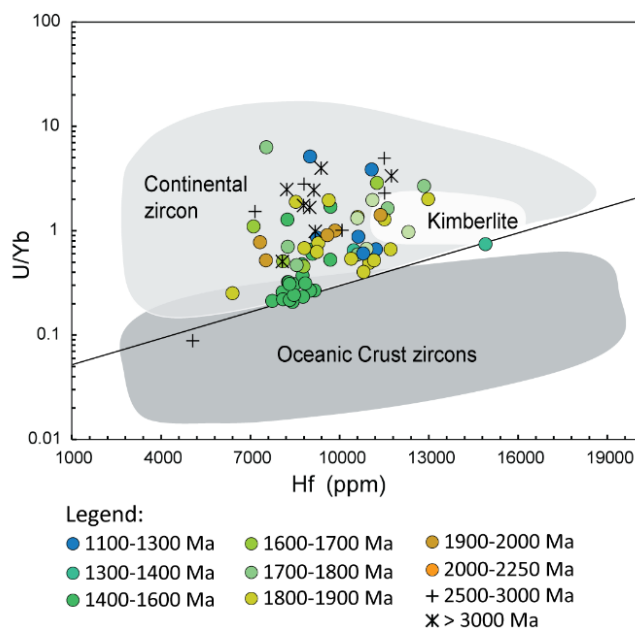
Fig. 11. Tectono-magmatic setting discrimination diagram for detrital zircon grains plotting U/Yb versus Hf concentration, modified after Grimes et al., (2015).

6.4 Late Mesoproterozoic tectonic evolution of the Capricorn Orogen region

U-Pb age data from metamorphic titanite, formed during intrusion by mafic magmas, suggests deposition within the Collier Basin to the south occurred at c. 1093 Ma, approximately 90 Ma after the 1385–1170 Ma Mutherbukin Tectonic Event. The basin depositional history was characterized by widespread mafic intrusive bodies, with peperite margins which (this study; Martin, 2003). Reactivation of normal faults recorded in the basin (Cutten et al., 2016), indicate that after the compressional Mutherbukin Tectonic Event a switch in the tectonic regime from compressional to extensional occurred in the Capricorn Orogen region (this study; Martin et al., 2003; Cutten et al., 2016). This change in tectonic regime was related to an interval of intracontinental extension in the Capricorn Orogen, coeval with mafic intrusions of the Warakurna Large Igneous Province at c. 1085 Ma in both the Capricorn Orogen and Central Australia (Wingate et al., 2004). Based on these observations the Collier Basin accumulation took place in an intracontinental rift setting (this study; Cutten et al., 2016).

Sediment supply for basal units of the Collier Basin has been correlated with the erosion of the southern Pilbara Craton margin, and the Palaeoproterozoic sedimentary basins overlying it (Ashburton, Blair and Edmund basins; Martin et al., 2008; Cutten et al., 2016). In contrast, paleocurrent indicators suggest that the sources of the top-most formation of the Collier Basin were variable and located to the north, south and east (Martin et al., 2008). In intracontinental rift settings it is common to find local

detritus, generated from horst structures alongside exotic detritus that have travelled along the rift axis (Lambiase et al., 1999). In the southern part of the Collier Basin, limited detrital zircon grains were recovered in this study to robustly assess the age of the sedimentary detritus and investigate potential source regions. However, the detrital grains that were recovered are mainly aged 1300–1100 Ma. These are significantly different from the detrital zircon age intervals reported in the past for the Collier Basin sediments or its proposed sources within the Capricorn Orogen (Martin et al., 2008; Cutten et al., 2016). Moreover, felsic rocks aged between 1300 and 1000 Ma are not found within the Capricorn Orogen (Fig. 11). The closest extensive felsic crystalline rocks with this age range are preserved in the Musgrave Province in central Australia and in the Albany-Fraser Orogen, in southern Western Australia, each of which may have acted as distal sources of sediments.

There is a paucity of information related to the depositional history of the southern part of the Collier Basin and the tectonic activity within the Capricorn Orogen during the deposition. The sequence analysed suggests deposition in a deep basin at c. 1093 Ma, approximately coeval and sharing similar characteristics (peperite) with the Backdoor Formation (Collier Basin) to the north. However, lithologically the sediment analysed (MJGD2), comprising deep marine sediments recording episodes of anoxic water, display greater similarity with the reportedly younger Ilgarari Formation (Martin et al., 2008). In addition, the strong dissimilarity between the ages of the detrital zircons of the samples analysed herein compared with the Backdoor Formation (Martin et al., 2008), suggest that the sediments have different origins. Therefore, it is likely that the sediments analysed in this study correlate with the Ilgarari Formation, which implies that the Ilgarari Formation in the southern part of the basin represents an equivalent facies of the deltaic complex of the Backdoor Formation found to the north (Fig. 12 a., b.). Following this hypothesis, the Ilgarari Formation prograded towards the north – northeast overlapping the Backdoor and Calyie formations as a result of progressive extensional tectonic activity in the region, and basin deepening (Fig. 12 c., d.).

The mafic complexes found in the Collier Basin aged 1093–1070 Ma (Kulkatharra Dolerite) are temporally equivalent to events recorded in the Musgrave Province and in the eastern Yilgarn Craton, coincident and likely related to or forming part of the

Warakurna Large Igneous Province (Warakurna LIP; Wingate et al., 2004). The emplacement of the Warakurna LIP was ultimately related to an extensional event in central Australia (Wingate et al., 2004) during the 1090–1040 Ma Giles Event (Howard et al., 2015). The presence of exotic detrital zircons within the age range of the Pitjantjatjara Supersuite (Musgrave Province) in the southern part of the Collier Basin and the mafic sills within the age of the Warakurna LIP, collectively indicate a link between the extensional tectonic activity recorded in the Collier Basin and the extensional tectonic activity recorded in central Australia. In this scenario, the Collier Basin probably developed as part of a larger intracratonic rift system, connecting the two regions. In this case, the rift would have initiated further south (Evins et al., 2010), during the Giles Event (Evins et al., 2010; Howard et al., 2015), and it could have propagated towards the northwest in the Capricorn Orogen, triggering deposition within the Collier Basin.
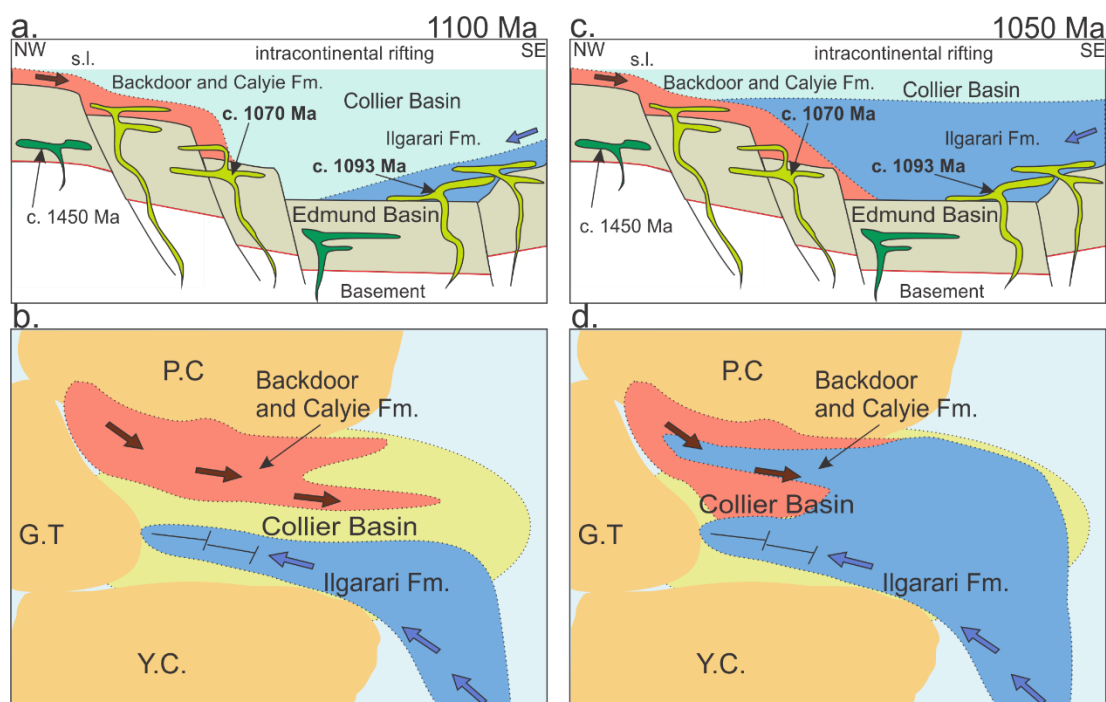
Fig. 12 a. Schematic section through the Collier Basin showing interpreted evolution of the basin with the inferred rifting propagation. Two sets of dolerite sills are indicated - one intruding only the Edmund Basin at c. 1465–1450 Ma (Narimbunna Dolerite; Wingate et al., 2002) and one intruding all the stratigraphy between 1093–1070 Ma (Kulkatharra Dolerite; this study; Wingate et al., 2004; s.l. = sea level); b. sources of the Collier Basin with schematic compartmentalization of the southern part that

received sediments from the southeast (Y.C. - Yilgarn Craton, P.C. - Pilbara Craton, G.T. - Glenburgh Terrane); c. and d. progradation of the Ilgarari Formation at c. 1050 Ma.

7. Conclusions

In the absence of other suitable dateable mineral phases, titanite crystallized in metamorphosed sediments in the contact aureole of intrusive units may become a useful target to establish the timing of sill and dyke complexes and help constrain regional geological histories. In the drill core MJGD27 from the Edmund Basin melt emplacement led to the crystallization of metamorphic titanite minerals within the contact metamorphosed aureole, which were used to indirectly date the intrusion at 1093 ± 21 Ma. The titanite age gave essential information to reconstruct the depositional history of the sediments and complemented the detrital zircon age information.

The maximum depositional age of the sediments in MJGD27 was established by detrital zircon at c. 1539 Ma. This age and the character of the detrital zircon age spectrum found, indicate that this section is likely a correlative of the Edmund Basin Devil Creek Formation (inferred age of ~1505 Ma; Martin et al., 2016). Detrital zircon grains from MJGD2 were derived from felsic parent rocks and aged between 1300 and 1100 Ma, with the youngest grains indicating a maximum depositional age of c. 1172 Ma. Based on this age and the identification of peperitic sill margins, typical of the Kulkatharra Dolerite, the c. 1093 Ma metamorphic age from the titanite of MJGD27 is interpreted to represents the minimum depositional age of the sediments from drill core MJGD2. According to the depositional age determined, the detrital zircon age record, and the deep-water marine facies preserved, the stratigraphic section of MJGD2 is interpreted to be coeval with the Collier Basin and to correlate with the topmost Ilgarari Formation and its deep marine water sediments.

The age of c. 1093 Ma from the metamorphic titanite was found to be within uncertainty of the c. 1070 Ma Kulkatharra Dolerite (Wingate, 2002). Widespread sills and dykes aged between 1093 and 1070 Ma intruding the Collier Basin are linked to a phase of lithospheric extension during which intracontinental rifting of the Capricorn Orogen occurred. The intracontinental rifting of the Capricorn Orogen is connected to the 1090–1040 Ma extensional Giles Event occurred in Central Australia (Howard et

al., 2015). Deposition of Collier Basin sediments is associated with a larger intracratonic rifting system, sourced by exotic sediment located south with respect to present geography. The intracratonic rift was previously described as the Ngaanyatjarra Rift, formed between the Western Australian Craton and central Australia (Musgrave Complex) and approximatively oriented south-north (Evins et al., 2010).

Acknowledgements

References

Aleinikoff, J. N., Wintsch, R. P., Tollo, R. P., Unruh, D. M., Fanning, C. M. & Schmitz, M. D. (2007). Ages and origins of rocks of the Killingworth dome, south-central Connecticut: Implications for the tectonic evolution of southern New England. *American Journal of Science,* 307, 63-118.

Anders, E. & Grevesse, N. (1989). Abundances of the elements: Meteoritic and solar. *Geochimica et Cosmochimica Acta,* 53, 197-214.

Blay O. A., Johnson S.P., Wingate M. T. D., Thorne A. M., Kirkland C. L., Tessalina S. G. & Cutten H. N. (2018). A new Mesoproterozoic mafic intrusive event in the Capricorn Orogen. Geological Survey Western Australia*,* Record 2018/4, 41.

Bodorkos, S., Stern, R. A., Kamo, S., Corfu, F. & Hickman, A. H. (2009). OG1: A Natural Reference Material for Quantifying SIMS Instrumental Mass Fractionation of Pb Isotopes During Zircon Dating. *American Geophysical Union*, Fall Meeting 2009, abstract #V33B-2044.

Bonamici, C. E., Fanning, C. M., Kozdon, R., Fournelle, J. H. & Valley, J. W. (2015). Combined oxygen-isotope and U-Pb zoning studies of titanite: New criteria for age preservation. *Chemical Geology,* 398, 70-84.

Camacho, A., Simons, B. & Schmidt, P. W. (1991). Geological and palaeomagnetic significance of the Kulgera Dyke Swarm, Musgrave Block, NT, Australia. *Geophysical Journal International,* 107, 37-45.

Corfu, F., Hanchar, J. M., Hoskin, P. W. O. & Kinny, P. (2003). Atlas of Zircon Textures. *Reviews in Mineralogy and Geochemistry,* 53, 469-500.

Cutten, H., Johnson, S., Thorne, A., Wingate, M., Kirkland, C., Belousova, E., Blay, O. & Zwingmann, H. (2016). Deposition, Provenance, Inversion History and Mineralization of the Proterozoic Edmund and Collier Basins, Capricorn Orogen. Geological Survey Western Australia, Report 127.

Dentith, M., Johnson, S. P., Evans, S., Aitken, A., Joly, A., Thiel, S. & Tyler, I. M. (2014). A magnetotelluric traverse across the eastern part of the Capricorn Orogen. Geological Survey of Western Australia, Report 135.

Dickinson, W. R. & Gehrels, G. E. (2009). Use of U-Pb ages of detrital zircons to infer maximum depositional ages of strata: A test against a Colorado Plateau Mesozoic database. *Earth and Planetary Science Letters,* 288, 115-125.

Evins, P. M., Smithies, R. H., Howard, H. M., Kirkland, C. L., Wingate, M. T. D. & Bodorkos, S. (2010). Devil in the detail; The 1150-1000 Ma magmatic and structural evolution of the Ngaanyatjarra Rift, west Musgrave Province, Central Australia. *Precambrian Research,* 183, 572-588.

Frost, B. R., Chamberlain, K. R. & Schumacher, J. C. (2000). Sphene (titanite): phase relations and role as a geochronometer. *Chemical Geology,* 172, 131-148.

Gao, X. Y., Zheng, Y. F. & Chen, Y. X. (2011). U-Pb ages and trace elements in metamorphic zircon and titanite from UHP eclogite in the Dabie orogen: Constraints on P-T-t path. *Journal of Metamorphic Geology,* 29, 721-740.

Gao, X. Y., Zheng, Y. F., Chen, Y. X. & Guo, J. (2012). Geochemical and U-Pb age constraints on the occurrence of polygenetic titanites in UHP metagranite in the Dabie orogen. *Lithos,* 136-139, 93-108.

Garber, J. M., Hacker, B. R., Kylander-Clark, A. R. C., Stearns, M. & Seward, G. (2017). Controls on Trace Element Uptake in Metamorphic Titanite: Implications for Petrochronology. *Journal of Petrology,* 58, 1031-1057.

Goldberg, A. S. (2010). Dyke swarms as indicators of major extensional events in the 1.9-1.2 Ga Columbia supercontinent. *Journal of Geodynamics* 50, 176-190.

Grimes, C. B., Wooden, J. L., Cheadle, M. J. & John, B. E. (2015). "Fingerprinting" tectono-magmatic provenance using trace elements in igneous zircon. *Contributions to Mineralogy and Petrology,* 170, 46-46.

Hoskin, P. W. O. & Schaltegger, U. (2003). The composition of zircon and igneous and metamorphic petrogenesis. *Reviews in Mineralogy and Geochemistry,* 53, 27-62.

Hoskin, P. W. O. (2005). Trace-element composition of hydrothermal zircon and the alteration of Hadean zircon from the Jack Hills, Australia. *Geochimica et Cosmochimica Acta,* 69, 637-648.

Houle' M. G., Gibson H. L., Lesher, C. M., Davis, P. C., Beresford, R. A. F. CAS, S. W. & Arndt, N. T. (2008). Komatiitic Sills and Multigenerational Peperite at Dundonald Beach, Abitibi Greenstone Belt, Ontario: Volcanic Architecture and Nickel Sulfide Distribution. *Economic Geology,* 103, 1269-1284.

Howard, H. M., Smithies, R. H., Kirkland, C. L., Kelsey, D. E., Aitken, A., Wingate, M. T. D., Quentin de Gromard, R., Spaggiari, C. V. & Maier, W. D. (2015). The burning heart - The Proterozoic geology and geological evolution of the west Musgrave Region, central Australia. *Gondwana Research,* 27, 64-94.

Hu, H., Li, J.-w., McFarlane, C. R. M., Luo, Y. & McCarron, T. (2017). Textures, trace element compositions, and U – Pb ages of titanite from the Mangling granitoid

pluton, East Qinling Orogen: Implications for magma mixing and destruction of the North China Craton. *Lithos,* 284-285, 50-68.

Jackson, S. E., Pearson, N. J., Griffin, W. L. & Belousova, E. A. (2004). The application of laser ablation-inductively coupled plasma-mass spectrometry to in situ U-Pb zircon geochronology. *Chemical Geology,* 211, 47-69.

Johnson, S. P., Sheppard, S., Rasmussen, B., Wingate, M. T. D., Kirkland, C. L., Muhling, J. R., Fletcher, I. R. & Belousova, E. A. (2010). The Glenburgh Orogeny as a record of Palaeoproterozoic continent-continent collision. Geological Survey of Western Australia, Record 2010/5.

Johnson, S. P., Sheppard, S., Wingate, M. T. D., Kirkland, C. L. & Belousova, E. A. (2011). Isotopic Evolution of the Glenburgh Terrane Basement: an Exotic Crustal Fragment I the Capricorn Orogen. Geological Survey of Western Australia, Report 110.

Johnson, S. P., Thorne, A. M., Tyler, I. M., Korsch, R. J., Kennett, B. L. N. N., Cutten, H. N., Goodwin, J., Blay, O., Blewett, R. S., Joly, A., Dentith, M. C., Aitken, A. R. A. A., Holzschuh, J., Salmon, M., Reading, A., Heinson, G., Boren, G., Ross, J., Costelloe, R. D. & Fomin, T. (2013). Crustal architecture of the Capricorn Orogen, Western Australia and associated metallogeny. *Australian Journal of Earth Sciences,* 60, 681-705.

Khan, T., Murata, M., Qasim Jan, M., Rehman, H. U., Zafar, M., Ozawa, H., Qadir, A. & Mehmood, S. (2017). Felsic dykes in the Neoproterozoic Nagar Parkar Igneous Complex, SE Sindh, Pakistan: geochemistry and tectonic settings. *Arabian Journal of Geosciences,* 10, 308.

Kirkland, C. L., Hollis, J., Danišík, M., Petersen, J., Evans, N. J. & McDonald, B. J. (2017). Apatite and titanite from the Karrat Group, Greenland; implications for charting the thermal evolution of crust from the U-Pb geochronology of common Pb bearing phases. *Precambrian Research,* 300, 107-120.

Konrad-Schmolke, M., Zack, T., O'Brien, P. J. & Jacob, D. E. (2008). Combined thermodynamic and rare earth element modelling of garnet growth during subduction: Examples from ultrahigh-pressure eclogite of the Western Gneiss Region, Norway. *Earth and Planetary Science Letters,* 272, 488-498.

Korhonen et al, (2017). Radiogenic heating and craton-margin plate stresses as drivers for intraplate orogeny. *Journal of Metamorphic Geology,* 31, 631-661

Kylander-Clark, A. R. C. (2013). Kylander-Clark et al. 2013. Laser ablation split stream ICP petrochronology. *Chemical geology*, 345, 99-112.

Lambiase, J. J., Morley, C. K., White, R. S., Watts, A. B., Bowler, D., Holroyd, R., Morley, C. K., (1999). Hydrocarbons in Rift Basins: The Role of Stratigraphy. *The Royal Society Publications*, 357,1753.

Li, Z. X., Bogdanova, S. V., Collins, A. S., Davidson, A., De Waele, B., Ernst, R. E., Fitzsimons, I. C. W., Fuck, R. A., Gladkochub, D. P., Jacobs, J., Karlstrom, K. E., Lu, S., Natapov, L. M., Pease, V., Pisarevsky, S. A., Thrane, K. & Vernikovsky, V. (2008). Assembly, configuration, and break-up history of Rodinia: A synthesis. *Precambrian Research,* 160, 179-210.

Ludwig, K. R. (2003). Isoplot 3.00: A geochronological toolkit for Microsoft Excel. *Berkeley Geochronology Center Special Publication*, 39, 91-445.

Marsh, J. H. & Smye, A. J. (2017). U-Pb systematics and trace element characteristics in titanite from a high-pressure mafic granulite. *Chemical Geology,* 466, 403-416.

Martin, D. M. (2003). Peperite in the Backdoor Formation and its significance to the age and tectonic evolution of the Bangemall Supergroup. Geological Survey of Western Australia Annual Review 2002–03, 53-59.

Martin, D. M. B., Johnson S. P., and Riganti A., Hogen-Esch J., White S. R., (2016). Geological Survey of Western Australia, 2016; 1:500 000 State interpreted bedrock geology of Western Australia. Geological Survey of Western Australia, digital data layer, www.dmp.wa.gov.au/geoview.

McCormick, K. A., Chamberlain, K. R. & Paterson, C. J. (2018). U – Pb baddeleyite crystallization age for a Corson diabase intrusion: possible Midcontinent Rift magmatism in eastern South Dakota. *Canadian Journal of Earth Science*s, 55, 111-117.

Paton, C., Woodhead, J. D., Hellstrom, J. C., Hergt, J. M., Greig, A. & Maas, R. (2010). Improved laser ablation U-Pb zircon geochronology through robust downhole fractionation correction. Geochemistry, Geophysics, Geosystems, 11, 3.

Pettke, T., Audetat, A., Schaltegger, U., Heinrich, C. A. (2005). Magmatic-to-hydrothermal crystallization in the W-Sn mineralized Mole Granite (NSW, Australia) - Part II: evolving zircon and thorite trace element chemistry. Chemical Geology, 220, 191-213

Piechocka, A. M., Sheppard, S., Fitzsimons, I. C. W., Johnson, S. P., Rasmussen, B., Jourdan, F. (2018). Neoproterozoic $^{40}Ar/^{39}Ar$ mica ages mark the termination of a billion years of intraplate reworking in the Capricorn Orogen, Western Australia. *Precambrian Research,* 310, 391-406.

Poli, S. & Schmidt, M. W., (1995). H2O transport and release in subduction zones - experimental constraints on basaltic and andesitic systems. Journal of Geophysical Research. Petrology of subducted slabs. *Earth Planetary Science Annual Review,* 30, 207-235.

Rasmussen, B. & Fletcher, I. R. (2002). Indirect dating of mafic intrusions by SHRIMP U-Pb analysis of monazite in contact metamorphosed shale: An example from the Palaeoproterozoic Capricorn Orogen, Western Australia. *Earth and Planetary Science Letters,* 197, 287-299.

Rasmussen, B., Fletcher, I. R. & Muhling, J. R. (2008). Pb/Pb geochronology, petrography and chemistry of Zr-rich accessory minerals (zirconolite, tranquillityite and baddeleyite) in mare basalt 10047. *Geochimica et Cosmochimica Acta,* 72, 5799-5818.

Rubatto, D. (2002). Zircon trace element geochemistry: Partitioning with garnet and the link between U-Pb ages and metamorphism. *Chemical Geology,* 184, 123-138.

Sepahi, A. A., Salami, S., Lentz, D., McFarlane, C. & Maanijou, M. (2018). Petrography, geochemistry, and U–Pb geochronology of pegmatites and aplites associated with the Alvand intrusive complex in the Hamedan region, Sanandaj–Sirjan zone, Zagros orogen (Iran). *International Journal of Earth Sciences,* 07,1059-1096.

Sheppard, S., Occhipinti, S. A. S. A. & Nelson, D. R. (2005). Intracontinental reworking in the Capricorn Orogen, Western Australia: The 1680-1620 Ma Mangaroon Orogeny. *Australian Journal of Earth Sciences,* 52, 443-460.

Sheppard, S., Rasmussen, B., Muhling, J. R., Farrell, T. R. & Fletcher, I. R. (2007). Grenvillian-aged orogenesis in the Palaeoproterozoic Gascoyne complex, Western

Australia: 1030-950 Ma reworking of the Proterozoic Capricorn Orogen. *Journal of Metamorphic Geology,* 25, 477-494.

Sheppard, S., Bodorkos, S., Johnson, S. P., Wingate, M. T. D. & Kirkland, C. L. (2010). The Palaeoproterozoic Capricorn Orogeny: intracontinental reworking not continent-continent collision. *Geological Survey of Western Australia,* Report 108.

Slama, J., Kosler, J., Condon, D. J., Crowley, J. L., Gerdes, A., Hanchar, J. M., Horstwood, M. S. A., Morris, G. A., Nasdala, L., Norberg, N., Schaltegger, U., Schoene, B., Tubrett, M. N. & Whitehouse, M. J. (2008). Plešovice zircon - A new natural reference material for U-Pb and Hf isotopic microanalysis. *Chemical Geology,* 249, 1-35.

Spandler, C., Hermann, J., Arculus, R. & Mavrogenes, J. (2003). Redistribution of trace elements during prograde metamorphism from lawsonite blueschist to eclogite facies; implications for deep subduction-zone processes. *Contributions to Mineralogy and Petrology,* 146, 205-222.

Spencer, K. J., Hacker, B. R., Kylander-Clark, A. R. C., Andersen, T. B., Cottle, J. M., Stearns, M. A., Poletti, J. E. & Seward, G. G. E. (2013). Campaign-style titanite U-Pb dating by laser-ablation ICP: Implications for crustal flow, phase transformations and titanite closure. *Chemical Geology,* 341, 84-101.

Stacey, J. S. & Kramers, J. D. (1975). Approximation of terrestrial lead isotope evolution by a two-stage model. *Earth and Planetary Science Letters,* 26, 207-221.

Stark, J. C., Wang, X. C., Denyszyn, S. W., Li, Z. X., Rasmussen, B., Zi, J. W., Sheppard, S. & Liu, Y. (2017). Newly identified 1.89 Ga mafic dyke swarm in the Archean Yilgarn Craton, Western Australia suggests a connection with India. *Precambrian Research*, 0-1.

Stearns, M. A., Cottle, J. M. & Hacker, B. R. (2016). Extracting thermal histories from the near-rim zoning in titanite using coupled U-Pb and trace-element depth profiles by single-shot laser-ablation split stream (SS-LASS) ICP-MS. *Chemical Geology,* 422, 13-24.

Wang, Y., Fan, W., Zhang, Y., Guo, F., Zhang, H. & Peng, T. (2004). Geochemical,40Ar/39Ar geochronological and Sr-Nd isotopic constraints on the origin of Paleoproterozoic mafic dikes from the southern Taihang Mountains and implications for the ca. 1800 Ma event of the North China Craton. *Precambrian Research,* 135, 55-77.

Wiedenbeck, M., AllÉ, P., Corfu, F., Griffin, W. L., Meier, M., Oberli, F., Quadt, A. V., Roddick, J. C. & Spiegel, W. (1995). Three Natural Zircon Standards for U-Th-Pb, Lu-Hf, Trace Element and Ree Analyses. *Geostandards Newsletter,* 19, 1-23.

Wingate, M. T. D., Pisarevsky, S. A. & Evans, D. A. D. (2002). Rodinia connections between Australia and Laurentia: No SWEAT, no AUSWUS? *Terra Nova,* 14, 121-128.

Wingate, M. T. D., Pirajno, F. & Morris, P. A. (2004). Warakurna large igneous province: A new Mesoproterozoic large igneous province in west-central Australia. *Geology,* 32, 105-108.

CHAPTER 5

FOOTPRINT OF A LARGE INTRACONTINENTAL RIFTING EVENT: COUPLED DETRITAL ZIRCON GEOCHRONOLOGY AND GEOCHEMISTRY FROM THE MESOPROTEROZOIC COLLIER BASIN, WESTERN AUSTRALIA

Armandola S.[a*], Barham M.[a,b], Reddy S. M.[a], Clark C.[a], Spinks S.[c]

[a] *School of Earth and Planetary Sciences, The Institute of Geoscience Research, Curtin University, GPO Box U1987, Perth, WA 6845, Australia*

[b] *Centre for Exploration and Targeting, Curtin University, GPO Box U1987, Perth, WA 6845, Australia*

[c] *Commonwealth Scientific and Industrial Research Organisation (CSIRO), PO box 1130 Bentley, WA 6102, Australia.*

*Corresponding author: sonia.armandola01@gmail.com

Keywords: provenance; Capricorn Orogen; intracratonic rift basin, Musgrave Orogeny, Ngaanyatjarra Rift.

Abstract

Intracontinental rifting of the Capricorn Orogen was accompanied by the emplacement of mafic intrusions at c. 1080 Ma, contemporaneous with deposition of siliciclastic and volcanoclastic sediment in the late Mesoproterozoic Collier Basin. In this work, we investigate the provenance of the Collier Basin sediment using U-Pb and trace element data of detrital zircons. Visual inspection of age data signatures and statistical Kolmogorov-Smirnov similarity tests integrated with trace element analysis of detrital zircon suggest that the Collier Basin contains two distinct sequences, in terms of sedimentary provenance and depositional history. The basal units of the Collier Basin were deposited in a deltaic setting and are dominated by early to middle Palaeoproterozoic detrital zircon ages matching older sedimentary rocks on the southern margin of the Pilbara Craton (Ashburton and Capricorn Groups), and

underlying Mesoproterozoic sedimentary sequences in the central Capricorn Orogen (Edmund Basin). The topmost sequence of the Collier Basin contains unimodal late Mesoproterozoic detrital zircon populations (1300–1100 Ma) interpreted to be associated with the ~1000 km distant Musgrave Province of central Australia. The sediment transport of the topmost unit occurred via a marine conduit in a rift environment, with its axis elongated from southeast to northwest. The data indicate that rifting within the Capricorn Orogen is linked to the 1090–1040 Ma intracontinental Ngaanyatjarra Rift of central Australia, which is interpreted to have facilitated dispersal of the Musgrave Province detritus between Western Australia and central Australia.

1. Introduction

Zircon is a common accessory mineral in siliciclastic sediments and faithfully retains U and Pb isotopes during weathering, erosion, transport, deposition, and low-grade metamorphism (Haughton et al., 1991; Cawood & Nemchin, 2000; Fedo, 2003; Guo et al., 2017). Consequently, detrital zircon U-Pb geochronology can be used to determine the age of mineral crystallization in the original source region, establish detrital grain provenance, and the contributions of different sources to sediments within basins (Griffin et al., 2004; Haines et al., 2016; Guo et al., 2017; Barham et al., 2018). Variations in detrital zircon age populations through the sediment pile, are a helpful tool in provenance studies since they point out erosion of different terranes, that is often linked with switches in source regions caused by tectonic activity (Griffin et al., 2004; Haines et al., 2016). Hence, zircon dating studies are also capable of tracking tectonic events and can be used to constrain tectonic reconstructions (e.g. Griffin et al., 2004; Haines et al., 2016; Guo et al., 2017; Barham et al., 2018). However, the use of zircon geochronology in provenance studies is limited where age data alone cannot resolve unique sources in instances of coeval zircon-growth in distinct areas (Spencer et al., 2016). In these cases, it is useful to complement detrital zircon age data with paleocurrent information or other geochemical data, such as detrital zircon trace elements (Kylander-Clark et al., 2013; Haines et al., 2016; Spencer et al., 2016). In northern Western Australia, the Capricorn Orogen is a collisional zone that records the Proterozoic amalgamation of the Yilgarn Craton, Pilbara Craton and Glenburgh Terrane (Johnson et al., 2013). The youngest sedimentary succession

associated with the Capricorn Orogen is the late Mesoproterozoic Collier Basin (c. 1070 Ma; Martin, 2003), which is exposed in a c. 800 km wide east-west trending belt in the central eastern region of the orogen. Limited data are available for the depositional history of the Collier Basin, which hinders understanding of the wider late Mesoproterozoic tectonic evolution of the Capricorn Orogen region (Wingate et al., 2002; Martin, 2003; Martin & Thorne, 2004; Wingate et al., 2004). Sediment derivation from the north (southern Pilbara Craton) was previously inferred for sedimentary rocks of the western Collier Basin (Martin et al., 2008; Cutten et al., 2016). However, due to the great variability of sedimentary facies manifested within the stratigraphy, these data cannot be convincingly extended to the central and eastern parts of the basin.

In this study we report detrital zircon U-Pb and trace element data, collected by laser split-stream ICP-MS, to constrain the sources of sediments for the Collier Basin, and to reconstruct the tectonic evolution of the basin. Eight samples were analysed from the Collier Basin stratigraphy, with a significant focus on the topmost formation, which has previously not undergone any detrital zircon geochronology studies. To inform the depositional and tectonic history of the basin, the U-Pb age data are compared with relevant proximal and distal source terranes and sedimentary reservoirs, across the West Australian Craton and central Australia (Musgrave Province). The time-constrained trace element composition of detrital zircon grains is assessed to reconstruct the lithologies of primary source rocks and used to refine the interpretation of sedimentary provenance.

2. Geological Framework

The Palaeoproterozoic Capricorn Orogen is an orogenic belt formed during a two stages continental collision of the Archean Pilbara Craton, Yilgarn Craton and Glenburgh Terrane. An early collision is recorded by the 2215–2145 Ma Ophthalmian Orogeny. Subsequently, continental amalgamation took place during the 2005–1950 Ma Glenburgh Orogeny (Fig. 1; Cawood & Tyler, 2004), resulting in the final accretion of the West Australian Craton. The continental collision was accompanied by the emplacement of voluminous intrusions around the cratonic sutures and throughout the Gascoyne Complex, represented by the 2005–1970 Ma Dalgaringa

Supersuite and the 1965–1945 Ma Bertibubba Supersuite (Fig. 1; Johnson et al., 2010; 2011). Following the amalgamation, intracratonic tectonic reactivations affected the Capricorn Orogen with accompanying sedimentation, deformation, metamorphism, and magmatism. The early 1820–1770 Ma Capricorn Orogeny and 1680–1620 Ma Mangaroon Orogeny were accompanied by magmatism of the 1850–1770 Ma Moorarie Supersuite and 1680–1620 Ma Durlacher Supersuite, respectively (Fig. 1; Sheppard et al., 2005; Johnson et al., 2011; Dentith et al., 2014). Consecutive tectonic reactivations (1321–1171 Ma Mutherbukin Tectonic Event and 1026–954 Ma Edmundian Orogeny), resulted in deformation, metamorphism, and intermittent magmatism (1100–950 Ma, Thirty Three Supersuite; Sheppard et al., 2007; Johnson et al., 2013; Korhonen & Johnson, 2015).

2.1. The Collier Basin

The Collier Basin is the youngest depositional element of the Capricorn Orogen (Fig. 1), with depositional age constraints provided by the c. 1070 Ma Kulkatharra Dolerite, which intruded the unconsolidated sediment of the lower formation (Backdoor Formation), during intracratonic extension of the Capricorn Orogen, (Martin, 2003; Warakurna Supersuite Large Igneous Province of Wingate et al., 2004). The Collier Basin unconformably overlies the Mesoproterozoic Edmund Basin (Coodardoo, Ullawarra, Devil Creek and Discovery formations), the Palaeoproterozoic Ashburton Basin and Capricorn Group (Blair Basin), the Moorarie and the Durlacher supersuites in the Gascoyne Complex, and the Bryah Basin in the south (Fig. 1; Sheppard et al., 2005; Martin et al., 2008). The largest volume of sediments are preserved in the east of the Collier Basin and are partly covered by the Officer Basin (Fig. 1; Cutten et al., 2016).

The Collier Basin comprises three lithostratigraphic units: the Backdoor, Calyie and Ilgarari formations (Fig. 2). The transition between the two uppermost formations marks a regional marine flooding surface (Fig. 2; Martin & Thorne, 2004). The Backdoor Formation is up to 1500 m thick and consists of a basal unit characterised by carbonate-dominated shelf limestone interbedded with siltstone, and thick siltstone interbedded with sandstone units (Fig, 2; Martin & Thorne, 2004). Deposition took place in a carbonate platform and subsequently in a coarsening upward progradational

delta system (Martin & Thorne, 2004; Martin et al., 2008). Paleocurrent directions measured in the Backdoor Formation suggest both a north-east and north-west source for the sediments that have been interpreted to result from intense reworking of the underlying Edmund Basin (Bagas, 2004; Martin et al., 2008).

The Calyie Formation is ~250 m thick and consists of two deltaic sequences of medium- to coarse-grained sandstones with beds increasing in thickness upwards. These two deltaic systems are separated by ~30 m of siltstone and fine-grained sandstone (Fig. 2; Martin & Thorne, 2004). Towards its top, the Calyie Formation displays evidence of intertidal to shallow-marine deposition (Martin & Thorne, 2004). Paleocurrent data indicate transportation from the north-west, northeast and southeast (Martin et al., 2008).

The Ilgarari Formation is ~700 m thick in the central and western Collier Basin and thickens to ~1500 m towards the southeast. Its original extent is thought to have been greater than what is preserved (Martin & Thorne, 2004). The Ilgarari Formation is dominated by silicified planar-laminated pyritic and carbonaceous siltstone, fine-grained sandstone with chert bands, and thin limestone (Fig. 2). To the east, occasionally tuffaceous layers are interbedded with thick (~500 m) laminated siltstones. The sediments are interpreted to have been deposited in a relatively deep-marine environment with periodic anoxia (Martin & Thorne, 2004).
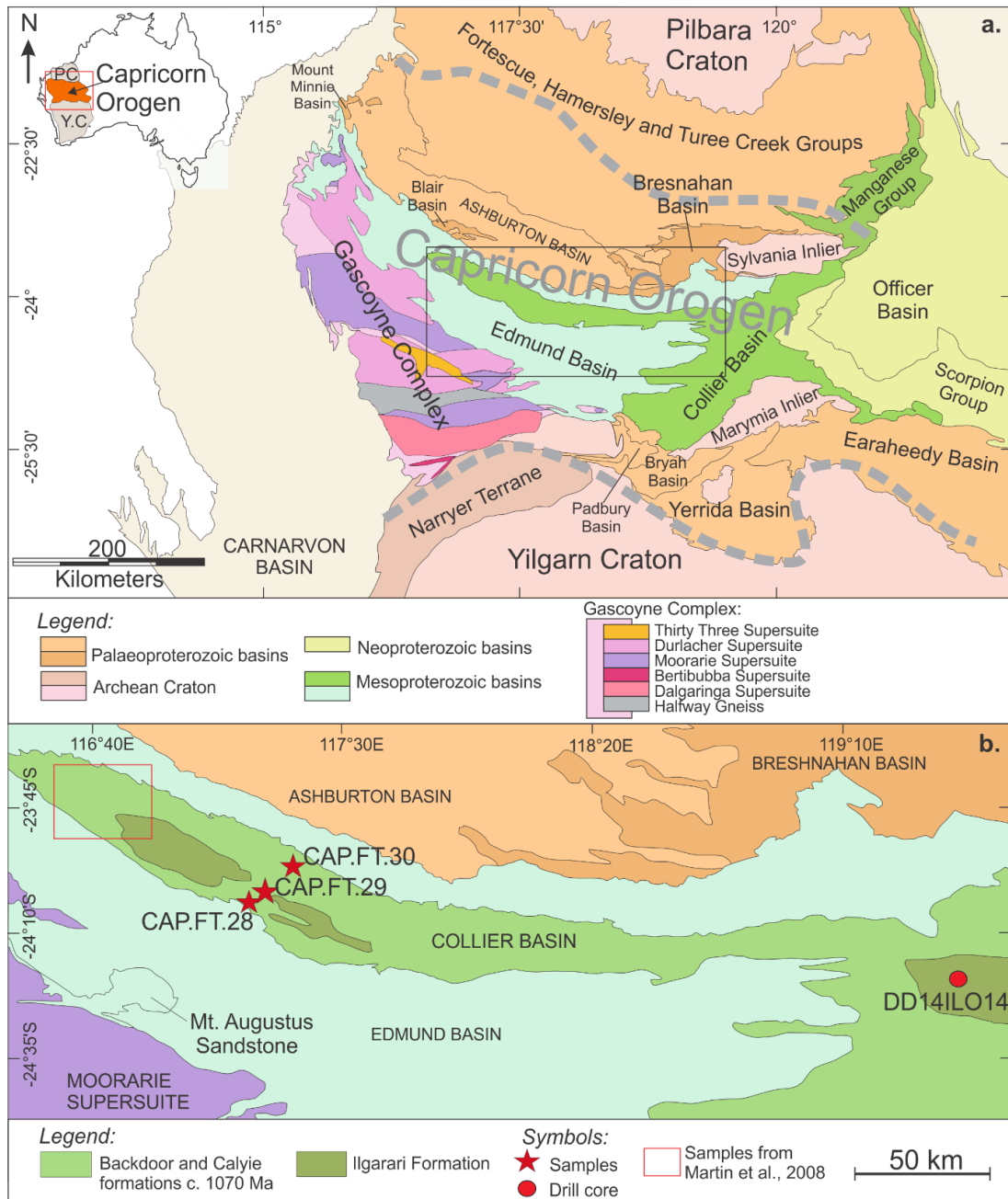
Fig. 1. a. Map illustrating the major tectonic units, structures and basins of the Capricorn Orogen and map of Australia with red box indicating the area shown. b. Sample locations through the central and western Collier Basin. P.C. - Pilbara Craton, Y.C. - Yilgarn Craton.
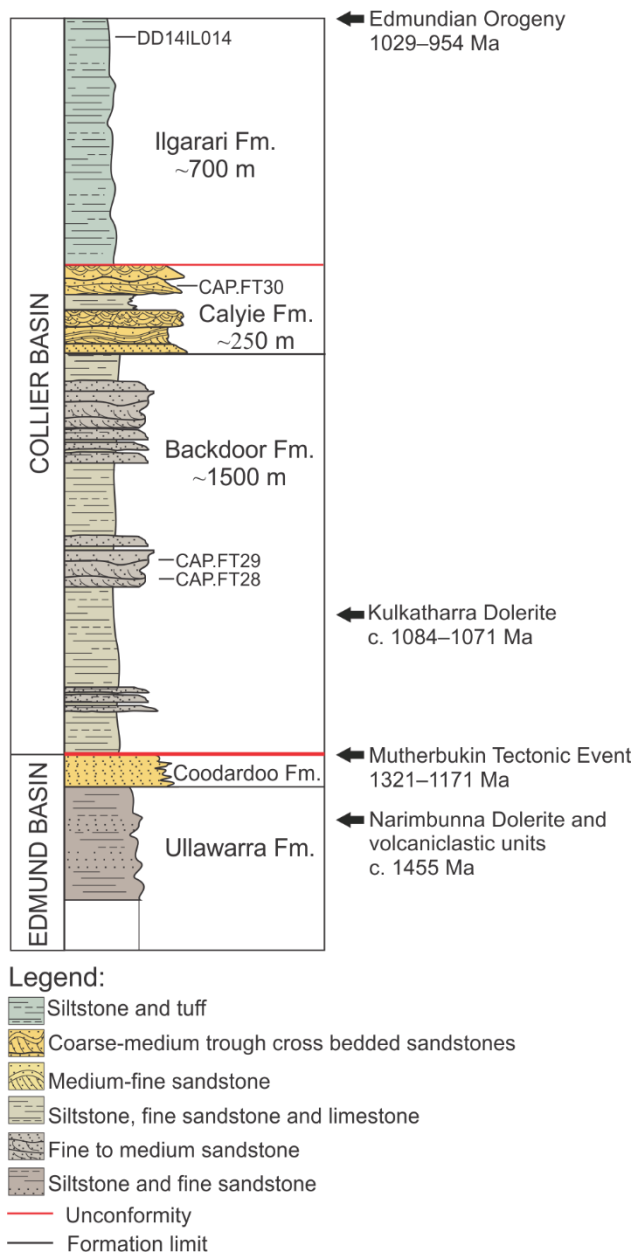
Fig. 2. Summarised stratigraphic section of the Collier Basin, with geochronological constraints and schematic sampling indicated (Wingate, 2002; Martin & Thorne 2004; Martin et al., 2008; Cutten et al., 2016).

3. Samples

Three c. 4 kg samples were taken from outcrop: two from the Backdoor Formation (CAP.FT28 and CAP.FT29), and one from the Calyie Formation (CAP.FT30; Table 1). Five samples – DD1, DD2, DD3, DD4 and DD5 of the Ilgarari Formation, were collected from the diamond drill core DD14IL014, drilled by Kumarina Resources Ltd. in 2014 (Fig. 2-3; Table 1). Samples DD1, DD2, DD4 and DD5 are composite from the combination of two sub-samples from each part of the stratigraphy (Table 1).

Drill core DD14IL014 reached a maximum depth of 589.1 m, and was drilled south of the Ilgarari Fault, interpreted from regional aeromagnetic data, with an azimuth of 345° and 60° plunge to intersect a Cu rich vein. The stratigraphy recorded in DD14IL014 is interpreted to represent the middle section of the Ilgarari Formation. The core succession is dominated by turbidite deposits, consisting of alternating medium-grained sandstone, siltstone and marl, which grade upward into fine siltstone and shale. Tuffaceous layers have been interpreted to be interbedded to the siltstone at different depths, between ~350 and 450 m. These tuffs layers lack associated pyroclastic rocks fragments (pumice and rhyolite) or minerals and are mixed within unconsolidated marl horizons. Three dolerite sills intrude the sedimentary rocks, with the topmost dolerite body having a considerable thickness of ~100 m (Fig. 3).

Table 1. Samples details

Sample ID	Easting	Northing	Formation	Lithology
(MGD94, MGZ_50)				
CAP.FT30	522232	7342421	Calyie Formation	Coarse sandstone with ripple lamination and basal quartz-pebble microconglomerate.
CAP.FT29	515643	7341509	Backdoor Formation	Grey coarse-grained quartz sandstone with planar and ripple lamination. Coarsening-upward.
CAP.FT28	515726	7341467	Backdoor Formation	Thick trough cross-bedded sandstone.
Sample ID	Depth intervals (m)		Formation	Lithology
763200E, 7304300N (MGD94, MGZ_51)				
DD1	361.4–361.7 365.4–365.7		Ilgarari Formation	Dark wave-laminated coarse siltstone and marl, tuffaceous layers.
DD2	426.2–426.45 446.35–446.65		Ilgarari Formation	Thick grey ripple laminated siltstone, marl, and thin dark mudstone levels.
DD3	464.35–464.75		Ilgarari Formation	Coarse sandstone (quartzite) with disseminated pyrite cubes.
DD4	495.05–495.25 502.2–502.45		Ilgarari Formation	Interbedded ripple laminated siltstone beds and laminated mudstone layers.
DD5	528.25–528.55 574.1-574.4		Ilgarari Formation	Fining-upward, mature, ripple laminated sandstone beds with subordinate centimetre scale silt layers.

Fig. 3. Stratigraphic log of drill core DD14IL014 with sample depths indicated.

4. Methodology

Sample processing was carried out at the John de Laeter Centre, Curtin University. Rock samples were separated into their constituent minerals using SelFrag electro-pulse disaggregation. The resulting grains were sieved with 500 μm and 210 μm mesh. Subsequently, the finer fraction (<210 μm) was separated with heavy liquid NaPT (sodium polytungstate) at 2.85 s.g., while the coarse fractions (>210 μm) were hand panned. Heavy minerals were further separated with Frantz Magnetic separation into a non-magnetic fraction (>1.7 A) and handpicked under an optical microscope. Representative zircons were mounted in a 25 mm epoxy resin disk and polished to half-grain thickness with 2000 grit wet sandpaper, 6 μm and 3 μm diamond-embedded plastic cloth and 1 μm diamond paste. Mounted zircons were imaged on a scanning electron microscope Tescan Mira 3 VP-FESEM. Cathodoluminescence (CL) imaging was undertaken using a Tescan panchromatic CL detector with 185–850 nm spectral range at 10 kV accelerating voltage and a working distance of 16.5 mm. The magmatic cores of the detrital zircons were targeted for later analyses.

118

Zircon U and Pb isotopes and trace element data were simultaneously analysed on a Laser Ablation Split Stream-ICP-MS – Resonetics S-155-LR 193 nm excimer laser ablation system, coupled to an Agilent 7700x quadrupole ICPMS and a Nu Instruments Plasma HR multi-collector ICP, with twelve Faraday cups and four low-mass ion counters. The laser was set to 2 Jcm^{-2} fluency at a 4 Hz repetition rate and circular 33 μm spot. The ablated material was carried to the mass spectrometers by combined He gas, with a flow rate of 3.2 mlmin^{-1}, Ar gas at 1 mlmin^{-1} flow rate and N gas at 1.2 mlmin^{-1} flow rate. The acquisition time including background signal registration was ~92 seconds. Elemental fractionation, down-hole correction fractionation and calibration drift were corrected by bracketing measurements of unknowns every 20 analyses with standards (Plešovice, GJ1, 91500, OG1). Plešovice (337.13 ± 0.37 Ma; Slama et al., 2008) was used as a primary standard for the U-Pb isotope calculations and GJ1 (608.5 ± 0.4 Ma; Jackson et al., 2004) was used as a reference for the trace element calculations (Appendix 1, standard U-Pb ages and standard trace elements). The accuracy of the determined age was resolved by measuring OG1 (3465.4 ± 0.6 Ma; Bodorkos et al., 2009; Stern, 2009) and 91500 (1061 ± 4.3 Ma; Wiedenbeck et al., 2004) as secondary standards. Data reduction was optimised with the *Iolite v2.5* software package (Paton et al., 2010). Analysis with ^{207}Pb/^{206}Pb and ^{238}U/^{206}Pb ages not within 90% of concordance were rejected, and ^{238}U/^{206}Pb ages were used for ages younger than 1.5 Ga (Spencer et al., 2016). Errors are given at 2σ. Concordia diagrams and probability density plots for all the samples were plotted with the application *Isoplotv4.15* (Ludwig, 2003). Comparison of the age modes of the samples with potential source rocks is made through kernel density plots (KDP) and using Kolmogorov-Smirnov tests (K-S test). The K-S test is a non-parametric test used to compare two sample datasets and assess whether their cumulative distributions are similar at >95% level of confidence. The probability is expressed through a value: *p>0.05* (Goodness-of-fit; Guynn & Gehrels, 2010; Table 2).

5. Results

5.1 Cathodoluminescence Imaging

Cathodoluminescence (CL) imaging highlights significant differences between zircons from drill core samples and those from outcrop samples (Fig. 4). Zircons from

drill core DD14ILO14 range in size between ~25 μm and ~100 μm on the longer axis and are elongated with rectangular shape, and rounded edges (samples DD1-2-4); many of these grains also have a weak CL response with poor zoning and core-rim contrast (Fig. 4). Zircons from samples DD3-5 are more spherical and rounded and exhibit core-rim structures under the CL (Fig. 4). The greatest number of rounded, subrounded and in some cases sub-spherical grains were found in outcrop samples CAP.FT28-29-30, in addition to the largest grains (up to ~200 μm in the long axis). Zircon grains from outcrop samples express a large variety of internal core-rim structures: (i) dark core and bright rim structures, (ii) weak contrast and oscillatory zoning, (iii) inherited cores cross-cut by rims (Fig. 4).
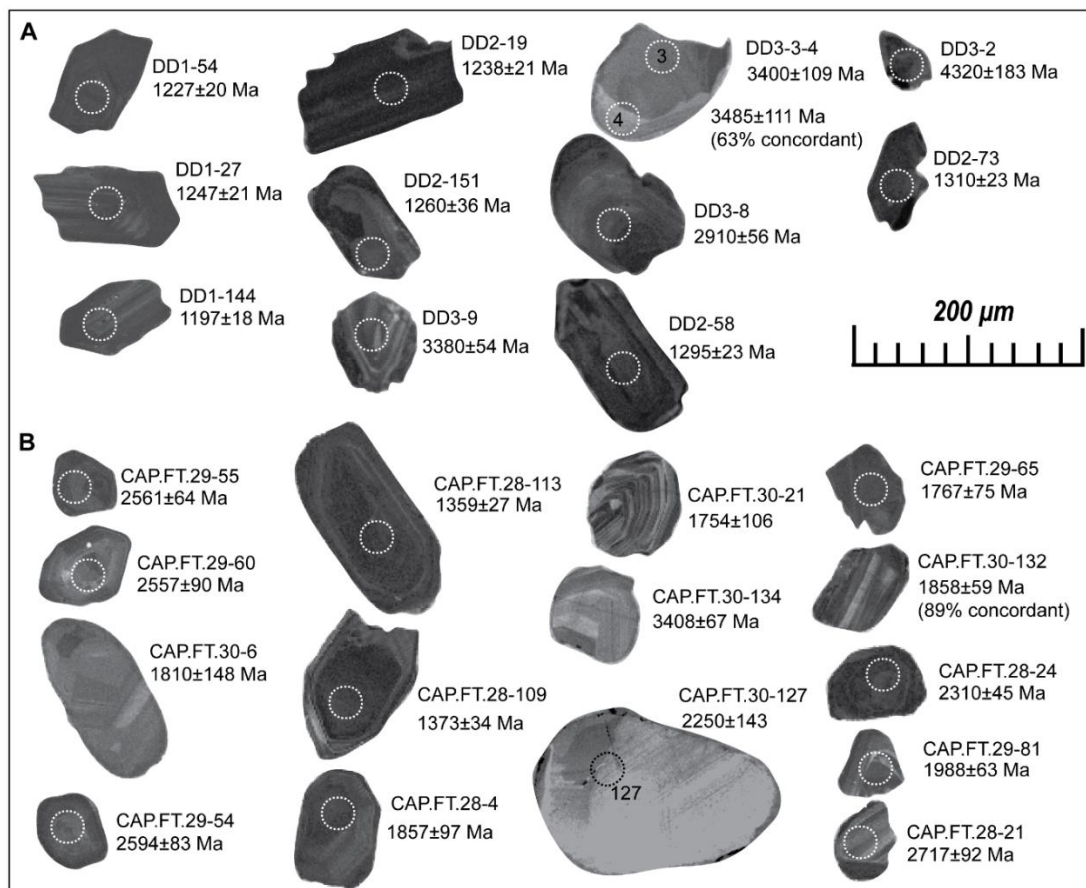
Fig. 4. Cathodoluminescence images of representative zircons from drill core DD14ILO14 samples (A), and outcrop samples CAP.FT (B). Ages listed are within 90% of concordance unless otherwise stated (DD3-4). Dashed circles indicate the analytical spot locations.
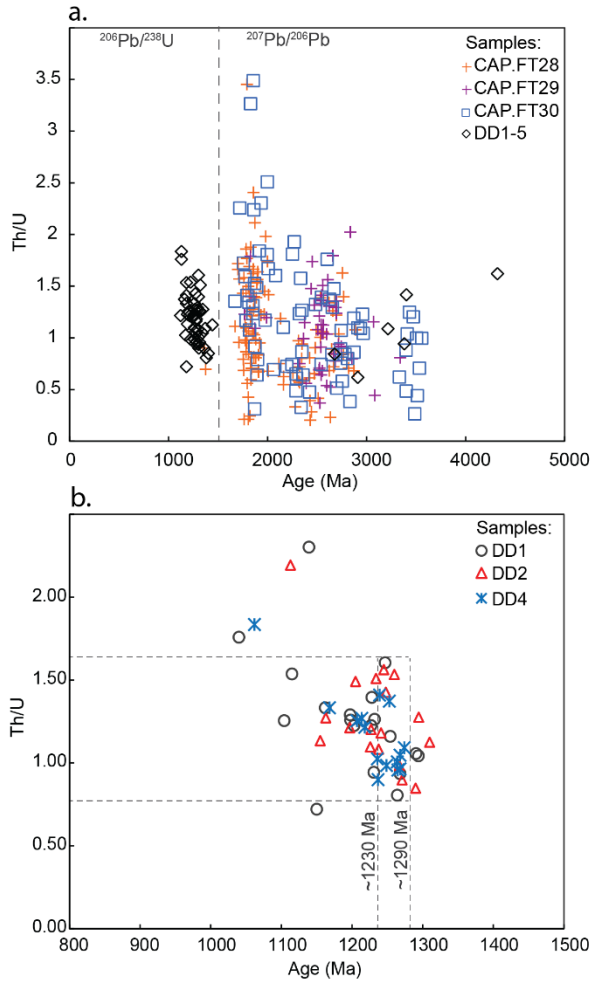
Fig. 5. Th/U ratios of the ≥90% concordant detrital zircon grains plotted versus their age. a. Outcrop and drill core samples; b. Samples DD1-DD2-DD4.

5.2 U/Pb geochronology and trace element geochemistry

The majority of the ≥90% concordant detrital zircon grains analysed have REE patterns characterized by depleted LREE and enriched HREE $(Gd/Yb)_N = 0.26$ to 6751), when normalized to the Chondrite values of Anders & Grevesse, (1989). All the analysed zircons have Th/U ratios >0.1 consistent with an igneous origin, except one detrital grain (CAP.FT30-38, 1996 ± 60 Ma), which has a Th/U ratio of 0.05, more characteristic of a metamorphic origin (Fig. 5; Hoskin & Black, 2000; Hoskin & Schaltegger 2003).

5.2.1 Sample CAP.FT28

Sample CAP.FT28 yielded two young grains with a weighted mean $^{238}U/^{206}Pb$ age of 1364 ± 21 Ma. A complex of 251 detrital grains was analysed. The dominant subpopulation ranges between 1900 and 1800 Ma, with a peak age of 1812 ± 12 Ma (MSWD=1.3, n=52). Other smaller age peaks lie between 2700 and 2300 Ma (Fig. 6-7). Trace elements indicate that the majority of detrital zircon grains are consistent with derivation from a granitoid source, having Eu/Eu*=0.45–0.15 and Y=5000–300 ppm (Belousova et al., 2002). A smaller number of grains match a lamproitic protolith or a mafic source rock, due to low concentrations of Y<300 ppm (e.g. CAP.FT28.59, age 1770 Ma Y=207, Hf= 8830 ppm, U=57ppm).

5.2.2 Sample CAP.FT29

The youngest detrital zircon grain (CAP.FT29-65) yielded an age of 1767 ± 75 Ma. A total of 82 grains was analysed. Approximately 76% of the concordant zircon grains are Archean (Fig. 6-7). The dominant subpopulation has a peak age of 2545 ± 13 Ma (MSWD=0.8, n=19), and a secondary subgroup at 2665 ± 20 Ma (MSWD=0.8, n=9; Fig. 6-7). Archean and early Palaeoproterozoic zircon grains between 2800 and 2300 Ma have trace elements that distribute in the granitoids and carbonatites rock field, with Y concentrations between 350 and 550 ppm, and Eu/Eu* ranging from 0.12 to 0.84 (Fig. 8).

5.2.3 Sample CAP.FT30

For sample CAP.FT30 153 grains were analysed. The detrital zircon age spectrum of CAP.FT30 is polymodal, with a dominant population ranging from 1900 to 1800 Ma, and peak age of c. 1855 ± 27 Ma (MSWD=0.22, n=17; Fig. 6-7). Zircon grains with ages between 1900 and 1700 Ma show probable granitoid protoliths for the minerals (Y >400 ppm, Eu/Eu*=0.09-1.2; Fig. 8). Variable trace element composition is observed for grains dated 1700–1600 Ma and 2000–1900 Ma that, along with zircon grains with crystallization ages spanning from 3000 to 2800 Ma, have inferred granite, syenite, mafic rocks and lamproite parents (Fig. 8). Compositional similarity is found within detrital zircon grains constituting the 2400–2300 Ma subpopulation with Y concentrations from 600 to 800 ppm likely deriving from a granitic protolith.

Similarly, zircon grains older than 3000 Ma have the lowest Y (<500 ppm) concentrations, with a poorly fractionated parent rock including lamproite and syenite (Fig. 8). Some of these grains have similar compositions, e.g. CAP.FT30-124 and 122 have Th/U of 1.25 and 1.20 respectively and might be linked to the same source.

5.2.4 Samples DD1 to DD5 (DD1ILO14)

The ≥90% concordant detrital zircon ages from DD1ILO14 drill core samples span between 3400 ± 109 Ma and 1104 ± 57 Ma, with a single Hadean zircon of 4320 ± 183 Ma. Samples DD1, DD2 and DD4 where respectively were analysed a total of 151,156 and 145 grains, yielded the greatest number of concordant grains and display very similar age distributions, ranging between 1300 and 1100 Ma, with dominant age peaks of 1247 ± 17 Ma, 1251 ± 16 Ma, 1248 ± 13 Ma, respectively (Fig. 6-7). Shoulders are also recognised in the peaks of age spectra at c. 1168 Ma and c. 1197 Ma (Fig. 6-7). The youngest concordant zircon grains from DD1 (1040 ± 36 Ma) and sample DD4 (1062 ± 33 Ma) were excluded because they are interpreted to result from a process of Pb loss, plotting on the horizontal array formed by the least concordant c. 1250 Ma detrital zircons (Fig. 6). Many detrital zircons of samples DD1, DD2 and DD4 are <90% concordant, and plot along an array propagating from the peak age of c. 1250 Ma toward lower $^{238}U/^{206}Pb$ values. This disturbance is interpreted to be due to extensive Pb-loss. Concordant zircon grains dated between 1300 and 1100 Ma yield Th/U ratios ranging from 0.69 to 2.29 (Fig. 5). Variations in the Th/U ratio are observed across subsets of the broad age population of 1300–1100 Ma: zircon grains dated 1290–1230 Ma have Th/U=1.1–0.9, while many of the grains younger than c. 1230 Ma have higher Th/U values ranging from 1.2 to 1.5, (Fig. 5). Zircon grains dated 1290–1230 Ma also show similar Eu/Eu* values (0.15–0.45), and high Y contents (>800 ppm) with respect to the detrital zircon grains from the other samples analysed. The trace element compositions of zircon grains dated 1300–1100 Ma constrain them to the granitoid, nepheline syenite and syenite pegmatite and dolerite parent rock fields (Fig. 8). Sample DD3 (total of 11 grains analysed) and DD5 (total of 5 grains analysed) yielded scattered detrital zircon minerals from 2400 Ma up to c. 3400 Ma (Fig. 6-7). These older zircon grains have trace element compositions matching a granitic protolith.
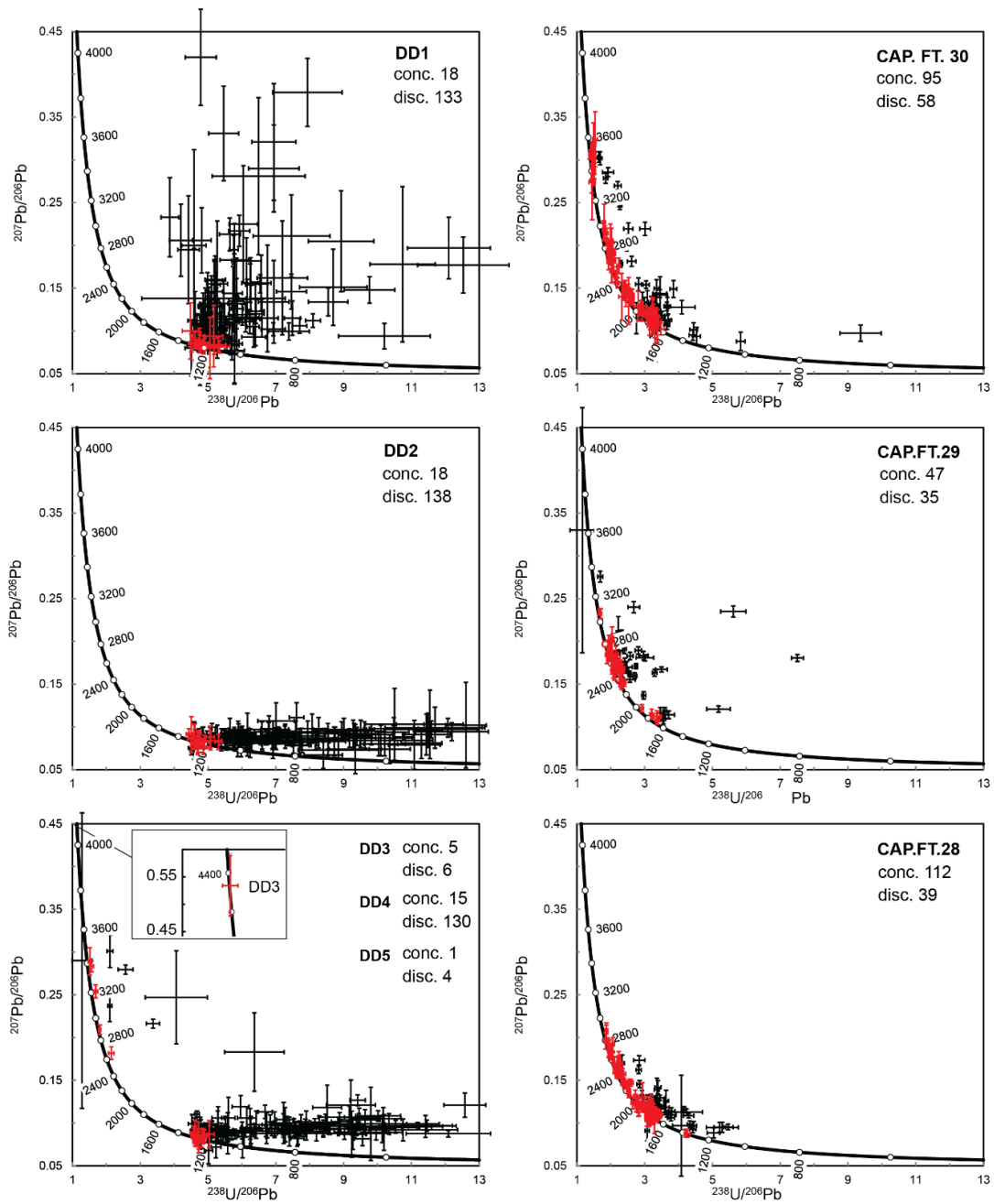
Fig. 6. Tera-Wasserburg Concordia diagrams for the studied samples. Concordant ages are shown in red, discordant in black (*Isoplot4.15*; Ludwig, 2003). Concordant and discordant number of grains are indicated. Samples DD3-4-5 are plotted together due to the scarce number of grains obtained from each. Some of the most discordant grains are not shown.

124
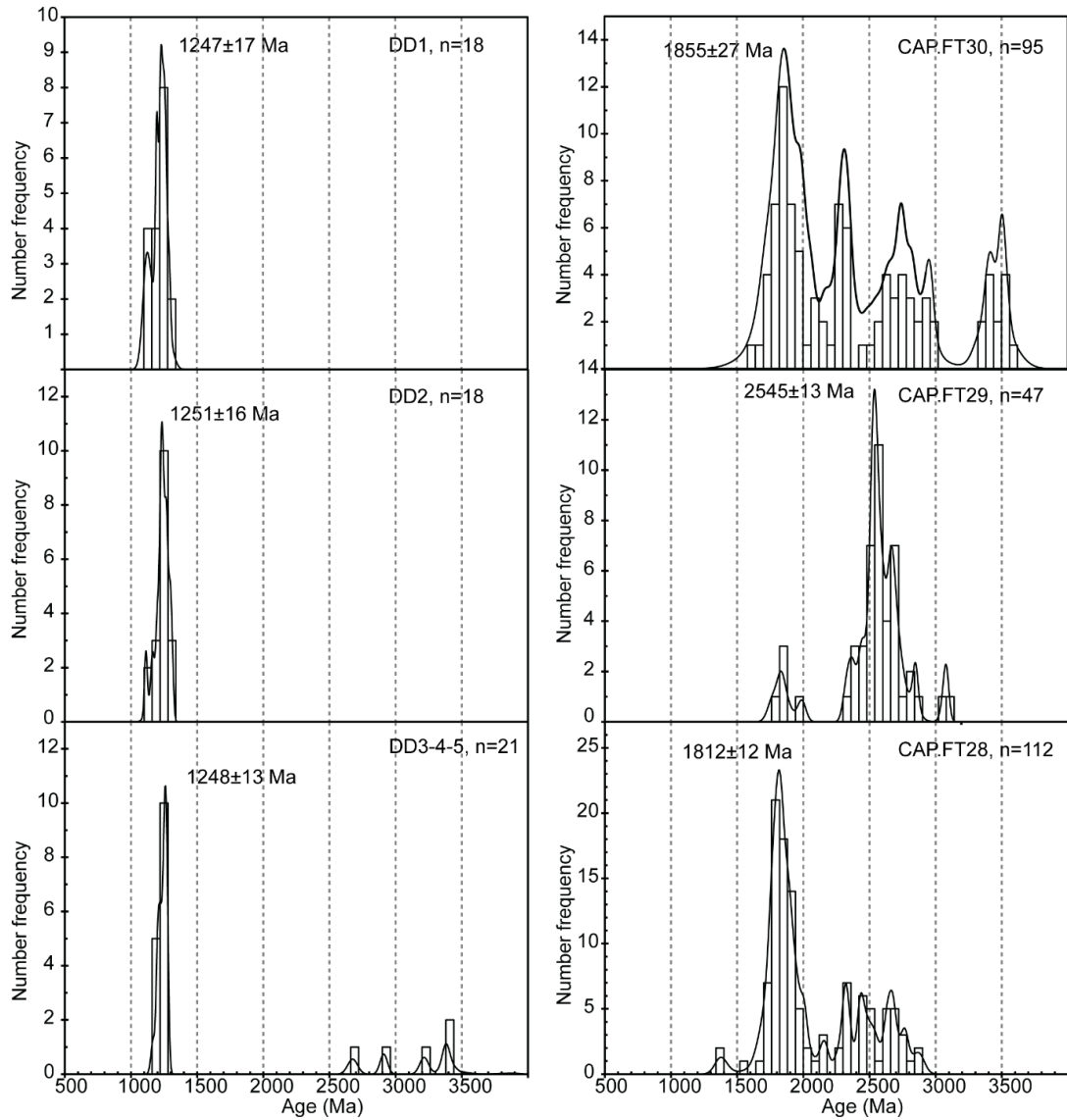
Fig. 7. Probability density plots (PDP) of the ≥90% concordant zircon (excluding the Hadean zircons of c. 4320 Ma). Weighted mean ages for mineral populations are calculated with *Isoplot4.15* (Ludwig, 2003). Populations have a bin width of 60 Ma. Samples DD3-4-5 are plotted together due to the small number of zircon grains recovered in DD3-5.
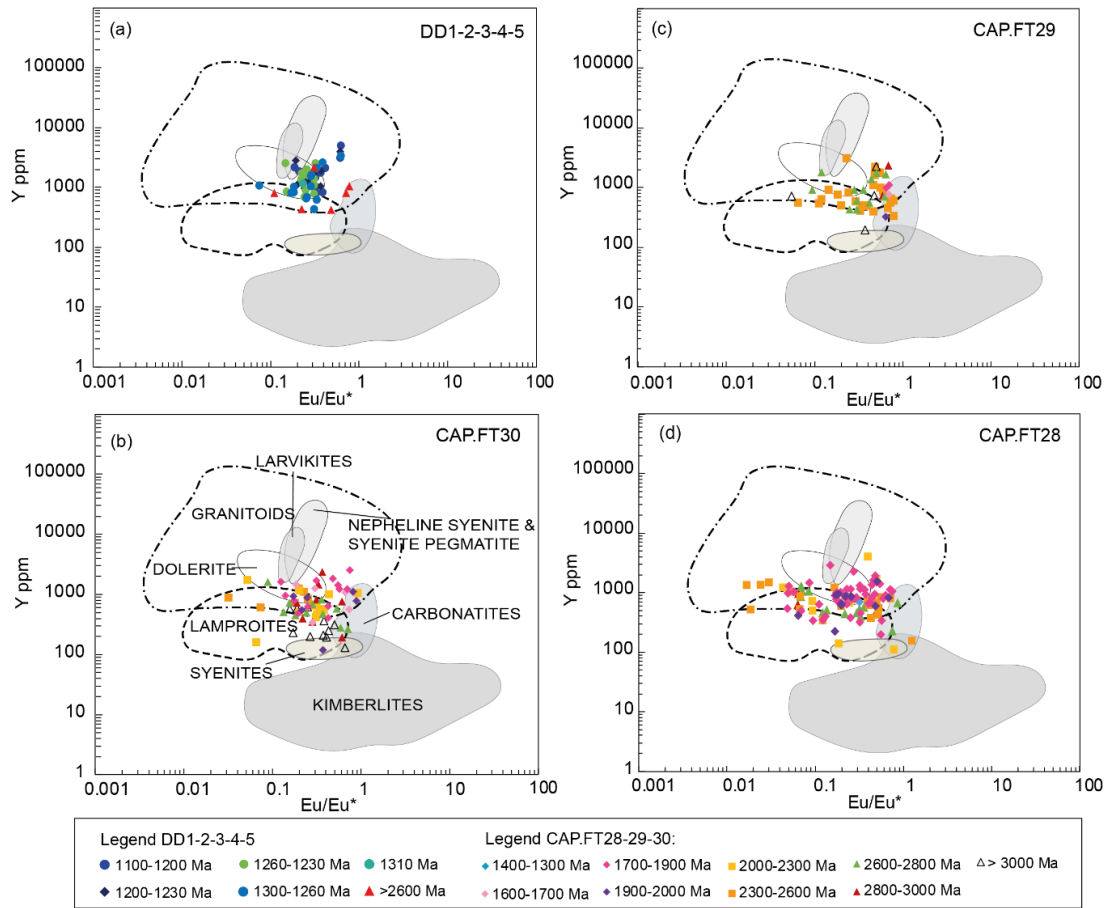
Fig. 8. Discrimination diagrams for the zircon trace elements indicated the mineral's parent rocks. Parental rock compositional fields have been modified from the discrimination diagrams established by Belousova et al. (2002). Analyses are colour coded by age groups relevant to major magmatic events that occurred across the Capricorn Orogen area.

6. Discussion

6.1 Zircon U-Pb age data for the Collier Basin and implications for sediment provenance

To track sediment transport in the Capricorn Orogen during deposition of the Collier Basin sedimentary rocks, new detrital zircon geochronology data obtained in this study were compared with published data from relevant older sediment reservoirs and regional crystalline basement.

126

6.1.1 Provenance of the Backdoor and Calyie formations

Sample CAP.FT28 displays a dominant mode of 1900–1700 Ma that corresponds with extensive magmatism of the Moorarie Supersuite (Fig. 9; Johnson et al., 2013). Zircon grains of this age are preserved widely across the Capricorn Orogen Paleoproterozoic basins (Cutten et al., 2016). Derivation via recycling of older sedimentary rocks is suggested by the presence of a broad Archean to early Palaeoproterozoic subpopulation in sample CAP.FT28 which are present in both the older Capricorn Group (Blair Basin) and in the Irregully Formation (Edmund Basin) age spectra, along with the dominant 1900–1700 Ma population (Fig. 9; Table 2). Moreover, the Capricorn Group and the Irregully Formation were both exposed to the north-northwest of the Collier Basin, in the Pingandy Shelf, a horst structure limited by the regional Lyon River Fault and are thus consistent with the paleocurrent data that indicate derivation from the northwest and northeast directions (Martin et al., 2008). Primary erosion of Rudall Complex magmatic suites might be partially reflected in the age group 1700–1900 Ma of sample CAP.FT28, given that part of the paleocurrent data broadly indicate northeast (Martin et al., 2008), and the overlap in the age of magmatism (1890–1750 Ma; Bagas, 2004) with the Moorarie Supersuite (Johnson et al., 2013). However, the Rudall Complex is located more than 1000 km distant toward the north east from the Capricorn Orogen and sediment transportation from that region within a delta is considered unlikely. Moreover, there are no indications of other Capricorn Orogen basins yielding a Rudall Complex signature. Furthermore, primary transportation from the Rudall Complex would be opposite to the overall progradational direction of the Backdoor Formation delta complex, interpreted to be eastward (Cutten et al., 2016). Therefore, primary recycling of underlying Edmund Basin sediments and partial recycling of the Capricorn Group likely sourced the basal sediments of the Collier Basin.

Sample CAP.FT29 (Backdoor Formation) displays a dominant detrital zircon population aged 2600–2450 Ma that corresponds with crystallization of the Halfway Gneiss, in the Gascoyne Complex (Dentith et al., 2014; Fig. 9). The sample also includes an older Archean secondary population, spanning 2750–2650 Ma within the age of the Yilgarn Craton magmatism, and a minor group, aged 1750–1850 Ma, coinciding with the Moorarie Supersuite. These ages altogether could suggest

derivation from south (Gascoyne Complex and Yilgarn Craton). However, the results of the K-S similarity tests for sample CAP.FT29 and paleocurrent data (Martin et al., 2008), are more consistent with predominant recycling of the underlying Coodardoo Formation and Ullawarra formations (Edmund Basin) and erosion of Ashburton Basin sedimentary rocks (Fig. 9; Table 2). Minor contributions from the Ashburton Basin are suggested by the scarce number of grains aged 2500–2400 Ma, in comparison with more prominent contributions from reworking of the Ullawarra and Coodardoo formations (2600–2450 Ma). Variation in the Backdoor Formation sources are demonstrated by the strikingly dissimilar spectra of samples CAP.FT28 and CAP.FT29. Moreover, K-S tests (Table2) demonstrate poor similarity between the samples analysed in this study and samples analysed from the western part of the Collier Basin (Martin et al., 2008). This evidence might suggest an increase in the source complexity towards east, according to the interpreted progradation direction of the delta system (Martin et al., 2008).

Sample CAP.FT30 has a polymodal detrital zircon age spectrum that suggests substantial source mixing and/or sediment recycling during its deposition (Fig. 9). Moreover, K-S tests find poor statistical similarity between sample CAP.FT30 and samples from the underlying Backdoor Formation (Fig. 9; Table 2). Consequently, during deposition of the Calyie Formation, new sources were involved in supplying the sediments in comparison to the Backdoor Formation. The dominant detrital zircon population in CAP.FT30 ranges between 1900 and 1750 Ma, which extend slightly older than the crystallization age of the Moorarie Supersuite (1850–1750 Ma; Fig. 9). Some of the detrital zircon grains from this age interval are interpreted to have derived from the Rudall Complex that records protracted magmatism at c. 1790 Ma (Bagas, 2004). This interpretation matches with the paleocurrent data for the Calyie Formation indicating north-eastern, and the suggestion of a tectonic reactivation of exotic crustal units, located east than the Capricorn Orogen (Cutten et al., 2016). Sample CAP.FT30 yields other relevant age intervals at 2400–2200 Ga, 2800–2600 Ga, and 3600–3400 Ga that are widely preserved in Archean and Palaeoproterozoic units from both the Pilbara and Yilgarn cratons (Fig. 9). Detrital zircons dated between 2800 and 2600 Ga approximate the detrital zircon age record of the Yilgarn Craton granites to the south and of the Hamersley Basin to the north (Trendall et al., 2004). Crystalline basement

units exposed in the Pilbara Craton, have ages of c. 3500 Ga, and approximate the oldest detrital zircons age group (Warrawoona Group, Buick et al., 1995).

The K-S test demonstrates similarities between the CAP.FT30 and the Calyie Formation samples analysed in the western part of the Collier Basin by Martin et al. (2008; Table 2). However, the detrital zircon population of CAP.FT30 is more strongly polymodal in comparison to the samples from Martin et al. (2008) that are more bimodal and characterized by a dominant age mode at 1750 Ma (Fig. 9). Distinct variability of sources might have characterized the deposition of the Calyie Formation with sediments deriving from both the northwest and northeast. Another potential explanation is the existence of distinct delta systems (fed by different catchments) during accumulation of the Calyie Formation, which would explain the variable paleocurrent patterns recorded by Martin et al., (2008) and the differences observed between the age spectra in the western and central part of the basin.

The detrital zircon grains of samples CAP.FT28-29-30 show similar trace element compositions that ultimately suggest that they originated from compositionally similar felsic sources (e.g., granites). Some of these sources were likely located in the Gascoyne Complex, (Moorarie Supersuite, Halfway Gneiss, Bertibubba Supersuite, and Dalgaringa Supersuite). However, the sediments of the Collier Basin were mainly sourced by Palaeoproterozoic to middle Mesoproterozoic basins that hosted detritus derived from the Gascoyne Complex. Thus, the Collier Basin sediments are the result of at least two cycles of sedimentary recycling.

The geochemical plots that were used to assess the protolith composition for the detrital zircon grains ultimately did not bring a significant contribution to the provenance interpretation. Rather the plots show large scatter of data and indicate a granitoid composition for the majority of the minerals examined.
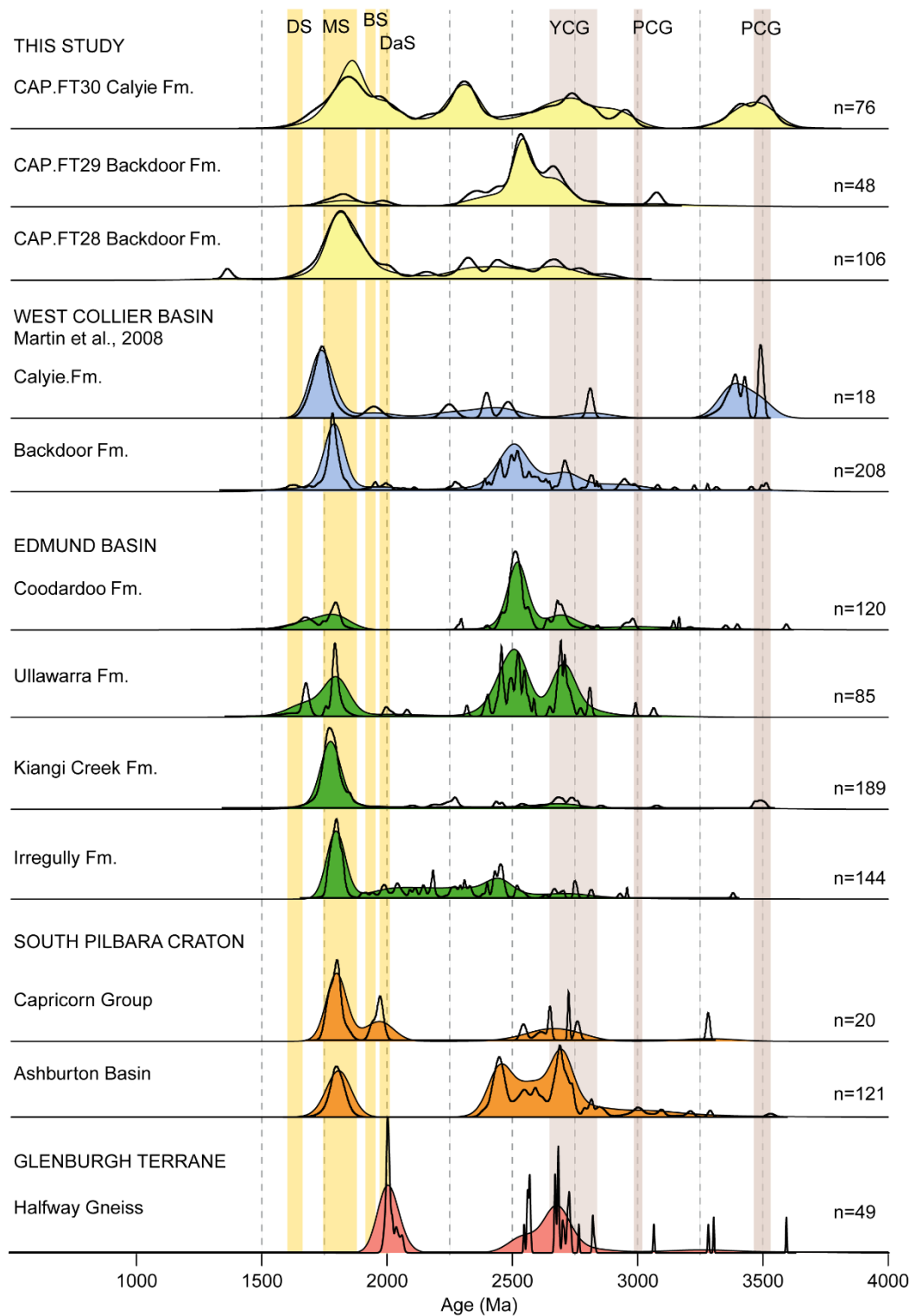
Fig. 9. Comparison of detrital zircon age data for the Collier Basin of this study (CAP.FT28, CAP.FT29, CAP.FT30) with selected detrital zircon data from published literature. The data are displayed with colour-filled kernel density plots (KDP; Provenance software, Vermeesch et al., 2016) and with probability density plots

represented by a black line (Ludwig, 2003). The potential sources are listed according to the geographical location in the Capricorn Orogen and by age with younger sources towards the top. Edmund Basin and west Collier Basin detrital zircon data (Martin et al., 2008). Ashburton Basin (Nelson, 2004a; 2004b; 2004c; Nelson, 2004d); Capricorn Group (Nelson, 2004e). Halfway Gneiss (Nelson, 2002a; 2002b; 2002c; Wingate, 2017). Vertical coloured bars indicate characteristic ages of regionally significant crystalline units. DS- Durlacher Supersuite, MS- Moorarie Supersuite, BS- Bertibubba Supersuite, DS- Dalgaringa Supersuite, YCG- Yilgarn Craton granites, PCG- Pilbara Craton granites (Cawood and Tyler, 2004; Johnson et al., 2013; Dentith et al., 2014).

6.1.2 Provenance of the Ilgarari Formation

Detrital zircon populations recovered from samples DD1 to DD2 and DD4 are dissimilar in age (1300-1100 Ma) in comparison to other detrital zircon grains analysed in previous studies across the Capricorn Orogen and yield relatively high Y concentrations (> 800 ppm; Fig. 5 & 8). Given the large age range of c. 200 Ma of the zircon populations, and the elongated and rounded shapes of the grains, showing some degree of transportation, the origin of the detrital zircons is difficult to reconcile with derivation from local tuffs. The youngest detrital zircons (1150–1100 Ma) found in samples DD1, DD2 and DD4 establish a maximum depositional age for the Ilgarari Formation at c. 1117 ± 34 Ma (MSWD=1, n=5), and provides a new temporal constraint for the uppermost Collier Basin sediments. Potential sources for detrital zircons within the age interval 1300–1100 Ma haven't been identified in the Capricorn Orogen region. Paleocurrent data for the Ilgarari Formation suggest transportation from the south–southeast (Martin et al., 2008). The most proximal known crystalline sources available within the 1300–1100 Ma age range are the Musgrave Province in central Australia, and more distal Albany–Fraser Orogen (AFO), on the southern and eastern margin of the Yilgarn Craton. Both the AFO and Musgrave Province exhibit significant rock-forming events in the 1300–1100 Ma interval (Kirkland et al., 2011; Reid et al., 2013; Howard et al., 2015; Fig. 10). Dispersal of AFO-derived sediment occurred northward in the Neoproterozoic (Ksienzyk et al., 2012) and Phanerozoic (Cawood & Nemchin, 2000), with detrital populations commonly characterised by both a 1300–1100 Ma, and a typically subordinate 1700–1600 Ma zircon age groups (Spaggiari et al., 2015; Barham et al., 2018). An exception to the two age

subpopulations of AFO-derived detritus was observed in the Perth Basin, where sediments lack the older Palaeoproterozoic component (Cawood & Nemchin, 2000; Lewis, 2017). However, given the predominant association of the 1300–1100 Ma age group with the c. 1600 Ma age group in Neoproterozoic basins linked to the AFO (Veevers et al., 2005), it is thought unlikely that the AFO supplied material to the unimodal Mesoproterozoic Ilgarari Formation.

During the early Neoproterozoic the Musgrave Province supplied sediments yielding a c. 1200 Ma unimodal age component to the Amadeus Basin (north) and West Officer Basin (northwest; Fig. 10; Reid et al., 2013; Haines et al., 2016). The unimodal age spectra observed in the two basins are comparable to the ages recovered in the Ilgarari Formation (Fig. 10). Therefore, it is more likely the Musgrave Province was the principal source for the 1300–1100 Ma detrital zircons found in the Ilgarari Formation, given overlap with crystalline rocks associated with the 1345–1293 Ma Mount West Orogeny, the 1220–1150 Ma Musgrave Orogeny and the 1085–1050 Ma Giles Event and the demonstrated dispersal of detritus during orogenic/tectonic events (Kirkland et al., 2011; Reid et al., 2013; Howard et al., 2015).

The Kolmogorov-Smirnov (K-S) test does not recognise any statistical similarity between the pooled DD1-5 detrital zircon age population and those from the Amadeus Basin or West Officer Basin samples (Table 2). This may be attributed to strong unimodal characteristics with slightly different Musgrave Province-associated age populations. The Ilgarari Formation yields a dominant age peak between 1260–1220 Ma, which is older than the dominant age peaks of the West Officer and Amadeus basins ranging 1200–1100 Ma (Fig. 10). A possible interpretation is that the crystalline units eroded from the Musgrave Province at the time of the Ilgarari Formation accumulation were slightly older and probably geographically distinct from the sources eroded in the Neoproterozoic West Officer and Amadeus basins (later exhumed younger crystalline material). The dominant detrital zircon group found in the Ilgarari Formation is older than the 1220–1150 Ma Pitjantjatjara Supersuite emplaced during the Musgrave Orogeny that covers half of the Musgrave Province (Reid et al., 2013; Howard et al., 2015). Thus, the older detrital zircon components, up to 1270 Ma, could correspond to crystalline bodies from the Pitjantjatjara Supersuite, now covered or entirely eroded. The presence of zircon grains aged 1310–1297 Ma in

the Ilgarari Formation samples analysed may be indicative of minor erosion of the 1345–1293 Ma Wankanki Supersuite, intruded during the Mount West Orogeny (Reid et al., 2013; Howard et al., 2015). Limited concordant Archean grains dated 3500–2600 Ma were also found in two of the samples analysed (DD3 and DD5) from the Ilgarari Formation (Fig. 10). The origin of these grains remains enigmatic due to their scarcity but likely derive from equivalent in age crystalline sources in the Yilgarn Craton (Fig. 10).

The West Officer Basin yields detrital zircon ages within the interval 1290–1110 Ma, overlapping with distinctive age intervals of the Ilgarari Formation, which may indicate a common origin from the Musgrave Province, or recycling of the broader sediment footprint related to the older Ilgarari Formation (Fig. 10). The finding of late Mesoproterozoic Musgrave-derived sediments in the Ilgarari formation demonstrate that continental-scale sediment dispersal occurred not just during the Neoproterozoic (e.g. 570–530 Ma central Australian Petermann Orogeny; Haines et al., 2016), but also earlier, after the 1220–1150 Ma Musgrave Orogeny (Howard et al., 2015). Therefore, widespread sediment dispersal from the Musgrave Province occurred repeatedly during intracratonic orogenic events.

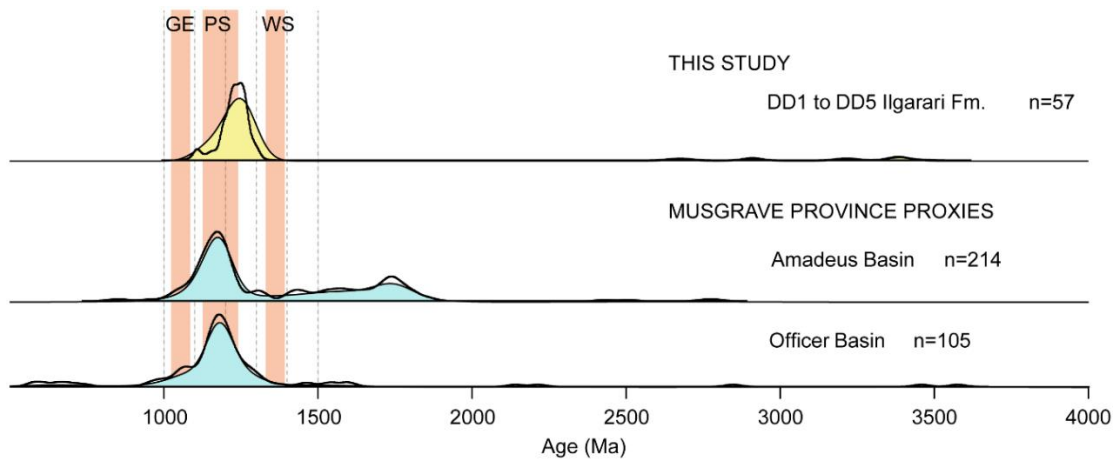Fig. 10. Detrital zircon ages from the Ilgarari Formation (samples DD1 to DD5) and potential provenance-equivalent samples. The data are displayed with kernel density plots (KDP) represented by coloured fills (Provenance software, Vermeesch et al., 2016) and probability density plots as a black line (Ludwig, 2003). Detrital zircons samples from the Officer Basin; 1706568 and 1661077 from Reid et al. (2013). Detrital

zircons samples from the basal Amadeus Basin; 199404, 199407 and 199408 from Haines et al. (2016). Musgrave Province magmatic events: GE- Giles Event, PS-Pitjantjatjara Supersuite; WS- Wankanki Supersuite (Howard et al., 2015).

	DD1-5	CAP.FT 30	CAP.FT 29	CAP.FT 28	Amadeus Basin	Officer Basin	Calyie Fm.	Backdoor Fm.	Coodardoo Fm.	Ullawarra Fm.	Kiangi Creek Fm.	Irregully Fm.	Capricorn Group	Ashburton Basin
DD1-5		0.000	0.000	0.000	0.000	0.000	0.000	0.000	0.000	0.000	0.000	0.000	0.000	0.000
CAP.FT30	0.000		0.001	0.004	0.000	0.000	**0.298**	**0.065**	0.001	0.043	0.000	0.001	0.013	0.000
CAP.FT29	0.000	0.001		0.000	0.000	0.000	0.046	0.004	**0.183**	**0.123**	0.000	0.000	0.000	**0.498**
CAP.FT28	0.000	0.004	0.000			0.000	0.047	0.000	0.000	0.000	0.000	**0.113**	**0.887**	0.000
Amadeus Basin	0.000	0.000	0.000	0.000		0.000	0.000	0.000	0.000	0.000	0.000	0.000	0.000	0.000
Officer Basin	0.000	0.000	0.000	0.000	0.000		0.000	0.000	0.000	0.000	0.000	0.000	0.000	0.000
Calyie Fm.	0.000	**0.298**	0.046	0.047	0.000	0.000		0.094	0.103	0.074	0.070	0.036	0.237	0.085
Backdoor Fm.	0.000	**0.065**	0.004	0.000	0.000	0.000	**0.094**		0.002	0.578	0.000	0.065	0.034	0.004
Coodardoo Fm.	0.000	0.001	**0.183**	0.000	0.000	0.000	**0.103**	0.002		0.202	0.000	0.000	0.001	0.015
Ullawarra Fm.	0.000	0.043	**0.123**	0.000	0.000	0.000	**0.074**	**0.578**	**0.202**		0.000	0.000	0.008	0.066
Kiangi Creek Fm.	0.000	0.000	0.000	0.000	0.000	0.000	**0.070**	0.000	0.000	0.000		0.000	0.121	0.000
Irregully Fm.	0.000	0.001	0.000	**0.113**	0.000	0.000	0.036	0.000	0.000	0.000	0.000		0.247	0.000
Capricorn Group	0.000	0.013	0.000	**0.887**	0.000	0.000	**0.237**	0.034	0.001	0.008	**0.121**	**0.247**		0.000
Ashburton Basin	0.000	0.000	**0.498**	0.000	0.000	0.000	**0.085**	0.004	0.015	**0.066**	0.000	0.000	0.000	

Table 2. Kolmogorov-Smirnov (K-S) statistical test results. The table shows the probability P-value calculated with the statistical tool from Guynn and Gehrels (2010). P-values <0.05 indicate that the difference between the populations tested are statistically significant and thus that they originate from distinct sources. P-values ≥ 0.05 indicate statistical similarity between the two populations that imply a degree of shared parenthood/similar sources (Massey, 1951).

6.2 Implication for intracontinental rifting in central and Western Australia

The Collier Basin is characterized by an overall transgressive sequence that likely evolved during intracratonic extensional activity of the Capricorn Orogen (this study; Wingate et al., 2004; Martin et al., 2008; Cutten et al., 2016). The basin deepens changing from a deltaic depositional environment to a deep marine environment through its Backdoor, Calyie and Ilgarari formations. At the top of the preserved Collier Basin sequence, analysis of drill core DD14IL014 and the detrital zircon grains recovered from it, indicate that the middle Ilgarari Formation accumulated in a marine shelf environment after a major switch in transportation direction, with transportation of detritus from the east-southeast, herein interpreted to be associated with the Musgrave Province (Fig. 11). Widespread mafic intrusions in the Capricorn Orogen (Kulkatharra Dolerite) are contemporaneous with deposition of the Backdoor Formation (peperite margins at c. 1070 Ma; Martin, 2003; Wingate et al., 2004) and

coeval to the c. 1080 Ma Warakurna Large Igneous Province, which intruded the Musgrave Province, during the 1090–1040 Ma Giles Event (Wingate et al., 2004; Howard et al., 2015). The extensional episode was linked to the development of a large intracratonic rift, the Ngaanyatjarra Rift, between central and Western Australia, coeval to extensional movements during the 1090–1040 Ma Giles Event (Howard et al., 2015). The Ngaanyatjarra Rift represents an ideal conduit for the distribution of Musgrave Province sediments to the Collier Basin, with sediment travelling along the rift axis more than 1000 km (Fig. 11). The Ilgarari Formation in the Collier Basin may thus represent a small part of a larger depositional system tracing an intracratonic rift between Western Australia and central Australia (Fig. 11). In this context, the marine transgression identified in the Ilgarari Formation sediments may be correlated with rift expansion toward the northwest; while deposition of equivalents to the Ilgarari Formation could have initiated to the southeast in the proximity of the Musgrave Province in the early phases of the 1090–1040 Ma Giles Event. Following the rift expansion, the Ilgarari Formation sedimentary system encompassed the Musgrave Province and reached the Capricorn Orogen.
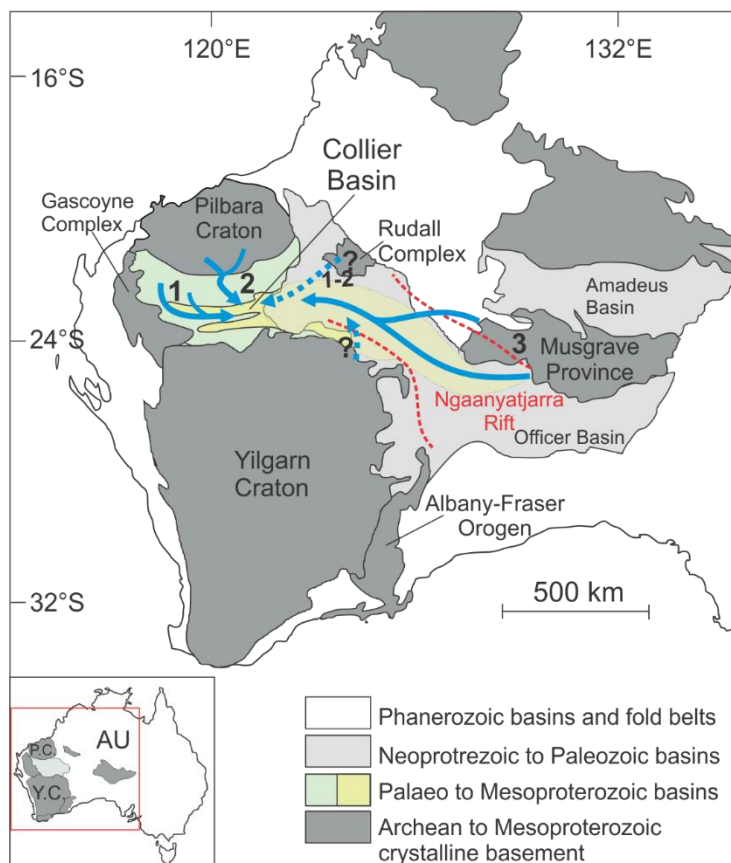

Fig. 11. Depositional history of the Collier Basin and its sources in central and Western Australia at c. 1100 Ma. Numbers indicate the order in which the sources contributed to the sedimentation, from the lowermost sequence to the top: 1- Backdoor Formation; 2- Calyie Formation, 3- Ilgarari Formation. Inferred location of the Ngaanyatjarra Rift is reported.

7. Conclusions

Detrital zircon geochronology indicates that sediments of the Collier Basin were initially (Backdoor Formation) largely recycled from the southern Pilbara Craton margin (Blair Basin; Ashburton Basin), from the underlying Edmund Basin and possibly derived from the Rudall Complex. Deposition in the overlying Calyie Formation was characterized by northward expansion of the sediment catchment systems to encompass the Blair Basin, the Ashburton Basin, the Hamersley Basin, the crystalline Pilbara Craton rocks and the Rudall Complex. The deposition for both the Backdoor Formation and Calyie Formation took place in a deltaic setting with episodes of basin shallowing and deepening. Variations in the sediment source rocks from east to west are interpreted to have occurred for both the Backdoor and Calyie formations. The Calyie Formation is interpreted to record strong sediment mixing due to the development of interdigitating deltas prograding from both the northwest and northeast, given the large number of sources represented in the sample analysed. The trace element compositions of the detrital zircons were similar for samples CAP.FT28, CAP.FT29 and CAP.FT30 and indicate compositional similarity of the primary sources for the sediments (mainly granites).

The detrital zircon population of the Ilgarari Formation is distinct from the underlying formations and has a unimodal age peak of 1300–1000 Ma, which suggests primary sourcing from a distinct region, interpreted to coincide with the Musgrave Complex. A maximum depositional age for the formation is established at 1117 ± 34 Ma (MSWD=1, n=5), from the youngest detrital zircon grains recovered. Deposition within the intracratonic Collier Basin took place after a switch from compressional to extensional tectonics. The sedimentation was coeval with the emplacement of the 1080 Ma Warakurna Large Igneous Province (locally called Kulkatharra Dolerite) during the 1090–1040 Ga Giles Event, and the spread of the intracontinental Ngaanyatjarra Rift (Wingate et al., 2004; Howard et al., 2015). The Ngaanyatjarra Rift spread from the southeast towards the northwest between the Musgrave Province and the Capricorn Orogen and is considered the carrier of exotic sediment to the Capricorn Orogen region. According to this, the Collier Basin had many catchments over its depositional history, and the area occupied by the basin and its catchments may have been larger than what has been estimated before. Moreover, it may be comparable to the extent of

the overlying Officer Basin, and not solely limited to the Capricorn Orogen in Western Australia.

Acknowledgements

References

Anders, E. & Grevesse, N. (1989). Abundances of the elements: Meteoritic and solar. *Geochimica et Cosmochimica Acta*, 53, 197-214.

Bagas, L. (2004). Proterozoic evolution and tectonic setting of the northwest Paterson Orogen, Western Australia. *Precambrian Research*, 128, 475-496.

Barham, M., Reynolds, S., Kirkland, C. L., O'Leary, M. J., Evans, N. J., Allen, H. J., Haines, P. W., Hocking, R. M. & McDonald, B. J. (2018). Sediment routing and basin evolution in Proterozoic to Mesozoic east Gondwana: A case study from southern Australia. *Gondwana Research*, 58, 122-140.

Belousova, E. A., Griffin, W. L., O'Reilly, S. Y. & Fisher, N. I. (2002). Igneous zircon: Trace element composition as an indicator of source rock type. *Contributions to Mineralogy and Petrology*, 143, 602-622.

Bodorkos, S., Stern, R. A., Kamo, S., Corfu, F. & Hickman, A. H. (2009). OG1: A Natural Reference Material for Quantifying SIMS Instrumental Mass Fractionation of Pb Isotopes During Zircon Dating. *American Geophysical Union, Fall Meeting* 2009, abstract #V33B-2044.

Buick, R., Thornett, J. R., McNaughton, N. J., Smith, J. B., Barley, M. E. & Savage, M. (1995). Record of Emergent Continental-Crust Similar-to-3.5 Billion Years Ago in the Pilbara Craton of Australia. *Nature*, 375, 574-577.

Cawood, P. A. & Nemchin, A. A. (2000). Provenance record of a rift basin: U/Pb ages of detrital zircons from the Perth Basin, Western Australia. *Sedimentary Geology,* 134, 209-234.

Cawood, P. A. & Tyler, I. M. (2004). Assembling and reactivating the Proterozoic Capricorn Orogen: Lithotectonic elements, orogenies, and significance. *Precambrian Research,* 128, 201-218.

Cutten, H., Johnson, S., Thorne, A., Wingate, M., Kirkland, C., Belousova, E., Blay, O. & Zwingmann, H. (2016). Deposition, Provenance, Inversion History and Mineralization of the Proterozoic Edmund and Collier Basins, Capricorn Orogen. Geological Survey Western Australia, Report 127.

Dentith, M., Johnson, S. P., Evans, S., Aitken, A., Joly, A., Thiel, S. & Tyler, I. M. (2014). A magnetotelluric traverse across the eastern part of the Capricorn Orogen. Geological Survey of Western Australia, Report 135.

Fedo, C. M. (2003). Detrital Zircon Analysis of the Sedimentary Record. *Reviews in Mineralogy and Geochemistry*, 53, 277-303.

Griffin, W. L., Belousova, E. A., Shee, S. R., Pearson, N. J. & Reilly, S. Y. O. (2004). Archean crustal evolution in the northern Yilgarn Craton: U – Pb and Hf-isotope evidence from detrital zircons. *Precambrian Research,* 131, 231-282.

Guo, L., Zhang, H. F., Harris, N., Xu, W. C. & Pan, F. B. (2017). Detrital zircon U–Pb geochronology, trace-element and Hf isotope geochemistry of the metasedimentary rocks in the Eastern Himalayan syntaxis: Tectonic and paleogeographic implications. *Gondwana Research*, 41, 207-221.

Guynn J. Gehrels G.E., 2006, Comparison of detrital zircon age distribution using the K-S test: University of Arizona LaserChron Center online manual, 16 p.

Haines, P. W., Kirkland, C. L., Wingate, M. T. D., Allen, H., Belousova, E. A. & Grau, Y. (2016). Tracking sediment dispersal during orogenesis: A zircon age and Hf isotope study from the western Amadeus Basin, Australia. Gondwana Research, 37, 324-347.

Haughton, P. D. W., Todd, S. P. & Morton, A. C. (1991). Sedimentary provenance studies. Developments in Sedimentary Provenance Studies (vol. 57, pp. 1-11). London: Geological Society, Special Publications.

Howard, H. M., Smithies, R. H., Kirkland, C. L., Kelsey, D. E., Aitken, A., Wingate, M. T. D., Quentin de Gromard, R., Spaggiari, C. V. & Maier, W. D. (2015). The burning heart - The Proterozoic geology and geological evolution of the west Musgrave Region, central Australia. Gondwana Research, 27, 64-94.

Jackson, S. E., Pearson, N. J., Griffin, W. L. & Belousova, E. A. (2004). The application of laser ablation-inductively coupled plasma-mass spectrometry to in situ U-Pb zircon geochronology. *Chemical Geology,* 211, 47-69.

Johnson, S. P., Sheppard, S., Rasmussen, B., Wingate, M. T. D., Kirkland, C. L., Muhling, J. R., Fletcher, I. R. & Belousova, E. A. (2010). The Glenburgh Orogeny as a record of Palaeoproterozoic continent-continent collision. Geological Survey of Western Australia, Record 2010/5.

Johnson, S. P., Sheppard, S., Rasmussen, B., Wingate, M. T. D., Kirkland, C. L., Muhling, J. R., Fletcher, I. R. & Belousova, E. A. (2011). Two collisions, two sutures: Punctuated pre-1950 Ma assembly of the West Australian Craton during the Ophthalmian and Glenburgh Orogenies. *Precambrian Research*, 189, 239-262.

Johnson, S. P., Thorne, A. M., Tyler, I. M., Korsch, R. J., Kennett, B. L. N. N., Cutten, H. N., Goodwin, J., Blay, O., Blewett, R. S., Joly, A., Dentith, M. C., Aitken, A. R. A. A., Holzschuh, J., Salmon, M., Reading, A., Heinson, G., Boren, G., Ross, J.,

Costelloe, R. D. & Fomin, T. (2013). Crustal architecture of the Capricorn Orogen, Western Australia and associated metallogeny. *Australian Journal of Earth Sciences*, 60, 681-705.

Kirkland, C. L., Spaggiari, C. V., Pawley, M. J., Wingate, M. T. D., Smithies, R. H., Howard, H. M., Tyler, I. M., Belousova, E. A. & Poujol, M. (2011). On the edge: U-Pb, Lu-Hf, and Sm-Nd data suggest reworking of the Yilgarn craton margin during formation of the Albany-Fraser Orogen. *Precambrian Research*, 187, 223-247.

Korhonen, F. J. & Johnson, S. P. (2015). The role of radiogenic heat in prolonged intraplate reworking: The Capricorn Orogen explained? *Earth and Planetary Science Letters,* 428, 22-32.

Ksienzyk, A. K., Jacobs, J., Boger, S. D., Košler, J., Sircombe, K. N. & Whitehouse, M. J. (2012). U–Pb ages of metamorphic monazite and detrital zircon from the Northampton Complex: evidence of two orogenic cycles in Western Australia. *Precambrian Research*, 198-199, 37-50.

Kylander-Clark, A. R. C., Hacker, B. R. & Cottle, J. M. (2013). Laser-ablation split-stream ICP petrochronology. *Chemical Geology*, 345, 99-112.

Lewis, C. J. (2017). SHRIMP U-Pb detrital zircon ages from GSWA Harvey 1, Western Australia. Geoscience Australia, 2017/20.

Ludwig, K. R. (2003). Isoplot 3.00: A geochronological toolkit for Microsoft Excel. Berkeley Geochronology Center Special Publication, 39, 91-445.

Martin, D. M. (2003). Peperite in the Backdoor Formation and its significance to the age and tectonic evolution of the Bangemall Supergroup. Geological Survey of Western Australia Annual Review 2002-03, 53-59.

Martin, D. M. B. & Thorne, A. M. (2004). Tectonic setting and basin evolution of the Bangemall Supergroup in the northwestern Capricorn Orogen. *Precambrian Research,* 128, 385-409.

Martin, D. M. B., Sircombe, K. N., Thorne, A. M., Cawood, P. A. & Nemchin, A. A. (2008). Provenance history of the Bangemall Supergroup and implications for the Mesoproterozoic palaeogeography of the West Australian Craton. *Precambrian Research*, 166, 93-110.

Massey, F. J. (1951). The Kolmogorov-Smirnov Test for Goodness of Fit. *Journal of the American Statistical Association*, 46, 68-78.

Nelson, D. R. (2002a). 169050: leucocratic gneiss, Mount Remarkable Bore. Geochronology dataset 124; in Compilation of geochronology.

Nelson, D. R. (2002b). 169048: leucocratic gneiss, Mount Remarkable Bore. Compilation of geochronology data, 2001: Western Australia.

Nelson, D. R. (2002c). 169048: leucocratic gneiss, Mount Remarkable Bore. Compilation of geochronology data, 2001: Western Australia.

Nelson, D. R. (2004a). Ferruginous sandstone, Miringee Well sample 169084.1, Ashburton Basin. Geochronology Record 43, Geological Survey Western Australia.

Nelson, D. R. (2004b). Pebbly sandstone, sample 169081, Ashburton Basin. Geochronology Record 116, Geological Survey Western Australia.

Nelson, D. R. (2004c). Crystal vitric tuff, Koonong Pool, sample 148922, Ashburton Basin. Geochronology Record 249, Geological Survey Western Australia.

Nelson, D. R. (2004d). Sandstone Meteorite Bore sample 169082, Ashburton Basin. Geochronology Record 42, Geological Survey Western Australia.

Nelson, D. R. (2004e). Coarse lithic sandstone, sample 148925, Capricorn Group. Geochronology Record 250, Geological Survey Western Australia.

Paton, C., Woodhead, J. D., Hellstrom, J. C., Hergt, J. M., Greig, A. & Maas, R. (2010). Improved laser ablation U-Pb zircon geochronology through robust downhole fractionation correction. Geochemistry, Geophysics, Geosystems, 11, 3.

Reid, A., Keeling, J., Boyd, D., Belousova, E. & Hou, B. (2013). Source of zircon in world-class heavy mineral placer deposits of the Cenozoic Eucla Basin, Southern Australia from LA-ICPMS U-Pb geochronology. Sedimentary Geology, 286-287, 1-19.

Sheppard, S., Occhipinti, S. A. S. A. & Nelson, D. R. (2005). Intracontinental reworking in the Capricorn Orogen, Western Australia: The 1680-1620 Ma Mangaroon Orogeny. *Australian Journal of Earth Sciences*, 52, 443-460.

Sheppard, S., Rasmussen, B., Muhling, J. R., Farrell, T. R. & Fletcher, I. R. (2007). Grenvillian-aged orogenesis in the Palaeoproterozoic Gascoyne complex, Western Australia: 1030-950Ma reworking of the Proterozoic Capricorn Orogen. *Journal of Metamorphic Geology*, 25, 477-494.

Slama, J., Kosler, J., Condon, D. J., Crowley, J. L., Gerdes, A., Hanchar, J. M., Horstwood, M. S. A., Morris, G. A., Nasdala, L., Norberg, N., Schaltegger, U., Schoene, B., Tubrett, M. N. & Whitehouse, M. J. (2008). Plešovice zircon - A new natural reference material for U-Pb and Hf isotopic microanalysis. *Chemical Geology*, 249, 1-35.

Spaggiari, C. V., Kirkland, C. L., Smithies, R. H., Wingate, M. T. D. & Belousova, E. A. (2015). Transformation of an Archean craton margin during Proterozoic basin formation and magmatism: The Albany-Fraser Orogen, Western Australia. *Precambrian Research*, 266, 440-466.

Spencer, C. J., Kirkland, C. L. & Taylor, R. J. M. (2016). Strategies towards statistically robust interpretations of in situ U-Pb zircon geochronology. *Geoscience Frontiers*, 7, 581-589.

Stern, R. A., Bodorkos S., Kamo S. L., Hickman A. H., Corfu F. (2009). Measurement of SIMS of Pb isotopes during Zircon dating. *Geostandards and Geoanalytical Research*, 33, 145-168.

Trendall, A. F., Compston, W., Nelson, D. R., De Laeter, J. R. & Bennett, V. C. (2004). SHRIMP zircon ages constraining the depositional chronology of the Hamersley Group, Western Australia. *Australian Journal of Earth Sciences,* 51, 621-644.

Veevers, J. J., Saeed, A., Belousova, E. A. & Griffin, W. L. (2005). U-Pb ages and source composition by Hf-isotope and trace-element analysis of detrital zircons in Permian sandstone and modern sand from southwestern Australia and a review of the paleogeographical and denudational history of the Yilgarn Craton. *Earth-Science Reviews*, 68, 245-279.

Vermeesch, P., Resentini, A. & Garzanti, E. (2016). An R package for statistical provenance analysis. *Sedimentary Geology,* 336, 14-25.

Wiedenbeck, M., Hanchar, J. M., Peck, W. H., Sylvester, P., Valley, J., Whitehouse, M., Kronz, A., Morishita, Y., Nasdala, L., Fiebig, J., Franchi, I., Girard, J. P., Greenwood, R. C., Hinton, R., Kita, N., Mason, P. R. D., Norman, M., Ogasawara, M., Piccoli, P. M., Rhede, D., Satoh, H., Schulz-Dobrick, B., Skår, O., Spicuzza, M.

J., Terada, K., Tindle, A., Togashi, S., Vennemann, T., Xie, Q. & Zheng, Y. F. (2004). Further Characterisation of the 91500 Zircon Crystal. *Geostandards and Geoanalytical Research*, 28, 9-39.

Wingate, M. T. D., Pirajno, F. & Morris, P. A. (2004). Warakurna large igneous province: A new Mesoproterozoic large igneous province in west-central Australia. *Geology*, 32, 105-108.

Wingate, M. T. D., Lu, Y., Kirkland, C. L. and Johnson, S. P. (2017). 188973: granodiorite gneiss, Mount James homestead. Geochronology Record 1361, Geological Survey of Western Australia.

CHAPTER 6

UNRAVELLING SECULAR CHANGE IN GEODYNAMIC SETTING WITH DETRITAL ZIRCON: A STUDY FROM THE CAPRICORN OROGEN, WESTERN AUSTRALIA

S. Armandola*[1], C.L. Kirkland[1], C.J. Spencer[1], M. Barham[1,2], S. M. Reddy[1], C. Clark[1], S. Spinks[4]

[1]School of Earth and Planetary Sciences, Curtin University, GPO Box U1987, Perth, WA 6845, Western Australia.

[2]Centre for Exploration and Targeting, Curtin Node, Curtin University, GPO Box U1987, Perth, WA 6845, Western Australia.

[3]Department of Earth Sciences, Downing Site, University of Cambridge, CB2 3EQ, Cambridge, United Kingdom.

[4]Commonwealth Scientific and Industrial Research Organisation PO box 1130 Bentley, (CSIRO), WA 6102, Australia.

Corresponding author: sonia.armandola01@gmail.com

Abstract

Laser Ablation Split Streaming represents an important advancement in linking geochronology with geochemistry where U-Pb age and trace element compositions of zircon grains can be measured rapidly, allowing the production of large datasets. Coupled with this analytical advancement, detrital zircon as a sampling medium has the advantage of recording source and composition through space and time, and thus, potentially holds a detailed record of crustal evolution. In this work trace elements from 1800 detrital zircon grains dated between 3.5 and 1.1 Ga, from the Palaeo- to Mesoproterozoic Yerrida, Edmund and Collier basins are evaluated through statistical model locally weighted scatter-plot smoother (LOESS), to obtain insight into the complex tectonic history of the Capricorn Orogen. LOESS curves systematically highlight variations in trace elements abundances (Y, Th/U, Gd/Yb, HREE/LREE and Eu/Eu*), corresponding to crust differentiation episodes, and pinpoint: (I) Broad changes in elemental fractionation trends of the host rocks, for example enrichment of

Y in detrital zircons after c. 2.5 Ga, coeval with the initiation of a subduction regime that increasingly fractionated incompatible elements (Fig. 1); (II) A shift from a continental arc setting to an intracratonic setting in the Capricorn Orogen after c. 1.95 Ga, (Fig. 1). (III) Poorly constrained tectonic reactivations of the Capricorn Orogen occurred at c. 1.72 and c. 1.88 Ga, marked by consistent peaks of the LOESS curves for Y, HREE/LREE (Fig. 1), Th/U, Gd/Yb and Eu/Eu*. Trace elements in zircon evaluated through time are a powerful tool in reconstructing the geodynamic history of long-lived orogens.

1. Introduction

The continental crust is periodically intruded by magmas, whose geochemical signature may track both crustal and mantle processes (Campbell & Allen, 2008; Harrison et al., 2008; Fu et al., 2009; Arndt & Davaille, 2013; Brown, 2013; Couzinié et al., 2016). A range of isotopic signatures in magmas (Rb/Sr, Sm/Nd, Lu/Hf and O) can be employed to chart the timing and nature of crust-forming events (e.g. McCulloch & Bennett, 1994; Taylor & McLennan, 1995; Wu et al., 2000; Valley et al., 2005; Dhuime et al., 2015; Liu et al., 2017; Spencer et al., 2017). Zircon U-Pb, Lu-Hf and O isotopes have been widely employed to study crust genesis and differentiation, due to the development of *in situ* isotopic analysis in zircon, which enables correlations between the age and isotopic information (Wu et al., 2000; Kemp et al., 2007; Wang et al., 2010; Kirkland et al., 2015; Couzinié et al., 2016). Although the combination of Lu-Hf and U-Pb in zircon is undoubtedly a powerful tool to track crustal differentiation, difficulties may arise in determining melt sources during crustal and mantle mixing. Oxygen isotopes may help refine such interpretations by indicating supracrustal rocks altered by the interaction with meteoric water near surface. Further limitations of the Lu-Hf and U-Pb in zircon method are the general lack of knowledge on the compositional evolution of the continental crust through mixing of highly fractionated melts, and the magnitude of the mantle input versus crustal input (Kemp et al., 2006; Couzinié et al., 2016).

In addition to its useful isotopic signatures, zircon incorporates considerable amounts of trace elements (e.g. Th, U and Y) and rare earth elements (REE), favouring heavy (H)REE over light (L)REE or middle (M)REE (Hoskin & Ireland, 2000; Whitehouse & Kamber, 2002). Incorporation of trace elements in zircon is controlled by several

factors, including the host melt composition and oxidation state, and the temperature and depth of the magmatic differentiation (Chapman et al., 2016). Additionally, crystallization of minerals like garnet, amphibole, and plagioclase, prior to or coeval with zircon, influence zircon REE content, by depleting the MREE and HREE available for incorporation to the zircon lattice (Hanchar & van Westrenen, 2007; Keller et al., 2015). Consequently, trace-element abundances and partitions can be used to fingerprint the melt composition and the geodynamic context of the magma system that generated the detrital zircons (e.g. Wang et al., 2010; Kylander-Clark, 2013; Iizuka et al., 2013; Chamberlain et al., 2014; McKenzie et al., 2018; Schannor et al., 2018).

Sedimentary rocks are well known to be an invaluable archive of information on their sources (e.g. McLennan et al., 1990; Licht & Hemming, 2017) and to host accessory minerals, like detrital zircon, that preserve the geochemical signature of their parent magma (e.g. Cawood et al., 2012; Guo et al., 2017). Moreover, sedimentary rocks have an intrinsic heterogeneous composition, determined by sourcing from distinct crustal units, sediment mixing and recycling, that altogether confer compositional variety to the sediment and their accessory mineral (e.g. Cawood & Nemchin, 2000; Martin et al., 2008). Therefore, sedimentary rocks can be an ideal target for studies aiming to capture a wide range of geochemical and geochronological data on the orogen adjacent to the sedimentary basins.

This study presents trace elements and U-Pb isotopic data for detrital zircon from the Capricorn Orogen (Western Australia) to help reconstruct its geodynamic history. Detrital zircons ages spanning 3500–1100 Ma, from three sedimentary basins (Palaeoproterozoic Yerrida Basin and the Mesoproterozoic Edmund and Collier basins), were analysed using LASS-ICP-MS. The detrital zircon trace elements data are assessed through statistic models, produced by plotting locally weighted scatter-plot smoothing curves (LOESS), for a range of defined trace element ratios. The statistical model defines negative and positive trends that provide insight into melt fractionation events, changes in the crustal depth of melting, differentiation over time, arc magmatism and cratonization processes and broad secular changes in the composition of the continental crust.

2. Geological framework

The Capricorn Orogen is an orogenic zone that records the continental collision of the Glenburgh Terrane, Yilgarn and Pilbara cratons, to form the West Australian Craton (Fig. 1; Cawood & Tyler, 2004; Johnson et al., 2013). The continental amalgamation took place during the 2215–2145 Ma Ophthalmian Orogeny when the Glenburgh Terrane accreted to the southern margin of the Pilbara Craton. Subsequently over the 1965–1950 Ma Glenburgh Orogeny, the Pilbara Craton - Glenburgh Terrane block collided with the Yilgarn Craton (Fig. 2; Occhipinti et al., 2004; Johnson et al., 2010; Johnson et al., 2011). The Glenburgh Orogeny was characterized by a continental arc setting and northward dipping subduction, beneath the Glenburgh Terrane (Johnson et al., 2010; Johnson et al., 2017). The subduction resulted in the intrusion of arc-related voluminous intermediate to felsic magmas in the Gascoyne Complex, as the 2005–1975 Ma Dalgaringa Supersuite (Fig. 1-2; Sheppard et al., 1998; 2004; Johnson et al., 2017).

Subsequent to the continental amalgamations the Capricorn Orogen records a further 1 Ga of intracratonic tectonic reactivations, and intermittent magmatism (Sheppard et al., 2010; 2016). The 1820–1770 Ma Capricorn Orogeny, was associated with compressional tectonic and magmatism, (Moorarie Supersuite Fig. 1-2; Sheppard et al., 2010). This was followed by the 1680–1620 Ma Mangaroon Orogeny, which was accompanied by the intrusion of the Durlacher Supersuite (Fig. 1-2; Sheppard et al., 2005). The compressional 1321–1171 Ma Mutherbukin Tectonic Event did not record any associated magmatism (Fig. 2; Korhonen et al., 2015), while the later 1030–955 Ma Edmundian Orogeny was characterized by the emplacement of the Thirty Three Supersuite (Fig. 1-2; Sheppard et al., 2007). Magmatism in the Capricorn Orogen region recorded progressive crustal differentiation, with decreasing contributions from mantle-derived melt, and increasing recycling of melted continental crust (Occhipinti et al., 2004; Johnson et al., 2017). Changes in the bulk-rock composition (Sheppard et al., 2004; Johnson et al., 2017) and accessory minerals (zircon Lu-Hf isotopes), were interpreted to correlate with a change from active margin to an intracratonic tectonic setting, after the continental amalgamation (Johnson et al., 2017).

The Capricorn Orogen hosts Palaeoproterozoic to Mesoproterozoic siliciclastic and volcanoclastic basins. Basin filling originated principally from the reworking of the

magmatic intrusive rocks (e.g. Dalgaringa, Bertibubba, Moorarie and Durlacher supersuites) and from the recycling of older meta-sedimentary rocks and the cratonic margins (Fig. 1; Pirajno, 2004; Johnson et al., 2013). Detrital zircon recovered from the basins' sedimentary rocks reflect such process of continental erosion, and the geological evolution of the eroded basement of the Capricorn Orogen (Hall et al., 2001; Halilovic et al., 2004; Martin et al., 2008).
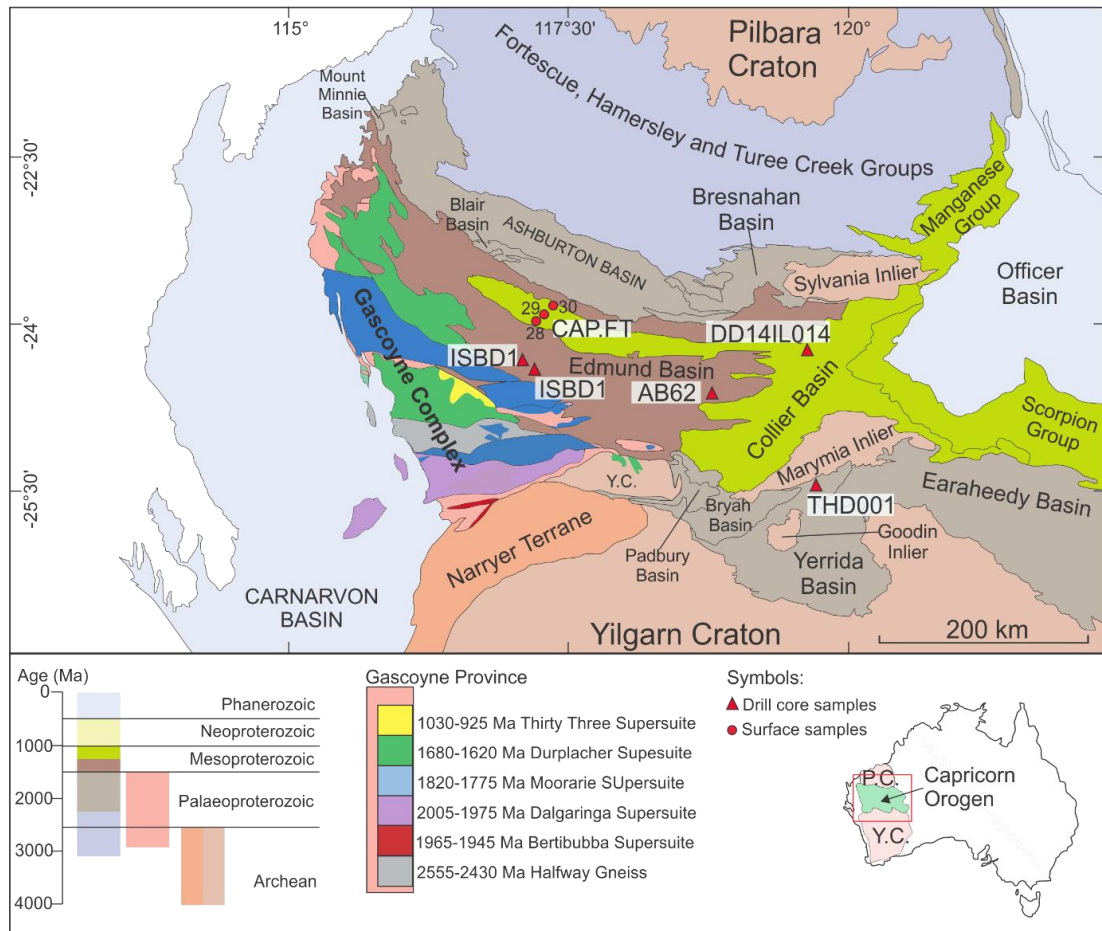
Fig. 1. Tectonic units of the Capricorn Orogen; drill core and samples location marked. P.C.-Pilbara Craton, Y.C.-Yilgarn Craton. Gascoyne Complex modified after Johnson et al., (2017).
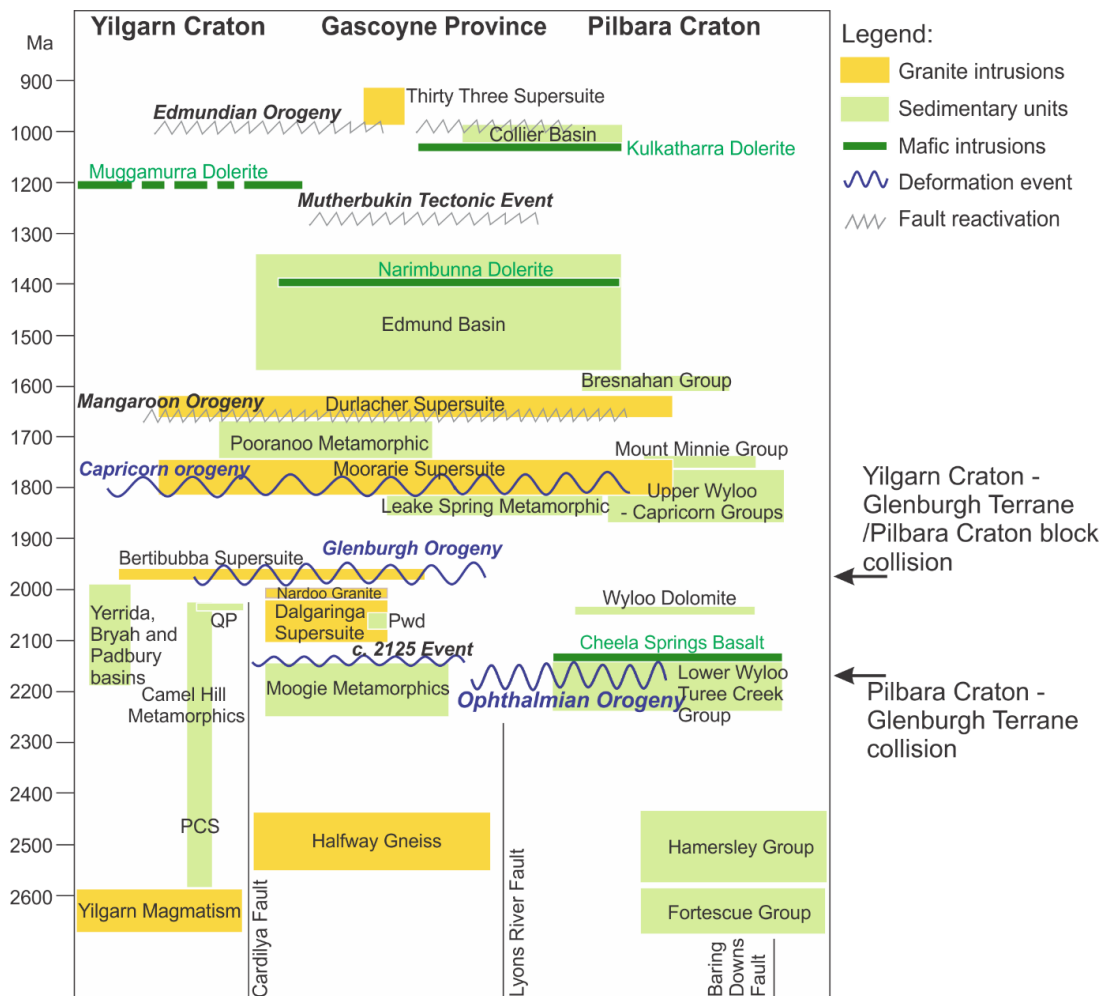
Fig. 2. Time-space event summary of the Capricorn Orogen (modified after Johnson et al., 2013; PCS = Petter Calc-silicate; QP = Quartpot Pelite; PWD = Paradise Well diatexite).

3. Analytical Methods

Detrital zircon were separated and analysed at the John the Laeter Centre and Microscopy & Microanalysis Facility housed at Curtin University, Australia. Non-magnetic heavy mineral separated were concentrated using SelFrag electro pulse fragmentation technique, heavy liquids (NaPT ~2.8 g/cm^3 s.g.) and magnetic separation methods, before representative zircons were handpicked under an optical microscope and enclosed in 2.5 cm diameter epoxy resin discs. Cathodoluminescence imaging of the detrital zircon was operated on a Tescan MIRA3 Field Emission SEM with Oxford Instruments Aztec, using a Tescan panchromatic CL detector. According to the growth histories evidenced by the cathodoluminescence (CL) images, magmatic grain cores were selected for ablation. The U-Pb isotopes and trace elements

concentrations were measured on a LASS-ICP-MS, fitted with a Resonetics S-155-LR 193 nm excimer laser ablation system, coupled to Nu Instruments Plasma HR multi-collector ICP and an Agilent 7700x quadrupole ICP-MS. The laser ablation area was set at 23 to 33 µm with a fluence of 2 J/cm^2 and repetition rate of 4 Hz. The carrier gas to the split system comprised He at 3.2 ml/min, Ar at 1 ml/min and N at 1.2 ml/min flow rate. Standard material was analysed during the analytical sessions to check the accuracy of the measurements, every 20 unknown zircons. Primary standard included Plešovice (337.13 ± 0.37 Ma; Slama et al., 2008), used for U-Pb isotopes calculation, and GJ1 (608.5 ± 0.4 Ma; Jackson et al., 2004) used for both U-Pb isotopes and trace element abundance calculations. Secondary standards included OG1 (3465.4 ± 0.6 Ma; Stern, 2009) and Z91500 (1061 ± 4.3 Ma; Wiedenbeck et al., 1995). Standard material analyses are reported in Appendix 1. The U-Pb isotope and trace element abundances were calculated with the software *Iolite2.5* on IgorPro (Paton et al., 2010). Zircon with >90% of concordance between the ^{207}Pb/^{206}Pb and ^{206}Pb/U^{238} isotopic systems were used for the discussion. Ages are indicated as ^{206}Pb/^{207}Pb if >1500 Ma and ^{206}Pb/^{238}U if <1500 Ma (Spencer et al., 2016). The probability density plot (PDP) of the detrital zircon U-Pb ages were calculated with *Isoplot 4.15* (Ludwig, 2003).

Temporal variations of the trace element concentrations for the concordant detrital zircon were examined through regression locally weighted scatterplot smoothing – LOESS (aka - LOWESS; LOcally WEighted Scatterplot Smoothing; Cleveland 1979, 1981) that were calculated with the software *Past3* (Hammer et al., 2001). Given a number of points (n) and a smoothing parameter (q) specified by the user, the program fits the nq points around each given point to a straight line, with a weighting function decreasing with distance. The new smoothed point is the value of the fitted linear function at the original x position (Hammer et al., 2001). The regressions were calculated with a smoothing factor of 0.05. Bootstrap was applied to the LOESS regression to calculate a 95% confidence limit band to the curve. The Bootstrap is based on 999 random replicates (Hammer et al., 2001). The LOESS smoothing produced a fitting model, which reveal relationships between variables and display trends in time versus composition plot (Fig. 4). The LOESS lines were detrended to estimate the impact on the curve of local variations in the sample dataset. The detrended curve ultimately obliterates the interference of primary correlations existing in the sample trace element concentrations.

4. Full detrital zircon dataset

The detrital zircon data (U-Pb age and trace elements), including geographic and stratigraphic information for the sedimentary samples from the three basins are provided in the Appendix. About 4250 detrital zircon grains from 32 samples separated from five drill cores and three surface samples were analysed, of which 1793 were within 10% of concordance. The ages of the > 90% concordant detrital zircons are displayed with probability density plots (Fig. 3), and their trace elements are displayed with their LOESS, to outline trace elements temporal variations (Fig. 4).

4.1.1 Zircon data from the Yerrida Basin

Detrital zircon analysed from the Yerrida Basin range in age from 3700 to 2100 Ma, with a dominant population at 2800–2550 Ma and two smaller age clusters at 3500–3300 and 2200–2100 Ma (Fig. 3). Detrital zircons have Th/U ratios ranging 0.03–7.8, and Y contents from 6810 to 54 ppm. The chondrite-normalized (Anders and Grevesse 1989) REE patterns highlighted europium anomalies (Eu/Eu*) spanning 2.2 to 0.01, (Eu* calculated as SQRT(Sm*Gd)). The REE patterns show variable degrees of fractionation as reflected by the LREE/HREE ratio varying from 13.4 to 0.02 (Fig. 4).

4.1.2 Zircon data from the Edmund Basin

Detrital zircons analysed from the Edmund Basin yielded

U-Pb ages from 3500 to 1500 Ma, and dominant population aged 1900–1700 Ma (Fig. 3). Detrital zircon exhibit Th/U ratios ranging from 6 to 0.015 and Y concentrations of 21100 to 91 ppm. The Chondrite-normalized REE patterns show europium anomalies Eu/Eu*=6.7–0.01. The REE patterns have weakly to highly fractionated REE paths, according to the LREE/HREE ratios varying from 4.00 to 0.018 (Fig. 4).

4.1.3 Zircon data from the Collier Basin

The Collier Basin detrital zircon have polymodal age modes, ranging from 3700 to 1100 Ma, (Fig. 3). The dominant age peak in the Collier Basin is dated between 1900 to 1700 Ma, another significant age group is dated from 1300 to 1100 Ma (Fig. 3). Zircon trace element concentrations display Th/U ratios of 3.48–0.05, while Y varies from 4990 to 116 ppm. The chondrite-normalized REE patterns yielded negative to

positive europium anomalies with Eu/Eu*=1.48–0.02. The REE patterns are fractionated as is evidenced by the LREE/HREE ratio varying from 1.11 to 0.07 (Fig. 4).
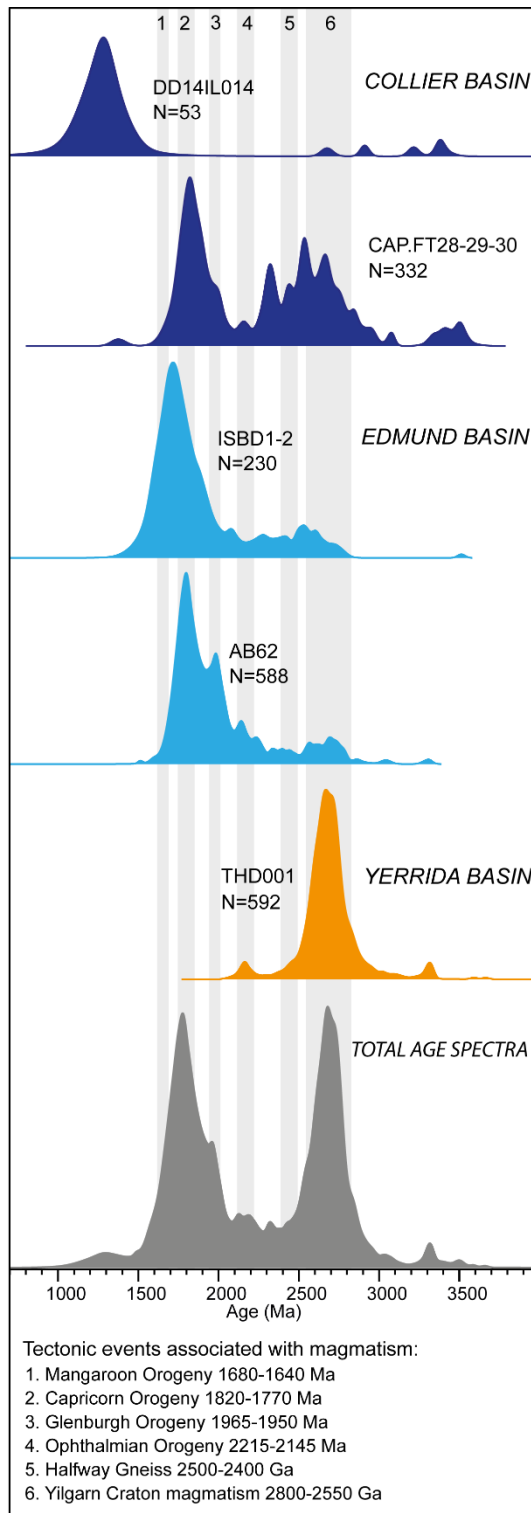

Fig. 3. Probability density plots of the >90% concordant detrital zircon analysed from the three basins examined. Age spectra are subdivided for drill cores. Outcrop samples are plotted together. Relevant tectonic events associated with magmatism and magmatic events are indicated with vertical grey bins.

5. Descriptive statistic of the trace-element temporal patterns

The rare earth elements (REE) of the detrital zircon dataset are examined through ratios except for the Y content, which is in ppm (Fig. 4). The LOESS curves and the upper and lower limits calculated for each LOESS point out variation of the geochemical dataset, though time, within the 95% limit confidence. The trace elements are described according to temporal ranges: the Archean (>2500 Ma), the early to mid-Palaeoproterozoic (2500–2050 Ma), and the late Palaeoproterozoic (2050–1600 Ma; Table 1). Detrital zircon analysed from the Yerrida, Edmund and Collier basins have particularly prolific U-Pb age data from 2800 Ma to 1600 Ma (Fig. 4). The ratios selected comprise: Eu/Eu* (with Eu* calculated as SQRT(Sm*Gd)), which is a marker for the plagioclase content of the melt and an indicator of the crustal depth at which the melt differentiation occurred (Trail et al., 2012); Gd/Yb records the MREE enrichment relative to HREE, due to garnet crystallizing contemporaneously with zircon (Hanchar & van Westrenen, 2007); LREE/HREE, which is linked to HREE depletion in zircon minerals crystallized after amphibole and garnet. Additionally, the LREE/HREE is a marker for fractionation in the lower crust, at high temperature and with pressure >1 GPa (Rapp, 1995; Hanchar & van Westrenen, 2007; Boehnke et al., 2013). Y abundance is a marker for the degree of the melt fractionation and positively correlates with the increase of the SiO_2 content within the melt (Belousova et al., 2002).

5.1 Yttrium temporal pattern

Overall the LOESS displays a positive trend in the age range 2800–1600 Ma by increasing its abundance. Y concentration in Archean detrital zircons (>2500 Ma) ranges from 4550 to 54 ppm, with a median of 696 ± 1148 ppm. In the early to mid-Palaeoproterozoic (2500–2050 Ma) the detrital zircon Y abundance ranges 6810–131 ppm, with median of 1053 ± 2030 ppm, while in the mid to late Palaeoproterozoic (2050–1600 Ma) the concentration of Y in the detrital zircons ranges from 21100 to 1145 ppm with median value of 1240 ± 2290 ppm. Several Y peaks in this interval also coincide with major tectonic events recorded in the Capricorn Orogen (Fig. 5).

5.2 Gd/Yb ratio temporal pattern

The Gd/Yb ratio in Archean detrital zircon varies from 0.574 to 0.005 with a median of 0.102 ± 0.14 and fluctuations in correspondence of the Yilgarn Craton magmatism (Fig. 4). In the early to mid-Palaeoproterozoic Gd/Yb ratios span 1.245–0.010 with a median value of 0.118 ± 0.34, whereas in the mid to late Palaeoproterozoic the Gd/Yb ratio is between 2.395–0.013 and has median value of 0.088 ± 0.30, which mark a broad negative trend. Two positive peaks match the Glenburgh Orogeny and the Capricorn Orogeny (Fig. 4).

5.3 LREE/HREE ratio temporal pattern

Archean detrital zircons have LREE/HREE ratios ranging from 2.265 to 0.011 and median of 0.147 ± 0.64. Large fluctuation and a positive trend of the LREE/HREE ratios characterized the zircons crystallized during the Yilgarn Craton magmatism (Fig. 4; the scale of the LREE/HREE is reduced to a maximum value of 0.7). In the early to mid Palaeoproterozoic zircon have LREE/HREE ratios spanning from 5.14 to 0.019 and a median of 0.136 ± 1.12. Mid to late Palaeoproterozoic detrital zircon have LREE/HREE ratios between 3.61 and 0.08 with a median value of 0.144 ± 0.52, which mark a negative trend from Archean to Mesoproterozoic (Fig. 4).

5.3 Eu/Eu* ratio temporal pattern

The Eu/Eu*ratio display the largest changes from all the geochemical proxies analysed. Detrital zircons aged >2500 Ma have Eu/Eu* ranging from 2.265 to 0.011 and with median value of 0.504 ± 0.646. In the early to mid-Palaeoproterozoic, the range expands to 3.083–0.022 with median of 0.419 ± 0.802. The detrital zircons of the mid to late Palaeoproterozoic have Eu/Eu* anomalies spanning from 6.714–0.007 and median value of 0.444 ± 0.876 (Fig. 4; the scale of the Eu anomaly has been reduced from 0 to 1).

The Eu anomaly shows a negative pattern from Archean to the Mesoproterozoic. Either peaks or troughs of the LOESS curves occur in coincidence with magmatic events of the Yilgarn Craton (peak at c. 2600, c. 2650 and c. 2700 Ma) and with orogenic events (Glenburgh Orogeny, the Capricorn Orogeny and the Mangaroon Orogeny; Fig. 4). Notably, other marked Eu/Eu* fluctuations do not coincide with tectonic events, e.g. after the Glenburgh Orogeny (c. 1900 Ma), at the end of the

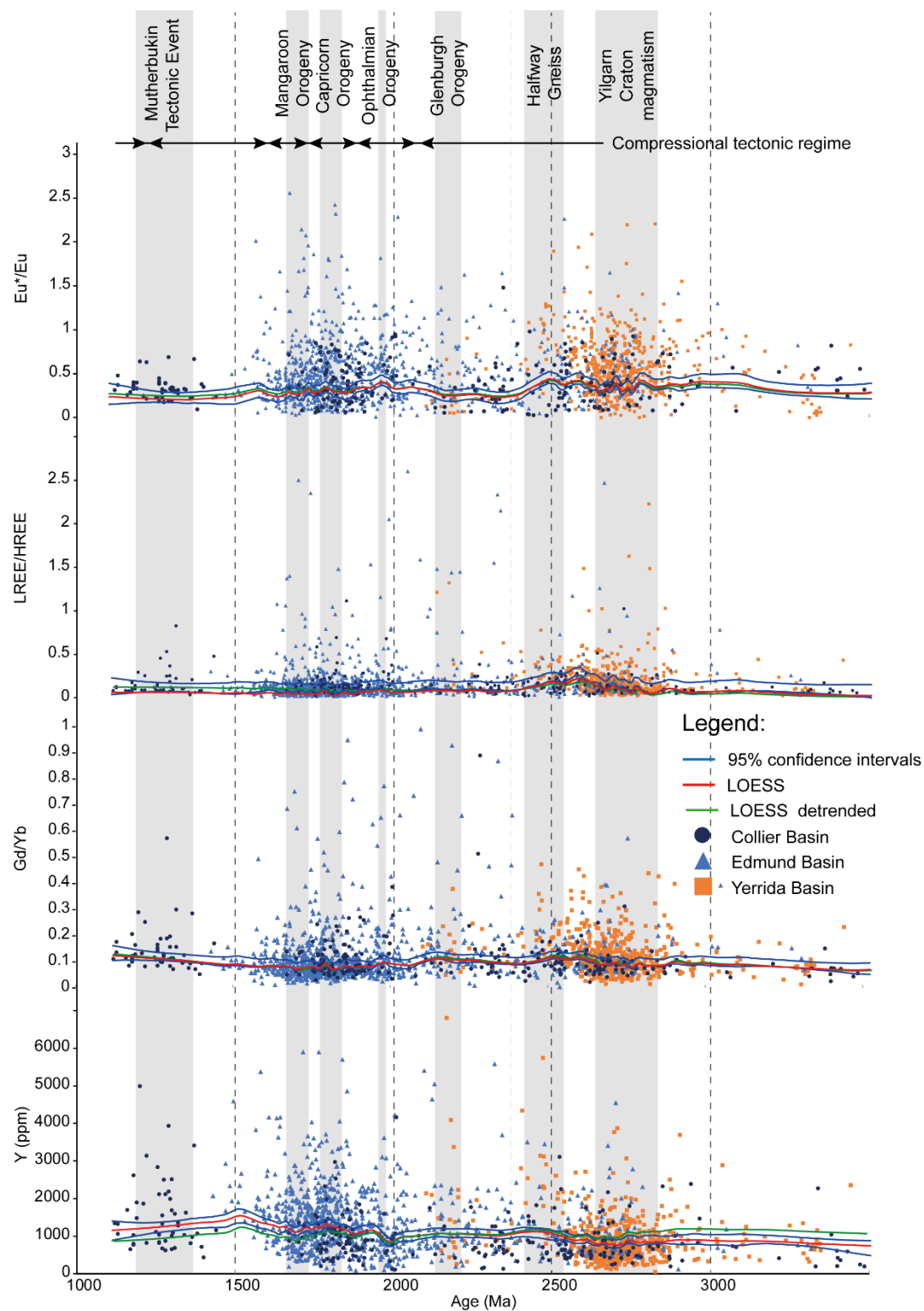Capricorn Orogeny (c. 1740 Ma) and just before the Mangaroon Orogeny (c. 1680 Ma).

Fig. 4. LOESS of the concordant detrital zircon trace elements. Zircon analysis are divided per sedimentary basin. Orogenic events and magmatism from Johnson et al.,

(2013). Zircons falling out of scale: Eu/Eu*=4.528 (AB5-5), 6.714 (AB13-20); LREE/HREE=13.435 (TD7-66), 5.135 (TD5-131), 4.0 (AB7-136), 3.605 (AB8-38); Gd/Yb= 2.395 (AB1-139), 1.245 (AB7-126), 1.124 (AB1-21), 1.076 (AB5-143), 1.066 (CAP.FT30.38), 1.003 (AB1-160); Y=21100 (AB4-52), 7900 (AB1-147, isbd2-14-129).

6. Tectono - magmatic setting for the zircon genesis

Detrital zircon trace element data from the Yerrida, Edmund and Collier basins fingerprint the tectono-magmatic provenance of their source rock by distinguishing between grains that crystallized from melts derived from oceanic or continental crust (Fig. 5a, c, e, g, U-Yb; Grimes et al., 2007) and that formed in magmatic arc versus mantle plume settings (Fig. 5b, d, f, h, U/Yb versus Nb/Yb; Grimes et al., 2015). The detrital zircon grains analysed present a large scatter and overlap with the continental crust field while few grains plot within the oceanic crust field (Fig. 5a, c, e, g). The tectono-magmatic setting discrimination diagrams, based on the U/Yb and Nb/Yb ratio, shows that almost all the zircon plot in the continental arc setting field (Fig. 5b, d, f, h). A small number of grains plot at the limit with the post-collisional tectonic setting, whereas an even smaller group plot in the oceanic island and E-MORB fields (Fig. 5d, f, h).

The detrital zircons younger than 2000 Ma are almost all consistent with a continental arc setting when plotted in the discrimination diagrams from Grimes et al., (2015; Fig. 5d, f, h). Moreover, zircons younger than 2000 Ma and those younger than 1850 Ma, lack a clear distinction between zircons formed within a continental arc setting from those formed in a post-collisional setting. According to the tectonic history of the Capricorn Orogen region after c. 1.9 Ga, when the continental amalgamation occurred, an evolution of the composition of the detrital zircons would be expected with groups of zircons aged <1850 Ma plotting in the post-collisional filed, and crystallized from source rocks emplaced in a post-collisional setting, and likely formed by progressively fractionated and crust-derived magmas (Johnson et al., 2017).

A small number of detrital zircons from the Yerrida Basin, Edmund Basin and Collier basins have compositions consistent with the ocean island setting, that overall indicate a mafic protolith for the minerals. These zircons with ages c. 2500 Ma, c. 2100 Ma, c. 1700 Ma and c. 1400 Ma and 1200 Ma originated from mafic source rocks likely

preserved in the Yilgarn Craton (Cassidy et al., 2010), Glenburgh Terrane (Johnson et al., 2017) and mafic sills and dykes intruding the Edmund Basin (Wingate et al., 2002).
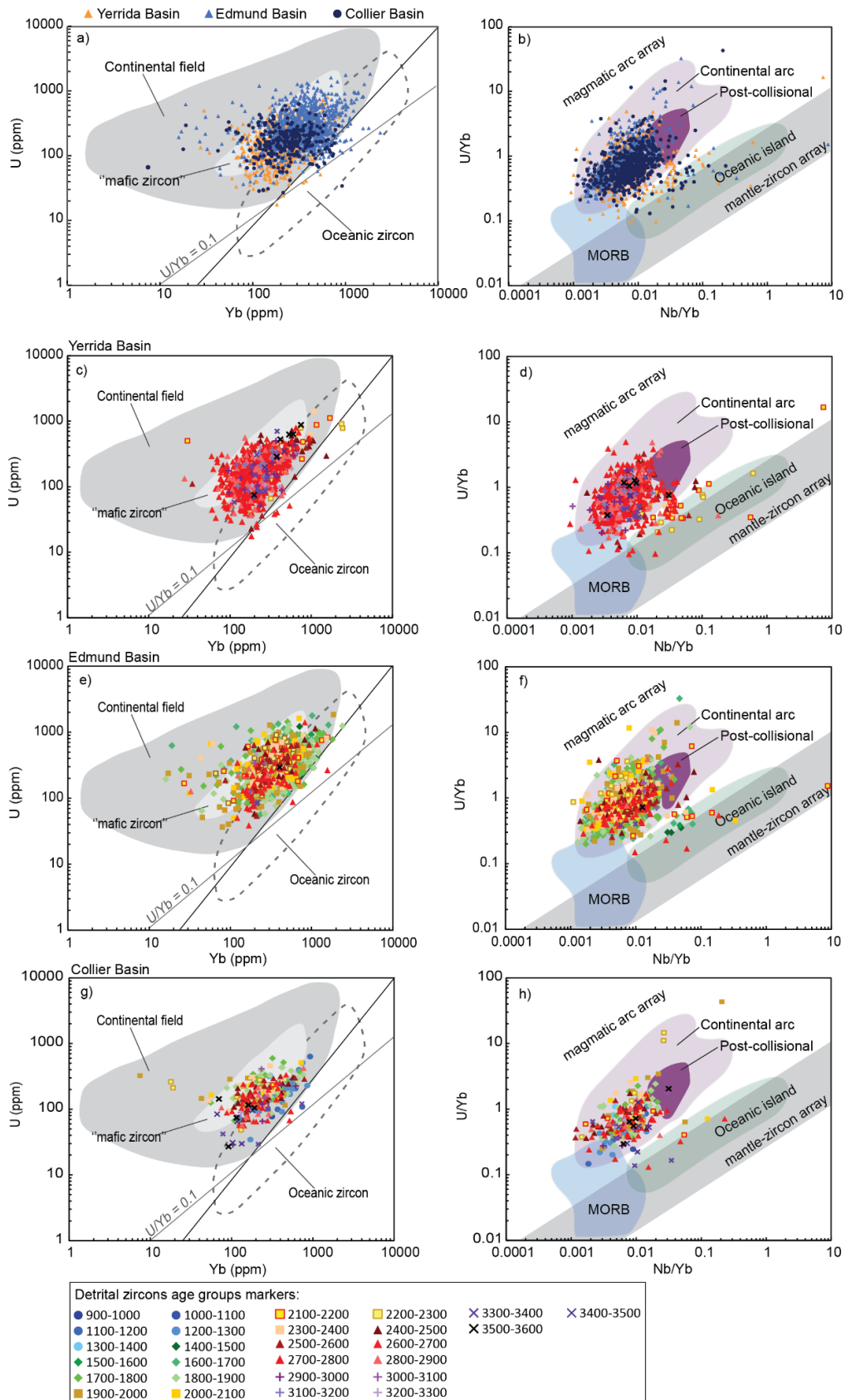
Fig. 5. U Vs Yb discrimination diagrams with the distinction between ocean crust and continental crust field from Grimes et al. (2007). Discrimination diagrams with U/Yb Vs Nb/Yb geochemical proxies from Grimes et al. (2015). a, b - represent all detrital zircon from the three basins, c, d, e, f, - diagrams for each basin follow, with detrital zircon divided by age groups of 100 Ma.

7. Secular changes and episodes of juvenile continental crust emplacement, recorded by the detrital zircon of the Capricorn Orogen.

7.1 Secular changes of Y abundance in the continental crust and continental arc magmatism

Y is an incompatible element within felsic to intermediate rock, formed by partial melting of subducted continental crust and sedimentary material. It is generally enriched in the continental crust (Y>500 ppm). Conversely, mafic rocks have depleted Y composition (Y<500 ppm; Belousova et al., 2002; Rudnick & Gao, 2003; Grimes et al., 2015). Y is a pathfinder for melt fractionation events, and highly fractionated melt versus mantle-like melts (Belousova et al., 2002). Zircon chemistry reflects these conditions and yields Y abundance that broadly correlates with the $\sum$REE abundance, and the depth of the Eu anomaly (Belousova et al., 2002; Rudnick & Gao, 2003; Grimes et al., 2015).

The Y concentration of the Archean zircon is consistent with continental crust formation via fractionation of primitive mantle-derived melt (Arndt & Davaille, 2013; Dhuime et al., 2015). During the Archean, the continental crust generated via mantle plume and mantle melt fractionation, while the formation of crust via subduction of early lithosphere is considered a sporadic process, consequently to rapid changes between active arc and passive margins (Martin et al., 2014; Reimink et al., 2014). Furthermore, recycled crust comprised predominantly TTG (tonalite-trondhjemite-granodiorite) rocks that are reportedly characterized by low Y concentrations compared to modern subducted material (Drummond & Defant, 1990; Griffin et al., 2004).

In the early Proterozoic, Y abundance of detrital zircon increased coincident with the break-up of the Kenorland Supercontinent, and the establishment of a stable subduction regime on the early Earth, (O'Neill et al., 2007; Bradley, 2011). After c.

2050 Ma and the continental collision of the Pilbara - Glenburgh and Yilgarn tectonic units, an increase in zircon Y concentrations marks the emplacement of highly fractionated magmas linked with a continental arc setting, presumably established outboard of the Glenburgh Terrane. Similar indications were obtained from the Lu-Hf isotopes of magmatic zircons analysed from the 2005–1965 Ma Dalgaringa Supersuite (Glenburgh Terrane), that indicate an active continental margin and subduction-related magma (Johnson et al., 2017). The subsequent increase of Y abundance coeval with the Capricorn Orogeny may signify intrusion of highly fractionated continental collisional granites, following the continental accretion and termination of the subduction. The Mangaroon Orogeny is also marked by another Y peak, however, in this case, Y abundance is similar to that of the Capricorn Orogen, which is interpreted to indicate change in tectonic setting from continental collisional to post-orogenic, characterised by ''decompression melting'' that promoted melt formation from both crust recycling and mantle contribution (Maniar & Piccoli, 1989).

7.2 Fractionation of Gd/Yb ratio and LREE/HREE to unravel the geodynamic history of the Capricorn Orogen

Zircon incorporates abundant HREE compared to LREE and MREE from the parent melt since its mineral crystal structure has limits in accommodating the large ionic radii of the LREE (Chapman et al., 2016). Nevertheless, while crystallizing zircon HREE abundance is also determined by the presence of other cogenetic minerals, notably amphibole and garnet, that compete for the HREE, and cause HREE depletion in zircon (Hanchar & van Westrenen, 2007). Fractionation of REE between zircon, garnet and amphibole has been linked with the lower crust, high temperatures and pressures greater than 1 GPa (Rapp, 1995; Boehnke et al., 2013). Exceptions are represented by zircons crystallized from melting of subducted oceanic crust that yield particularly low LREE (Drummond & Defant, 1990). On contrary high amounts of LREE can be incorporated by zircons in the presence of REE enriched melt that causes LREE to enter the zircon lattice generating atypical LREE concentrations (Hanchar & van Westrenen, 2007). The dataset shows a small population of zircons with high LREE/HREE ratios that can be linked with crystallization in a high-pressure environment coeval with garnet and/or amphibole (Hanchar & van Westrenen, 2007)

The Gd/Yb ratio is a good proxy for monitoring the MREE enrichment relative to HREE (MREE/HREE) that is indicative of a "garnet signature" in the parent melt, and/or growth of zircon with or after garnet (Hanchar & van Westrenen, 2007; Grimes et al., 2015). Fractionation of common accessory minerals that sequester light and middle REE (e.g., titanite, apatite, monazite) may shift the Gd/Yb ratio toward lower values, in opposition to the garnet signature, corresponding to high MREE (Hanchar & van Westrenen, 2007; Grimes et al., 2015).

The LREE/HREE and Gd/Yb ratios of the detrital zircon grains examined are remarkably consistent in their temporal patterns. They indicate a positive trend over the Archean, a flattened pattern over the early to mid-Palaeoproterozoic, and a declining trend for the mid to late Palaeoproterozoic. The positive trend observed during the Archean indicates the progression in the melt fraction under the Yilgarn Craton and an increasing depth for the magmatic differentiation, between 2900 and 2600 Ma. The early to mid-Palaeoproterozoic is characterized by scarce data, likely because this time interval has been interpreted to represent a protracted time of magmatic and tectonic quiescence marked by a break in the Earth magmatism (Spencer et al., 2018). Another possibility is a break in the magmatism in the region examined and it is possible that the small amount of magma differentiation occurred at shallower depths. In the mid to late Palaeoproterozoic, the almost flattened paths LREE/HREE and Gd/Yb ratios probably correlate with a progressive shallowing of the depth of magma differentiation under the Capricorn Orogen, initiated after the Glenburgh Orogeny.

7.3 The Eu anomaly of detrital zircon and its temporal modifications

Eu anomaly (Eu/Eu*) in zircon is dependent on reducing conditions (Eu^{2+}) in the parent melt and the contemporaneous crystallization of plagioclase (Trail et al., 2012; Boehnke et al., 2013). Higher values are correlated with melt differentiation at deep levels of the crust, where suppression of plagioclase crystallization may cause Eu enrichment in zircon (Trail et al., 2012). The Eu negative anomaly can also be promoted by the presence of water in the melt, which raises the saturation point of zircon for this element (Keller et al., 2015).

From the Archean to the Mesoproterozoic the Eu anomaly of zircon displays a broadly negative trend, through several peaks and troughs, which is consistent with an increase

of reducing conditions, and crystallization of plagioclase in the source magmas of the detrital zircon. This trend is also linked with decreasing depth of the crustal differentiation process.

During the Archean, the Eu anomaly is not as negative as in the Palaeoproterozoic, and several peaks and troughs yield similar maximum and minimum values indicating that crystallization was occurring in the absence of abundant plagioclase, and in depth (Rapp et al., 1991; Moyen, 2011). This is consistent with the predominant rock type recorded for the Archean (Arndt et al., 2013) and differentiation led by partial melting of mantle plumes (Reimink et al., 2014). The Eu anomaly trend changes in the early to mid-Palaeoproterozoic where it displays marked negative values, suggesting abundant plagioclase and shallow differentiation. During the Glenburgh Orogeny, the Eu anomaly shows a marked peak that highlights differentiation in the deep crust, suppression of plagioclase crystallization when zircon was growing, and/or potential contributions of mantle sources. Significantly the Eu anomaly of the Glenburgh Orogeny is comparable with the Eu anomaly of the Archean magmatic rocks, which might be indicative of subduction and recycling of TTG rocks from the Yilgarn Craton, via subduction. In comparison with the Glenburgh Orogeny the successive tectono-thermal events, show a remarkable negative trend of the Eu/Eu* (values between 0.4 and 0.3), which is consistent with crustal recycling at increasingly shallower crustal depth.

8. Crustal differentiation history of the Capricorn Orogen, between 2200 and 1600 Ma

The paths observed for the zircons trace elements suggest that detrital zircon of the Capricorn Orogen region preserve a signal of their parent melts. The zircon dataset aged 2200–1600 Ma, records (i) secular changes of the plate tectonics in the Proterozoic, which is in agreement with what has been observed globally from geochemical data, and (ii) a shift from a continental arc setting (2050–1900 Ma), toward a post-collisional setting (1900–1600 Ma), that match past observations on the geodynamic evolution of the Capricorn Orogen region (e.g. Sheppard et al., 2004; 2005; Alghamdi et al., 2017; Johnson et al., 2017).

The 2200–2000 Ga zircons constitute a minor component and are considered representative of sporadic magmatism in the Yilgarn Craton and Glenburgh Terrane

(Johnson et al., 2013, 2017). Within the age interval of the Glenburgh Orogeny (1965–1950 Ma), zircon trace-element data are compatible with a magmatic arc characterized by deep recycling of continental crust. The Eu anomaly recorded in this interval, which is less negative than the Eu anomaly of subsequent orogenic events, has several interpretations: it might be due to deep magmatic differentiation within the subduction zone, and/or it might be a marker for subduction and recycling of TTG rocks in the arc. However, the positive trends and marked peaks of Y, LREE/HREE, Gd/Yb indicate strong magmatism, melt differentiation deep in the crust and at high pressure, and are in agreement with a subduction-related active continental margin model (Fig. 4).

The successive Capricorn (1820–1770 Ma) and Mangaroon (1680–1640 Ma) orogenies are characterized by lower values of the LREE/HREE, Gd/Yb and Eu/Eu* ratios, and increasing Y, indicating together: progressive shallowing of the magmatic differentiation, highly fractionated melts, crust thickening and dominant crustal recycling processes (Fig. 4). These data overall agree in recording a shift toward a post-collisional environment and the cratonization process of the continental crust under the Capricorn Orogen, initiated after c. 1950 Ma.

The statistical modelling of the detrital zircons trace elements highlights the occurrence of magmatic episodes not coeval with the orogenic event reported (Fig. 4). For example, data at c. 1720 Ma form a distinct peak from those that characterized the age interval of the Capricorn Orogeny, which potentially indicates intrusion of magmas in the Gascoyne Complex region following some late unknown thermal reactivation.

9. Limitations of the zircon trace elements approach

The application of descriptive statistic (LOESS) to detrital zircon trace element datasets, with the aim of constraining the evolution of orogenic systems, has proved effective. Moreover, this method is highly efficient for describing broad changes in geodynamic setting and secular changes in the elemental composition of the continental crust, providing information comparable and in overall agreement with those available (e.g. Sheppard et al., 2004; 2005; Johnson et al., 2017). However, the potential of integrated zircon age data and trace-element geochemistry needs to be further explored. Although the elemental ratios chosen are established markers of

fractionation processes, they yielded complex paths, some of which are challenging to interpret in a global perspective. For example, the Eu/Eu* of zircon within the age range of the Glenburgh Orogeny is similar to the Eu/Eu* signature of TTG rocks and is in contrast with what has generally been observed for the Eu anomaly in subduction settings. The trace elements trends and fractionation paths highlight the necessity of a better understanding of the trace elements distribution in zircon in relation to the geodynamic environment and geological time.

The discrimination diagrams from Grimes et al. (2015) that distinguish origin from the oceanic crust, continental arc and post-collisional crystalline units, did not identify post-collisional derived detrital zircon, despite this scenario being supported for the magmatic rocks younger than 1800 Ma (Sheppard, 2003; Sheppard et al., 2004; 2010; Johnson et al., 2017). Moreover, the Oceanic Island setting outlined in the plot of Grimes et al., (2015), do not likely represent the tectonic environment in which the protolith of the detrital zircons crystallized. In this case, the Oceanic Island setting may represent an indicator of a mafic geochemical signature of the zircons. Similarly, the E-MORB compositional filed do not indicate that E-MORB sourced the mafic zircons but indicate an overall mafic composition for the detrital zircons. This is especially true considering the tectonic history of the area studied over the time frame 2.0-1,6 Ga.

The discrepancies might be an indicator of poor applicability of the discrimination diagrams of Grimes et al. (2015), to the detrital zircon. According to what has been observed in this study and given the current state of knowledge on the geochemistry of zircons, the plots provide a useful tool to understand the mafic versus felsic composition of the zircons' parent rocks. Nevertheless, interpretations of the tectono-magmatic setting yield limitations and need complementary information on the tectonic history of the sedimentary and source rocks.

10. Conclusion

Statistical modelling (LOESS) of temporarily constrained detrital zircon trace element data can be used to unravel the geodynamic history of long-lived orogens. The Y, Gd/Yb, HREE/LREE and Eu/Eu* signatures of the detrital zircon, modelled with the LOESS, outline positive and negative trends which fingerprint distinct geodynamic environments.

The Capricorn Orogen zircon trace elements (Y, Gd/Yb, HREE/LREE and Eu/Eu*) examined through statistical modelling, show good agreement in defining the geodynamic history of the region and highlight the existence of a magmatic arc between 2050 and 1950 Ma, then a shift toward collisional setting, between 1820 and 1770 Ma and finally a post-collisional environment between 1680 and 1620 Ma.

Acknowledgements

References

Alghamdi, A. H., Aitken, A. R. A. & Dentith, M. C. (2017). The composition and structure of the deep crust of the Capricorn Orogen. *Australian Journal of Earth Sciences*, 0, 1-16.

Arndt, N. & Davaille, A. (2013). Episodic Earth evolution. *Tectonophysics,* 609, 661-674.

Belousova, E. A., Griffin, W. L., O'Reilly, S. Y. & Fisher, N. I. (2002). Igneous zircon: Trace element composition as an indicator of source rock type. *Contributions to Mineralogy and Petrology*, 143, 602-622.

Boehnke, P., Watson, E. B., Trail, D., Harrison, T. M. & Schmitt, A. K. (2013). Zircon saturation re-revisited. *Chemical Geology,* 351, 324-334.

Bradley, D. C. (2011). Secular trends in the geologic record and the supercontinent cycle. *Earth-Science Reviews*, 108, 16-33.

Brown, M. (2013). Granite: From genesis to emplacement. *Bulletin of the Geological Society of America*, 125, 1079-1113.

Cleveland, W.S. 1979. Robust locally weighted fitting and smoothing scatterplots. Journal of the American Statistical Association 74:829-836. Cleveland, W.S. 1981. A program for smoothing scatterplots by robust locally weighted fitting. *The American Statistician*, 35-54.

Campbell, I. H. & Allen, C. M. (2008). Formation of supercontinents linked to increases in atmospheric oxygen. *Nature Geoscience*, 1, 554-558.

Cawood, P. A. & Nemchin, A. A. (2000). Provenance record of a rift basin: U/Pb ages of detrital zircons from the Perth Basin, Western Australia. *Sedimentary Geology,* 134, 209-234.

Cawood, P. A. & Tyler, I. M. (2004). Assembling and reactivating the Proterozoic Capricorn Orogen: Lithotectonic elements, orogenies, and significance. *Precambrian Research,* 128, 201-218.

Cawood, P. A., Hawkesworth, C. J. & Dhuime, B. (2012). Detrital zircon record and tectonic setting. *Geology*, 40, 875-878.

Chamberlain, K. J., Wilson, C. J. N., Wooden, J. L., Charlier, B. L. A. & Ireland, T. R. (2014). New Perspectives on the Bishop Tuff from Zircon Textures, Ages and Trace Elements. *Journal of Petrology*, 55, 395-426.

Chapman, J. B., Gehrels, G. E., Ducea, M. N., Giesler, N. & Pullen, A. (2016). A new method for estimating parent rock trace element concentrations from zircon. *Chemical Geology*, 439, 59-70.

Couzinié, S., Laurent, O., Moyen, J.-F., Zeh, A., Bouilhol, P. & Villaros, A. (2016). Post-collisional magmatism: Crustal growth not identified by zircon Hf–O isotopes. *Earth and Planetary Science Letters,* 456, 182-195.

Dhuime, B., Wuestefeld, A. & Hawkesworth, C. J. (2015). Emergence of modern continental crust about 3 billion years ago. *Nature Geoscience*, 8, 552-555.

Drummond, M. S. & Defant, M. J. (1990). A model for Trondhjemite-Tonalite-Dacite Genesis and crustal growth via slab melting: Archean to modern comparisons. *Journal of Geophysical Research,* 95, 503-521.

Fu, B., Mernagh, T. P., Kita, N. T., Kemp, A. I. S. & Valley, J. W. (2009). Distinguishing magmatic zircon from hydrothermal zircon: A case study from the Gidginbung high-sulphidation Au-Ag-(Cu) deposit, SE Australia. *Chemical Geology,* 259, 131-142.

Griffin, W. L., Belousova, E. A., Shee, S. R., Pearson, N. J. & Reilly, S. Y. O. (2004). Archean crustal evolution in the northern Yilgarn Craton: U – Pb and Hf-isotope evidence from detrital zircons. *Precambrian Research,* 131, 231-282.

Grimes, C. B., John, B. E., Kelemen, P. B., Mazdab, F. K., Wooden, J. L., Cheadle, M. J., Hanghøj, K. & Schwartz, J. J. (2007). Trace element chemistry of zircons from oceanic crust: A method for distinguishing detrital zircon provenance. *Geology*, 35, 643-643.

Grimes, C. B., Wooden, J. L., Cheadle, M. J. & John, B. E. (2015). "Fingerprinting" tectono-magmatic provenance using trace elements in igneous zircon. *Contributions to Mineralogy and Petrology*, 170, 46-46.

Guo, L., Zhang, H. F., Harris, N., Xu, W. C. & Pan, F. B. (2017). Detrital zircon U–Pb geochronology, trace-element and Hf isotope geochemistry of the metasedimentary rocks in the Eastern Himalayan syntaxis: Tectonic and paleogeographic implications. *Gondwana Research,* 41, 207-221.

Halilovic, J., Cawood, P. A., Jones, J. A., Pirajno, F. & Nemchin, A. A. (2004). Provenance of the Earaheedy Basin: Implications for assembly of the Western Australian Craton. *Precambrian Research*, 128, 343-366.

Hall, C. E., Powell, C. M. & Bryant, J. (2001). Basin setting and age of the Late Palaeoproterozoic Capricorn Formation, Western Australia. *Australian Journal of Earth Sciences*, 48, 731-744.

Hammer, Ø., Harper, D. A. T. & Ryan, P. D. (2001). PAST - PAlaeontological STatistics.

Hanchar, J. M. & van Westrenen, W. (2007). Rare Earth Element Behavior in Zircon–Melt Systems. *Elements*, 3, 37-42.

Harrison, T. M., Schmitt, A. K., McCulloch, M. T. & Lovera, O. M. (2008). Early (≥4.5 Ga) formation of terrestrial crust: Lu-Hf, δ18O, and Ti thermometry results for Hadean zircons. *Earth and Planetary Science Letters*, 268, 476-486.

Hoskin, P. W. O. & Ireland, T. R. (2000). Rare earth element chemistry of zircon and its use as a provenance indicator. *Geology*, 28, 627-630.

Iizuka, T., Campbell, I. H., Allen, C. M., Gill, J. B., Maruyama, S. & Makoka, F. (2013). Evolution of the African continental crust as recorded by U-Pb, Lu-Hf and O isotopes in detrital zircons from modern rivers. *Geochimica et Cosmochimica Acta*, 107, 96-120.

Jackson, S. E., Pearson, N. J., Griffin, W. L. & Belousova, E. A. (2004). The application of laser ablation-inductively coupled plasma-mass spectrometry to in situ U-Pb zircon geochronology. *Chemical Geology*, 211, 47-69.

Johnson, S. P., Sheppard, S., Rasmussen, B., Wingate, M. T. D., Kirkland, C. L., Muhling, J. R., Fletcher, I. R. & Belousova, E. A. (2010). The Glenburgh Orogeny as a record of Palaeoproterozoic continent-continent collision. Geological Survey of Western Australia, Record 2010/5.

Johnson, S. P., Sheppard, S., Wingate, M. T. D., Kirkland, C. L. & Belousova, E. A. (2011). Temporal and hafnium isotopic evolution of the Glenburgh Terrane basement: an exotic crustal fragment in the Capricorn Orogen. Geological Survey of Western Australia, Report 110, 27.

Johnson, S. P., Thorne, A. M., Tyler, I. M., Korsch, R. J., Kennett, B. L. N. N., Cutten, H. N., Goodwin, J., Blay, O., Blewett, R. S., Joly, A., Dentith, M. C., Aitken, A. R. A. A., Holzschuh, J., Salmon, M., Reading, A., Heinson, G., Boren, G., Ross, J., Costelloe, R. D. & Fomin, T. (2013). Crustal architecture of the Capricorn Orogen, Western Australia and associated metallogeny. *Australian Journal of Earth Sciences,* 60, 681-705.

Johnson, T. E., Brown, M., Gardiner, N. J., Kirkland, C. L. & Smithies, R. H. (2017). Earth's first stable continents did not form by subduction. *Nature*, 543, 239-242.

Keller, C. B., Schoene, B., Barboni, M., Samperton, K. M. & Husson, J. M. (2015). Volcanic-plutonic parity and the differentiation of the continental crust. *Nature*, 523, 301-307.

Kemp, A. I., Hawkesworth, C. J., Paterson, B. A. & Kinny, P. D. (2006). Episodic growth of the Gondwana supercontinent from hafnium and oxygen isotopes in zircon. *Nature,* 439, 580-583.

Kemp, A. I. S., Hawkesworth, C. J., Foster, G. L., Paterson, B. A., Woodhead, J. D., Hergt, J. M., Gray, C. M. & Whitehouse, M. J. (2007). Magmatic and Crustal Differentiation History of Granitic Rocks from Hf-O Isotopes in Zircon. *Science,* 323, 141-144.

Kirkland, C. L., Smithies, R. H., Taylor, R. J. M., Evans, N. & McDonald, B. (2015). Zircon Th/U ratios in magmatic environs. *Lithos*, 212-215, 397-414.

Korhonen, F. J., Johnson, S. P., Fletcher, I. R., Rasmussen, B., Sheppard, S., Muhling, J. R., Dunkley, D. J., Wingate, M. T. D., Roberts, M. P. & Kirkland, C. L. (2015). Pressure – Temperature – Time Evolution of the Mutherbukin Tectonic Event, Capricorn Orogen Pressure – Temperature – Time Evolution of the Mutherbukin Tectonic Event, Capricorn Orogen. Geological Survey of Western Australia, Report 146.

Kylander-Clark, A. R. C., Hacker, B. R. & Cottle, J. M. (2013). Laser-ablation split-stream ICP petrochronology. *Chemical Geology,* 345, 99-112.

Licht, K. J. & Hemming, S. R. (2017). Analysis of Antarctic glaciogenic sediment provenance through geochemical and petrologic applications. *Quaternary Science Reviews*, 164, 1-24.

Liu, X.-C., Wu, Y.-B., Fisher, C. M., Hanchar, J. M., Beranek, L., Gao, S. & Wang, H. (2017). Tracing crustal evolution by U-Th-Pb, Sm-Nd, and Lu-Hf isotopes in detrital monazite and zircon from modern rivers. *Geology,* 45, 103-106.

Ludwig, K. R. (2003). Isoplot 3.00: A geochronological toolkit for Microsoft Excel. *Berkeley Geochronology Center Special Publication*, 39, 91-445.

Maniar, P.D & Piccoli, P.P.M. (1989). Tectonic discrimination of granitoids. *Geological Society of America Bulletin,* 101, 635-643.

Martin, D. M. B., Sircombe, K. N., Thorne, A. M., Cawood, P. A. & Nemchin, A. A. (2008). Provenance history of the Bangemall Supergroup and implications for the Mesoproterozoic palaeogeography of the West Australian Craton. *Precambrian Research,* 166, 93-110.

Martin, H., Moyen, J.-F., Guitreau, M., Blichert-Toft, J. & Le Pennec, J.-L. (2014). Why Archaean TTG cannot be generated by MORB melting in subduction zones. *Lithos,* 198-199, 1-13.

McCulloch, M. T. & Bennett, V. C. (1994). Progressive growth of the Earth's continental crust and depleted mantle: Geochemical constraints. *Geochimica et Cosmochimica Acta*, 58, 4717-4738.

McKenzie, N. R., Smye, A. J., Hegde, V. S. & Stockli, D. F. (2018). Continental growth histories revealed by detrital zircon trace elements: A case study from India. *Geology*, 46, 275-278.

McLennan, S. M., Taylor, S. R., McCulloch, M. T. & Maynard, J. B. (1990). Geochemical and Nd-Sr isotopic composition of deep-sea turbidites: Crustal evolution and plate associations. *Geochimica and Cosmochimica Acta*, 54, 2015-2050.

Moyen, J.-F. (2011). The composite Archaean grey gneisses: Petrological significance, and evidence for a non-unique tectonic setting for Archaean crustal growth. *Lithos,* 123, 21-36.

O'Neill, C., Lenardic, A., Moresi, L., Torsvik, T. H. & Lee, C. T. A. (2007). Episodic Precambrian subduction. *Earth and Planetary Science Letters,* 262, 552-562.

Occhipinti, S. A., Sheppard, S., Bryah, T., Basins, P., Yilgarn, A. & Complex, G. (1999). e Palaeoproterozoic tectonic evolution of the southern margin of the Capricorn Orogen, Western Australia. *Geological Society of Australia Abstract*, 53, 173-174.

Occhipinti, S. A., Sheppard, S., Passchier, C., Tyler, I. M. & Nelson, D. R. (2004). Palaeoproterozoic crustal accretion and collision in the southern Capricorn Orogen: The Glenburgh Orogeny. *Precambrian Research*, 128, 237-255.

Paton, C., Woodhead, J. D., Hellstrom, J. C., Hergt, J. M., Greig, A. & Maas, R. (2010). Improved laser ablation U-Pb zircon geochronology through robust downhole fractionation correction. *Geochemistry, Geophysics, Geosystems,* 11, 3.

Pirajno, F. (2004). Metallogeny in the Capricorn Orogen, Western Australia, the result of multiple ore-forming processes. *Precambrian Research,* 128, 411-439.

Rapp, R. P., Watson, B. E. & Miller, C. F. (1991). Partial melting of amphibolite/eclogite and the origin of Archean trondhjemites and tonalites. *Precambrian Research*, 51, 1-25.

Rapp, R. P. (1995). Amphibole-out phase boundary in partially melted metabasalt, its control over liquid fraction and composition, and source permeability. *Journal of Geophysical Research: Solid Earth*, 100, 15601-15610.

Reimink, J. R., Chacko, T., Stern, R. A. & Heaman, L. M. (2014). Earth's earliest evolved crust generated in an Iceland-like setting. *Nature Geoscience,* 7, 529-533.

Rudnick, R. L. & Gao, S. (2003). Composition of the Continental Crust. *Treatise on Geochemistry*, 3, 1-64.

Schannor, M., Lana, C. & Fonseca, M. A. (2019). São Francisco–Congo Craton break-up delimited by U–Pb–Hf isotopes and trace-elements of zircon from metasediments of the Araçuaí Belt. *Geoscience Frontiers*, 10/2, 611-628 .

Sheppard, S., Occhipinti, S. A., Tyler, I. M. & Nelson, D. R. (1999). The nature of c . 2 . 0 Ga crust along the southern margin of the Gascoyne Complex. *Geological Survey of Western Australia Annual Review*, 56-61.

Sheppard, S., Occhipinti, S. A. & Tyler, I. M. (2004). A 2005-1970 Ma Andean-type batholith in the southern Gascoyne Complex, Western Australia. *Precambrian Research,* 128, 257-277.

Sheppard, S., Occhipinti, S. A. S. A. & Nelson, D. R. (2005). Intracontinental reworking in the Capricorn Orogen, Western Australia: The 1680-1620 Ma Mangaroon Orogeny. *Australian Journal of Earth Sciences*, 52, 443-460.

Sheppard, S., Rasmussen, B., Muhling, J. R., Farrell, T. R. & Fletcher, I. R. (2007). Grenvillian-aged orogenesis in the Palaeoproterozoic Gascoyne complex, Western Australia: 1030-950Ma reworking of the Proterozoic Capricorn Orogen. *Journal of Metamorphic Geology,* 25, 477-494.

Sheppard, S., Bodorkos, S., Johnson, S. P., Wingate, M. T. D. & Kirkland, C. L. (2010). The Palaeoproterozoic Capricorn Orogeny: intracontinental reworking not continent-continent collision. Geological Survey of Western Australia, Report 108.

Sheppard, S., Fletcher, I. R., Rasmussen, B., Zi, J. W., Muhling, J. R., Occhipinti, S. A., Wingate, M. T. D. & Johnson, S. P. (2016). A new Paleoproterozoic tectonic history of the eastern Capricorn Orogen, Western Australia, revealed by U-Pb zircon dating of micro-tuffs. *Precambrian Research,* 286, 1-19.

Slama, J., Kosler, J., Condon, D. J., Crowley, J. L., Gerdes, A., Hanchar, J. M., Horstwood, M. S. A., Morris, G. A., Nasdala, L., Norberg, N., Schaltegger, U., Schoene, B., Tubrett, M. N. & Whitehouse, M. J. (2008). Plešovice zircon - A new natural reference material for U-Pb and Hf isotopic microanalysis. *Chemical Geology*, 249, 1-35.

Spencer, C. J., Kirkland, C. L. & Taylor, R. J. M. (2016). Strategies towards statistically robust interpretations of in situ U-Pb zircon geochronology. *Geoscience Frontiers*, 7, 581-589.

Spencer, C. J., Roberts, N. M. W. & Santosh, M. (2017). Growth, destruction, and preservation of Earth's continental crust. *Earth-Science Reviews*, 172, 87-106.

Spencer, C. J., Murphy, J. B., Kirkland, C. L., Liu, Y. & Mitchell, R. N. (2018). A Palaeoproterozoic tectono-magmatic lull as a potential trigger for the supercontinent cycle. *Nature Geoscience,* 11, 97-101.

Stern, R. A., Bodorkos S., Kamo S. L., Hickman A. H., Corfu F. (2009). Measurement of SIMS of Pb isotopes during Zircon dating. *Geostandards and Geoanalytical Research*, 33, 145-168.

Taylor, S. R. & McLennan, S. M. (1995). The geochemical evolution of the continental crust. *Reviews of Geophysics*, 33, 241-265.

Trail, D., Bruce Watson, E. & Tailby, N. D. (2012). Ce and Eu anomalies in zircon as proxies for the oxidation state of magmas. *Geochimica et Cosmochimica Acta*, 97, 70-87.

Valley, J. W., Lackey, J. S., Cavosie, A. J., Clechenko, C. C., Spicuzza, M. J., Basei, M. A. S., Bindeman, I. N., Ferreira, V. P., Sial, A. N., King, E. M., Peck, W. H., Sinha, A. K. & Wei, C. S. (2005). 4.4 billion years of crustal maturation: Oxygen isotope ratios of magmatic zircon. *Contributions to Mineralogy and Petrology*, 150, 561-580.

Wang, Z., Wilde, S. A. & Wan, J. (2010). Tectonic setting and significance of 2.3-2.1 Ga magmatic events in the Trans-North China Orogen: New constraints from the Yanmenguan mafic-ultramafic intrusion in the Hengshan-Wutai-Fuping area. *Precambrian Research*, 178, 27-42.

Whitehouse, M. J. & Kamber, B. S. (2002). On the overabundance of light rare earth elements in terrestrial zircons and its implication for Earth's earliest magmatic di¡erentiation. *Earth and Planetary Science Letters,* 204, 333-346.

Wiedenbeck, M., AllÉ, P., Corfu, F., Griffin, W. L., Meier, M., Oberli, F., Quadt, A. V., Roddick, J. C. & Spiegel, W. (1995). Three Natural Zircon Standards for U-Th-Pb, Lu-Hf, Trace Element and Ree Analyses. *Geostandards Newsletter*, 19, 1-23.

Wingate, M. T. D., Pisarevsky, S. A. & Evans, D. A. D. (2002). Rodinia connections between Australia and Laurentia: No SWEAT, no AUSWUS? *Terra Nova*, 14, 121-128.

Wingate, M. T. D., Pirajno, F. & Morris, P. A. (2004). Warakurna large igneous province: A new Mesoproterozoic large igneous province in west-central Australia. *Geology*, 32, 105-108.

Wu, F.-y., Jahn, B.-m., Wilde, S. & Sun, D.-y. (2000). Phanerozoic crustal growth: U–Pb and Sr-Nd isotopic evidence from the granites in northeastern China. *Tectonophysics*, 328, 89-113.

CHAPTER 7

CONCLUSIONS

The provenance investigation of the Palaeoproterozoic to Mesoproterozoic Yerrida, Edmund and Collier basins carried out in this work, have resulted in revised and novel geological interpretations. The provenance studies have highlighted a variety of depositional environments linked with distinct catchments changing from the late Palaeoproterozoic to the late Mesoproterozoic across the history of the Capricorn Orogen.

(I) The Palaeoproterozoic Yerrida Basin on the northern margin of the Yilgarn Craton deposited after 2175 Ma, during intracratonic rifting. The basin detritus was entirely sourced from Yilgarn Craton-affiliated granites. The Marymia Inlier has been interpreted to have drifted from the Yilgarn Craton during the development of the Yerrida Basin. Geochronology of detrital zircon populations and multidimensional scaling (MDS) suggest that the rift development of the Yerrida Basin coincided with a change in sources westward. Detrital zircon grains with ages 2200–2100 Ma have trace element geochemistry consistent with mafic rocks, including continental flood and MOR basalts, and are considered to have originated from syndepositional volcanic deposits. Major causes for the intracratonic rifting of the north Yilgarn Craton margin are linked with a mantle plum under the Yilgarn Craton. The continental collision of the Glenburgh Terrane and the Pilbara Craton may have acted as a subordinate factor to the intracontinental rifting.

(II) The Edmund Basin accumulation took place after 1626 Ma, during intracratonic extension of the Capricorn Orogen, just after the Mangaroon Orogeny. The sedimentary succession that constitutes the Edmund Basin is complex and characterized by sharp changes of depositional environments and unconformities. These altogether suggest that the Edmund Basin stratigraphy may require revision and that the basin should be subdivided in at least two sub-basins. Moreover, a time gap of c. 100 Ma was found between depositional packages 1-2 and depositional package 3. The Edmund Basin comprises a lower sequence that records a transgression from fluvial to deep-water sedimentation (Yilgatherra, Irregully, Gooragoora and Blue Billy formations) that formed about ~1600 My ago and a younger sequence, which hosts fluvial sediments (Kiangi Creek Formation) succeeded by sediments attributed to deep

marine environments (Coodardoo Formation) deposited between 1450–1200 My ago. The genesis of the Abra polymetallic deposit is linked to the deposition of the lower sequence of the Edmund Basin and hosted within the basal deposits of the Blue Billy Formation. Elsewhere, from the analysis of other portions of the topmost part of the stratigraphy of the Edmund Basin (drill cores MJGD27 and ISBD1 and 2) support for the sub-division of the Edmund Basin is provided by the consistent recovery of young zircon grains aged 1470–1450 Ma within the topmost part of the Kiangi Creek Formation (drill core MJGD27) and the Discovery Formation (drill core ISBD1-2).

(III) Deposition of the Collier Basin, in the southern Capricorn Orogen, occurred between 1117 Ma (detrital zircon maximum depositional age) and 1093 Ma, which is the minimum depositional age given by metamorphic titanite associated with sills intruding unconsolidated sediments of the Collier Basin. Metamorphic titanite has been demonstrated to be an effective technique for indirect dating of tectono-thermal events that are associated with contact metamorphism and hydrothermal circulation within sedimentary successions.

The Collier Basin sampled comprises two successions, the lowest yields polymodal detrital zircon age spectra that indicate sourcing from the Gascoyne Complex, Ashburton Basin and Capricorn Group and transportation in a deltaic setting from northwest towards the east. In contrast, the topmost succession records opening of an intracratonic rift from the south towards the north, between the Musgrave Province and the West Australia Craton, with detritus derived from the Musgrave Province. The depositional package 5 (Backdoor and Calyie Formation) formed locally on the southern Pilbara Craton margin, in a deltaic setting, while depositional package 6 initiated to the south during the Ngaanyatjarra Rift expansion towards north.

(IV) The geochemical plots of Belousova et al., (2002), i.e., Y versus Eu/Eu* and Y versus $(Yb/Sm)_N$, and the rock-type fields that they delineate, show limitations in assessing the protolith rock, when compared with the trace element signature of the detrital zircon grains from this study. Zircon groups defined by their crystallization age did not plot into the discrete compositional fields identified by Belousova et al. (2002), but were significantly scattered, and overlapped a large number of compositional fields. Hence most of the detrital zircon grains broadly indicate granitoid compositions, with a restricted capacity of resolution of the parent lithology.

The plots from Grimes et al. (2015) were fundamental to distinguish between mafic and felsic protolith for the detrital zircon grains examined and provided clues on the origin of the minerals and tectono-thermal setting in which their parent magma developed. In some cases, geochemical trends for distinct generations of zircons were visible, pointing out links with changes in tectonic setting of the area studied.

The detrital zircon trace elements can be used as a proxy to interpret the differentiation history of the detrital zircon sources in the Capricorn Orogen. Y enrichment and fluctuations mark secular changes in the overall Y abundance of the Earth's crust and track partial melting linked with subduction events. The trace elements ratios (Gd/Yb, LREE/HREE, Eu/Eu*) highlighted: 1- crustal recycling coeval with the 1965–1945 Ma Glenburgh Orogeny, 2- a shift between continental arc setting to collisional setting for the emplacement of the magmatic rock in the Capricorn Orogen during the c. 1880 Ma Capricorn Orogeny, 3- transition to a post-orogenic setting associated with ''decompressional melting'' synchronous to the 1680 Ma Mangaroon Orogeny.

APPENDICES

LABORATORY TECHNIQUES

Separation procedure of the minerals analysed is described in this appendix. Workflow is showed in Fig. 1.
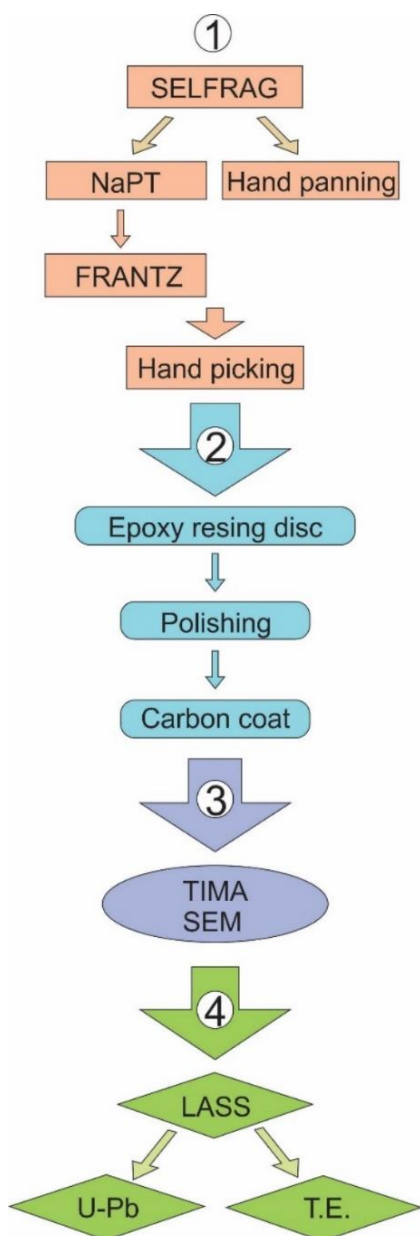

Fig. 1. Work diagram showing the mineral separation techniques and analytical steps. 1 – Mechanical, magnetic and chemical mineral separation techniques. 2 – Preparation of epoxy resin discs. 3 – Imaging with field emission scanning electron microscope (FE-SEM) and Integrated Mineral Analyser (TIMA). 4 – Laser ablation split-stream, ICP-MS (LASS), analysis of U-Pb systematic and Trace Elements (T.E.).

1. Mineral separation techniques

1.1 SELFRAG - Electrical pulse disaggregation technique

All the samples were disaggregated using the SelFrag facility at the Department of Applied Geology, Curtin University. Between 1 and 2 kg of sample was disaggregated using SelFrag high-voltage pulse power fragmentation (www.selfrag.com). Table 1 report the settings used for the different rock types that were disaggregated in this study.

The sample is placed into a steel cylinder filled with deionised water and sealed with a steel cap. The capsule is then inserted into the Selfrag Electrical facility. In the course of only a few micro seconds, a HV discharge (up to 400 kV, with an energy of 10 – 300 J per cm depending on the rock sample type) is deposited in the discharge plasma channel. The operation takes up to 1 hour and many consecutive electric pulses are

employed to separate the rock minerals. High-pressure impulses propagate through the solids causing them to be destroyed due to mechanical stress. Reflections from acoustic inhomogeneities induce tensile stress in areas of grain boundaries, inclusions or interfaces of composites, causing the material to break predominantly at these inhomogeneities. As the sample was progressively disaggregated, grains and fragments fell through an integrated mesh and into a collection vessel, which is isolated from further electrical pulses (Table 1), (www.selfrag.com), (Reddy et al., 2016).

Table1.

Sample Type	Lithology type	Frequency	Voltage	Mesh size
Sandstone and conglomerate	Fine or coarse, soft or hard	Between 2 and 3 Hz	Between 120 - 140 kV. Voltage was adjusted by small increments to the optimal value	Bottom sieve size varies from the 360 µm to 540 µm
Siltstone and mudstone	Fine-grained, soft or hard	Between 1 and 3 Hz	Between 90 - 140 kV. Voltage was adjusted by small increments to the optimal value	Bottom sieve size varies from the 360 µm to 320 µm
Oxidized/iron-rich sediments/ BIFs	Fine, hard, dark/brown, red or purple	3 Hz	Voltage was adjusted by decrements from 180kV to 130kV (very hard) or 160kV to 130KV (medium hard)	Bottom sieve size of 320 µm
Sandstone and conglomerate	Fine or coarse, soft or hard	Between 2 and 3 Hz	Between 120 - 140 kV. Voltage was adjusted by small increments to the optimal value	Bottom sieve size varies from the 360 µm to 540 µm
Siltstone and mudstone	Fine-grained, soft or hard	Between 1 and 3 Hz	Between 90 - 140 kV. Voltage was adjusted by small increments to the optimal value	Bottom sieve size varies from the 360 µm to 320 µm
Oxidized/iron-rich sediments/ BIFs	Fine, hard, dark/brown, red or purple	3 Hz	Voltage was adjusted by decrements from 180kV to 130kV (very hard) or 160kV to 130KV (medium hard)	Bottom sieve size of 320 µm

1.2 Sieving

The disaggregated samples were sieved using disposable mesh of 500 µm, 360 µm and 210 µm size. Samples from the drill cores: MJGD2, MJGD27, ISBD2, ISBD1, DD14IL014 were sieved with 500 µm, 360 µm and 210 µm meshes. Samples from AB62 and THD-001 and the outcrop samples CAP.FT28 -29 and CAP.FT30, mainly made of coarse sandstone and conglomerates, were sieved with 500 µm and 360 µm meshes.

Samples were sieved to obtain grains <210 μm that were then loaded on separatory funnels for heavy liquid separation.

Samples ranging 210-360 μm were separated with the hand pan.

1.3 Heavy liquid - Na Polytungstate (NaPT)

Heavy Liquids were used to separate the heavy mineral fraction of samples from the drill cores: MJGD2, MJGD27, ISBD2, ISBD1 and DD14IL014 that were generally made of fine lithologies and hosted sulphides and iron rich levels. The sieved <210 μm powder was separated with the heavy liquid technique (Fig. 2). The NaPt is a new generation heavy liquid type that is a non-toxic solution of Na polytungstate and distilled water, mixed with different proportions to obtain the desired density for the liquid. To separate the heavy minerals (zircon and titanite) a density of 2.89 s.g. was used. The heavy liquid of 2.89 s.g. and the crushed samples were loaded on 500 ml separatory funnel. The samples were mixed with the liquid with a stirring rod for three times waiting for c. 15 minutes between each time, and a final 30 minutes, before pouring the minerals into the filter paper. The heavy fraction that deposited at the bottom of the funnel was first poured into filter paper (Fig. 1), filtered from the NaPT and then rinsed with deionised water, to collect and recycle the NaPT liquid, for future usage. The lighter minerals, floating at the top of the funnel, were also separately collected into clean filter paper and rinsed with deionized water, to collect and recycle the NaPT.
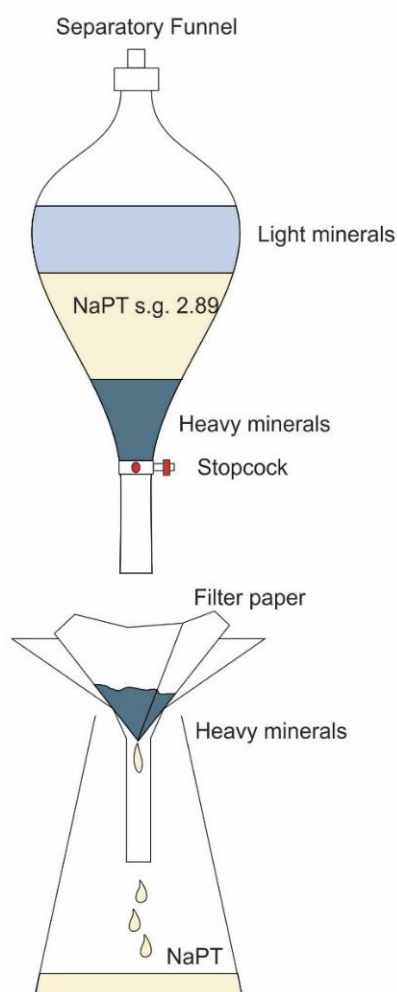
Fig. 2. Separatory Funnel and heavy and light minerals. Filter paper was used to collect the minerals and the NaPT was filtered and collected into a beaker.

1.4 Hand panning

The hand pan was used to separate the heavy minerals of the samples from the drill cores THD-001 and AB62 and the outcrop samples CAP.FT28 -29 and CAP.FT30, made of fine to coarse sandstone and conglomerate. Hand panning was done on both the sieved fraction <500 μm and <360 μm. Under flushing water, a heavy mineral fraction was separated based on the difference between the minerals' densities in water. Most of the minerals composing the samples were made by silicate minerals, which yield relatively low densities, and thus were flushed by the water through the hand pan steps into a container. The heavy fraction was collected from the bottom of the hand pan with a pipette. This method was particularly efficient for samples that did not contain associations of heavy minerals phases like magnetite, hematite, pyrite, chalcopyrite and galena that would otherwise load the manual pan of too many heavy minerals, causing problems in isolating the detrital accessory phases.

1.5 Frantz magnetic separator

The Frantz magnetic separator was used on samples from drill cores: MJGD2, MJGD27, ISBD2, ISBD1, DD14IL014 and AB62 and on the outcrop samples CAP.FT28 CAP.FT. 29 and CAP.FT30. While THD-001 was not processed through the Frantz magnetic separator.

Minerals with high magnetic susceptibility (such as magnetite) were removed using a low-level hand magnet (McClenaghan, 2011; Reddy et al., 2016). The hand magnet

also was used to remove any metallic residue from the SelFrag. Other minerals having high magnetic susceptibility were separated by using the Frantz magnetic separator, which incorporates an electromagnet with two elongate pole pieces arranged so that the in one side the magnetic field is stronger than the other side. A vibrating metal chute run parallels the pole pieces. Mineral particles are introduced into the upper end of the chute and slide toward the lower end. Those with higher magnetic susceptibility move toward the side of the chute where the magnetic flux is greater. The separator is mounted so that it can be rotated both in the direction of grain movement (slope) and in a direction normal to the direction of grain movement (tilt). The way in which mineral particles separate as they move along the length of the chute depends on (1) the tilt of the chute, (2) the amperage applied to the electromagnet and, to some extent, (3) the slope and rate of feed to the chute. At the lower end of the chute, the particles are separated into two streams, one consisting of grains of higher susceptibility than that corresponding to the amperage setting used, the other consisting of grains of lower susceptibility (McClenaghan, 2011).

To separate the heavy minerals the following set up was used:

- Slope of 30°-35°. Depending on the size of the minerals in the samples it was adjusted, lower tilt was used for coarse material, like sandstone.
- Tilt of 15°-18°. High tilt c. 18° was used with highly magnetic minerals and lower amperage.

The amperage was incremented of 0.2 - 0.5 A each step:

- Magnetic at 0.2 A was used to separate highly magnetic minerals like magnetite.
- Magnetic at 0.4 A separates magnetic minerals, like ferromagnetic minerals, aggregates, chloritoid and chromite and ferrous clay aggregates.
- Magnetic at 0.7 A.
- Magnetic at 1.2 A.
- Magnetic at 1.5 A. This was the last step and titanite and zircons were in the non-magnetic fraction.

2. Mounts

2.1 Optical microscope hand-picking

The non-magnetic (>1.5 A) fraction was then hand-picked for zircon and titanite under the light of the optical microscope (Reddy et al., 2016). All the zircons and titanite found were hand-picked. The hand-picked minerals were placed on sticky paper attached on a glass slide, for the epoxy resin mount preparation.

2.2 Mount making procedure

Zircon and titanite minerals were enclosed in 2.5 cm diameter epoxy resin discs (Fig. 3). The minerals were positioned in a square or rounded space of c. 0.7 to 1.2 cm in size. The epoxy resin was prepared with the following steps:

A ratio of 5 to 1 was used for the epoxy and the hardener respectively. The quantity was measured in grams on a digital scale (5g+1g= One epoxy disc). Quantities were adjusted based on the number of discs that were done in one session (from 1 to 3 epoxy discs at a time).

Procedure:

- 5g epoxy resin. Pour 5g epoxy resin in a small cup container previously placed on the digital scale.
- Heat the cup for 30 sec. in the oven at c. 40° C.
- Place 1g of hardener and stir (cup on the digital scale, avoid bubbles in the mixture, wooden stick to stir).
- Heat the cup in the oven 15 sec. at c. 40° C.
- Pour the mixture of epoxy and hardener into the mould (yellow plastic ring of 2.5 cm diameter) from the side, slowly, (do not move minerals from their position on the sticky tape, do not mix different samples).
- The epoxy resin was left three days to dry in the open air.

2.3 Polishing

Before the epoxy discs polishing the side without minerals of the disc was cut with an electric saw to diminish the disc thickness from c. 1.5 cm to c. 0.8 cm and obtain a flat surface for both sides (Fig. 3). The surface of the epoxy resin disc was polished during a series of steps, to expose the flat surfaces of the minerals. Zircon and titanite were abraded until half of their thickness (Fig. 3). The epoxy resin discs were all cleaned

179

with petroleum ether after every step of the polishing process. A cup filled with the petroleum ether and the resin discs was placed into an ultrasonic bath for 30 seconds, with the surface hosting the minerals oriented down. The degree and quality of the surface abrasion were estimated on the optical microscope, looking at the reflectivity of the mineral surfaces and the presence of scratch lines after and during each polishing step. Finally, the polished mineral surface was cleaned with compressed air. The polishing procedure of the mineral surface and of the mount surface was done following these steps:

- Both the mount epoxy resin disc surfaces were abraded with 2000 grit wet sandpaper for few seconds.
- Both the two sides of the disc were abraded with 6 μm wet plastic lap films for 2 minutes.
- 1 μm wet plastic lap films for 3 minutes, applied on the surface with the minerals enclosed.
- 3 μm soft cloth with diamond paste and lubricant for 30 seconds (obtain relief for the minerals.
- 1 μm soft cloth with diamond paste and lubricant for 1 minute.

At the end the surface of each resin disc was vacuum carbon coated on the polished mineral surface with a thin layer of 150 Microns before the mineral imaging.

Fig. 3. Characteristics, size and main steps of the epoxy resin disc preparation in chronological order from the top.

3. Mineral imaging

The detrital zircon and titanite mineral grains were imaged using the Tescan MIRA3 Field Emission Scanning Electron Microscope (FE-SEM) and the TESCAN Integrated Mineral Analyser (TIMA) at the Microscopy and Microanalysis Facility (John de Laeter Centre) Curtin University. The FE-SEM is
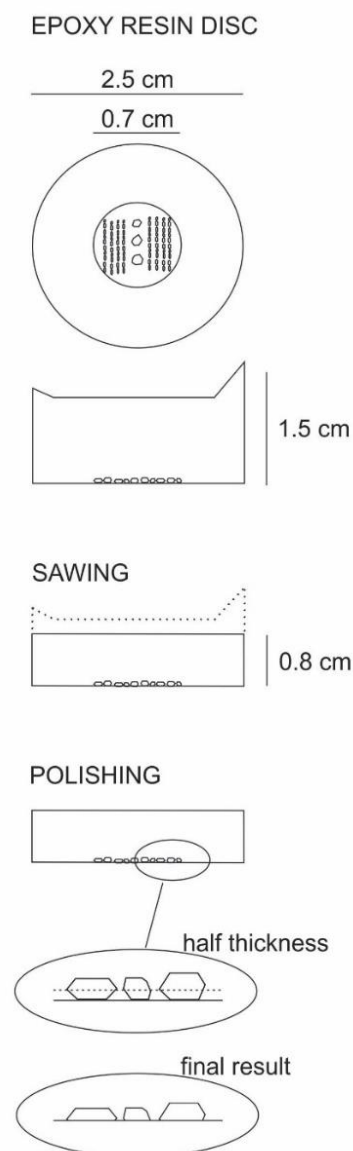
equipped with secondary electron (SE), backscatter electron (BSE), cathodoluminescence (CL), energy dispersive spectrometer (EDS) and EBSD detectors. The TIMA yields a high-resolution Field Emission Scanning Electron Microscope (FESEM) and four fully integrated Energy Dispersive Spectroscopy (EDS) detectors, for fully automated data collection, RGB colour cathodoluminescence detector (CL), SE and BSE detectors. The Tescan MIRA3 Field Emission Scanning Electron Microscope (FE-SEM) and the TESCAN Integrated Mineral Analyser (TIMA) operate with Oxford Instruments Aztec 2.4 software.

The automated EDS imaging with the TIMA was operated on samples particularly rich of heavy minerals. The automated EDS was useful to recognise mineral phases enclosed in the mount and to distinguish zircon and titanite from other heavy minerals. Then zircon and titanite were imaged with the SEM. Zircons were imaged in SE and CL modes, while the titanites were imaged with SE and BSE modes. Images were taken for 4 to 6 grains at one time. The acquisition parameters for the TIMA and SEM are listed in Table 2.

Samples from drill cores MJGD2, MJGD27, ISBD2, ISBD1, THD-001 and AB62 were imaged with both the TIMA and the SEM.
Samples from drill core DD14IL014 and the outcrop samples CAP.FT28, CAP.FT 29 and CAP.FT30 were imaged with the SEM.

Table 2.

Microscope	Detector	Scan Mode	HV (accelerating voltage)	Working Distance (WD)	Beam Intensity
TIMA	BSE-EDS	Resolution	25 kV	15 mm	~18 nA
SEM	BSE - CL	Resolution	10 kV	16.5 mm	~10 nA
SEM	SE -BSE	Resolution	15 kV	15 mm	~14 nA

4. ICP-MS (LASS) analytical technique

The U-Pb isotopes and elemental composition of zircon and titanite minerals were measured using the laser ablation split-stream ICP-MS (LASS) analytical set-up at the

John the Laeter Centre, Curtin University, and at the University of California, Santa Barbara (UCSB) (Kylander-Clark et al., 2013).

4.1 University of California, Santa Barbara, ICP-MS (LASS) analytical technique

At the University of California, Santa Barbara (UCSB) the laser ablation split-stream ICP-MS (LASS) analytical set-up consists of a Photon Machines 193 nm ArF Excimer laser coupled to a Nu Instruments Plasma multicollector inductively coupled plasma mass spectrometer (HR MC-ICPMS), and a Nu AttoM SC-ICPMS, measuring U-Pb isotopic and trace-element compositions respectively (Kylander-Clark et al., 2013). The laser aerosol is carried by He, from the sample cell to a mixing bulb in which the sample + He is mixed with Ar to stabilize the aerosol input to the plasma, afterwards the He–Ar aerosol is immediately split upon exiting the mixing bulb, with approximately half the ablation stream directed into each of the two mass spectrometers (Kylander-Clark et al., 2013). The spot size for the mineral analyses used was of 20 μm for the zircon grains and of 30 μm for the titanite grains. The laser fluence was of 3.5 J/cm^2, and the repetition rate of 4 Hz (Table 3), (Kylander-Clark et al., 2013). The samples analysed at the UCSB were from the drill cores MJGD27 and MJGD2, (Table 3 and Table 4) (year 2015).

For the U–Th–Pb analyses of the zircon and titanite minerals, the signals for masses ^{202}Hg, ^{204}(Pb+Hg), ^{206}Pb, ^{207}Pb, ^{208}Pb, ^{232}Th, and ^{238}U were acquired, with ^{235}U calculated from the measured ^{238}U concentration using the relationship ^{238}U/^{235}U=137.88. The Nu Instruments Plasma multicollector (MC-ICP-MS) consists of 12 Faraday cups and four ETP discrete dynode ion counters. The ^{238}U and ^{232}Th were measured using the Faraday cups and the ^{206}Pb, ^{207}Pb, ^{208}Pb and ^{204}Pb + Hg were measured on the ion counters.

The trace elements and REE abundances of the zircon and titanite minerals were measured on the AttoM SC-ICPMS in E-Scan mode. In E-Scan mode, the magnet is set to a fixed position and the post-electrostatic analyser (ESA) deflector voltages are altered to change the mass seen by the detector (Kylander-Clark et al., 2013). Trace element analyses included the masses ^{29}Si, ^{49}Ti, ^{89}Y, ^{139}La, ^{140}Ce, ^{141}Pr, ^{146}Nd, ^{147}Sm, ^{153}Eu,^{157}Gd, ^{159}Tb, ^{163}Dy, ^{165}Ho, ^{166}Er, ^{169}Tm, ^{172}Yb, ^{175}Lu, ^{178}Hf, ^{181}Ta, ^{232}Th and ^{238}U, measured sequentially. E-Scan mode generally yields a 2SE precision of 2–5% for elements more abundant than 100 ppm, 5–10% for elements down to 1 ppm, and >10%

for those less than 1 ppm (Kylander-Clark et al., 2013). Curtin University, Western Australia, ICP-MS (LASS) analytical technique

4.2 Curtin University, Western Australia, ICP-MS (LASS) analytical technique

The Department of Applied Geology (John de Laeter Centre), at the Curtin University, houses a Resonetics S-155-LR 193 nm excimer laser ablation system, coupled to Nu Instruments Plasma HR multi-collector ICP and an Agilent 7700x quadrupole ICP-MS, measuring U-Pb isotopic and trace element compositions respectively. The Nu Instrument Plasma is equipped with a fixed collector array of 12 Faraday cups and four low-mass ion counters. The gas He is mixed with Ar and N gasses, the aerosol is split to deliver approximately even proportions of the mix to each ICP-MS, for U–Th–Pb isotope and trace element analysis, respectively. The ablated material is carried to the mass spectrometers by He gas with a flow rate of 3.2 ml/min, Ar gas at 1 ml/min flow rate and N gas at 1.2 ml/min flow rate. During the analytical session, the laser was adjusted to 2 Jcm^{-2} fluency at a 4 Hz repetition rate, (Table 3). The ablated spot size used for the zircon was of 23 μm and 33 μm. Half of the samples of THD-001 (TD10 to TD7) were ablated with a spot size of 23 μm, while all the remaining samples from drill cores THD-001, AB62, ISBD1, ISBD2, DD14IL014 and outcrop samples CAP.FT 28, CAP.FT 29, CAP.FT 30, were ablated with a spot size of 33 μm (years 2016 and 2017). Samples with laser spot size of 23 μm had the ^{238}U and ^{232}Th masses measured using the Faraday cups and the ^{206}Pb, ^{207}Pb, ^{208}Pb and ^{204}Pb + Hg masses measured on the ion counters, with a similar set up to the analytical set up followed at the UCSB, (Kylander-Clark, 2013). All the samples analysed with the 33 μm laser spot size had masses ^{202}Hg, ^{204}(Pb + Hg), ^{206}Pb, ^{207}Pb, ^{208}Pb, ^{232}Th, and ^{238}U acquired on the Faraday cups, and ion counters switched off. ^{235}U was calculated from the measured ^{238}U concentration using the relationship ^{238}U/^{235}U = 137.88.

Trace elements and REE of the zircon minerals abundances were measured sequentially on the Agilent 7700x quadrupole ICP-MS analyses. The analyses included the masses ^{29}Si, ^{49}Ti, ^{89}Y, ^{139}La, ^{140}Ce, ^{141}Pr, ^{146}Nd, ^{147}Sm, ^{153}Eu, ^{157}Gd, ^{159}Tb, ^{163}Dy, ^{165}Ho, ^{166}Er, ^{169}Tm, ^{172}Yb, ^{175}Lu, ^{178}Hf, ^{181}Ta, ^{232}Th, and ^{238}U.

4.3 Standard and elemental abundance calculation technique

Elemental abundances and their uncertainties were calculated by interleaving matrix-matched reference materials among samples and then reducing the collected data using

the Iolite v2.5 software for both zircon and titanite minerals. The U-Pb isotopes were calculated using the Geochronology DRS and the trace elements abundance was calculated using Trace Elements DRS in Iolitev2.5 (Paton et al., 2010; Kylander-Clark et al., 2013). Background signal subtractions, down-hole fractionation correction, were corrected in Iolitev2.5 for the analysed minerals (Paton et al., 2010). The U-Pb exported $^{206}Pb/^{238}U$ and $^{207}Pb/^{206}Pb$ ratios and ages were at 1σ error. The $^{206}Pb/^{238}U$ and $^{207}Pb/^{206}Pb$ ratios and ages were then propagated to a 2σ error that was calculated based on the standard error at 2σ. The trace elements were exported with 2σ errors (Kylander-Clarck et al., 2013).

The following standards were measured along with the unknown zircon minerals using the common standard-sample-standard bracketing method during each analytical session. Along with the detrital zircons were measured: Plešovice (337.13 ± 0.37 Ma; Sláma et al., 2008), GJ1 (608.5 ± 0.4 Ma; Jackson et al., 2004), OGC (3465.4 ± 0.6 Ma, Bodorkos et al., 2009) and 91500 (1061 ± 4.3 Ma; Wiedenbeck et al., 1995), Temora (416.75 ± 0.24 Ma, Black et al., 2003). The standard BLR was used as primary standard for the titanite mineral (BLR 1047.1 ± 0.4 Ma, Aleiniknoff et al., 2007). Glass NIST610 (440 ± 16 ppm Zr) and NBS612 were measured before and during all the analytical sessions along with the natural zircon and titanite standards (Gao et al., 2002). The element used as internal standard for the trace elements calculation was Si. The internal standards used in each analytical session and the primary standards for the calculation of the isotopic and elemental concentrations used are listed in Table 4.

Table 4.

Drill core	Sample ID	Mineral	Standards	Primary standard for U-Pb	Primary standard for trace elements
MJGD2-MJGD27	MJGD27-3 toMJGD27- 5 and MJG2-7 to MJG2-18	zircon	NBS612, NIST610, 91500,OGC, GJ1, Ples, Tem	91500	GJ1
MJGD2-MJGD27	MJGD27-3 to MJGD27-5	titanite	NIST, BLR	BLR	BLR
THD-001	TD1 to TD10	zircon	NIST610, 91500, OGC, GJ1, Ples	GJ1	GJ1
AB62	AB1 to AB4	zircon	NBS612, NIST610, 91500,OGC, GJ1, Ples	91500	GJ1
AB62	AB5 to AB13	zircon	NBS612, NIST610, 91500,OGC, GJ1, Ples	Ples	GJ1
DD14IL014	DD1 to DD5	zircon	NBS612, NIST610, 91500,OGC, GJ1, Ples	Ples	GJ1
	CAP.FT28 CAP.FT29 CAP:FT30	zircon	NBS612, NIST610, 91500,OGC, GJ1, Ples	Ples	GJ1
ISBD1 - ISBD2	ISBD-1 to ISBD-5, ISBD2-7 to ISBD2-16	zircon	NBS612, NIST610, 91500,OGC, GJ1, Ples	Ples	GJ1

5. Sample coordinates

Table 1.

Drillcore	Tectonic_unit	Grid zone	Easting	Northing
DD14IL014	Collier Basin	UTM zone 51J	763200	7304300
CAP.FT28	Collier Basin	UTM zone 50J	515726	7341467
CAP.FT29	Collier Basin	UTM zone 50J	515643	7341509
CAP.FT30	Collier Basin	UTM zone 50J	522232	7342421
MJGD27	Collier Basin	UTM zone 50J	587140	7270403
MJGD2	Edmund Basin	UTM zone 50J	593040	7268753
ISBD1	Edmund Basin	UTM zone 51J	506739	7292138
ISBD2	Edmund Basin	UTM zone 51J	506431	7292588
AB62	Edmund Basin	UTM zone 51J	662152	7274152
THD001	Yerrida Basin	UTM zone 50J	774304	7187543

References

Aleinikoff, J.N., Wintsch, R.P., Tollo, R.P., Unruh, D.M., Fanning, C.M., Schmitz, M.D., 2007. Ages and origins of rocks of the Killington dome, south-central Connecticut: Implications for the tectonic evolution of southern New England. *American Journal of Science,* 307, 63–118.

Black, L. P., Kamo, S. L., Allen, C. M., Aleinikoff, J. N., Davis, D. W., Korsch, R. J. & Foudoulis, C. (2003). TEMORA 1: A new zircon standard for Phanerozoic U-Pb geochronology. *Chemical Geology,* 200, 155-170.

Bodorkos, S., Stern, R. A., Kamo, S., Corfu, F. & Hickman, A. H. (2009). OG1: A Natural Reference Material for Quantifying SIMS Instrumental Mass Fractionation of Pb Isotopes During Zircon Dating. *American Geophysical Union*, Fall Meeting 2009, abstract #V33B-2044.

Gao, S., Liu, X., Yuan, H., Hattendorf, B., Günther, D., Chen, L., Hu, S., 2002. Determination of Forty Two Major and Trace Elements in USGS and NIST SRM Glasses by Laser Ablation-Inductively Coupled Plasma-Mass Spectrometry. J. *Geostandard Geoanalasys,* 26, 181–196.

Jackson, S. E., Pearson, N. J., Griffin, W. L. & Belousova, E. A. (2004). The application of laser ablation-inductively coupled plasma-mass spectrometry to in situ U-Pb zircon geochronology. *Chemical Geology,* 211, 47-69.

Kylander-Clark, A. R. C., Hacker, B. R. & Cottle, J. M. (2013). Laser-ablation split-stream ICP petrochronology. *Chemical Geology,* 345, 99-112.

Paton, C., Woodhead, J. D., Hellstrom, J. C., Hergt, J. M., Greig, A. & Maas, R. (2010). Improved laser ablation U-Pb zircon geochronology through robust downhole fractionation correction. *Geochemistry, Geophysics, Geosystems* 11, 3.

Slama, J., Kosler, J., Condon, D. J., Crowley, J. L., Gerdes, A., Hanchar, J. M., Horstwood, M. S. A., Morris, G. A., Nasdala, L., Norberg, N., Schaltegger, U., Schoene, B., Tubrett, M. N. & Whitehouse, M. J. (2008). Plešovice zircon - A new natural reference material for U-Pb and Hf isotopic microanalysis. *Chemical Geology,* 249, 1-35.

Wiedenbeck, M., AllÉ, P., Corfu, F., Griffin, W. L., Meier, M., Oberli, F., Quadt, A. V., Roddick, J. C. & Spiegel, W. (1995). Three Natural Zircon Standards for U-Th-Pb, Lu-Hf, Trace Element and Ree Analyses. *Geostandards Newsletter,* 19, 1-23.